Cergy Paris Université — U.F.R. des Sciences

Habilitation à Diriger des Recherches

discipline: Physique

présentée par David PAPOULAR

Interactions, évaporation, et non–ergodicité dans des assemblées d'atomes froids et de Rydberg

à soutenir le 14 octobre 2024 devant le Jury composé de

M. J. AVAN
M. M. BERRY, rapporteur
M. I. DOTSENKO
M. B. DOUÇOT
M. A. HONECKER
M. B. LABURTHE, rapporteur
M. N. PAVLOFF
Mme. A. SINATRA
M. D. ULLMO, rapporteur
M. J. WALRAVEN

Interactions, evaporation, and non–ergodicity of assemblies of cold and Rydberg atoms

A theoretical approach

David J. Papoular

Laboratoire de Physique Théorique et Modélisation
UMR 8089 — CNRS — CY Cergy Paris Université

June 27, 2024

Abstract

Trapped cold or Rydberg atoms are versatile systems in which to seek novel phenomena and test established theories. In this memoir summarising the theoretical work I have performed since obtaining my PhD (U–PSud, 2011), I illustrate four of their facets: *(i)* bosonic transport, *(ii)* interatomic interactions, *(iii)* thermodynamics, and *(iv)* non–ergodicity.

Firstly, we have shown theoretically that the *transport* of cold bosonic atoms through a constricted geometry relies on collective effects involving quantum evaporation, leading to a single, enhanced conductance step.

Secondly, concerning *interactions*, we have characterised the Rydberg blockade affecting two trapped atoms (^{87}Rb and ^{85}Rb) in the case where one of them is promoted to a Rydberg state. In the course of a collaboration with experimentalists from Wuhan, China, we have used it to realise the first CNOT gate for two distinguishable atoms, and to entangle them.

Thirdly, we have constructed a *thermodynamic* description for the evaporative cooling of a chain of Rydberg atoms, and predicted that it will yield a unidimensional crystal close to its ground state. Our analysis involves a truncated Boltzmann distribution for the excitations of the chain, and a semiclassical expansion of the thermodynamic quantities. It hinges on the assumption of ergodicity.

This assumption is not innocuous. For the fourth and most recent part of our work, we have focussed on the system comprised of three interacting bosonic particles in a circular trap. This system is within experimental reach owing to recent advances in Rydberg atom trapping. We have theoretically identified two different mechanisms *impeding ergodicity* in this system. First, a quantum scar, due to a classically unstable periodic trajectory, impacts multiple quantum levels whose energies we have analysed using Gutzwiller's trace formula. Second, classical localisation occurs near stable periodic trajectories. We have characterised the energies and wavefunctions of the localised quantum states using the Einstein–Brillouin–Keller theory, highlighting the impact of discrete symmetries.

Résumé

Les systèmes d'atomes piégés, froids ou dans des états de Rydberg, constituent des systèmes polyvalents au sein desquels on peut chercher de nouveaux phénomènes ou tester des théories bien établies. Ce mémoire résume l'activité théorique que j'ai effectuée depuis l'obtention de mon doctorat (LPTMS, Université Paris–Sud, 2011). J'y illustre quatre de leurs facettes: *(i)* le transport bosonique, *(ii)* les interactions entre atomes, *(iii)* la thermodynamique, et *(iv)* les situations caractérisées par l'absence d'ergodicité.

Premièrement, nous avons montré théoriquement que le *transport* d'atomes froids bosoniques dans une géométrie présentant un étranglement repose sur des effets collectifs qui font intervenir l'évaporation quantique. Ceci conduit à un seul pallier de conductance, dont la valeur est amplifiée par rapport à son équivalent fermionique.

Deuxièmement, en ce qui concerne les *interactions*, nous avons caractérisé le blocage de Rydberg se produisant avec deux atomes piégés distinguables (^{87}Rb et ^{85}Rb) lorsque l'un d'eux est excité dans un état de Rydberg. Dans le cadre d'une collaboration avec des expérimentateurs du WIPM (Wuhan, Chine), nous l'avons utilisé pour réaliser la première porte quantique CNOT pour deux atomes distinguables, et pour en obtenir un état intriqué.

Troisièmement, nous avons construit une description *thermodynamique* pour le refroidissement évaporatif d'une chaîne d'atomes de Rydberg. Nous avons montré que ce mécanisme permettra l'obtention d'un cristal unidimensionnel proche de son état fondamental. Notre analyse fait intervenir une distribution de Boltzmann tronquée appliquée aux excitations de la chaîne, ainsi qu'un développement en puissances de $\hbar$ des fonctions thermodynamiques. Cette approche repose sur l'hypothèse d'un comportement ergodique.

Cette hypothèse n'est pas anodine. Dans la quatrième phase de notre travail, qui en est aussi la plus récente, nous nous sommes concentrés sur le système constitué de trois particules bosoniques en interaction dans un piège circulaire. Ce système est expérimentalement réalisable à l'aide des récentes avancées dans les techniques de piégeage pour atomes de Rydberg. Nous avons identifié pour ce système deux mécanismes *s'opposant à l'ergodicité.* Tout d'abord, une cicatrice quantique, due à une trajectoire périoque classiquement instable, a un impact sur plusieurs niveaux quantiques dont nous avons analysé les énergies en termes de la formule de la trace de Gutzwiller. Ensuite, un phénomène de localisation classique se produit au voisinage des trajectoires périodiques classiqment stables. Nous avons caractérisé les énergies et les fonctions d'onde des états localisés à l'aide de la théorie semi–classique d'Einstein–Brillouin–Keller, en soulignant le rôle des symétries discrètes.

Contents

Acknowledgements ix

1 Introduction 1
- 1.1 Two related families of atomic systems 1
  - 1.1.1 Cold ground–state atoms 1
  - 1.1.2 Rydberg atoms 3
- 1.2 Outline of the present memoir 4

2 Earlier work: bosonic transport, atomic interactions 5
- 2.1 Quantum evaporation of a Bose gas 5
- 2.2 Entanglement of two distinguishable atoms using the CNOT gate 8
- Article 1: Quantised bosonic conductance 11
- Article 2: Entangling two distinguishable atoms 17

3 Evaporative cooling of a chain of Rydberg atoms 23
- 3.1 From cold atomic gases to Rydberg atom chains 24
  - 3.1.1 Evaporative cooling of cold atomic gases 24
  - 3.1.2 Evaporative cooling of a chain of Rydberg atoms 24
- 3.2 Quasi–equilibrium thermodynamics of a chain 25
  - 3.2.1 The considered system 25
  - 3.2.2 Classical thermodynamics 26
  - 3.2.3 Quantum thermodynamics 28
- 3.3 Thermodynamics of the evaporation process 29
  - 3.3.1 Thermodynamic description without assuming a long chain 30
  - 3.3.2 Quasi–universality for longer chains 31
- 3.4 Conclusion 33
- Article 3: Evaporative cooling of a chain of Rydberg atoms 35

4 Mechanisms hindering ergodicity for three Rydberg atoms in a circular trap 45
- 4.1 The considered system 46
  - 4.1.1 Experimental prospects 46
  - 4.1.2 Rotational invariance: reduction to two degrees of freedom 46
  - 4.1.3 Discrete symmetries of the interaction potential V 48
  - 4.1.4 Classical mechanics 50
  - 4.1.5 Quantum mechanics 51
  - 4.1.6 Analogy with the Hénon–Heiles Hamiltonian 56

4.2 Mixed classical phase space, Berry–Robnik statistics 57
  4.2.1 Mixed classical phase space 58
  4.2.2 Berry–Robnik statistics for the quantum energy levels 60
4.3 Classical periodic trajectories 62
4.4 Quantum scars: Eigenstates localised near the unstable Trajectory B . . . 65
  4.4.1 Quantum scarred eigenstates for the Hamiltonian $H_{2\mathrm{D}}$ 65
  4.4.2 Semiclassical analysis of quantum scars: trace formula 66
  4.4.3 Comparison with other quantum scars and many–body scars 67
4.5 Classical localisation: Eigenstates localised near the stable Trajectories A, C 69
  4.5.1 Fourier analysis of conditionally periodic motion 70
  4.5.2 Semiclassical energies 72
  4.5.3 Semiclassical wavefunctions 74
4.6 Conclusion 78
Article 4: Three–particle quantum scar 79
Article 5: Classical localisation 87

5 Prospects for future work 99
5.1 Classical periodic trajectories beyond families A, B, C 99
5.2 Dynamics of the quantum scar 101
5.3 From the quantum regime to the semiclassical one 101
5.4 Four particles in a circular trap 102
5.5 Stabilising Trajectory B through periodic modulation 102
5.6 Resonance in the interaction between Rydberg atoms 103

Bibliography 105

Curriculum vitae 113

Acknowledgements

This memoir illustrates my research activities since my PhD defence in July 2011, focussing on the work I have carried out since my arrival at Laboratoire de Physique Théorique et Modélisation (LPTM), in Cergy–Pontoise, in October 2015.

I warmly thank Professor M. Berry, Dr. B. Laburthe–Tolra, and Dr. D. Ullmo for readily accepting to act as Referees. In particular, I am very grateful to Professor Berry for his encouragements and helpful suggestions. I am indebted to all members of the Jury for their interest in my work and their willingness to take part in the Defence.

I thank Prof. Ph. Lecheminant and Dr. J. Avan, Directors of LPTM, for their warm welcome and continuous support since my arrival in their lab in October 2015.

I extend my heartfelt gratitude to Prof. A. Honecker (LPTM), who patiently guided my first steps in the lab in autumn 2015, and, nine years later, has readily agreed to supervise my application to the degree of *Habilitation à Diriger des Recherches.*

I am very grateful to Prof. S. Stringari and to the late Prof. L. Pitaevskii, both from the University of Trento (Italy), for supervising my post–doctoral stay in their Institute, and for fruitful discussions that have extended well beyond my appointment there. I am no less grateful to my former PhD adviser, Prof. G. Shlyapnikov (LPTMS, Orsay, France), who has introduced me to the experimentalists in Wuhan, China, in collaboration with whom one of the activities illustrated in this memoir has been carried out.

My sincere thanks go to Profs. A. Sinatra (LKB) and Ph. Lecheminant (LPTM) for providing me with teaching opportunities at École Normale Supérieure, Paris, and in Cergy.

I thank Dr. M. Brune, DRCE and head of the Rydberg atoms group at LKB, and Prof. J.M. Raimond, for hosting me at their weekly group meeting at Collège de France.

It is always a pleasure to interact with the administrative team in Cergy–Pontoise. In particular, Mmes. H. Gary, A. Leprat, and S. Villemin have always sorted out all issues quickly, efficiently, and with a smile. Many thanks to them for their diligence and patience.

Last, but not least, I thank my parents, whose unwavering support, sound advice, and infinite benevolence have been essential to my carrying out the work presented here.

1 Introduction

This memoir illustrates the research activities I have carried out since my PhD defence (11 July 2011, at Université Paris–Sud, Orsay, France). I have chosen to focus on four articles [1–4] and one recent preprint [5], all of which report work that I have performed after my arrival, in October 2015, at Laboratoire de Physique Théorique et Modélisation (LPTM, Cergy–Pontoise, France) as a faculty researcher at CNRS (chargé de recherche CRCN7).

My research activity is theoretical. I consider conceptually simple systems, made experimentally accessible by recent developments in atomic trapping. There, I seek to apply known mechanisms to novel situations, such as the evaporative cooling [6] of a Rydberg atom chain described in chapter 3, and to implement experimentally accessible analogs of model Hamiltonians, such as the Hénon–Heiles model [7, chap. 8.2] which plays a role in chapter 4. In this memoir, phenomena relying on longer–ranged interactions (rather than the usual contact interactions of cold ground–state atoms) are emphasized.

I have thoroughly benefited from the proximity to experiments. One of the articles I present (Ref. [2], discussed in Sec. 2.2), was co–written with Prof. M.S. Zhan's experimental group in Wuhan, China, and reports measurements in good agreement with my theoretical results. Another article (Ref. 3, discussed in Chap. 3) was co–written with Dr. M. Brune, who leads the experimental group focussing on Rydberg atoms at LKB–Collège de France (Paris, France). All papers contain experimentally accessible proposals.

1.1 Two related families of atomic systems

The systems we consider are comprised of cold or Rydberg atoms, which are experimented on around the world. In France, they are especially well represented in and near Paris[1]

We now briefly review these two families of atomic systems.

1.1.1 Cold ground–state atoms

Alkali (or alkaline–earth) atoms may be trapped and cooled, and then manipulated coherently, using optical techniques. These are reviewed in Ref. [9], which is a book providing a

---

[1] Laboratories in the greater Paris area conducting experiments on cold and/or Rydberg atoms include LAC (Orsay), LCF (Palaiseau), LKB (Paris), LP–ENS (Paris), SYRTE (Paris), and LPL (Villetaneuse). Experimental and theoretical laboratories whose activities involve "quantum technologies" are federated in a single entity called QuanTiP, which LPTM takes part in.

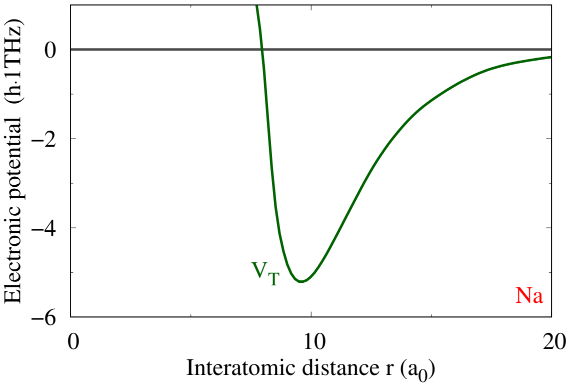

Figure 1.1: Potential $V(r)$ characterising the interaction between two ^{23}Na atoms in their electronic ground states. (This is the triplet potential, see e.g. Ref. [8].)

general introduction to cold atoms illustrated with many experiments. In contrast to the Rydberg states presented in Sec. 1.1.2, the atoms considered here are in their electronic ground states. Systems of trapped cold atoms offer experimental control over multiple parameters, including:

- The number of trapped atoms, ranging from 10^5 to two atoms or even a single one;
- The trapping geometry, e.g. a harmonic or box trap, or a spatially periodic lattice;
- The spatial dimensionality, which may be reduced from the usual 3D to 2D or 1D using stringently confining potentials along one or two directions;
- The distinguishable or identical (bosonic or fermionic) nature of the trapped atoms;
- The attractive or repulsive nature of the interatomic interaction, and its strength.

Among these, the last point, concerning interactions, deserves a special discussion.

Interactions between two cold atoms. They play a role in all contemporary applications of cold atomic systems. Depending on the goal, their role may be minimised (as in metrological applications with e.g. atomic fountain clocks [9, Sec. 18.2]), or they may be the source of superfluid behaviour in an interacting ultracold gas [10, chaps. 14 & 19].

The interaction potential between two (non–magnetic) cold atoms is illustrated in Fig. 1.1 in the case of two cold ^{23}Na atoms. Its long–distance behaviour is of the van der Waals type, $V(r) = -C_6/r^6$, where r is the interatomic distance and the coefficient $C_6 > 0$ sets the strength of the interaction. It sets the van der Waals length $l_{\mathrm{vdW}} = (mC_6/\hbar^2)^{1/4}$, with m being the mass of a single atom, which characterises the range of the interaction [11, Sec. III.A]. The length l_{vdW}, of the order of $100\,a_0 = 5\,\mathrm{nm}$ for alkali atoms, should be compared with the mean interatomic distance, which is typically of the order of 500 nm in a cold atomic gas, i.e. 100 times larger. This highlights a key feature of cold atoms: *the interatomic interaction is short–ranged.* This feature is both an advantage and a limitation.

It is an advantage because it allows for a representation of the interparticle interaction in terms of an effective contact interaction [9, chap. 15] parametrised by a single parameter, the scattering length a. The effective interaction is repulsive or attractive depending on the sign of a, and its strength is set by the absolute value $|a|$. Both its sign and its amplitude are routinely tuned in experiments by exploiting low–energy scattering resonance phenomena.

The limitation is that short–ranged interactions do not affect well–separated atoms. This makes them less effective e.g. in the realisation of multiple–qubit gates [12, Sec. 1.3.2], mentioned in Sec. 2.2. Neither do they directly yield crystallisation[2], a phenomenon sought in chap. 3. Finally, chaotic phenomena[3] due to interatomic interactions, such as those described in chap. 4, rely on the presence of longer–ranged interactions.

The restriction to short–ranged interactions may be overcome by exploiting the properties of the dipole–dipole interaction. This has been achieved experimentally in a variety of ways, relying e.g. on magnetic atoms [17] or dipolar molecules [18]. These systems will not be considered in the present report. We shall focus instead on a third family of systems exhibiting dipole–dipole interactions, i.e. systems comprised of Rydberg atoms.

1.1.2 Rydberg atoms

A Rydberg state of a (usually alkali) atom [19] is a quantum state in which the outer electron is characterised by a *large principal quantum number* n (typically the integer n is the order of 50). Hence, unlike cold atoms, Rydberg atoms are in a highly excited electronic state. Nevertheless, the lifetimes of these excited states are amenable to experiments. Among all Rydberg states, the longest–lived are the circular states [20, Sec. 5.2.1], which are such that the angular momentum $l = n - 1$ achieves its maximal value. Their lifetime exceeds 30 ms for $n = 50$. They have been exploited experimentally for more than forty years [21]. The lifetime of low–angular–momentum Rydberg states, though shorter (of the order of $100\,\mu$s for $n = 50$), is still experimentally viable [22, 23]. Thanks to recent experimental advances [24–26], atoms in Rydberg states may now be optically trapped in various geometries, enhancing the similarity with cold atoms.

The key feature offered by atoms in Rydberg states is their *very large off–diagonal dipole moment*, proportional to $d = |q|a_0\,n^2$ with a_0 being the Bohr radius. This entails that Rydberg atoms strongly couple to external electromagnetic fields, a property that has been thoroughly exploited in earlier experiments. The focus has now turned to the *strong dipole–dipole interaction* which also stems from this large dipole moment [23, 27, 28]. Depending on the considered Rydberg states and distances, the obtained interaction behaves either like C_3/r^3 or like C_6/r^6 (both regimes are illustrated in this memoir). In both cases, the corresponding length scales are comparable to, or greatly exceed, the interatomic distance, which is of the order of 5 to $10\,\mu$m. Hence, Rydberg atoms provide the longer–ranged interaction required for the applications mentioned at the end of Sec. 1.1.1.

---

[2] Nevertheless, spatially periodic structures, such as the Abrikosov vortex lattice, have been obtained within ultracold gases exhibiting short–ranged interactions [13, 14].

[3] Cold atoms have been an excellent test–bed for chaotic phenomena involving single particles [15, 16].

1.2 Outline of the present memoir

My papers [1–5] are presented in chronological order.

Earlier work. Chapter 2 briefly presents two different papers cowritten with my former postdoctoral supervisors and doctoral adviser. The first one [1], cowritten with my former postdoctoral advisers Profs. L.P. Pitaevskii and S. Stringari (Trento, Italy), identifies the role of evaporation in the transport properties of gases of cold bosonic atoms. The second paper [2], cowritten with my former PhD adviser Prof. G.V. Shlyapnikov (LPTMS, Orsay, France) along with experimentalists from Wuhan, China, describes the realisation of a *two–qubit gate* used to entangle two distinguishable atoms. These 'earlier' papers contain ideas that have played an important role in my subsequent activity. More specifically, the evaporation mechanism identified in the first paper bears a resemblance to the one analysed in chapter 3. The second paper is my first published work dealing with Rydberg atoms, which are present in all other chapters of this memoir.

Evaporative cooling of Rydberg atom chains. In chapter 3, we present the article [3], cowritten with Dr. M. Brune (LKB–Collège de France, Paris). There, we revisit evaporation, now used as a cooling mechanism applied to a chain of Rydberg atoms to obtain a (finite–sized) *long unidimensional crystal.* [3]. We describe the cooling mechanism thermodynamically using a truncated Boltzmann distribution. Our description of the quantum regime involves a *semiclassical approximation to the thermodynamic functions.* Our analysis of the cooling scheme relies on the key assumption of *ergodicity.*

Three Rydberg atoms in a circular trap. Chapter 4 describes our most recent activity. It stemmed from a desire to illustrate that the ergodic hypothesis of chapter 3 is not innocuous, and was stimulated by the observation, around that time, of a 'many–body scar' [22, 29]. In the published article [4], we propose the experimentally accessible system comprised of three Rydberg atoms in a circular trap, and identify a *quantum scar* in the motion of the interacting atoms. We analyse it semiclassically in terms of *Gutzwiller's trace fomula.* In the recent preprint [5], we identify quantum eigenstates localised in the vicinity of *classically stable periodic orbits*, for which we explicitly construct semiclassical *Einstein–Brillouin–Keller wavefunctions.* Chapter 4 is the most detailed part of this memoir.

Prospects. In Chapter 5, we briefly present a few possible extensions of our work described the preceding chap. 4. Our theoretical analysis of the interaction between Rydberg atoms, illustrated in Sec. 2.2, also plays a role. We point out that the *few–particle systems* we are considering may shed additional light on the role of mixed phase space and parametric excitation in recent experiments involving many Rydberg atoms [22, 30].

2 Earlier work: bosonic transport, atomic interactions

This brief chapter illustrates two different activities carried out during my earlier years in Cergy–Pontoise (October 2015 – October 2017), which have influenced my later work.

Section 2.1 is devoted to the impact of quantum evaporation on the transport properties of Bose gases. This work, published as Ref. [1], was performed in collaboration with my former post–doctoral supervisors Profs. L.P. Pitaevskii and S. Stringari (Trento, Italy).

Section 2.2 presents the realisation of an entangled pair of two non–identical atoms using a two–qubit gate. This work, published as Ref. [2], combines experiment and theory. It was performed in collaboration with my former PhD adviser, Prof. G. Shlyapnikov (LPTMS, Orsay, France), along with the experimental group led by Prof. M.S. Zhan (Wuhan, China).

2.1 Quantum evaporation of a Bose gas

This section describes my work on the transport properties of Bose gases [1]. We emphasize the role of *evaporation*, considered again in a different context in the subsequent chap. 3.

My work illustrated here is the latest of three contributions [1, 31, 32], all involving the same coauthors, devoted to the role of superfluidity in the transport properties of cold bosonic gases trapped in geometries inspired from mesoscopic physics[1].

---

[1] The book [10] reviews experimental and theoretical progress concerning superfluidity in dilute atomic systems. Transport phenomena in mesoscopic systems are introduced in the book [33].

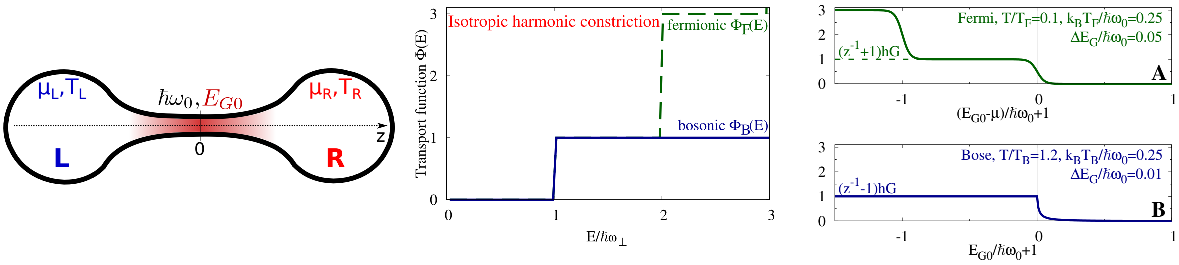

Figure 2.1: Left: Two reservoirs L, R exchange particles through a constriction, inside which the attractive gate potential E_G is varied. **Centre:** Transport function of an isotropic harmonic constriction for fermions (thin dashed line) and for bosons (full solid curve). **Right:** Quantised conductance for *(a)* ultracold fermions ($T \ll T_F$) and *(b)* cold bosons ($T > T_B$), rescaled by the step heights $1/(z^{-1} \pm 1)$. Here, T_F and T_B are the Fermi and Bose temperatures, respectively.

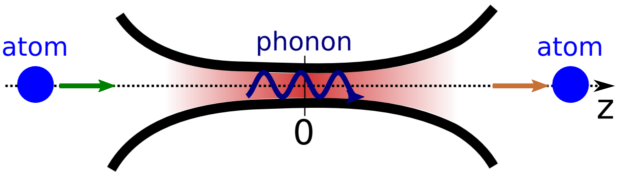

Figure 2.2: Bosonic transport through the constriction involves the condensation of an atom, exciting a phonon which propagates through the constriction and causes an atom to evaporate at its other end.

The phenomenon considered here is the *quantisation of conductance*, first observed in the electronic conductance through a quantum point contact [34]. There, the conductance G is defined in terms of the electric current I and the voltage U in between two reservoirs as $I = GU$. It depends on the gate voltage E_G applied to the quantum point contact. At low temperatures, $G(E_G)$ exhibits a sequence of well–defined steps of height q^2/h, where q is the electron charge and h is Planck's constant. The same effect was later observed in a degenerate Fermi gas of neutral fermionic atoms at temperatures much smaller than the Fermi temperature, trapped in a constricted geometry comprised of two reservoirs separated by a constriction. In this novel neutral context, G relates the time derivative of the number imbalance between two reservoirs, $\partial_t \delta N$, to the chemical potential imbalance $\delta\mu$, through the relation $\partial_t \delta N = -G\delta\mu$, and it is now quantised in units of $1/h$.

We analyse the conductance quantisation in a Bose gas trapped in a similar constricted geometry, focussing on the regime where *the gas in the reservoirs is not Bose–condensed.*

Equilibrium state. We consider a smoothly tapered constriction connecting the two reservoirs, as shown on the left panel of Fig. 2.1. At its most stringent point, we model it using a 2D isotropic harmonic oscillator with the frequency ω_0. The gate potential E_G applied in the constriction is negative. In the case of an ideal gas, all atoms would fall inside the constriction, and Bose–condense there for $E_G + \hbar\omega_0 < \mu$, where the chemical potential $\mu < 0$ characterises the non–condensed gas in the reservoirs. This would preclude the observation of transport between the reservoirs. The situation is more favourable in the presence of a weak repulsive interaction between the atoms. Then, experimentally accessible parameters may be chosen (box–trap reservoirs; temperature $T > 1.1\,T_B$, with T_B being the Bose condensation temperature defined in the reservoirs; sufficiently stringent constriction) such that a condensate does form inside the constriction, but it contains few atoms, whereas most atoms remain in the reservoirs as a non–condensed gas.

Quantum evaporation. The transport of a thermal atom from one reservoir to the other requires it to cross the condensate–filled constriction. In the considered situation, single–particle transport is blocked by the mean–field shift it experiences due to collisions with atoms in the condensate. Hence, transport must rely on a collective phenomenon, whereby an atom impinges on one end of the condensate–filled constriction and excites a phonon inside it (condensation). This phonon propagates to the other end of the constriction, where an atom is emitted (evaporation). This mechanism is illustrated in Fig. 2.2. It is the equivalent, for a superfluid Bose gas, of the quantum evaporation previously observed [35, 36] and analysed theoretically [37, 38] in the context of liquid helium.

Linear–response description. We assume that the two reservoirs have the same temperature T, and that the chemical potential imbalance $\delta\mu$ is small. In this linear regime, the Landauer–Büttiker formalism [33, chap. 1] leads to the following expression for the conductance G as a function of the gate potential E_G:

$$G(E_G) \quad = \quad h \int_0^\infty dE\, \Phi(E - E_G)\, \left.\frac{\partial f^B}{\partial \mu}\right|_{E,T} . \tag{2.1}$$

In Eq. (2.1), $f^B = 1/[z^{-1}\exp(E/(k_\mathrm{B}T)) - 1]$ is the Bose distribution function characterising the reservoirs, with $z = \exp[\mu/(k_\mathrm{B}T)]$. The transport function $\Phi(E)$ characterises the constriction: it counts the number of open channels at the energy E. We compare the transport functions for Fermi and Bose gases on the centre panel of Fig. 2.1. In the fermionic case, $\Phi_F(E)$ exhibits multiple steps, leading to the multiple plateaux observed there. However, for the bosonic case we consider, $\Phi_B(E)$ exhibits a single step, which corresponds to the gate energy E_G^step such that $E_G^\mathrm{step} + \hbar\omega_0 = \mu$. It reflects the fact that bosonic transport through quantum condensation followed by quantum evaporation is possible for all gate energies $E_G \leq E_G^\mathrm{step}$. Accordingly, unlike for fermions, we predict the occurrence of a single step in the quantised conductance for bosonic gases, as shown on the right panel of Fig. 2.1. Moreover, the height of this step is enhanced, with respect to fermions, by the factor $1/(z^{-1} - 1)$, due to the large values taken by the Bose distribution function for small energies. This enhancement factor is of the order of 30 for the experimentally accessible parameters considered in Ref. [1].

To sum up, the quantisation of conductance in a weakly–interacting, non–condensed Bose gas exhibits two important differences with respect to the fermionic case:

- A single conductance step occurs,
  which is a signature of the collective transport mechanism at play;
- The height of the step is strongly enhanced with respect to its fermionic counterpart.

An experiment similar to that of Ref. [39], performed with a Bose gas at a temperature just above the condensation temperature T_B, would allow for a confirmation of our results: To our knowledge, such an experiment[2] has not yet been performed.

---

[2] The experiment reported in Ref. [40], though related, has not been performed in the linear response regime giving direct access to the conductance.

2.2 Entanglement of two distinguishable atoms using the CNOT gate

This section illustrates my earliest article [2] dealing with atoms in Rydberg states. It is the second of two papers involving the same coauthors, both of which report joint experimental and theoretical investigations [2, 41].

In this work, Rydberg atoms are considered in view of their application to quantum computation[3]. We consider two non–identical atoms: one ^{87}Rb atom and one ^{85}Rb atom, trapped in separate single–atom microtraps. Each atom represents a qubit, i.e. a quantum mechanical two–state system. Our key result is *the realisation of an entangled pair of these two atoms through the application of a Controlled–NOT (CNOT) quantum gate.*

The CNOT gate. Quantum gates [12, Sec. 1.3] are unitary linear mappings applied to a set of qubits. The simplest gates involve single qubits or two qubits. The CNOT gate is a two–qubit gate. We call $|\uparrow\rangle$, $|\downarrow\rangle$ the basis states of the first, 'control', qubit, and $|\Uparrow\rangle$, $|\Downarrow\rangle$ those of the second, 'target' qubit. Then, the CNOT gate is represented by the following matrix, expressed in the two–qubit basis $(|\uparrow\Uparrow\rangle\,, |\uparrow\Downarrow\rangle\,, |\downarrow\Uparrow\rangle\,, |\downarrow\Downarrow\rangle)$:

$$U_{\mathrm{CNOT}} = \begin{array}{c} \\ \langle\uparrow\Uparrow| \\ \langle\uparrow\Downarrow| \\ \langle\downarrow\Uparrow| \\ \langle\downarrow\Downarrow| \end{array} \begin{array}{c} \begin{array}{cccc} |\uparrow\Uparrow\rangle & |\uparrow\Downarrow\rangle & |\downarrow\Uparrow\rangle & |\downarrow\Downarrow\rangle \end{array} \\ \begin{pmatrix} 0 & 1 & 0 & 0 \\ 1 & 0 & 0 & 0 \\ 0 & 0 & 1 & 0 \\ 0 & 0 & 0 & 1 \end{pmatrix} \end{array} \tag{2.2}$$

The matrix U_{CNOT} of Eq. (2.2) expresses the following behaviour. If the control qubit is in the state $|\downarrow\rangle$, the target qubit is left unchanged. If the control qubit is in the state $|\uparrow\rangle$, the target qubit is flipped, i.e. the state $|\Downarrow\rangle$ is mapped into $|\Uparrow\rangle$ and vice versa.

The importance of the CNOT gate stems from the following universality property [12, Sec. 4.5.2]: any unitary operation involving multiple qubits may be written as a product of single–qubit gates and two–qubit CNOT gates. In particular, the entangled state $(|\uparrow\Uparrow\rangle + |\downarrow\Downarrow\rangle)/\sqrt{2}$ may be obtained in two steps from the initial state $|\uparrow\Uparrow\rangle$. First, a single–qubit gate is applied to the control qubit so as to map it into the superposition $(|\uparrow\rangle + |\downarrow\rangle)/\sqrt{2}$. Then, the CNOT gate is applied to the resulting two–qubit state:

$$U_{\mathrm{CNOT}}\left[\frac{|\uparrow\rangle + |\downarrow\rangle}{\sqrt{2}}\,|\Downarrow\rangle\right] \quad = \quad \frac{U_{\mathrm{CNOT}}\,|\uparrow\Downarrow\rangle + U_{\mathrm{CNOT}}\,|\downarrow\Downarrow\rangle}{\sqrt{2}} \quad = \quad \frac{|\uparrow\Uparrow\rangle + |\downarrow\Downarrow\rangle}{\sqrt{2}}\,. \tag{2.3}$$

Single–qubit operations may be achieved by applying electromagnetic fields. The CNOT gate, like all other two–qubit gates, requires interactions between the two qubits.

---

[3] The book [12] provides a general overview of the field of quantum computation, and realisations using Rydberg atoms are reviewed in Ref. [27].

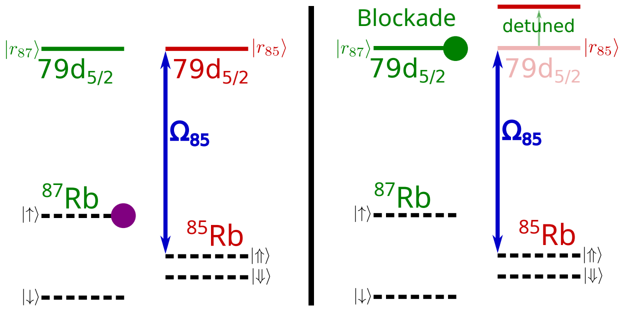

Figure 2.3: *Rydberg blockade.* On the left half of the figure, the ^{87}Rb atom is in its ground state $|\uparrow\rangle$, and the ^{85}Rb atom undergoes Rabi oscillations between its ground $|\Uparrow\rangle$ and Rydberg $|r_{85}\rangle$ states. The right half of the figure shows the blockade regime: the ^{87}Rb atom is in the Rydberg state $|r_{87}\rangle$, and the ^{85}Rb atoms remains in its ground state $|\Uparrow\rangle$.

The considered atomic states. The two selected states for ^{87}Rb, $|\downarrow\rangle = |F = 1, M_F = 0\rangle$ and $|\uparrow\rangle = |F = 2, M_F = 0\rangle$, are both within its ground hyperfine manifold. Similarly, the two selected states for ^{85}Rb are $|\Downarrow\rangle = |F = 2, M_F = 0\rangle$ and $|\Uparrow\rangle = |F = 3, M_f = 0\rangle$. The atoms are separated by distances of the order of $5\,\mu$m, which greatly exceeds the short range of the interaction between atoms in their ground states (see Sec. 1.1.1).

In order to obtain longer–ranged interactions, we exploit their Rydberg states. For both atoms, the considered Rydberg state is $|r\rangle = |79D_{5/2}, m_j = 5\rangle$, meaning that the principal and angular quantum numbers are $n = 79$ and $l = 2$, respectively. We highlight two differences with respect to the situation considered in the subsequent chapters 3 and 4:

- This is a Rydberg state with low angular momentum (in contrast to circular Rydberg states whose quantum numbers satisfy $l = n - 1$);
- In this experiment, atoms in the states $|\downarrow\rangle$, $|\uparrow\rangle$, $|\Downarrow\rangle$, $|\Uparrow\rangle$ are trapped, but atoms in Rydberg states are not trapped.

Rydberg blockade. This is the key phenomenon in the experiment. It has already been demonstrated e.g. for two identical ^{87}Rb atoms in Refs. [42, 43]. We have realised it for two distinguishable atoms. The principle of the blockade is illustrated in Fig. 2.3. The states $|\Uparrow\rangle$ and $|r_{85}\rangle$ of the ^{85}Rb atom are coupled by a two–photon transition. If the ^{87}Rb is not in the Rydberg state $|r_{87}\rangle$, the ^{85}Rb atom undergoes Rabi oscillations between these two states. However, if the ^{87}Rb is excited to the Rydberg state $|r_{87}\rangle$, the strong interaction between the two Rydberg states shifts the state $|r_{85}\rangle$ away from resonance, and the Rabi oscillations of ^{85}Rb no longer occur: this is the blockade regime.

Numerical approach. We analyse the Rydberg blockade numerically by considering the two–atom Hamiltonian H which accounts for:

- the dipole–dipole interaction between the atoms in Rydberg states;
- the Rydberg level structure;
- the Zeeman term due to the static magnetic field $\boldsymbol{B}$ present in the experiment;

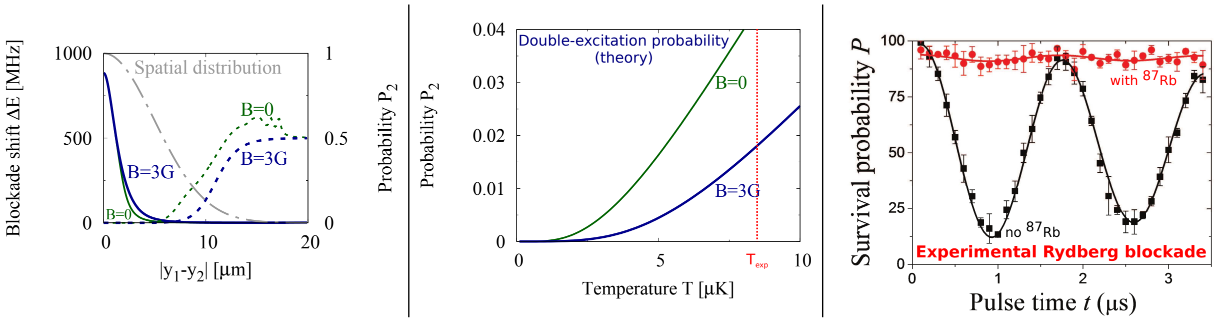

Figure 2.4: **Left:** Calculated blockade shift ΔE (left axis) and double excitation probability P_2 (right axis) as a function of the offset y in the atomic positions. **Centre:** Calculated double–excitation probability P_2 averaged over the spatial density distribution as a function of the temperature T. The vertical dashed red line shows the experimental temperature T_{exp}. **Right:** Measured probability of finding ^{85}Rb in the state $|{\Uparrow}\rangle$ as a function of time, in the case where ^{87}Rb is in the state $|{\uparrow}\rangle$ (black Rabi oscillations) or $|r_{87}\rangle$ (red points in the blockade regime).

- the state mixing due to the misalignment between $\boldsymbol{B}$ and the internuclear axis.

We restrict the Hamiltonian to a subspace spanning 437 two–atom states. These include the initial two–atom state $|r_{87} \Uparrow\rangle$, and 436 two–atom states representing both atoms in Rydberg states, including the state $|r_{87}, r_{85}\rangle$. We account for an offset $y = |y_{87} - y_{85}|$ in the positions of the two atoms within their respective microtraps. We calculate the time–dependent double excitation probability, $P_2(y,t) = 1 - |\langle r_{87} \Uparrow| e^{-iHt/\hbar} | r_{87} \Uparrow\rangle|^2$, its time–averaged value $P_2(y)$, and the corresponding blockade shift, $\Delta E(y) = \hbar\Omega_{85}(1/P_2(y) - 1)^{1/2}$, shown on the left panel of Fig. 2.4. Here, the Rabi frequency Ω_{85} characterises the coupling between the states $|{\uparrow}\rangle$ and $|r_{85}\rangle$ of the ^{85}Rb atom. Finally, we account for the thermal broadening by averaging $P_2(y)$ over the spatial probability distribution for the atoms. Our numerical results for the thermal–averaged $P_2(T)$ are shown on the central panel of Fig. 2.4. At the mean experimental temperature T_{exp}, we predict the average double–excitation probability $P_2(T_{\text{exp}}) \approx 0.013$. This is of the same order of magnitude as the observed quench of the Rabi oscillation amplitude shown on the right panel of Fig. 2.4.

The CNOT gate is realised by combining the Rydberg blockade with single–atom operations, and used to entangle the atoms according to Eq. 2.3. The fidelity [12, Sec. 9.2.2] of the realised entangled state is on par with the similar experiments realised with identical atoms [42, 43]. The originality of our work resides in the fact that the entangled atoms are distinguishable: ours is the first realisation of a CNOT gate for distinguishable atoms, and we provide an explicit example of an entangled state of two distinguishable particles.

PHYSICAL REVIEW A **94**, 023622 (2016)

Quantized conductance through the quantum evaporation of bosonic atoms

D. J. Papoular,[1,2,*] L. P. Pitaevskii,[1,3] and S. Stringari[1]
[1] *INO-CNR BEC Center and Dipartimento di Fisica, Università di Trento, 38123 Povo, Italy*
[2] *LPTM, UMR 8089 of CNRS and Université de Cergy-Pontoise, 95302 Cergy-Pontoise, France*
[3] *Kapitza Institute for Physical Problems, Kosygina 2, 119334 Moscow, Russia*

(Received 9 June 2016; published 17 August 2016)

We analyze theoretically the quantization of conductance occurring with cold bosonic atoms trapped in two reservoirs connected by a constriction with an attractive gate potential. We focus on temperatures slightly above the condensation threshold in the reservoirs. We show that a conductance step occurs, coinciding with the appearance of a condensate in the constriction. Conductance relies on a collective process involving the quantum condensation of an atom into an elementary excitation and the subsequent quantum evaporation of an atom, in contrast with ballistic fermion transport. The value of the bosonic conductance plateau is strongly enhanced compared to fermions and explicitly depends on temperature. We highlight the role of the repulsive interactions between the bosons in preventing them from collapsing into the constriction. We also point out the differences between the bosonic and fermionic thermoelectric effects in the quantized conductance regime.

DOI: 10.1103/PhysRevA.94.023622

I. INTRODUCTION

In mesoscopic systems, where the motion of quantum particles occurs over distances of the order of their coherence length, transport phenomena exhibit quantum signatures [1]. The quantization of conductance [2] is a hallmark among these effects. It reflects the discrete nature of the transport channels inside a strongly constricted geometry and occurs if the spread in energies of the incident particle distribution is smaller than the energy separation of these channels. It was first observed in electronic transport through a quantum point contact [3] as a series of plateaus in the conductance when the distance between the gate electrodes was increased. In this fermionic case, the conductance quantum $G_K = e^2/h$ involves fundamental constants only, making it relevant for metrology [4]. Unlike the quantum Hall effect [5], it occurs in the absence of a magnetic field and has been predicted to affect neutral helium atoms [6]. The recently observed universal value for the low-temperature thermal conductance [7–10] is a related effect.

Conductance quantization has recently been observed in ultracold fermionic gases [11]. Atomic gases allow a clean observation in a simple setup involving two reservoirs connected by a constriction within which an attractive gate potential $E_G < 0$ is varied (see Fig. 1). Experiments on ultracold fermions aim at simulating electronic systems using neutral particles [11–14]. In the fermionic experiment of Ref. [11], conductance quantization has been observed at temperatures much lower than both the Fermi temperature T_F and the confinement energy of the constriction, in analogy with the original results on electronic transport [3] where only particles near the Fermi surface take part in transport phenomena. This raises the question of whether conductance quantization also affects bosons. Previous observations in an optical setup [15,16] and predictions with cold matter waves [17] have focused on systems where all particles have the same incident energy, mimicking fermionic transport at the Fermi energy. To our knowledge, the specific role of bosonic statistics in quantized conductance situations has not yet been investigated. Cold atom setups allow the exploration of mesoscopic physics in situations where the Bose distribution plays a key role [18–20]. They are also expected to exhibit the phenomenon of quantum evaporation, whereby an elementary excitation of a superfluid reaches its surface and causes the evaporation of a single atom. This phenomenon had so far been studied experimentally [21,22] and theoretically [23,24] in superfluid ^{4}He, and we consider it here in the context of superfluid atomic gases.

In this article, we show that conductance quantization occurs with bosonic atoms as well, and that the Bose statistics strongly enhance the value of the conductance step compared to fermions. Unlike for fermions, this value explicitly depends on temperature, and the effect occurs with bosons up to temperatures higher than with fermions. Furthermore, we show that the underlying transmission mechanism is very different from the fermionic case and leads to the occurrence of a single conductance plateau as the gate potential is varied, coinciding with the appearance of a condensate in the constriction. Transmission through the constriction relies on quantum condensation followed by quantum evaporation: an atom impinging on one end of the constriction excites a phonon in the condensate, which travels through the constriction and causes the evaporation of a single atom at its other end. Hence, transport through the constriction involves a collective mechanism, as in Ref. [25]. However, we focus on weakly interacting Bose gases with temperatures T slightly above the critical temperature T_B in the reservoirs, so that these contain a thermal gas and no superflow occurs, in contrast to Refs. [25–27] where the condensate is also present in the reservoirs.

The two reservoirs L and R of Fig. 1 can exchange particles via a constriction of length l_C produced by the potential $V_C(r,z)$. At its most stringent point $z = 0$, we model it by the radial harmonic trap $V(r,0) = m\omega_0^2 r^2/2$. We assume that the gate potential $E_G(z) < 0$ also reaches its maximum value $|E_{G0}|$ at $z = 0$.

II. EQUILIBRIUM STATE

We first state two conditions on the strength of the interatomic interactions which are required for our analysis to hold for bosons. These interactions should be (i) weak

---

[*] david.papoular@u-cergy.fr

©2016 American Physical Society

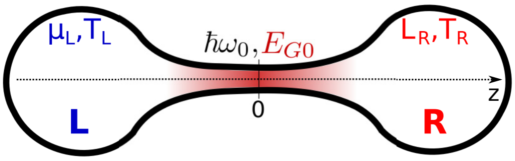

FIG. 1. Two reservoirs (L, R) can exchange particles through a smoothly tapered constriction inside which the spatially dependent and attractive gate potential E_G is varied.

enough for the reservoir thermodynamics to be dominated by single-particle effects for temperatures $T \gtrsim T_B$, and (ii) strong enough to avoid a collapse of the system into the attractive constriction. These conditions are compatible and easily realized with bosonic atoms trapped in box-like potentials [28].

(i) The effects of weak interactions in uncondensed Bose gases are well described by Hartree-Fock theory (see Chap. 13 in Ref. [29]). It predicts the chemical potential $\mu(n,T) = \mu^{(0)}(n,T) + 2gn$, with $\mu^{(0)} < 0$ being the ideal-gas value, n the density, and $g > 0$ the interaction strength. In this theory, the Bose distribution reads $f^B(E) = 1/[e^{(E+2gn-\mu)/k_BT} - 1] = 1/[z^{-1}e^{E/k_BT} - 1]$, where the ideal-gas fugacity $z = \exp(\mu^{(0)}/k_BT)$ and $E = p^2/2m$. The quantity $\partial f^B/\partial\mu|_T$, relevant for linear response, can be replaced by $\partial f^B/\partial\mu^{(0)}|_T$ if $2gn\kappa_T \ll N$. Here, N is the atom number in one reservoir, and the isothermal compressibility $\kappa_T = \partial N/\partial\mu|_T$ is linked to its ideal-gas value by $N/\kappa_T = 2gn + N/\kappa_T^{(0)}$. For $T \gtrsim T_B$, $\kappa_T^{(0)} k_B T_B/N = \sqrt{\pi}/[\zeta(3/2)\sqrt{1-z}]$, and the condition $2gn\kappa_T \ll N$ means $1 - z \gg (gn/k_BT_B)^2 4\pi/\zeta^2(3/2)$. For a uniform gas, this condition is well satisfied for $T/T_B \geqslant 1.1$. We focus on box-trap reservoirs which, for Bose gases, are more favorable than the harmonically trapped case, as interactions play a weaker role within uniform gases ($gn/k_BT_B \approx 0.02$) than in trapped geometries ($gn/k_BT_B \approx 0.2$) [19]. Thus, we can describe the atoms in the reservoirs as an ideal Bose gas with μ negative and small. We take $\mu/\hbar\omega_0 \approx -0.01$ in the following.

(ii) Despite the assumption $T > T_B$, condensation occurs in the constriction [30–32] if the gate potential $E_{G0} < -\hbar\omega_0 + \mu$ is attractive enough for the energy of the first transverse state in the constriction to match the chemical potential of the gas in the reservoirs. Then, in the absence of interactions, the atoms would collapse into the constriction, impeding the investigation of transport. The presence of weak repulsive interactions between the bosons prevents this collapse by making the presence of too many atoms in the constriction energetically disfavored. Neglecting the dilute thermal cloud, the condensate wave function $\Psi_0(r)$ at $z = 0$, which depends only on the distance r to the axis, is the lowest energy solution to the Gross-Pitaevskii (GP) equation:

$$(\mu - E_{G0})\Psi_0 = \left(-\frac{\hbar^2}{2m}\Delta_r + \frac{1}{2}m\omega_0^2 r^2 + g|\Psi_0|^2\right)\Psi_0\,, \quad (1)$$

where the radial Laplacian satisfies $r\Delta_r\Psi_0 = d(rd\Psi_0/dr)/dr$, $g = 4\pi\hbar^2 a/m$, and a is the scattering length encoding the interactions. The density $|\Psi_0|^2$ at the point $z = 0$ is determined by the effective chemical potential $\mu - E_{G0} > 0$. Figure 2 shows the linear density $n_1 = \int 2\pi r dr |\Psi_0|^2$ as a function of E_{G0}. For $\mu - E_{G0} < \hbar\omega_0$, the constriction is empty. For $(\mu - E_{G0})$ just above $\hbar\omega_0$, the condensate wave function is nearly a Gaussian with the extent $l_0 = (\hbar/m\omega_0)^{1/2}$, and $gn_1/l_0^2 = 2\pi(\mu - E_{G0} - \hbar\omega_0)$. For more attractive gate potentials, the Thomas-Fermi profile is quickly reached, leading to $gn_1/l_0^2 = \pi(\mu - E_{G0})^2/\hbar\omega_0$. In all three cases, for E_{G0} up to a few $\hbar\omega_0$, the atom number in the constriction $N_C < l_C/a$. Hence, N_C/N is small if the constriction is short enough, in which case the atom number in the reservoirs is unaffected by the small condensate in the constriction. On the other hand, the one-dimensional (1D) density $n_1 \gg a/l_0^2$, so that the condensate does not enter the strongly confined 1D regime ([29], Chap. 24).

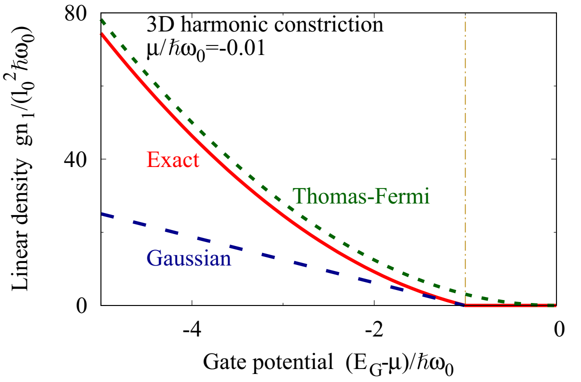

FIG. 2. Linear condensate density at the center of the constriction as a function of the gate potential. The exact numerical result (thick red line) interpolates in between the Gaussian approximation (dashed blue), valid for $|E_{G0}| \gtrsim \hbar\omega_0$, and the Thomas-Fermi result (dotted green), holding for large $|E_{G0}|$.

III. TRANSPORT PROPERTIES

We focus on small deviations from the equilibrium situation where both reservoirs are characterized by the same chemical potential μ and temperature T. An important difference between fermionic and bosonic transport phenomena concerns the energies of the particles undergoing transport. In the linear response regime, these are the energies for which the derivative $\partial f^{F,B}/\partial\mu|_{E,T}$ of the (Fermi or Bose) distribution function with respect to μ is non-negligible. For fermions, this derivative is strongly peaked near the Fermi energy k_BT_F with a width $\sim k_BT$ [see Fig. 3(b)], confirming the key role of the Fermi surface. These fermions have nonvanishing energies and efficiently traverse even sharply defined constrictions [33]. By contrast, for bosons, the derivative $\partial f^B/\partial\mu|_{E,T}$ nearly diverges for the energy $E = 0$, and the mobile particles have energies $\lesssim (1 - z)k_BT_B \approx |\mu|$ [see Fig. 3(c)]. This divergent behavior leads to the bosonic enhancement of conductance. Our choice of $T \gtrsim T_B$ means that $|\mu| \ll k_BT_B$, and we assume in the following that $k_BT_B \lesssim \hbar\omega_0$, hence, mobile bosonic atoms have energies $\ll\hbar\omega_0$. Low-energy reflections at the ends of the constriction [34] can be made negligible by smoothly connecting it to the reservoirs [35] with a radius of curvature R which is large compared to the characteristic atom wavelength $(\hbar^2/m|\mu|)^{1/2} \sim 10 l_0$. Such a smoothly tapered constriction was already used in the experiment of Ref. [11] where the Fermi momentum k_F satisfies $k_F R \sim 100$.

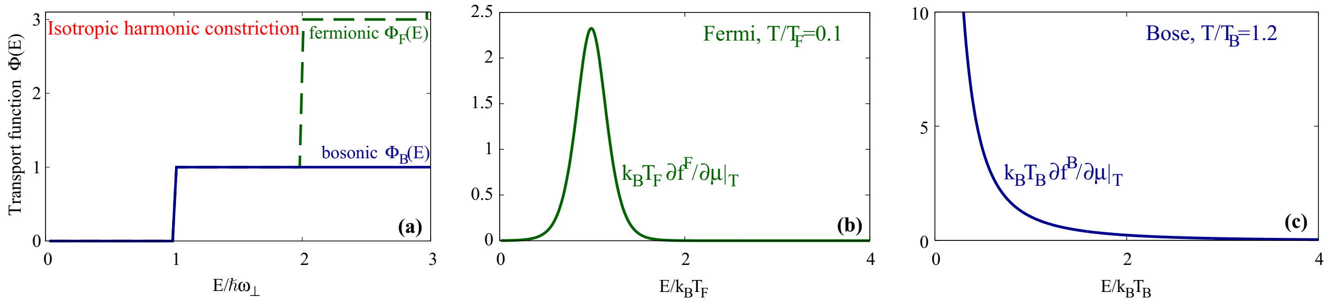

FIG. 3. (a) Transport function of an isotropic harmonic constriction for fermions (thin dashed line) and for bosons (full solid curve). (b) and (c): Derivatives $\partial f^F/\partial\mu|_T$ and $\partial f^B/\partial\mu|_T$ of the Fermi ($T/T_F = 0.1$) and Bose ($T/T_B = 1.2$) distributions.

Introducing the small differences in atom numbers, $\delta N = N_R - N_L$, and chemical potentials, $\delta\mu = \mu_R - \mu_L$, between the reservoirs, we define the isothermal conductance G by the relation $\partial_t \delta N = -G\partial\delta\mu$ (we go beyond the isothermal approximation in Sec. V). The Landauer-Büttiker formalism (see Chap. 1 in Ref. [1]) leads to the expression $hG(E_G) = L_0$, where for any α, L_α reads

$$L_\alpha = \int_0^{+\infty} dE\, \Phi^{F,B}(E - E_G)\left(\frac{E-\mu}{k_BT}\right)^\alpha \frac{\partial f^{F,B}}{\partial\mu}\bigg|_{E,T}. \quad (2)$$

This equation holds for both fermionic and bosonic systems. It is applicable whatever the reservoir geometry, encoded in the value of the degeneracy temperature $T_D = T_{F,B}$ ([29], Chap. 10). Equation (2) shows that $G(E_G)$ is the convolution of two functions, which both depend on the quantum statistics: (i) the transport function $\Phi^{F,B}(E)$ of the constriction, and (ii) the derivative of the (Fermi or Bose) distribution function $f^{F,B}(E) = 1/[z^{-1}\exp(E/k_BT) \pm 1]$ of the reservoirs.

We first summarize the fermionic results of Ref. [11]. Pauli exclusion ensures that the constriction remains empty, so that transmission is a single-particle ballistic effect. The transport function $\Phi^F(E)$, which counts the transport channels whose threshold energies are $\leqslant E$, is determined by the most stringent part of the constriction. It reads $\Phi^F(E/\hbar\omega_0) = \lfloor E/\hbar\omega_0\rfloor(\lfloor E/\hbar\omega_0\rfloor + 1)/2$, where $\lfloor x\rfloor$ stands for the integer part of x. It exhibits jumps for energies that are integer multiples $p\hbar\omega_0$ of the constriction strength, reflecting the opening of additional transport channels [dashed green line in Fig. 3(a)]. These jumps are the cause of the quantization of conductance.

We now consider bosonic atoms. If the gate potential $E_{G0} > -\hbar\omega_0 + \mu$, the constriction is empty (see Fig. 2). For sufficiently smooth spatial variations of $V_C(\mathbf{r})$ and $E_G(z)$, the motion of single thermal particles impinging on it is quasiclassical [35]. These experience a repulsive barrier of height $(\hbar\omega_0 + E_{G0})$, so that low-energy transmission through the constriction is blocked. Instead, for $E_{G0} < -\hbar\omega_0 + \mu$, the constriction is filled with a condensate whose presence strongly affects the nature of the transport mechanism within the channel. The energies $\lesssim |\mu|$ of the incident atoms are smaller than gn_0 at the center of the constriction, so that transport is now a collective process. It involves quantum condensation followed by quantum evaporation [21,23,24], which rely on the superfluidity of the condensate and, hence, on the presence of interactions in between the bosons. A thermal atom in a reservoir impinging on the constriction with energy E condenses into an elementary excitation inside the superfluid with energy $\epsilon = E - \mu$, which crosses the constriction and evaporates an atom at its other end. We describe this process using the Bogoliubov equations (see Ref. [29], Chap. 12). The condensate density $n_0(r,z)$, which appears in these equations, varies along the z axis, and the Bogoliubov equations reduce to the Schrödinger equation in the reservoirs, where $n_0 = 0$. Under our assumption of a smoothly tapered constriction, the condensate can locally be described as translationally invariant along the axial direction for each z, and the corresponding Bogoliubov spectrum varies adiabatically with z. The transport properties of the system are dictated by the strongly constricted region near $z = 0$, where the condensate density is maximal. There, the density profile $n_0(r)$ is nearly that of a condensate trapped in the elongated radial harmonic trap $m\omega_0^2r^2/2$ with the effective chemical potential $(\mu - E_{G0})$. The corresponding Bogoliubov excitation spectrum has multiple branches reflecting the 3D geometry [36]. However, the condensate occupies the lowest energy solution of the GP, Eq. (1), hence, its low-energy excitations belong to the first branch. For $|E_{G0}|/\hbar\omega_0 \gtrsim 1.1$, the incident atoms have energies $\lesssim |\mu| \ll gn_0$ and the excitations crossing the constriction are phononic. Regardless of the value of E_{G0}, the second branch has the threshold energy $2\omega_0$ [36,37], which is much greater than the incident energies, so that this branch is never involved. The smooth spatial variation of $V_{\text{ext}}(\mathbf{r})$ ensures a full conversion of the incident atoms into excitations of the superfluid.

To sum up, if the constriction is empty because the energy of its first transverse mode is $>\mu$, bosonic transmission is blocked; instead, if E_G is sufficiently attractive for the constriction to contain a condensate, transmission is allowed and relies on a collective phenomenon involving quantum condensation and evaporation. These two mechanisms lead to a bosonic transport function which exhibits a single step. Under our assumption of a smoothly tapered constriction, it reads $\Phi^B(E/\hbar\omega_0) = \Theta(E/\hbar\omega_0 - 1)$, where Θ is the Heaviside step function [see Fig. 3(a)].

IV. QUANTIZED CONDUCTANCE

The conductance $G(E_G/\hbar\omega_0)$ calculated from Eq. (2) depends on T/T_D and $\hbar\omega_0/k_BT_D$. We compare the fermionic and bosonic predictions in Fig. 4 ($T/T_F = 0.1$ for fermions and $T/T_B = 1.2$ for bosons; $\hbar\omega_0/k_BT_D = 4$ in both cases).

The fermionic prediction has the multiple step structure observed in Refs. [3,11] due to the stepwise structure of the ballistic $\Phi^F(E)$. By contrast, the bosonic graph exhibits one single step, relating to the single step of $\Phi^B(E)$. It occurs for $E_G = -\hbar\omega_0$ and, hence, coincides with the appearance of the condensate in the constriction (see Fig. 2). For bosons, Eq. (2) can be integrated analytically; an analogous result is obtained for the first fermionic step by accounting for a single transport channel. We find

$$hG^{F,B} = \begin{cases} \frac{1}{z^{-1}\exp[(E_G+\hbar\omega_0)/k_\mathrm{B}T]\pm 1} & \text{if } E_G > -\hbar\omega_0, \\ \frac{1}{z^{-1}\pm 1} & \text{if } E_G \leqslant -\hbar\omega_0, \end{cases} \tag{3}$$

where the $+$ and $-$ signs respectively apply to fermions and bosons. Equation (3) reveals three differences between fermions and bosons, concerning the step positions, their heights, and the widths of the transition regions between two plateaus: (i) For fermions, the step is centered on $E_G = -\hbar\omega_0 + \mu$, reflecting the key role of the Fermi surface at energies $\sim\mu$. For bosons, the low-energy divergence discussed above causes the step to occur at $E_G = -\hbar\omega_0$. (ii) For ultracold fermions, the fugacity $z \to \infty$, leading to the step height $1/(z^{-1}+1) \approx 1$. Instead, for bosons, $z \lesssim 1$ for $T \gtrsim T_B$, leading to the very large step height $1/(z^{-1}-1) \approx 27$ for $T/T_B = 1.2$. (iii) For fermions, the width of the transition region is $\Delta E_G^F \sim 2k_\mathrm{B}T$, whereas the corresponding width for bosons is $\Delta E_G^B \sim (1-z)k_\mathrm{B}T \approx |\mu|$. The conductance step is well defined if $\Delta E_G \ll \hbar\omega_0$. Hence, Bose systems are greatly favored, as seen on Fig. 4 where $k_B T/\hbar\omega_0$ is ten times as large for bosons than for fermions, but the bosonic step width is quenched by the factor $(1-z)$.

The conductance G is positive, hence, the current $\partial_t \delta N$ opposes the atom number difference δN, which relaxes to equilibrium as $\delta N = \delta N_0 \exp(-t/\tau_1)$. The decay time $\tau_1 = \kappa_T/G$ is proportional to N and is conveniently expressed in units of $\tau_D = Nh/k_B T_D$. Its measurement allows for an access to $G(E_G/\hbar\omega_\perp)$. It has recently been measured with fermions [11], where $\kappa_T k_\mathrm{B} T_F/N = 3/2$ at small T, so that $\tau_1 = 3\tau_D/2 \sim$ a few seconds for the first conductance plateau. For bosons, the isothermal compressibility diverges as one approaches the critical temperature, but the stronger divergence of G leads to shorter decay times $\tau_1 = \tau_D(1-z)^{1/2}\sqrt{\pi}/\zeta(3/2) \sim$ a few hundred ms for the single conductance plateau.

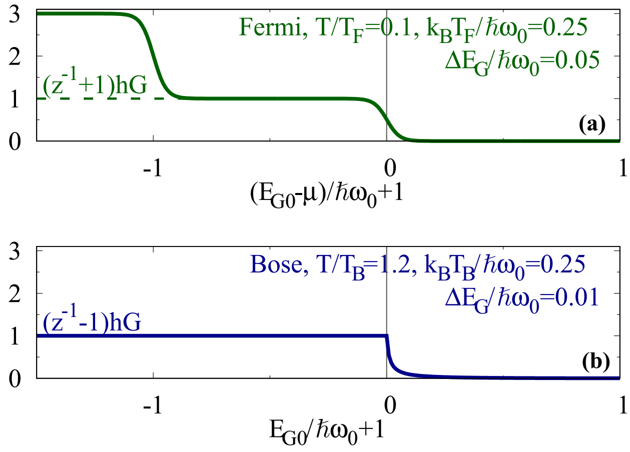

FIG. 4. Quantized conductance for (a) ultracold fermions ($T/T_F = 0.1$) and (b) cold bosons ($T/T_B = 1.2$). In both cases, $\hbar\omega_0/k_B T_D = 4$. For fermions, the thick solid line is the exact solution $G(E_{G0})$ and the thin dashed curve is the single-transport-channel prediction of Eq. (3). The results have been vertically rescaled by the step heights $1/(z^{-1} \pm 1)$.

V. THERMOELECTRIC EFFECTS

The preceding analysis neglects the impact of temperature changes $\delta T(t)$ on the dynamics of δN. We evaluate this impact using the transport model of Refs. [14,19]:

$$\tau_1 \frac{d}{dt}\begin{pmatrix} \delta N/N \\ \delta T/T \end{pmatrix} = \begin{pmatrix} -1 & \mathcal{S}\frac{\kappa_T k_\mathrm{B} T}{N} \\ \mathcal{S}\frac{N k_\mathrm{B}}{C_N} & -\tau_1/\tau_T \end{pmatrix}\begin{pmatrix} \delta N/N \\ \delta T/T \end{pmatrix}. \tag{4}$$

The coupling between particle and heat currents, proportional to the Seebeck coefficient $\mathcal{S} = -\partial\mu/\partial T|_N - L_1/L_0$, plays a role over times of the order of the thermalization time $\tau_T = C_N/(hL_2 T)$, where $C_N = T\partial S/\partial T|_N$ is the heat capacity and the integrals L_α are given by Eq. (2). For short times $t \ll \tau_1$, δT is negligible and Eq. (4) reduces to the isothermal limit investigated above. Before the bosonic conductance step or the first fermionic conductance step, both G and the thermal conductance hL_2 are small. This leads to times τ_T which are longer than the characteristic time over which the transport phenomenon can be observed (a few seconds in the case of Ref. [11]) both for bosons and for fermions, which justifies the isothermal analysis presented above. However, τ_T becomes shorter with increasing $|E_G|$. Starting from the (first) conductance step, thermal effects cause the relaxation of $\delta N(t)$ towards equilibrium to slow down, and an accurate modeling of this relaxation requires two exponential terms accounting for both time scales τ_1 and τ_T. This is illustrated in Fig. 5. Both the fermionic and bosonic plots, resulting from a

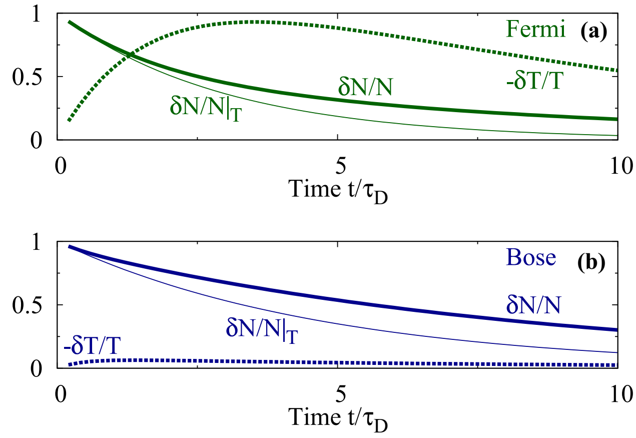

FIG. 5. Atom number difference $\delta N(t)/N$ (thick solid line), its isothermal approximation $\delta N(t)/N|_T$ (thin solid line), and temperature difference $\delta T(t)/T$ (dashed line), following an atom number mismatch δN_0, for (a) fermions and (b) bosons, obtained by solving Eq. (4) numerically with the parameters of Fig. 4. The value of E_G is chosen at the conductance step for bosons, and at the first conductance step for fermions. All plotted quantities should be multiplied by $\delta N_0/N$.

numerical solution of Eq. (4) for values of E_G corresponding to the (first) conductance step, differ from the isothermal prediction for times $\gtrsim \tau_T$. The coupling between particle and heat currents also yields a thermoelectric effect, whereby an initial atom imbalance δN_0 yields a transient change in temperature $\delta T(t)$ [14,38]. This thermoelectric effect is weak for bosons. However, for fermions, its amplitude is enhanced for gate potentials corresponding to a step in the particle conductance G. This is due to the existence of maxima in the quantity $\mathcal{S}/\tau_1$, appearing in the off-diagonal elements of Eq. (4), which have previously been observed in electronic transport experiments [39].

VI. DISCUSSION AND CONCLUSION

The quantization of bosonic conductance involving quantum evaporation precludes its interpretation as the diffraction of atomic matter waves, in contrast with previous studies [3,15,17]. It also requires an attractive gate potential, unlike for fermions where conductance may be scanned by varying the constriction width [3,11].

The bosonic enhancement of conductance near the Bose-Einstein condensate transition is the transport analog of the enhancement of the isothermal compressibility. It is due to the possibility of accommodating multiple bosons in the lowest energy transport channel, which is more populated at temperatures closer to T_B. This enhancement signals a departure from the fermionic conductance quantum $G_K = 1/h$ observed both with electrons [3] and with neutral fermions [11]. Its observation in a regime where conductance is not quantized has recently been reported [20]. Both the compressibility κ_T and the conductance G, which diverge in the ideal-gas model, depend on many-body effects in the critical region near the transition [40], where their characterization remains an open problem from both the theoretical and experimental points of view. The measurement of the relaxation time τ_1 in bosonic systems with temperatures very close to T_B will provide more insight into these two quantities.

Challenging open questions include (i) conductance quantization in 2D bosonic systems, where the quasicondensate enhances the role of interactions [41–43], and (ii) its impact in the presence of a superfluid, whose investigation has been initiated by recent experiments with strongly interacting Fermi gases [13,44,45].

ACKNOWLEDGMENTS

We thank J.-P. Brantut and T. Esslinger for stimulating discussions. This work has been supported by the European Research Council (ERC) through the QGBE grant, by the QUIC grant of the Horizon 2020 FET program, and by Provincia Autonoma di Trento.

---

[1] Y. Nazarov and Y. Blanter, *Quantum Transport: Introduction to Nanoscience* (Cambridge University, New York, 2009).
[2] H. van Houten and C. Beenakker, Phys. Today **49**, 22 (1996).
[3] B. J. van Wees, H. van Houten, C. W. J. Beenakker, J. G. Williamson, L. P. Kouwenhoven, D. van der Marel, and C. T. Foxon, Phys. Rev. Lett. **60**, 848 (1988).
[4] W. Nawrocki, *Introduction to Quantum Metrology* (Springer, New York, 2015), Chap. 7.
[5] J. E. Avron, D. Osadchy, and R. Seiler, Phys. Today **56**, 38 (2003).
[6] Y. Sato, B. Eom, and R. Packard, J. Low Temp. Phys. **141**, 99 (2005).
[7] L. G. C. Rego and G. Kirczenow, Phys. Rev. Lett. **81**, 232 (1998).
[8] K. Schwab, E. A. Henriksen, J. M. Worlock, and M. L. Roukes, Nature **404**, 974 (2000).
[9] M. Meschke, W. Guichard, and J. P. Pekola, Nature **444**, 187 (2006).
[10] S. Jezouin, F. D. Parmentier, A. Anthore, U. Gennser, A. Cavanna, Y. Yin, and F. Pierre, Science **342**, 601 (2013).
[11] S. Krinner, D. Stadler, D. Husmann, J.-P. Brantut, and T. Esslinger, Nature **517**, 64 (2015).
[12] J.-P. Brantut, J. Meneike, D. Stadler, S. Krinner, and T. Esslinger, Science **337**, 1069 (2012).
[13] D. Stadler, S. Krinner, J. Meineke, J.-P. Brantut, and T. Esslinger, Nature **491**, 736 (2012).
[14] J.-P. Brantut, C. Grenier, J. Meineke, D. Stadler, S. Krinner, C. Kollath, T. Esslinger, and A. Georges, Science **342**, 713 (2013).
[15] E. A. Montie, E. C. Cosman, G. W. t. Hooft, M. B. van der Mark, and C. W. J. Beenakker, Nature **350**, 594 (1991).
[16] H. van Houten and C. W. J. Beenakker, in *Analogies in Optics and Microelectronics*, edited by W. van Haeringen and D. Lenstra (Kluwer, Dordrecht, 1990).
[17] J. H. Thywissen, R. M. Westervelt, and M. Prentiss, Phys. Rev. Lett. **83**, 3762 (1999).
[18] D. J. Papoular, G. Ferrari, L. P. Pitaevskii, and S. Stringari, Phys. Rev. Lett. **109**, 084501 (2012).
[19] D. J. Papoular, L. P. Pitaevskii, and S. Stringari, Phys. Rev. Lett. **113**, 170601 (2014).
[20] S. Eckel, J. G. Lee, F. Jendrzejewski, C. J. Lobb, G. K. Campbell, and W. T. Hill, Phys. Rev. A **93**, 063619 (2016).
[21] W. D. Johnston and J. G. King, Phys. Rev. Lett. **16**, 1191 (1966).
[22] F. R. Hope, M. J. Baird, and A. F. G. Wyatt, Phys. Rev. Lett. **52**, 1528 (1984).
[23] P. W. Anderson, Phys. Lett. A **29**, 563 (1969).
[24] F. Dalfovo, A. Fracchetti, A. Lastri, L. Pitaevskii, and S. Stringari, Phys. Rev. Lett. **75**, 2510 (1995).
[25] D. B. Gutman, Y. Gefen, and A. D. Mirlin, Phys. Rev. B **85**, 125102 (2012).
[26] T. Karpiuk, B. Grémaud, C. Miniatura, and M. Gajda, Phys. Rev. A **86**, 033619 (2012).
[27] D. P. Simpson, D. M. Gangardt, I. V. Lerner, and P. Krüger, Phys. Rev. Lett. **112**, 100601 (2014).
[28] A. L. Gaunt, T. F. Schmidutz, I. Gotlibovych, R. P. Smith, and Z. Hadzibabic, Phys. Rev. Lett. **110**, 200406 (2013).
[29] L. P. Pitaevskii and S. Stringari, *Bose-Einstein Condensation and Superfluidity*, 2nd ed. (Oxford University, Oxford, 2016).
[30] P. W. H. Pinkse, A. Mosk, M. Weidemüller, M. W. Reynolds, T. W. Hijmans, and J. T. M. Walraven, Phys. Rev. Lett. **78**, 990 (1997).

[31] D. M. Stamper-Kurn, H. J. Miesner, A. P. Chikkatur, S. Inouye, J. Stenger, and W. Ketterle, Phys. Rev. Lett. **81**, 2194 (1998).

[32] N. J. van Druten and W. Ketterle, Phys. Rev. Lett. **79**, 549 (1997).

[33] A. Szafer and A. D. Stone, Phys. Rev. Lett. **62**, 300 (1989).

[34] L. D. Landau and E. M. Lifshitz, *Quantum Mechanics: Non-relativistic Theory*, 3rd ed. (Butterworth-Heinemann, Boston, 1977), Sec. 25.

[35] L. I. Glazman, G. B. Lesovik, D. E. Khmel'nitskii, and R. I. Shekhter, JETP Lett. **48**, 238 (1988).

[36] C. Tozzo and F. Dalfovo, New J. Phys. **5**, 54 (2003).

[37] L. P. Pitaevskii and A. Rosch, Phys. Rev. A **55**, R853(R) (1997).

[38] A. Rançon, C. Chin, and K. Levin, New J. Phys. **16**, 113072 (2012).

[39] L. W. Molenkamp, H. van Houten, C. W. J. Beenakker, R. Eppenga, and C. T. Foxon, Phys. Rev. Lett. **65**, 1052 (1990).

[40] L. Verney, L. Pitaevskii, and S. Stringari, Europhys. Lett. **111**, 40005 (2015).

[41] N. Prokof'ev and B. Svistunov, Phys. Rev. A **66**, 043608 (2002).

[42] R. J. Fletcher, M. Robert-de-Saint-Vincent, J. Man, N. Navon, R. P. Smith, K. G. H. Viebahn, and Z. Hadzibabic, Phys. Rev. Lett. **114**, 255302 (2015).

[43] R. Desbuquois, T. Yefsah, L. Chomaz, C. Weitenberg, L. Corman, S. Nascimbène, and J. Dalibard, Phys. Rev. Lett. **113**, 020404 (2014).

[44] D. Husmann, S. Uchino, S. Krinner, M. Lebrat, T. Giamarchi, T. Esslinger, and J.-P. Brantut, Science **350**, 1498 (2015).

[45] S. Krinner, M. Lebrat, D. Husmann, C. Grenier, J.-P. Brantut, and T. Esslinger, arXiv:1511.05961.

Entangling Two Individual Atoms of Different Isotopes via Rydberg Blockade

Yong Zeng,[1,2,3] Peng Xu,[1,2,*] Xiaodong He,[1,2] Yangyang Liu,[1,2,3] Min Liu,[1,2] Jin Wang,[1,2]
D. J. Papoular,[4] G. V. Shlyapnikov,[5,6,7,8] and Mingsheng Zhan[1,2,†]
[1]*State Key Laboratory of Magnetic Resonance and Atomic and Molecular Physics,*
Wuhan Institute of Physics and Mathematics,
Chinese Academy of Sciences—Wuhan National Laboratory for Optoelectronics, Wuhan 430071, China
[2]*Center for Cold Atom Physics, Chinese Academy of Sciences, Wuhan 430071, China*
[3]*School of Physical Sciences, University of Chinese Academy of Sciences, Beijing 100049, China*
[4]*LPTM, UMR8089 of CNRS and Université de Cergy-Pontoise, F-95302 Cergy-Pontoise, France*
[5]*LPTMS, UMR8626 of CNRS and Université Paris-Sud, F-91405 Orsay, France*
[6]*SPEC, CEA & CNRS, Université Paris-Saclay, CEA Saclay, F-91191 Gif–sur–Yvette, France*
[7]*Russian Quantum Center, Novaya Street, Skolkovo, Moscow Region R–143025, Russia*
[8]*Van der Waals-Zeeman Institute, Institute of Physics, University of Amsterdam, The Netherlands*

(Received 12 March 2017; published 18 October 2017)

We report on the first experimental realization of the controlled-NOT (CNOT) quantum gate and entanglement for two individual atoms of different isotopes and demonstrate a negligible cross talk between two atom qubits. The experiment is based on a strong Rydberg blockade for ^{87}Rb and ^{85}Rb atoms confined in two single-atom optical traps separated by 3.8 μm. The raw fidelities of the CNOT gate and entanglement are 0.73 ± 0.01 and 0.59 ± 0.03, respectively, without any corrections for atom loss or trace loss. Our work has applications for simulations of many-body systems with multispecies interactions, for quantum computing, and for quantum metrology.

DOI: 10.1103/PhysRevLett.119.160502

Quantum entanglement is crucial for simulating and understanding exotic physics of strongly correlated many-body systems [1–3] and it is the key quantity for quantum information processing [4–6]. Entanglement of nonidentical particles provides a richer correlation physics, and for quantum information the interspecies entanglement has unique advantages in connecting quantum networks [7] for quantum nondemolition readout and for memory protection [8,9]. The entanglement of different qubits [10] has recently been demonstrated for two different ions [11,12].

Among various platforms that have allowed the realization of quantum entanglement, trapped neutral atoms offer unique possibilities for quantum computing and simulations. This is because, in contrast to ions, they allow for an excellent control of the interaction strength over 12 orders of magnitude [5,13] and for the creation of tunable multidimensional arrays of single atoms [14]. Although important experiments have been done towards realizing useful quantum information processing and quantum simulation with atomic systems [14–20], there are several primary challenges to be solved [10]. One of them is quantum nondemolition (QND) and low cross talk qubit measurement with a few μm qubit spacing. The two-element neutral atom system shows an important advantage here, since substantially different resonant frequencies of the two species allow the spectral isolation and individual addressing of the qubits. Also, manipulating multielement single atoms can provide extra degrees of freedom for quantum simulations. In realizing a Rydberg quantum simulator [21] another species atomic qubit can work as an auxiliary qubit to manipulate or mediate the many-body spin interaction in target qubits, or provide a dissipative element when being optically pumped.

In this Letter, we present the first realization of quantum entanglement of two individual neutral atoms of different isotopes. We obtain an entangled state of ^{87}Rb and ^{85}Rb atoms confined in single-atom optical traps separated by 3.8 μm. The entanglement is generated from a heteronuclear CNOT quantum gate, which is created using the Rydberg blockade. We encode the control qubit in the ground hyperfine states $|F = 1, M_F = 0\rangle = |\downarrow\rangle$ and $|2, 0\rangle = |\uparrow\rangle$ of ^{87}Rb, whereas the target qubit is encoded in the states $|2, 0\rangle = |\Downarrow\rangle$ and $|3, 0\rangle = |\Uparrow\rangle$ of ^{85}Rb. For both atoms, the Rydberg state is $|r\rangle = |79D_{5/2}, m_j = 5/2\rangle$. Unlike in the case of the same atoms, we exploit the difference in the resonant frequencies of the two atoms to individually address and manipulate them. In this way, we ensure a negligible cross talk during state measurements and qubit operations at short interatomic separations. This makes the entanglement of different isotopes very different from the entanglement of identical atoms that are distinguishable by their spatial location with no overlap of their wave functions like in the experiment of Ref. [22].

The experimental apparatus and the single-atom trapping procedure for ^{87}Rb and ^{85}Rb atoms have been described in our recent work [23] [see Fig. 1(b)]. We then optically pump ^{87}Rb to the $|\uparrow\rangle$ state and ^{85}Rb to the $|\Uparrow\rangle$ state. After

© 2017 American Physical Society

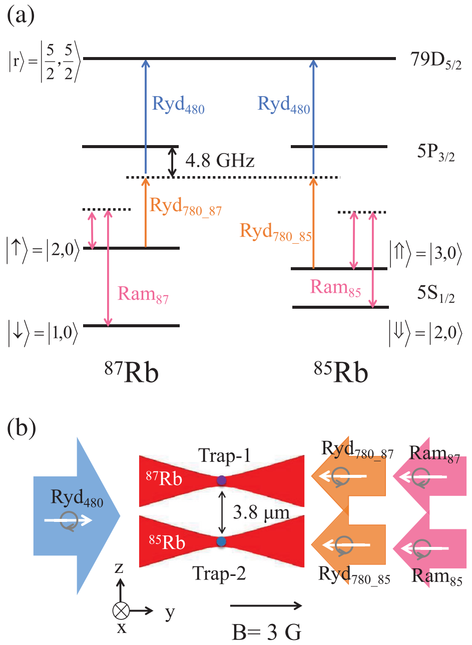
(a)
$|r\rangle=\left|\frac{5}{2},\frac{5}{2}\right\rangle$
79D5/2
Ryd480
Ryd480
4.8 GHz
5P3/2
Ryd780_87
Ryd780_85
$|\uparrow\rangle=|2,0\rangle$
$|\Uparrow\rangle=|3,0\rangle$
Ram87
Ram85
5S1/2
$|\downarrow\rangle=|1,0\rangle$
$|\Downarrow\rangle=|2,0\rangle$
87Rb
85Rb
(b)
Ryd480
Trap-1
87Rb
3.8 μm
85Rb
Trap-2
Ryd780_87
Ram87
Ryd780_85
Ram85
z
y
x
B= 3 G

FIG. 1. Experimental setup. (a) Energy levels and lasers for ^{87}Rb and ^{85}Rb. Atoms are excited to Rydberg states through Raman transitions using 480 ($^{\mathrm{Ryd}}480$) and 780 nm ($^{\mathrm{Ryd}}780$) σ^+-polarized lasers. The laser $^{\mathrm{Ryd}}480$ is blue detuned by 4.8 GHz from the intermediate state, and its waist 12.8 μm covers both atoms. The lasers $^{\mathrm{Ryd}}780-87$ and $^{\mathrm{Ryd}}780-85$, whose frequencies differ by 1.13 GHz, address ^{87}Rb and ^{85}Rb. The degeneracy of the Rydberg states $|79D_{5/2}, m_j\rangle$ is lifted by the static magnetic field $B = 3$ G along the quantization axis y, and the laser frequencies are resonant with the $m_j = 5/2$ state. Single qubit operations are performed through Raman transitions using the 795 nm lasers $^{\mathrm{Ram}}85$ and Ram_{87}, which are red detuned by 50 GHz from the $5S_{1/2} \to 5P_{1/2}$ transition. (b) Experimental geometry. Two 830 nm lasers have the beam waist 2.1 μm to form two dipole traps separated by 3.8 μm along the z direction.

that the trapping potentials are adiabatically lowered from 0.6 to 0.1 mK. Both microtraps have trapping frequencies $\omega_y/2\pi = 1.39 \pm 0.01$ kHz in the longitudinal direction and $\omega_r/2\pi = 16.9 \pm 0.1$ kHz in the radial direction [see Fig. 1(b)]. We measure the atom temperatures $T_{87} = 8 \pm 1$ and $T_{85} = 9 \pm 1$ μK using the release and recapture method [24]. Next, we combine Rydberg excitation pulses and single qubit operations with Raman lasers in order to demonstrate the heteronuclear Rydberg blockade, implement the CNOT gate, and entangle the two heteronuclear atoms. It is worth noting that both dipole traps are turned off during 6 μs for adding the Rydberg excitation pulses. The atom loss induced by turning off the traps is less than 2% in our setup. At the end of each sequence, we detect the qubit state by using a resonant laser to "blow away" $|\uparrow\rangle$ and $|\Uparrow\rangle$ atoms, so that the survival probabilities refer to the atoms in the $|\downarrow\rangle$ and $|\Downarrow\rangle$ states.

As the first step of our experiment, we show a negligible cross talk between the two atom qubits in state measurements and qubit operations. This is crucial for our setup because all lasers cover both atoms, and the individual addressing of a single atom relies on the frequency difference of ^{87}Rb and ^{85}Rb rather than on the spatial distribution. During qubit state measurements the resonant blow away laser of ^{85}Rb may destroy the coherent state of ^{87}Rb due to unwanted scattering since the laser is detuned 1.1 GHz from ^{87}Rb, and vice versa We check this influence by adding the blow away pulse of ^{85}Rb in between the ^{87}Rb ground state Rabi oscillation and the ^{87}Rb blow away pulse. We then compare the Rabi oscillations of ^{87}Rb with and without the pulse of ^{85}Rb as shown in Fig. 2(a). The amplitudes of the Rabi oscillations are equal within the measurement uncertainty, which shows a negligible cross talk in the state measurement. For Rydberg excitation, we use the two-photon transitions with the total Rabi frequency of about 1 MHz as shown in Fig. 1. Thus, the GHz spectral difference can provide enough protection for the qubit operations with each single atom. We also observe almost no excitation of ^{85}Rb when adding the Rydberg excitation laser of ^{87}Rb as shown in Fig. 2(b). Thanks to the negligible cross talk between the two atom qubits, we can put two atoms close enough to each other to reach a sufficiently strong Rydberg interaction for suppressing the blockade errors.

To demonstrate the heteronuclear Rydberg blockade, we first calculate the expected Rydberg blockade shift, which is different from that for the same atoms. If both atoms are in the $|r\rangle$ state, their interaction is dominated by the Förster resonance between the two-atom states in the $(79d_{5/2}, 79d_{5/2})$, $(80p_{3/2}, 78f)$, and $(81p_{3/2}, 77f)$ manifolds. We restrict the Förster interaction Hamiltonian to a subspace spanned by 436 states corresponding to distinguishable

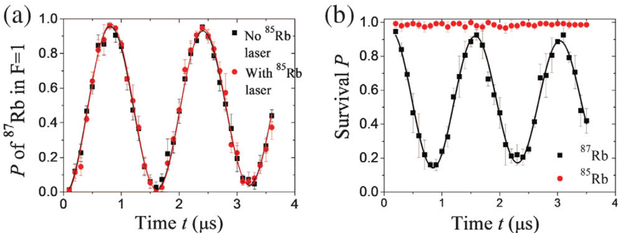

FIG. 2. Cross talk between ^{85}Rb and ^{87}Rb. (a) Rabi oscillations between the ^{87}Rb $|\uparrow\rangle$ and $|\downarrow\rangle$ states of ^{87}Rb (black squares). The red circles show the experimental data obtained when using the ^{85}Rb blow away laser before measuring the state of ^{87}Rb. The solid curves are damped sinusoidal fits $P = P_0 + Ae^{-t/t_0}\cos[2\pi f(t-t_c)]$, with $A = 0.49 \pm 0.01$, $f = 0.625 \pm 0.002$ MHz, and $t_0 = 28 \pm 7$ μs for black squares and $A = 0.50 \pm 0.02$, $f = 0.625 \pm 0.003$ MHz, $t_0 = 27 \pm 15$ μs for red circles. (b) The ^{87}Rb Rydberg excitation laser covers both ^{87}Rb in trap 1 (black squares) and ^{85}Rb in trap 2 (red circles). The ^{87}Rb atom shows coherent Rabi oscillations between the $|\uparrow\rangle$ and $|r\rangle$ states. The solid curves are damped sinusoidal fits with $A = 0.41 \pm 0.01$, $f = 0.685 \pm 0.008$ MHz, and $t_0 = 19 \pm 5$ μs. The ^{85}Rb atom is almost unaffected, which shows a negligible cross talk.

atoms. Taking the initial two-atom state $|r\Uparrow\rangle$ we account for its coupling to the Förster states and calculate the time evolution of the probability for both atoms to be in any of the excited Rydberg states taking part in the Förster resonance, $P_{85}(y,t) = 1 - |\langle r\Uparrow|e^{-iHt/\hbar}|r\Uparrow\rangle|^2$, and its average over time, $P_{85}(y)$. The latter depends on the offset $y = |y_2 - y_1|$ of the two atoms along the y direction. The blockade shift $\Delta E(y)$ is deduced from the relation $P_{85}(y) = (\hbar\Omega_{85})^2/[(\hbar\Omega_{85})^2 + \Delta E^2]$ [25], where Ω_{85} is the effective Rabi frequency for ^{85}Rb. At zero temperature, for the distance $z = 3.8\ \mu$m between the microtraps, assuming a spatial offset $y = 1\ \mu$m, the effective Rydberg interaction between the atoms is close to the strongly interacting Förster regime [5]. Accordingly, the numerical results yield $P_{85} \approx 10^{-6}$ and a very large blockade shift $\Delta E/h = 600$ MHz [26]. The finite temperature of the atoms causes them to explore larger values of the offset, $y \gtrsim 10\ \mu$m, leading to the mean double-excitation probability $\langle P_{85}\rangle \approx 0.013$ for our temperatures $T_{87} = 8$ and $T_{85} = 9\ \mu$K.

We realize the Rydberg blockade by applying a Rydberg π pulse on ^{87}Rb, waiting for 0.3 μs, and applying a Rydberg pulse of variable duration on ^{85}Rb [Fig. 3(a)]. We measure the Rabi oscillations between the ^{85}Rb $|\Uparrow\rangle$ and $|r\rangle$ states as a function of the second pulse duration [Fig. 3(b)]. The Rydberg states are detected through the atom loss with an efficiency of ~90%, and the Rydberg excitation efficiency for ^{87}Rb and ^{85}Rb is ~96% (see Supplemental Material [26]). The lifetime of the $|r\rangle$ state is over 180 μs, providing a long enough blockade for ^{85}Rb. We do not record the experimental data when ^{87}Rb is still in the trap after the sequence, so as to eliminate unblockaded events when ^{87}Rb is not excited to the $|r\rangle$ state. The peak-to-peak amplitude of ^{85}Rb Rabi oscillations between the $|\Uparrow\rangle$ and $|r\rangle$ states is 0.91 ± 0.02 in the absence of ^{87}Rb in trap 1 [Fig. 3(b)]. In its presence, the experimental data show a strong Rydberg blockade that suppresses the oscillation amplitude to 0.03 ± 0.01, in accordance with our theoretical prediction. The remaining weak oscillations of ^{85}Rb are mainly due to not perfect experimental conditions, including the loss of ^{87}Rb and transitions to other Rydberg states.

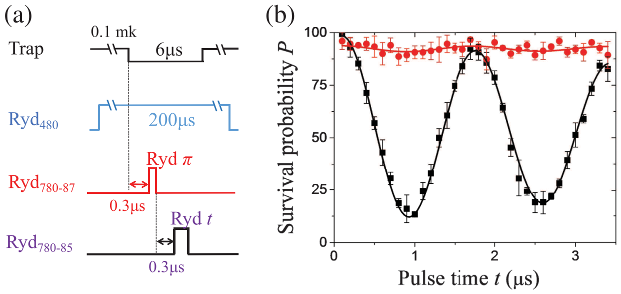

FIG. 3. Heteronuclear Rydberg blockade. (a) Time sequence. (b) Rabi oscillations between the ^{85}Rb $|\Uparrow\rangle$ and $|r\rangle$ states. The experimental data are shown both in the absence (black squares) and in the presence (red circles) of ^{87}Rb in trap 1. The solid curves are damped sinusoidal fittings with $P = P_0 + Ae^{-t/t_0}\cos[2\pi f(t - t_c)]$. The fitting parameters are $A = 0.455 \pm 0.008$, $f = 0.600 \pm 0.003$ MHz, $t_0 = 10 \pm 1\ \mu s$ for black squares. We preset $f = 0.6$ MHz, $t_0 = 10\ \mu s$ for red circles to get $A = 0.017 \pm 0.006$. Each data point is an average value of 150 measurements.

Next, we use the Rydberg blockade to generate a heteronuclear CNOT gate following the protocol of Ref. [32]. This involves three Rydberg pulses [Fig. 4(a)]: (i) a π pulse on ^{87}Rb between the $|\uparrow\rangle$ and $|r\rangle$ states, (ii) a 2π pulse on ^{85}Rb between $|\Uparrow\rangle$ and $|r\rangle$, and (iii) a π pulse on ^{87}Rb between $|r\rangle$ and $|\uparrow\rangle$. Then, combining two Hadamard gates realized using Raman $\pi/2$ pulses between the $|\Uparrow\rangle$ and $|\Downarrow\rangle$ states, we demonstrate the heteronuclear CNOT gate shown in Fig. 4. Its intrinsic coherence is illustrated by measuring the oscillation of the output probabilities as a function of the relative phase between the two Hadamard gates [Fig. 4(b)]. Setting the relative phase to 0 (π), the CNOT gate will flip the target qubit if the control qubit is $|\uparrow\rangle$ ($|\downarrow\rangle$).

The fidelity of the CNOT gate is determined by measuring its truth table probabilities [Fig. 4(c)]. We add an extra Raman π pulse before acting with the blow away laser to transfer the $|\uparrow\rangle$ state ^{87}Rb atoms to $|\downarrow\rangle$ and the $|\Uparrow\rangle$ state ^{85}Rb atoms to $|\Downarrow\rangle$, in order to exclude other atom losses as in Ref. [33]. The raw fidelity of the CNOT gate is $F = \mathrm{Tr}[|U_{\mathrm{ideal}}^T|U_{\mathrm{CNOT}}]/4 = 0.73(1)$. It is mainly limited by technical reasons and can be improved by stabilizing the Raman pulse powers and by increasing the Rydberg excitation efficiency.

Finally, we generate a heteronuclear entangled state of ^{87}Rb and ^{85}Rb. Starting with the two-atom state

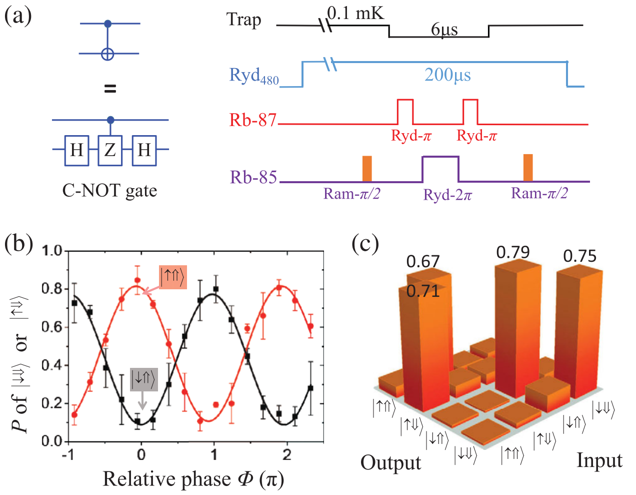

FIG. 4. Heteronuclear CNOT gate. (a) Experimental time sequence. (b) Output states as a function of the relative phase between the Raman $\pi/2$ pulses, for the initial states $|\downarrow\Uparrow\rangle$ (black squares) and $|\uparrow\Uparrow\rangle$ (red circles). The solid curves are sinusoidal fits yielding the phase difference of $(0.94 \pm 0.01)\pi$ between the two signals. (c) Measured truth table matrix U_{CNOT} for the CNOT gate with the relative phase between the $\pi/2$ pulses set to 0.

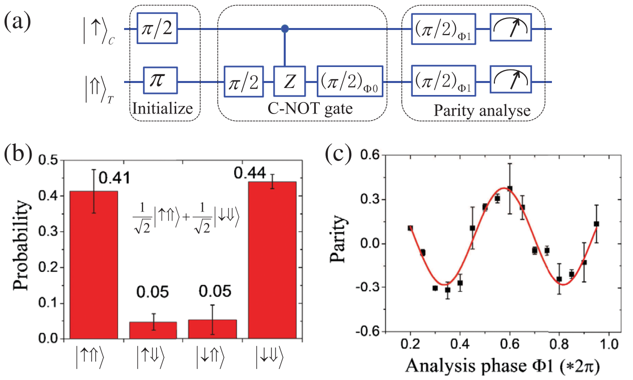

FIG. 5. Entanglement of two heteronuclear atoms. (a) Time sequence. (b) Measured probabilities for the entangled state. (c) The parity signal P. The solid curve is a sinusoidal fit with $P=2\mathrm{Re}(C_2)-2|C_1|\cos(2\phi_1+\xi)$, where $\mathrm{Re}(C_2)=0.02\pm0.02$, $|C_1|=0.16\pm0.01$.

$(|\uparrow\rangle+i|\downarrow\rangle)|\Downarrow\rangle/\sqrt{2}$, we apply the CNOT gate to create the entangled state $(|\uparrow\Uparrow\rangle+|\downarrow\Downarrow\rangle)/\sqrt{2}$. In order to quantify the entanglement of our created Bell state, we measure the coherence C_1 between the $|\uparrow\Uparrow\rangle$ and $|\downarrow\Downarrow\rangle$ states by studying the response of the system to the simultaneous rotation of the two qubits [34]. For that purpose, we apply to both atoms $\pi/2$ pulses carrying the same phase ϕ_1 relative to the initial pulses [Fig. 5(a)] and measure the oscillations of the parity signal $P=P_{\uparrow\Uparrow}+P_{\downarrow\Downarrow}-P_{\uparrow\Downarrow}-P_{\downarrow\Uparrow}$ as a function of ϕ_1 [Fig. 5(c)]. This gives us access [30,34] to the coherence $|C_1|=0.16\pm0.01$ which, combined with the populations $P_{\uparrow\Uparrow}=0.41$ and $P_{\downarrow\Downarrow}=0.44$ [Fig. 5(b)], leads to the entangled state fidelity $F=(P_{\uparrow\Uparrow}+P_{\downarrow\Downarrow})/2+|C_1|=0.59\pm0.03$. The obtained fidelity is clearly above the threshold of 0.5 ensuring the presence of entanglement. We obtain it without any corrections for atom or trace losses. It is lower than the fidelity of our CNOT gate mainly because of the motion of ^{87}Rb. Following Ref. [30] we evaluate that at our temperatures and CNOT gate fidelity the upper bound of the entanglement fidelity is $F_{\text{ent-max}}=0.65$, which is somewhat above our experimental result.

To conclude, we have realized a CNOT gate between two individual single atoms of different isotopes and demonstrated a negligible cross talk between two atom qubits. The gate is based on a strong heteronuclear Rydberg blockade, and the raw fidelity is 0.73 ± 0.01. The entanglement of two different atoms is then deterministically generated with the raw fidelity 0.59 ± 0.03. Our work makes a significant step towards the manipulation of heteronuclear atom systems. We use a difference in the transition frequencies to individually address a single atom. Therefore, two atoms can be put at a short separation while maintaining individual addressing to explore the physics in a very strong Rydberg interaction regime [35]. Moreover, the atoms of different species can be trapped in an array with an arbitrary geometry to realize a Rydberg quantum simulator of exotic spin models, such as the Kitaev toric code, color code, or coherent energy transfer [21]. The difficulty for one to create a pattern with dozens of single atoms of different species is no more than those works done recently with the same species atoms [19,20]. That is, single atoms are first loaded into a large ensemble of dipole traps randomly, and then a deeper moveable trap is used to transport single atoms into different traps of desired pattern. Our results pave a way towards quantum computing with heteronuclear systems [10] and towards the realization of high fidelity state detection, which has recently been predicted not to have any fundamental limit even at room temperature [31].

This work was supported by the National Key Research and Development Program of China under Grants No. 2016YFA0302800, No. 2017YFA0304501, and No. 2016YFA0302002, the Strategic Priority Research Program of the Chinese Academy of Sciences under Grant No. XDB21010100, the National Natural Science Foundation of China under Grants No. 11674361 and No. 11227803, and Youth Innovation Promotion Association CAS No. 2017378. D. J. P. and G. V. S. acknowledge support from IFRAF and emphasize that the research leading to their results in this Letter has received funding from the European Research Council under the European Community's Seventh Framework Programme (FP7/2007-2013 Grant Agreement No. 341197).

---

[*] etherxp@wipm.ac.cn

[†] mszhan@wipm.ac.cn

[1] S. Sachdev, Emergent gauge fields and the high-temperature superconductors, Phil. Trans. R. Soc. A **374**, 20150248 (2016).

[2] N. Laflorencie, Quantum entanglement in condensed matter systems, Phys. Rep. **646**, 1 (2016).

[3] L. Amico, R. Fazio, A. Osterloh, and V. Vedral, Entanglement in many-body systems, Rev. Mod. Phys. **80**, 517 (2008).

[4] M. A. Nielsen and I. L. Chuang, *Quantum Computation and Quantum Information* (Cambridge University Press, Cambridge, England, 2000).

[5] M. Saffman, T. G. Walker, and K. Mølmer, Quantum information with Rydberg atoms, Rev. Mod. Phys. **82**, 2313 (2010).

[6] D. Leibfried, M. D. Barrett, T. Schaetz, J. Britton, J. Chiaverini, W. M. Itano, J. D. Jost, C. Langer, and D. J. Wineland, Toward Heisenberg-limited spectroscopy with multiparticle entangled states, Science **304**, 1476 (2004).

[7] B. B. Blinov, D. L. Moehring, L. M. Duan, and C. Monroe, Observation of entanglement between a single trapped atom and a single photon, Nature (London) **428**, 153 (2004).

[8] M. Schulte, N. Lorch, I. D. Leroux, P. O. Schmidt, and K. Hammerer, Quantum Algorithmic Readout in Multi-Ion Clocks, Phys. Rev. Lett. **116**, 013002 (2016).

[9] I. I. Beterov and M. Saffman, Rydberg blockade, Forster resonances, and quantum state measurements with different atomic species, Phys. Rev. A **92**, 042710 (2015).
[10] M. Saffman, Quantum computing with atomic qubits and Rydberg interactions: progress and challenges, J. Phys. B **49**, 202001 (2016).
[11] C. J. Ballance, V. M. Schafer, J. P. Home, D. J. Szwer, S. C. Webster, D. T. C. Allcock, N. M. Linke, T. P. Harty, D. P. L. A. Craik, D. N. Stacey, A. M. Steane, and D. M. Lucas, Hybrid quantum logic and a test of Bell's inequality using two different atomic isotopes, Nature (London) **528**, 384 (2015).
[12] T. R. Tan, J. P. Gaebler, Y. Lin, Y. Wan, R. Bowler, D. Leibfried, and D. J. Wineland, Multi-element logic gates for trapped-ion qubits, Nature (London) **528**, 380 (2015).
[13] C. Chin, R. Grimm, P. Julienne, and E. Tiesinga, Feshbach resonances in ultracold gases, Rev. Mod. Phys. **82**, 1225 (2010).
[14] H. Labuhn, D. Barredo, S. Ravets, S. de Leseleuc, T. Macri, T. Lahaye, and A. Browaeys, Tunable two-dimensional arrays of single Rydberg atoms for realizing quantum Ising models, Nature (London) **534**, 667 (2016).
[15] A. M. Kaufman, B. J. Lester, M. Foss-Feig, M. L. Wall, A. M. Rey, and C. A. Regal, Entangling two transportable neutral atoms via local spin exchange, Nature (London) **527**, 208 (2015).
[16] Y. Y. Jau, A. M. Hankin, T. Keating, T. H. Deutsch, and G. W. Biedermann, Entangling atomic spins with a Rydberg-dressed spin-flip blockade, Nat. Phys. **12**, 71 (2016).
[17] T. Xia, M. Lichtman, K. Maller, A. W. Carr, M. J. Piotrowicz, L. Isenhower, and M. Saffman, Randomized Benchmarking of Single-Qubit Gates in a 2D Array of Neutral-Atom Qubits, Phys. Rev. Lett. **114**, 100503 (2015).
[18] Y. Wang, A. Kumar, T. Y. Wu, and D. S. Weiss, Single-qubit gates based on targeted phase shifts in a 3D neutral atom array, Science **352**, 1562 (2016).
[19] D. Barredo, S. de Leseleuc, V. Lienhard, T. Lahaye, and A. Browaeys, An atom-by-atom assembler of defect-free arbitrary two-dimensional atomic arrays, Science **354**, 1021 (2016).
[20] M. Endres, H. Bernien, A. Keesling, H. Levine, E. R. Anschuetz, A. Krajenbrink, C. Senko, V. Vuletic, M. Greiner, and M. D. Lukin, Cold Matter Assembled Atom-by-Atom, Science **354**, 1024 (2016).
[21] H. Weimer, M. Muller, I. Lesanovsky, P. Zoller, and H. P. Buchler, A Rydberg quantum simulator, Nat. Phys. **6**, 382 (2010).
[22] H. Krauter, C. A. Muschik, K. Jensen, W. Wasilewski, J. M. Petersen, J. I. Cirac, and E. S. Polzik, Entanglement generated by dissipation and steady state entanglement of two macroscopic objects, Phys. Rev. Lett. **107**, 080503 (2011).
[23] P. Xu, J. H. Yang, M. Liu, X. D. He, Y. Zeng, K. P. Wang, J. Wang, D. J. Papoular, G. V. Shlyapnikov, and M. S. Zhan, Interaction-induced decay of a heteronuclear two-atom system, Nat. Commun. **6**, 7803 (2015).
[24] C. Tuchendler, A. M. Lance, A. Browaeys, Y. R. P. Sortais, and P. Grangier, Energy distribution and cooling of a single atom in an optical tweezer, Phys. Rev. A **78**, 033425 (2008).
[25] E. Urban, T. A. Johnson, T. Henage, L. Isenhower, D. D. Yavuz, T. G. Walker, and M. Saffman, Observation of Rydberg blockade between two atoms, Nat. Phys. **5**, 110 (2009).
[26] See Supplemental Material at http://link.aps.org/supplemental/10.1103/PhysRevLett.119.160502 for details of laser system, error budget of entanglement, and calculations of heteronuclear Rydberg blockade, which includes Refs. [5, 25, 27–31].
[27] A. Browaeys, D. Barredo, and T. Lahaye, Experimental investigations of dipole-dipole interactions between a few Rydberg atoms, J. Phys. B **49**, 152001 (2016).
[28] K. M. Maller, M. T. Lichtman, T. Xia, Y. Sun, M. J. Piotrowicz, A. W. Carr, L. Isenhower, and M. Saffman, Rydberg-blockade controlled-not gate and entanglement in a two-dimensional array of neutral-atom qubits, Phys. Rev. A **92**, 022336 (2015).
[29] A. Gaetan, Y. Miroshnychenko, T. Wilk, A. Chotia, M. Viteau, D. Comparat, P. Pillet, A. Browaeys, and P. Grangier, Observation of collective excitation of two individual atoms in the Rydberg blockade regime, Nat. Phys. **5**, 115 (2009).
[30] T. Wilk, A. Gaetan, C. Evellin, J. Wolters, Y. Miroshnychenko, P. Grangier, and A. Browaeys, Entanglement of Two Individual Neutral Atoms Using Rydberg Blockade, Phys. Rev. Lett. **104**, 010502 (2010).
[31] L. S. Theis, F. Motzoi, F. K. Wilhelm, and M. Saffman, High-fidelity Rydberg-blockade entangling gate using shaped, analytic pulses, Phys. Rev. A **94**, 032306 (2016).
[32] D. Jaksch, J. I. Cirac, P. Zoller, S. L. Rolston, R. Cote, and M. D. Lukin, Fast Quantum Gates for Neutral Atoms, Phys. Rev. Lett. **85**, 2208 (2000).
[33] L. Isenhower, E. Urban, X. L. Zhang, A. T. Gill, T. Henage, T. A. Johnson, T. G. Walker, and M. Saffman, Demonstration of a Neutral Atom Controlled-NOT Quantum Gate, Phys. Rev. Lett. **104**, 010503 (2010).
[34] Q. A, Turchette, C. S. Wood, B. E. King, C. J. Myatt, D. Leibfried, W. M. Itano, C. Monroe, and D. J. Wineland, Deterministic Entanglement of Two Trapped Ions, Phys. Rev. Lett. **81**, 3631 (1998).
[35] Compared to the 2 atoms of different elements, the hyperfine structure splitting of distinct isotopes of the same element is in the above GHz level, and the splitting of Rydberg energy levels is small. As we demonstrate in experiments, in two-photon Rydberg excitation, 2 isotope atoms can conveniently use a single 480 nm laser beam. This greatly simplifies the experimental system of lasers. In addition, the ac-Stark frequency shift of the different atoms of the same element is small and the same dipole trap laser system can be used. The challenge with distinct isotopes lies on the GHz laser wavelength difference, which is much smaller than those used for distinct elements. The small difference may cause cross talk error. But our current experiment does not detect any cross talk error.

3 Evaporative cooling of a chain of Rydberg atoms

This chapter deals with the evaporative cooling of a chain of Rydberg atoms[1]. It summarises the work reported in my published paper [3], co–written with Dr. M. Brune. This work has initiated my discussions with his experimental group which continue to this day.

Many–particle systems whose constituents interact via long–ranged, repulsive interactions exhibit crystalline phases. For example, crystallisation occurs in systems comprised of electrons [45, 46] or trapped ions [47] due to their Coulomb repulsion. Crystallisation in low–dimensional systems has attracted specific interest. In this context, thermal and quantum fluctuations both preclude long–ranged order in infinite systems [48]. However, finite–sized crystals do exist. In particular, unidimensional crystals have been obtained, in the absence of any external periodic potential, in small systems comprising 18 ions [49] or 10 electrons [50]. The realisation of longer 1D crystals requires going deep into the quantum regime. There, thermal fluctuations are suppressed, and long–range order is only limited by quantum fluctuations, which are less stringent [48].

The key result of this work is a proposal for the realisation of long unidimensional crystals close to their quantum ground state. The considered crystals are comprised of alkali atoms which are all in the same Rydberg state. These atoms exhibit strong repulsive interactions, so that crystallisation is achieved for low temperatures. We rely on an evaporative cooling scheme applicable to chains of Rydberg atoms initially proposed in Ref. [28, appendix E] in terms of a classical dynamics simulation. We provide a thermodynamic description for this scheme which is applicable in the quantum regime of low temperatures.

Our thermodynamic analysis combines two fruitful ideas from other contexts:

- The *truncated Boltzmann distribution* has been used to describe the evaporative cooling of gases of cold ground–state atoms [6], where it is applied to individual atoms. We apply it to the collective excitations of the Rydberg chain, and highlight the enhancement of the role of truncation in this novel context.
- The consecutive atomic expulsions providing the cooling are driven by a many–body mechanism whereby the phonons hosted by the trapped chain lead to the expulsion of a single atom. Hence, this mechanism is related to the *quantum evaporation* of liquid helium [35, 37, 38]. I have taken part in the theoretical characterisation of the similar effect which occurs with cold bosonic atoms [1], briefly described in Sec. 2.1.

---

[1] General references on evaporative cooling in the context of atomic systems include the articles [6, 44]. The exploration of many–body phenomena with Rydberg atoms is reviewed in Refs. [23, 28].

Unlike for gases [51], the Rydberg chain in the quantum regime is not represented by a truncated Bose–Einstein distribution. Instead, we exploit a semiclassical approximation to the thermodynamic functions [52, §33] which smoothly relates to non–truncated thermodynamics for very low temperatures.

3.1 From cold atomic gases to Rydberg atom chains

3.1.1 Evaporative cooling of cold atomic gases

Evaporative cooling was first demonstrated in the context of trapped atomic gases with magnetically trapped hydrogen [53]. Since then, it has been an essential step for reaching quantum degeneracy in almost[2] all experiments on degenerate quantum gases [9, Secs. 15.1]. This cooling scheme does not conserve the number of trapped particles: the system is made quantum degenerate at the expense of losing the highest–energy atoms [9, Sec. 21.3]. This is achieved using a truncated trap with the finite depth U_0. Elastic two–body collisions between the trapped atoms may lead to an atom acquiring an energy greater than U_0. This atom is no longer trapped and escapes from the trap. The kinetic energy per particle of the remaining trapped atoms is lower than the one characterising the system before the atom was expelled. The evaporation process, involving consecutive atomic expulsions, may be represented thermodynamically using a non–equilibrium distribution [6, Secs. VI and VII].

We highlight three essential features of the evaporative cooling of *cold atomic gases*:

1. Any single atom whose energy exceeds the trap depth is expelled;

2. The final temperature is set by the depth of the trap, which must be lowered during the evaporation sequence to achieve quantum degeneracy [9, Sec. 21.3.3];

3. Quantum degenerate bosonic gases undergoing evaporation may be described using a truncated Bose–Einstein distribution [51, Sec. II.A].

We shall show in this chapter that the evaporative cooling of a chain of Rydberg atoms exhibits none of these three properties.

3.1.2 Evaporative cooling of a chain of Rydberg atoms

The cooling mechanism we analyse in this chapter was first proposed in Ref. [28]. We consider N alkali atoms, all in the same circular Rydberg state, are confined in a unidimensional[3] geometry. As shown in Fig. 3.1, the atoms are trapped between two optical plugs providing the longitudinal potential:

$$V_T(x) = V_L \exp[-2(x - x_L)^2/w^2] + V_R \exp[-2(x - x_R)^2/w^2] \ . \tag{3.1}$$

---

[2] The experiments reported in Refs. [54–56] are notable exceptions.

[3] The required radial trapping may be achieved using a Laguerre–Gauss laser beam [57].

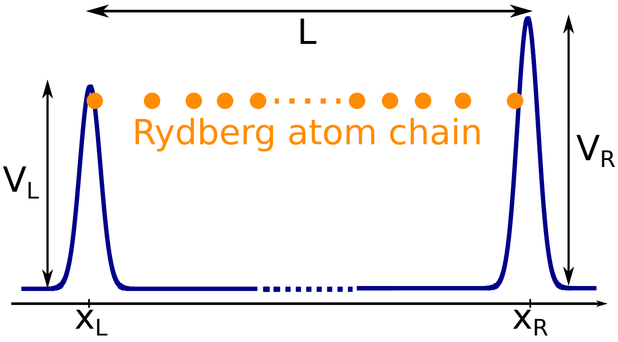

Figure 3.1: A chain of Rydberg atoms (orange disks) confined in a 1D trap of size L. The potential maxima V_L and V_R satisfy $V_L < V_R$, so that atoms are expelled from the left edge of the trap.

No periodic potential is included. The barrier width w and heights $V_L < V_R$ are kept constant. The chain is compressed by slowly decreasing the trap size $L = x_R - x_L$ from its initial value. This induces successive atomic expulsions, providing the evaporative cooling.

In Ref. [28, appendix E], this scheme was illustrated numerically in the classical regime, by solving the equations of motion for the trapped atoms. There, the authors consider the initial number $N_I = 100$ of trapped ^{87}Rb atoms, all in the circular Rydberg state[4] $50C$. Two such atoms interact via the strong, repulsive van der Waals interaction C_6/d^6, with d being the interatomic distance, $C_6 = h \times 3\,\text{GHz}\,\mu\text{m}^6$ the interaction strength, and h Planck's constant. The barrier width and heights are, respectively, $w = 30\,\mu$m, $V_L/h = 3\,$MHz, and $V_R/h = 4\,$MHz. The numerical results show that, proceeding with the evaporation until $N_F = 40$ atoms are left in the trap, the final kinetic energy per particle for the trapped atoms is reduced by a factor ten with respect to its initial value.

3.2 Quasi–equilibrium thermodynamics of a chain

We describe the evaporation process thermodynamically. Our motivation is two–fold:

- Our thermodynamic description holds both in the classical and the quantum regimes;
- It is applicable to longer atom chains
  (we have considered chains initially comprised of up to $N_I = 1000$ atoms).

Our description hinges on the use of a truncated Boltzmann distribution generalising that of Ref. [6] to that of a trapped chain of interacting atoms. We illustrate our model with the parameters summarised in Sec. 3.1.2, which are accessible in current experiments [28].

In this section, we consider a fixed number N of atoms, confined in the 1D trapping potential of Eq. (3.1) with the fixed size $L = x_R - x_L$ (we relax the constraints of fixed N and L in Sec. 3.3 below).

3.2.1 The considered system

The equilibrium positions $x_1^0, \ldots, x_N^0$ of the N atoms are evenly spaced in the bulk of the chain, two neighbouring atoms being distant by $l \approx 5\,\mu$m. However, they are not evenly spaced near the edges, because the barrier widths w cover multiple atom spacings l. We describe the atomic vibrations in terms of a quadratic Hamiltonian:

---

[4] The cicular Rydberg state $50C$ bears the electronic quantum numbers $n = 50$ and $l = m = 49$.

$$H = \sum_{k=1}^{N} \left[\frac{\tilde{p}_k^2}{2m} + \frac{1}{2} m \omega_k^2 \tilde{u}_k^2 \right] \text{ with } \tilde{u}_k = \sum_{n=1}^{N} R_{nk} u_n \ . \tag{3.2}$$

In Eq. (3.2), the N collective vibrational modes $\{\tilde{u}_k\}$ have the frequencies $\omega_1 < \ldots < \omega_N$, and the $\{\tilde{p}_k\}$ are their conjugate momenta. They are related to the atomic displacements $\{u_n = x_n - x_n^0\}$ through the orthogonal matrix R. The applicability of Eq. (3.2) requires that the averages $\langle (u_{n+1} - u_n)^2 \rangle^{1/2}$ involving two neighboring atoms remain small compared to the mean distance $l = L/N$. This is well satisfied for all the chains we have considered, including the longer ones of Sec. 3.3.2.

3.2.2 Classical thermodynamics

A given configuration, i.e. a solution to the classical equations of motion for the Hamiltonian H, is specified by giving the mode energies ϵ_k and phases ϕ_k, for $1 \leq k \leq N$. We focus on the leftmost atom, i.e. the one closest to the barrier with the lower maximum V_L. Its displacement u_1 with respect to its equilibrium position x_1^0 reads, as a function of time t:

$$u_1(t) = \sum_k R_{1k} \left(\frac{2\epsilon_k}{m\omega_k^2} \right)^{1/2} \cos(\omega_k t + \phi_k) \ . \tag{3.3}$$

Up to this point, no coupling between the vibrational modes k has been taken into account. We introduce this coupling now. It results from the condition that the leftmost atom should remain trapped. This condition reads $|u_1(t)| < u_M$, where $u_M = x_1^0 - x_L$.

Expulsion criterion. We consider the time–averaged mean–square displacement $\langle u_1^2 \rangle = u_M^2 \sum_{k=1}^{N} \epsilon_k / E_{Mk}$. Here, the energies $E_{Mk} = m\omega_k^2 u_M^2 / R_{1k}^2$ increase with the mode index k. We shall assume that the configurations satisfying $\langle u_1^2 \rangle^{1/2} > \alpha\, u_M$, for a suitable value of α, are expelled from the trap. The value of α is selected through the following argument. For a given α, the lowest–energy configurations such that $\langle u_1^2 \rangle^{1/2} = \alpha\, u_M$ are those where only the mode $k = 1$ is excited, with the energy $\epsilon_1 = \alpha^2 E_{M1}$. Then, Eq. (3.3) provides $u_1(t) = \sqrt{2}\, \alpha\, u_M \cos(\omega_1 t + \phi_1)$. Thus, choosing $\alpha = 1/\sqrt{2}$, the leftmost atom barely reaches x_L with vanishing velocity. This corresponds to the lowest–energy untrapped configurations. Their energy $E_M^{\mathrm{cl}} = m\omega_1^2 u_M^2 / (2R_{11}^2)$ is not directly related to the barrier maxima V_L or V_R.

Ergodicity. The numerical results of Ref. [28, appendix E] indicate that the trapped atoms undergo chaotic classical motion. This motivates *the assumption that the system is ergodic* for the considered parameter range. This is not an innocuous assumption, and mechanisms hindering ergodicity in a simpler system will be described in chapter 4. In the present context, ergodicity is assumed to be ensured by the anharmonic effects coupling the vibrational modes, which are neglected in the quadratic Hamiltonian of Eq. (3.2).

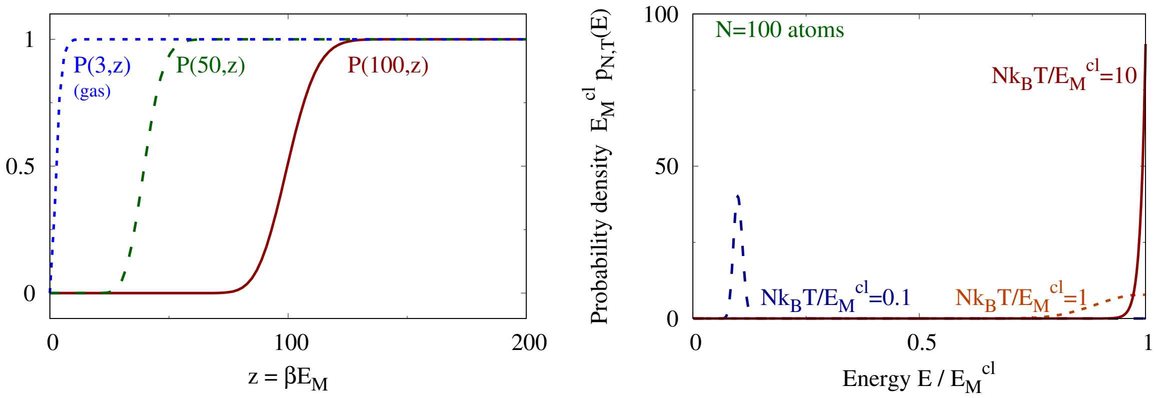

Figure 3.2: Left: Normalised incomplete gamma function $P(a, z)$, as a function of $z = \beta E_M$, for $a = 3$ (blue, case of a trapped gas), 50, and 100. **Right:** Probability density, extracted from Eq. (3.4) with $N = 100$ atoms, for finding a (classical) configuration with the energy E, for $Nk_{\mathrm{B}}T/E^{\mathrm{cl}}_{\mathrm{M}} = 0.1$ (blue), 1 (orange), and 10 (red).

Quasi–equilibrium distribution. Exploiting ergodicity, the trapped configurations are those whose energies satisfy $E < E^{\mathrm{cl}}_M$. We describe the quasi–equilibrium thermodynamics of the chain using a Boltzmann distribution for the vibrational configurations, truncated at the energy E^{cl}_M. The partition function Z^{cl} representing the classical regime reads:

$$Z^{\mathrm{cl}} = \int_{E<E^{\mathrm{cl}}_M} \frac{\prod[d\tilde{p}_k d\tilde{u}_k]}{h^N}\, e^{-\beta E} = \frac{P(N, \beta E^{\mathrm{cl}}_M)}{\beta^N \hbar\omega_1 \dots \hbar\omega_N}\ . \tag{3.4}$$

In Eq. (3.4), $\beta = 1/(k_{\mathrm{B}}T)$ is the inverse temperature, $E = H(\{\tilde{p}_k, \tilde{u}_k\})$ and $P(a, z) = \gamma(a, z)/\Gamma(N)$ is the normalised lower incomplete gamma function. The mean energy $U^{\mathrm{cl}}(L, T)$ and the entropy $S^{\mathrm{cl}}(L, T)$ may be extracted from Z^{cl} through the usual statistical physics relations [58, Sec. 7.1], namely, $U^{\mathrm{cl}} = -\partial_\beta \ln Z^{\mathrm{cl}}$ and $S^{\mathrm{cl}}/k_{\mathrm{B}} = \ln Z^{\mathrm{cl}} - \beta\partial_\beta \ln Z^{\mathrm{cl}}$.

Incomplete gamma function. The function $P(a, z)$ entering Eq. (3.4) is defined as [59]:

$$P(a, z) = \frac{\gamma(a, z)}{\Gamma(a)} = \frac{1}{\Gamma(a)} \int_0^a dt\, e^{-t} t^{z-1}\ . \tag{3.5}$$

It is illustrated on the left panel of Fig. 3.2. It resembles a step function which is equal to 0 for small $z = \beta E^{\mathrm{cl}}_M$ (accounting for the truncation for large T) and 1 for large z (truncation plays no role for small T). The smooth transition occurs for $z \approx a$.

Comparison between trapped gases and trapped Rydberg chains. The function $P(a, z)$ also plays a role in the thermodynamic description of the evaporation of a trapped gas [6]. For a gas in a three–dimensional harmonic trap, $a = 3$, reflecting the 3 spatial degrees of freedom. By contrast, for Rydberg chains comprised of N trapped atoms, $a = N$ ranges from 40 to 1000. Hence, the role of truncation is strongly enhanced with respect to gases.

For gases, atomic expulsions quickly follow collisions during which one atom has acquired enough energy. The situation is different in a chain of Rydberg atoms trapped in the potential represented on Fig. 3.1. There, only the left–most atom of the chain may be expelled. Anharmonic processes occur along the chain, driving it toward quasi–equilibrium. This makes it possible to access the high–temperature regime, where $k_{\mathrm{B}}T \gtrsim E_M^{\mathrm{cl}}/N$. For large T, the exponential factor in Eq. (3.4) is approximately 1, so that all trapped configurations are equally populated. The probability density for a configuration to have the energy E is $NE^{N-1}/(E_M^{\mathrm{cl}})^N$, hence, nearly all configurations have energies $\sim E_M^{\mathrm{cl}}$ (see the right panel of Fig. 3.2). Both $U^{\mathrm{cl}}(T)$ and $S^{\mathrm{cl}}(T)$ reach finite maxima. These may be determined analytically from the following expansion of $\ln(Z^{\mathrm{cl}})$ for small $\beta = 1/(k_{\mathrm{B}}T)$:

$$\ln(Z^{\mathrm{cl}}) \quad = \quad \ln\left(\frac{(E_M^{\mathrm{cl}})^N/N!}{\hbar\omega_1\cdots\hbar\omega_N}\right) \quad - \frac{N}{N+1}\,\beta E_M^{\mathrm{cl}} \quad + O[(\beta E_M^{\mathrm{cl}})^2]\,. \tag{3.6}$$

Equation (3.6) yields the expressions for the maximum energy $U_{\max}^{(N)}(L)$ and entropy $S_{\max}^{(N)}(L)$:

$$U_{\max}^{(N)} = \frac{NE_M^{\mathrm{cl}}}{N+1} \quad \text{and} \quad S_{\max}^{(N)} = k_{\mathrm{B}}\ln\left(\frac{(E_M^{\mathrm{cl}})^N/N!}{\hbar\omega_1\cdots\hbar\omega_N}\right). \tag{3.7}$$

3.2.3 Quantum thermodynamics

For lower quadratic energies, we use a quantum description, presented in Ref. [3, Sec. IV].

Difference with respect to gases. For gases of cold ground–state atoms, the truncation selects trapped single–particle modes without constraining their populations, yielding a truncated Bose–Einstein distribution [51]. Instead, for Rydberg chains, the truncation involves the energies of the N–particle configurations. This prevents Z^{quant} from factorising and reflects the correlations between the trapped phonon modes. Thus, the corresponding quasi–equilibrium state is not characterised by a truncated Bose–Einstein distribution.

Calculation of $U(T)$ and $S(T)$ for all temperatures. The threshold energy E_M^{quant} for trapped configurations in the quantum regime exceeds both E_M^{cl} and the zero–point energy of the chain, $E_{\mathrm{ZP}} = \sum_{k=1}^N \hbar\omega_k/2$. We assume $E_M^{\mathrm{quant}} \gg E_{\mathrm{ZP}} + \hbar\omega_N$, a condition which is well satisfied for all parameters we have considered. Then, we consider two different regimes depending on the value of temperature with respect to E_M^{quant}/N:

- For $k_{\mathrm{B}}T < E_M^{\mathrm{quant}}/N$, the truncation plays no role: the energy $U(T)$ and entropy $S(T)$ are those of a non–truncated chain of harmonic oscillators, whose partition function is $Z_0 = \prod_{k=1}^N [\mathrm{csch}(\beta\hbar\omega_k/2)/2]$.
- For $k_{\mathrm{B}}T \gtrsim E_M^{\mathrm{quant}}/N$, our description involves Eq. (3.4), but quantum effects are not negligible: we account for the leading–order quantum correction. Following the procedure outlined in Ref. [52, §33], we seek the quantum partition function in the form $Z^{\mathrm{quant}} = Z^{\mathrm{cl}}(1+\hbar^2\langle\chi_2\rangle)$, where the correction $\langle\chi_2\rangle$ is expressed in terms of the moments $\langle u_k^2\rangle_{\mathrm{cl}}$, $\langle p_k^2\rangle_{\mathrm{cl}}$ and $\langle u_k^2 p_k^2\rangle_{\mathrm{cl}}$ of the classical distribution represented by Z^{cl}.

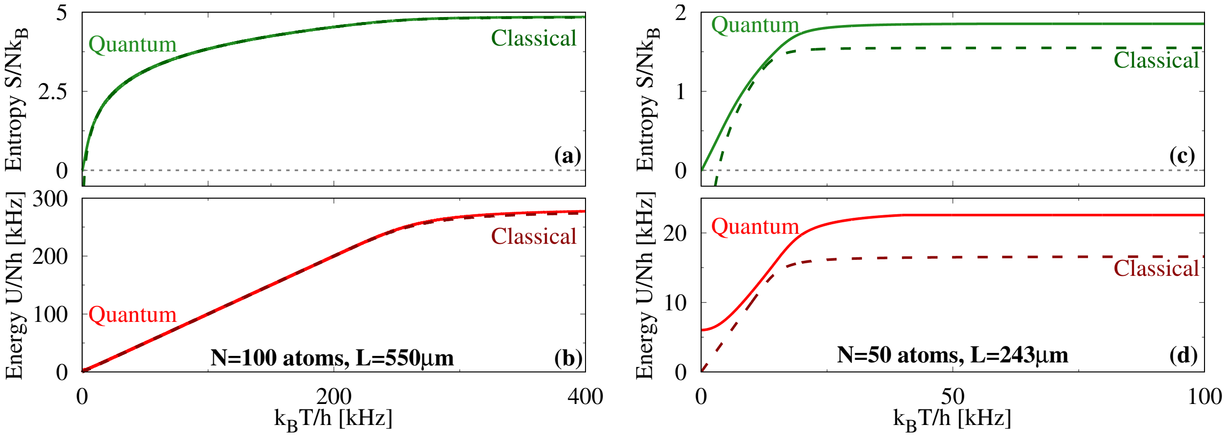

Figure 3.3: *(a)* Entropy $s = S/N$ and *(b)* energy $u = U/N$ per particle for $N = 100$ atoms in a trap of size $L = 550\,\mu$m, at the beginning of the evaporation in Fig. 3.5. The solid and dashed lines show the quantum and classical predictions, respectively. Panels *(c)* and *(d)* show s and u for $N = 50$ atoms in a trap of size $L = 243\,\mu$m, close to the end of the evaporation in Fig. 3.5.

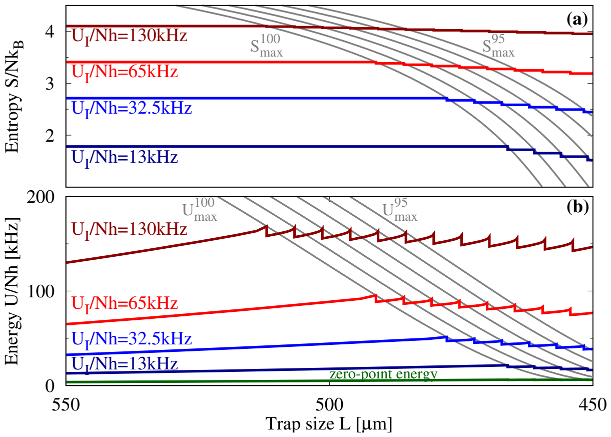

Figure 3.4: The first few expulsions for a chain initially comprising $N_I = 100$ atoms in a trap of length $L_I = 550\,$m, with various initial energies. Panels *(a)* and *(b)* show the entropy S/N and energy U/N per particle. The maxima $S^{(N)}_{\max}/N$ and $U^{(N)}_{\max}/N$ are shown in gray. Each expulsion leads to a discontinuity in both S and U.

The thermodynamic functions extracted from Z_0 overlap with those extracted from Z_{quant} for a range of values of T, yielding the full quantum thermodynamic functions $S(T)$ and $U(T)$. These satisfy the expected low–temperature behaviours, namely, $S(T = 0) = 0$ and $U(T = 0) = E_{\text{ZP}} > 0$. The functions $S(T)$ and $U(T)$ are compared to the corresponding classical results on Fig. 3.3. At the beginning of the evaporation (panels *(a)* and *(b)*), they only differ over a narrow range of temperatures near $T = 0$; the difference becomes more pronounced at the end of the evaporation (panels *(c)* and *(d)*).

3.3 Thermodynamics of the evaporation process

In this section, we relax the assumption of fixed atom number N and trap size L of Sec. 3.2, so as to characterise the evaporative cooling process. This process is driven by a slow compression of the chain due to a trap length $L(t)$ which decreases as a function of time. Our key assumption is that, *apart from the atomic expulsions, the trapped chain is at all times in a quasi–equilibrium state characterised by the truncated distribution of Sec. 3.2.* This requires the compression of the chain to occur adiabatically.

We first formulate our thermodynamic description without assuming that the chain is long. We illustrate it on the chain of 100 atoms of Ref. [28, appendix E], and extend the description given there to account for quantum phenomena occurring at low temperatures. Then, turning to a chain initially comprising 1000 atoms, we highlight the quasi–universal features that the evaporation curve exhibits for longer chains.

3.3.1 Thermodynamic description without assuming a long chain

We start from a chain initially comprised of $N = N_I$ atoms confined in a trap with the initial length $L = L_I$. Its quadratic energy is $U_I = U^{(N_I)}(L_I)$. For all considered parameters, the two following assumptions concerning the initial state I are well satisfied:

- The energy U_I is much greater than the zero–point energy of the chain, so that the chain is initially well described by classical physics;
- The energy U_I is much smaller than the threshold energy E^{cl}_{MI}, so that its thermodynamics is initially not affected by the truncation.

Under these two assumptions, the equipartition theorem [58, Sec. 6.4] relates the initial energy U_I to the initial temperature T_I through $U_I = Nk_{\mathrm{B}}T_I$. The initial temperature determines the entropy $S = S_I^{(N)}$.

Now, we adiabatically compress the chain by slowly decreasing L. As long as no atom is expelled, the process is reversible and the entropy $S^{(N)}$ remains constant. However, decreasing L means that the maximum value $S^{(N)}_{\mathrm{max}}(L)$ decreases, as shown by the gray lines on Fig. 3.4(a). Hence, the adiabatic phase continues until the trap size L reaches the value $L_f^{(N)}$ such that $S^{(N)}_{\mathrm{max}} = S^{(N)}$. At this point, adiabatic compression is no longer possible, and the leftmost atom is expelled from the trap.

Just before the expulsion, the condition $S^{(N)} = S^{(N)}_{\mathrm{max}}$ means $T \to \infty$, so that $U_f^{(N)} = U^{(N)}_{\mathrm{max}}$. We assume that the expelled atom leaves the trap with the minimal energy V_L allowing it to overcome the left barrier. Just after the expulsion, the remaining $N-1$ trapped atoms reach a new quasi–equilibrium state at the energy $U_i^{(N-1)}$ such that:

$$V_0^{(N)} + U_f^{(N)} \quad = \quad V_0^{(N-1)} + U_i^{(N-1)} \ + V_L \ . \tag{3.8}$$

In Eq. (3.8), the quantities $V_0^{(N)}$ and $V_0^{(N-1)}$ are the static equilibrium energies for N and $N-1$ atoms in a trap of the same size $L_f^{(N)} = L_i^{(N-1)}$. The value of $U_i^{(N-1)}$ sets the new entropy $S^{(N-1)}$. Then, adiabatic compression resumes until the next expulsion, which occurs for the trap size $L_f^{(N-1)}$ such that $S_{\mathrm{max}}(L_f^{(N-1)}) = S^{(N-1)}$. The complete evaporation curve consists of a repeated sequence of adiabatic compressions and expulsions.

Figure 3.4 shows the entropy and energy per particle along the beginning of the evaporation curve for the trapped chain characterised by the initial parameters $N_I = 100$, $L_I = 550\,\mu$m of Ref. [28, appendix E]. We highlight two of its important features:

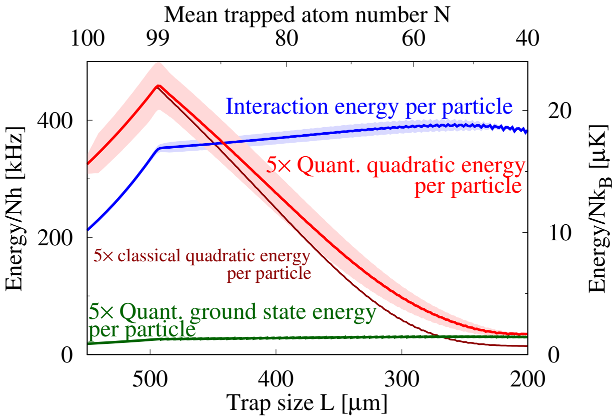

Figure 3.5: Mean quadratic energy (red), interaction (blue) and ground–state energies (green) per particle during the evaporation, starting from $N_I = 100$ atoms in a trap of size $L_I = 550\,\mu$m, down to $N_F = 40$ atoms in a trap of size $L_F = 200\,\mu$m. The shaded red and blue areas show the standard deviations on the quadratic and interaction energies. The trap size and the mean trapped atom number *decrease* as the horizontal axes are read from left to right.

- During each adiabatic compression phase, the energy U/N and entropy S/N *increase*;
- Both quantities undergo a discontinuous *decrease* each time an atom is expelled.

The chain undergoes evaporative cooling if the net effect of the two phases is a decrease in energy and entropy. This occurs for all parameters considered in this chapter.

Figure 3.5 shows the full evaporation curve for the same initial conditions, with the initial energy $U_I/(N_I h) = 65\,\text{kHz}$. Starting from $N_I = 100$ atoms and expelling 60 of them, the quadratic energy per particle of the final chain is $U_F/(N_F h) = 7\,\text{kHz}$, so that it has been reduced by a factor of almost 10. The final energy is just above the quantum zero–point energy $E_{\text{ZP}}(L_F)/(N_F h) = 5.9\,\text{kHz}$.

Uncertainty on the initial energy. Under the two assumptions stated at the beginning of the present section, the initial chain is well described by Boltzmann statistics applied to N_I uncoupled harmonic oscillators (these are the vibrational modes entering the Hamiltonian of Eq. 3.2). This leads [58, Sec. 7.2] to the fluctuations $\Delta U_I = U_I/\sqrt{N_I}$ about the mean energy $U_I = N_I k_{\text{B}} T_I$. These fluctuations, shown on Fig. 3.5, wash out the jaggedness of the quadratic and interaction energies due to the atomic expulsions.

Numerical calculation. We calculate the evaporation curves of Figs. 3.5 and 3.6 numerically using our own C++ code. The evaluation of the thermodynamic functions $S(L,T)$ and $U(L,T)$ hinges on the calculation of the function $P(a,z)$, where $a = N$, the trapped atom number, ranges from 40 to 1000. To capture the steep variation of this function in the transition region $z \sim a$, we resort to arbitrary–precision numerics using the Boost.Multiprecision C++ library [60].

3.3.2 Quasi–universality for longer chains

Finally, we focus on longer chains. Under this assumption, the spatial inhomogeneities near the trap edges are negligible. Hence, the entropy $s = S/N$ and energy $u = U/N$ per

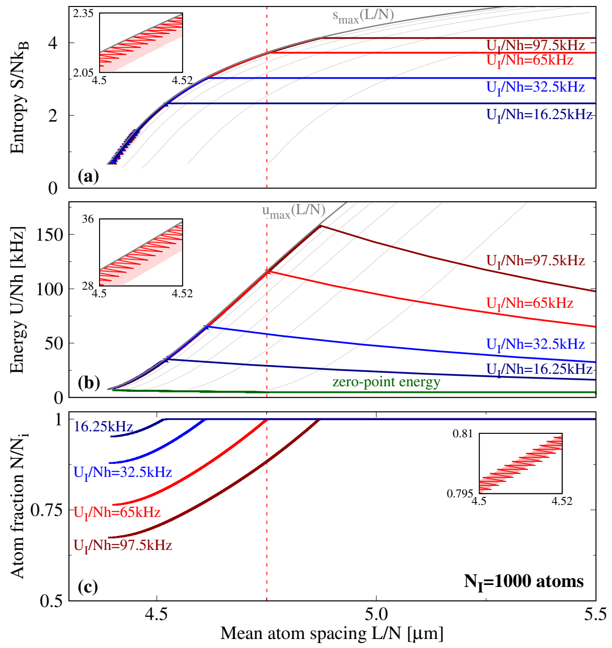

Figure 3.6: Quasi–universal evaporation of a chain initially comprised of $N_I = 1000$ atoms with the mean spacing $l_I = 5.5\,\mu$m. Panels *(a)* and *(b)* show the entropy S/N and energy U/N per particle for various initial temperatures, which are both near–universal. Panel *(c)* shows the non–universal atom fraction N/N_I. The vertical red line shows the first expulsion for $U_I/(N_I h) = 65\,$kHz. The insets zoom in on the same small fraction of all curves so as to show their jagged nature before averaging.

particle depend only on the mean interparticle spacing $l = L/N$ and the temperature T. Their maxima $s_{\text{max}}(l) = S_{\text{max}}(L,N)/N$ and $u_{\text{max}}(l) = U_{\text{max}}(L,N)/N$ depend only on l.

Figure 3.6 illustrates the evaporation of a long chain on the case where the initial number of atoms is $N_I = 1000$. The mean interparticle spacing $l_I = L/N_I = 5.5\,\mu$m and the considered initial quadratic energies per particle are the same as for Figs. 3.4 and 3.3.

The evaporation curve may now be divided in two different stages:

1. The initial adiabatic compression phase, which depends on the initial energy per particle u_i. Its role is to bring the system from the thermal regime into the regime where the thermodynamics is dominated by truncation effects;
2. All subsequent expulsions and adiabatic compressions, during which the thermodynamic functions s and u remain close to the universal curves $s_{\text{max}}(l)$ and $u_{\text{max}}(l)$.

Hence, starting from the first expulsion, the entropy and energy per particle nearly follow a universal law. By contrast, the fraction $n = N/N_I$ of remaining trapped atoms is not universal, as shown on Fig. 3.6(c). It reaches a stationary value which is a decreasing function of the initial energy per particle $u_i = U_I/N_I$.

The mean distance l decreases during each adiabatic compression, and increases at each expulsion. On average, l decreases, and the evaporation brings the system towards the zero–point energy per particle $e_{\text{ZP}}(l) = E_{\text{ZP}}(N,L)/N$. The curves in Fig. 3.6 are truncated at the minimum value $l_{\text{min}} = 4.4\,\mu$m. For $l < l_{\text{min}}$, the assumption $E_M^{\text{quant}} \gtrsim E_{\text{ZP}} + \hbar\omega_N$ we have made in Sec. 3.2.3 no longer holds. Then, the calculation of the thermodynamic functions in the quantum regime is more involved and goes beyond the scope of this work.

Starting from the initial temperature $k_B T_I/h = 65\,$kHz, the final chain comprises $N_F = 764$ atoms with the energy $U_F/(N_F h) = 8.5\,$kHz, close to $E_{\text{ZP}}/(N_F h) = 6.6\,$kHz. In the

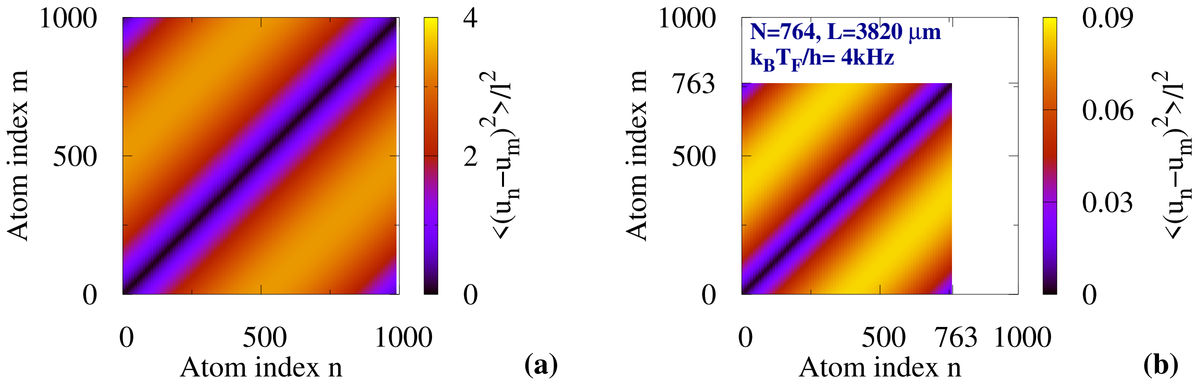

Figure 3.7: Average values $\langle (u_n - u_m)^2 \rangle / l^2$ *(a)* at the beginning ($N_I = 1000$, $L_I = 5500\,\mu$m, $U_I/(N_I h) = 65\,$kHz) and *(b)* at the end ($N_F = 764$, $L_I = 3820\,\mu$m, $U_F/(N_F h) = 8.5\,$kHz) of the evaporation represented in Fig. 3.6.

final state, the averages $\langle (u_n - u_m)^2 \rangle$ are all much smaller than l^2 (see Fig. 3.7). Hence, this final state is a unidimensional crystal.

3.4 Conclusion

We have introduced a thermodynamic model for the evaporative cooling scheme of unidimensional chains of Rydberg atoms initially introduced in Ref. [28, appendix E]. Unlike the classical dynamics results presented there, our model is applicable in the quantum regime of low temperatures, and it allows for the analysis of long chains.

Our thermodynamic model relies on the use of a truncated Boltzmann distribution applied to the excitations in the chain. Truncated Boltzmann distributions had already been introduced [6] to describe the evaporative cooling of gases. For gases, the evaporation criterion involves single atoms. By contrast, for Rydberg atom chains, it involves N–particle configurations. This has two consequences. Firstly, it means that the statistical distribution in the quantum regime is not a truncated Bose–Einstein distribution. Secondly, it leads to a strong enhancement of the role of truncation, which strongly affects the thermodynamics of the evaporation. In particular, the final temperatures obtained after evaporation are set by the maximum energy supported by a trap of given length, which is smaller than the barrier heights by three orders of magnitude.

Using experimentally accessible parameters, we have shown that this evaporative cooling scheme leads to a unidimensional Rydberg crystal near its quantum ground state. The spatial order arises on a length scale which is comparable to the size of the system, despite the absence of any spatially periodic potential. It may be fully characterised experimentally through microwave spectroscopy and spatially–resolved ground–state imaging [61, 62].

PHYSICAL REVIEW RESEARCH **2**, 023014 (2020)

Evaporative cooling to a Rydberg crystal close to its ground state

M. Brune[1] and D. J. Papoular[2]
[1]*Laboratoire Kastler Brossel, Collège de France, CNRS, ENS-Université PSL, Sorbonne Université, France*
[2]*LPTM, UMR 8089 CNRS & Université Cergy–Pontoise, France*

(Received 5 September 2019; accepted 6 March 2020; published 8 April 2020)

We theoretically show how to obtain a long one-dimensional crystal near its quantum ground state. We rely on an evaporative cooling scheme applicable to many-body systems with nonzero-ranged interactions. Despite the absence of periodic potentials, the final state is a crystal that exhibits long-range spatial order. We describe the scheme thermodynamically, applying the truncated Boltzmann distribution to the collective excitations of the chain, and we show that it leads to a novel quasiequilibrium many-body state. For longer chains, comprising about 1000 atoms, we emphasize the quasiuniversality of the evaporation curve. Such exceptionally long one-dimensional (1D) crystals are only accessible deep in the quantum regime. We perform our analysis on the example of an initially thermal chain of circular Rydberg atoms confined to a 1D geometry. Our scheme may be applied to other quantum systems with long-ranged interactions such as polar molecules.

DOI: 10.1103/PhysRevResearch.2.023014

I. INTRODUCTION

Systems presenting long-ranged interactions exhibit strongly correlated crystalline phases [1–4]. Among them, quantum crystals are those whose constituents undergo large-amplitude zero-point motion [5]. The collective nature of their excitations leads to spectacular phenomena including the Tkachenko oscillations of a vortex lattice in a superfluid [6,7], the giant plasticity of helium crystals [8], and supersolidity in ultracold gases presenting interactions beyond the contact limit [9–13].

Up to now, the investigation of one-dimensional (1D) quantum crystals has been hindered by the difficulty of obtaining large crystals in this geometry, where thermal and quantum fluctuations both destroy long-range order in macroscopic systems [14]. Nevertheless, crystallization does occur in finite-sized systems [15]. It has been unambiguously observed in the absence of any external periodic potential only in small systems of up to 50 ions [16–19] or 10 electrons [20,21]. The realization of larger 1D crystals requires going deep into the quantum regime. There, thermal fluctuations are suppressed, and long-range order is only limited by quantum fluctuations, which are less stringent [14]. The realization of large 1D crystals will pave the way toward the investigation of 1D quantum crystals, where one may look for, e.g., giant plasticity through the tunneling of defects [22,23].

We focus on one way of obtaining spatial order that relies on strong nonzero-range dipole interactions between Rydberg atoms [24]. Rydberg atoms are ideally suited for quantum information processing [25,26] and quantum simulation [27,28]. Nontrivial many-body states [29–31] of up to 50 atoms manipulated with optical tweezers have been prepared through resonant coupling to Rydberg states [32–35]. Rydberg states may be weakly admixed to the atomic ground state [36–38] or resonantly excited [39] so as to study the interplay between anisotropic interactions and disorder or frustration [40]. Quantum gases resonantly coupled to Rydberg states have been predicted to exhibit a quantum phase transition to a Rydberg crystal [41], leading to a universal scaling behavior observed in the critical region [42].

In all those cases, low-angular-momentum Rydberg states were considered, leading to a strong limitation on the lifetime (100 μs per atom, a few μs for many atoms), limiting the size of the system. Circular Rydberg atoms [43–46], whose excited electron has maximal orbital and magnetic quantum numbers, overcome this limitation and offer a very promising platform for the quantum simulation of many-body problems [27]. Using spontaneous emission inhibition [47,48], their already long lifetime (30 ms) is expected to be extended to more than 1 min. This timescale allows for implementing an evaporative cooling scheme applicable to Rydberg atoms [27], whose classical analysis shows great promise for reaching extremely low temperatures.

In this article, we show that large 1D Rydberg crystals may be prepared very close to their quantum ground state in realistic experimental conditions [27,49] through this evaporative cooling scheme. Despite the absence of any spatially periodic potential, these crystals exhibit long-range spatial order. This is in stark contrast to the classical analysis of 1D systems, which would predict the absence of long-range order [14]. We introduce a quantum thermodynamic model, applying the truncated Boltzmann distribution to the collective excitations of the chain. We show that it leads to a novel quasiequilibrium regime that differs from the truncated Bose-Einstein distribution applicable to quantum-degenerate gases [50]. In contrast to dilute systems in which the evaporation is driven by two-body collisions [51], the mechanism we describe here

---

Published by the American Physical Society under the terms of the Creative Commons Attribution 4.0 International license. Further distribution of this work must maintain attribution to the author(s) and the published article's title, journal citation, and DOI.

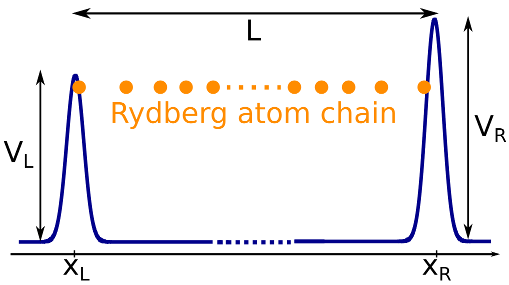

FIG. 1. A Rydberg-atom chain (orange) confined in a 1D trap of size L. The potential maxima V_L and V_R satisfy $V_L < V_R$, so that atoms are expelled from the left edge of the trap.

hinges on many-body physics, whereby the phonons present in the chain lead to the expulsion of a single atom. Hence, it is related to the quantum evaporation of liquid helium [52–54], also predicted to affect cold bosonic atoms [55].

II. THE SYSTEM AND THE HAMILTONIAN UNDER CONSIDERATION

We first consider a fixed number N of Rydberg atoms confined in a 1D trap of fixed size L (see Fig. 1). We illustrate our model using the parameters of Ref. [27]. The atoms are confined radially using the ponderomotive potential [56] induced by a Laguerre-Gaussian laser beam (Ref. [57], Chap. 2). They are trapped axially between two optical plugs yielding the potential $V_T(x) = V_L \exp[-2(x-x_L)^2/w^2] + V_R \exp[-2(x-x_R)^2/w^2]$. The barrier width and heights are, respectively, $w = 30\ \mu$m, $V_L/h = 3$ MHz, and $V_R/h = 4$ MHz. The trap size $L = x_R - x_L$ is slowly decreased from its initial value so as to induce successive atomic expulsions, providing the evaporative cooling. Unlike for gases, the barrier heights remain constant during the whole process. The atoms interact via the strongly repulsive van der Waals interaction $V(x_i, x_j) = C_6/|x_i - x_j|^6$ with $C_6/h = 3$ GHz μm^6, corresponding to ^{87}Rb atoms with the principal quantum number $n = 50$. The equilibrium positions $x_1^0, \dots, x_N^0$ are evenly spaced in the bulk of the chain, but not on the edges, due to the finite spatial extent of the barriers. Two neighboring atoms are distant by $l \approx 5\ \mu$m, leading to interaction energies $C_6/l^6 \approx h \times 200$ kHz.

We describe the atomic vibrations in terms of a quadratic Hamiltonian:

$$H = \sum_{k=1}^{N} \left[\frac{\tilde{p}_k^2}{2m} + \frac{1}{2} m\omega_k^2 \tilde{u}_k^2 \right] \text{ with } \tilde{u}_k = \sum_{n=1}^{N} R_{nk} u_n. \qquad (1)$$

In Eq. (1), the N vibrational modes $\{\tilde{u}_k\}$ have the frequencies $\omega_1 < \cdots < \omega_N$, and the $\{\tilde{p}_k\}$ are their conjugate momenta. They are related to the atomic displacements $\{u_n = x_n - x_n^0\}$ through the orthogonal matrix R. The applicability of Eq. (1) only requires local order (see Appendix A 1): the averages $\langle (u_{n+1} - u_n)^2 \rangle^{1/2}$ involving two neighboring atoms should remain small compared to $l = L/N$. For a thermal chain at the temperature T, this requires $k_B T < 2C_6/l^6$, and is well satisfied for up to 1000 atoms with $l \sim 5\ \mu$m and $k_B T \lesssim h \times 100$ kHz $\approx k_B \times 5\ \mu$K.

III. CLASSICAL THERMODYNAMICS

For a given configuration characterized by the phonon mode energies $\{\epsilon_k\}_{1\leqslant k\leqslant N}$ and phases $\{\phi_k\}_{1\leqslant k\leqslant N}$, the position of the leftmost atom at time t is $u_1(t) = \sum_k R_{1k}[2\epsilon_k/(m\omega_k^2)]^{1/2} \cos(\omega_k t + \phi_k)$. It remains trapped as long as $|u_1(t)| < u_M$, where $u_M = x_1^0 - x_L$. We consider the time-averaged mean-square displacement $\langle u_1^2 \rangle = u_M^2 \sum_{k=1}^N \epsilon_k / E_{Mk}$, where the quantities $E_{Mk} = m\omega_k^2 u_M^2 / R_{1k}^2$ increase with k. Hence, for a given α, the lowest-energy configurations for which $\langle u_1^2 \rangle^{1/2} = \alpha u_M$ are those where only the mode $k = 1$ is excited, with the energy $E = \epsilon_1 = \alpha^2 E_{M1}$. For $\alpha = 1/\sqrt{2}$, they correspond to atom 1 barely reaching $u_1 = -u_M$, i.e., to the lowest-energy untrapped configurations. Their energy $E_M^{\text{cl}} = m\omega_1^2 u_M^2/(2R_{11}^2)$ is set by ω_1. Furthermore, numerical simulations of the classical (cl) dynamics of the atom chain [58] have shown the atomic motion to be chaotic. Hence, exploiting ergodicity, the trapped configurations are those with $E < E_M^{\text{cl}}$. We describe the quasiequilibrium thermodynamics of the chain using a Boltzmann distribution truncated at the energy E_M^{cl}, whose partition function reads

$$Z^{\text{cl}} = \int_{E<E_M^{\text{cl}}} \frac{\prod [d\tilde{p}_k d\tilde{u}_k]}{h^N} e^{-\beta E} = \frac{P(N, \beta E_M^{\text{cl}})}{\beta^N \hbar\omega_1 \cdots \hbar\omega_N}. \qquad (2)$$

In Eq. (2), $\beta = 1/(k_B T)$ is the inverse temperature, $E = H(\{\tilde{p}_k, \tilde{u}_k\})$, and $P(a, z) = \gamma(a, z)/\Gamma(N)$ is the normalized lower incomplete gamma function [59]. The mean (quadratic) energy $U^{\text{cl}}(L, T)$ associated with the Hamiltonian H and the entropy $S^{\text{cl}}(L, T)$ follow from $U^{\text{cl}} = -\partial_\beta \ln Z^{\text{cl}}$ and $S^{\text{cl}}/k_B = \ln Z^{\text{cl}} - \beta\partial_\beta \ln Z^{\text{cl}}$.

The function $P(a, z)$ also appears in the thermodynamics of the evaporation of a gas ($a = 3$ for a harmonic trap) [51]. Here, $a = N$ ranges from 40 to 1000, so that the role of truncation is strongly enhanced with respect to gases of ground-state atoms (see Appendix A 3). It is important for $k_B T \gtrsim E_M^{\text{cl}}/N$. For larger T, all trapped configurations are equally populated. The probability density for a configuration to have the energy E is $NE^{N-1}/(E_M^{\text{cl}})^N$, hence nearly all configurations have energies $\sim E_M^{\text{cl}}$. Both U^{cl} and S^{cl} reach finite maxima $U_{\max}^N(L)$ and $S_{\max}^N(L)$ (see Fig. 2), where

$$U_{\max}^{(N)} = \frac{NE_M^{\text{cl}}}{N+1} \text{ and } S_{\max}^{(N)} = k_B \ln\left(\frac{\left(E_M^{\text{cl}}\right)^N/N!}{\hbar\omega_1 \cdots \hbar\omega_N} \right). \qquad (3)$$

For fixed N, both maxima increase with L, because less stringent traps will accommodate higher-energy excitations. This novel regime is inaccessible with gases, where an atom whose energy is close to the evaporation threshold is expelled when it undergoes a collision [51,60]. However, it is accessible for a Rydberg chain (see Appendix A 2).

IV. QUANTUM THERMODYNAMICS

For lower quadratic energies, we use a quantum (quant) description. Assuming ergodicity in the quantum regime, we introduce the energy $E_{\mathbf{n}} = \sum_{k=1}^N \hbar\omega_k(n_k + 1/2)$ of the configuration labeled by the integer multiplet $\mathbf{n} = \{n_k\}_{1\leqslant k\leqslant N}$. The

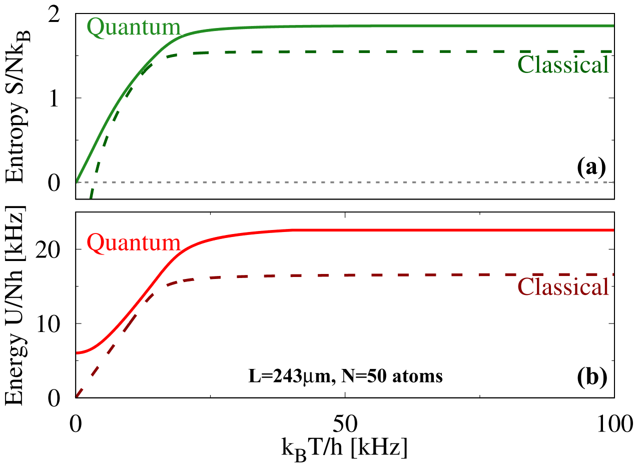

FIG. 2. (a) Entropy and (b) energy per particle for $N = 50$ atoms in a trap of size $L = 243$ μm (close to the end of the evaporation for the chain of Fig. 4). The solid (dashed) lines show the quantum (classical) prediction.

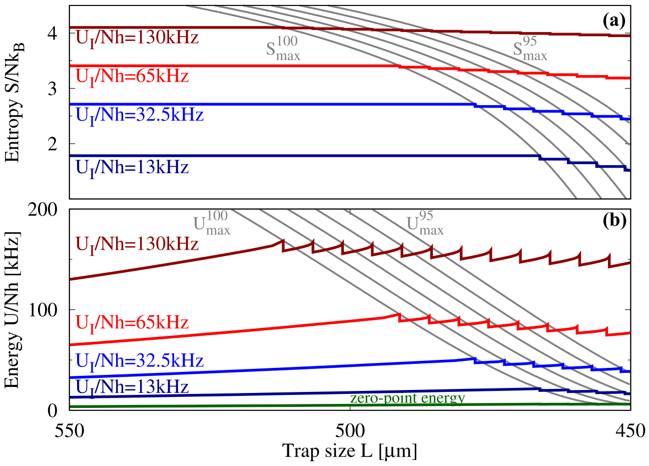

FIG. 3. The first few expulsions for a chain with $N_I = 100$ atoms and $L_I = 550$ μm, in terms of (a) entropy S/N and (b) energy U/N per particle, for various initial energies. The maxima $S_{\max}^{(N)}(L)/N$ and $U_{\max}^{(N)}(L)/N$ are shown in gray. Each expulsion yields a discontinuity in both S and U.

threshold energy E_M^{quant} for trapped configurations satisfies

$$E_M^{\text{quant}} = \min_{\mathbf{n}} \left[E_{\mathbf{n}} \text{ with } \sum_{k=1}^{N} \frac{\hbar\omega_k(n_k + 1/2)}{E_{Mk}} \geqslant \alpha^2 \right], \tag{4}$$

where we choose $\alpha = 1/\sqrt{2}$ as in the classical case. The energy E_M^{quant} exceeds both E_M^{cl} and the zero-point energy $E_{\text{ZP}} = \sum_{k=1}^{N} \hbar\omega_k/2$. The quantum partition function reads $Z^{\text{quant}} = \sum_{\mathbf{n}} e^{-\beta E_{\mathbf{n}}}\, \Theta(E_M^{\text{quant}} - E_{\mathbf{n}})$, where Θ is the Heaviside function, illustrating an important difference with respect to gases of ground-state atoms. There, the truncation selects the trapped single-particle modes without constraining their populations, yielding a truncated Bose-Einstein distribution [50]. Instead, for Rydberg chains, the truncation involves the configuration energies $E_{\mathbf{n}}$. This prevents Z^{quant} from factorizing and reflects the correlations between the trapped phonon modes, leading to a novel quasiequilibrium state that does not obey a truncated Bose-Einstein distribution.

We assume $E_M^{\text{quant}} \gg E_{\text{ZP}} + \hbar\omega_N$, which is well satisfied for all parameters considered in this paper. Then, $E_M^{\text{quant}} \approx E_M^{\text{cl}} + E_{\text{ZP}}$. For $k_{\text{B}}T \gtrsim E_M^{\text{quant}}/N$, we evaluate the quantum energy $U^{\text{quant}}(L, T)$ and entropy $S^{\text{quant}}(L, T)$ (see Appendix A 3) starting from Eq. (2), replacing E_M^{cl} by E_M^{quant} and including the leading quantum correction, proportional to $\hbar^2$ (Ref. [61], Sec. 33). For $k_{\text{B}}T < E_M^{\text{quant}}/N$, the energy and entropy reflect the nontruncated thermodynamics of a harmonic-oscillator chain. They overlap with U^{quant}, S^{quant} for a range of values of T, yielding the full quantum thermodynamic functions (see Fig. 2).

V. EVAPORATION

We now describe the evaporation process. Initially, the chain is comprised of $N = N_I$ atoms in a trap of size $L^{(N)} = L_I$, with the energy $U^{(N)} = U_I$. For all considered parameters, $U_I \gg E_{\text{ZP}}$, signaling the classical regime, and $U_I \ll E_{MI}^{\text{cl}}$, so that it is described by nontruncated thermodynamics. Thus, $U_I/N_I = k_{\text{B}}T_I$ is the initial temperature. We adiabatically compress the chain by slowly decreasing L (see Fig. 3). Hence, the entropy $S^{(N)}$ remains constant. Expelling an atom is irreversible, therefore N also remains constant. However, T and $U^{(N)}$ increase, whereas $U_{\max}^{(N)}(L)$ and $S_{\max}^{(N)}(L)$ decrease. The compression proceeds until the trap no longer accommodates the entropy, i.e., up to the trap size $L_f^{(N)}$ such that $S_{\max}^{(N)}(L_f^{(N)}) = S^{(N)}$. This implies $T \to \infty$, hence $U_f^{(N)} = U_{\max}^{(N)}(L_f^{(N)})$. At this point, the leftmost atom is expelled from the trap, its kinetic energy being the barrier height V_L. The $(N-1)$ remaining atoms thermalize to the new initial energy $U_i^{(N-1)}$, where

$$U_i^{(N-1)} = U_f^{(N)} + V_0^{(N)} - V_0^{(N-1)} - V_L. \tag{5}$$

Here, $V_0^{(N)}$ and $V_0^{(N-1)}$ are the static equilibrium energies for N and $(N-1)$ atoms in a trap of size $L_f^{(N)}$. Then, adiabatic compression resumes until the next expulsion.

The complete evaporation curve consists of a repeated sequence of these two steps. Figure 4 compares our classical (dark red) and quantum (red) predictions, down to the trap size $L_F = 200$ μm, where $E_M^{\text{quant}} \gtrsim E_{\text{ZP}} + \hbar\omega_N$. The result of our classical model closely matches the classical-dynamics simulations reported in Ref. [27] (Fig. 14, phase II). Our quantum approach predicts that, starting from $N_I = 100$ atoms, the final state with $N_F = 40$ atoms obeys a Bose-Einstein distribution with $U_F/(N_F h) = 7.0$ kHz, slightly above the zero-point energy $E_{\text{ZP}}/(N_F h) = 5.9$ kHz. The shown average energies account for the uncertainty $\Delta U_I = U_I/\sqrt{N_I} = h \times 6.5$ kHz on U_I, which washes out their jaggedness due to the expulsions (see Fig. 3 and Appendix A 4). The final state is in the 1D regime if the radial confinement frequency $\omega_\perp/(2\pi) \gg U_F/(N_F h)$. Smaller values of $\omega_\perp$ will lead to quasi-1D chains exhibiting the "zigzag" transition observed with ion chains [23,62] and in electronic systems [63].

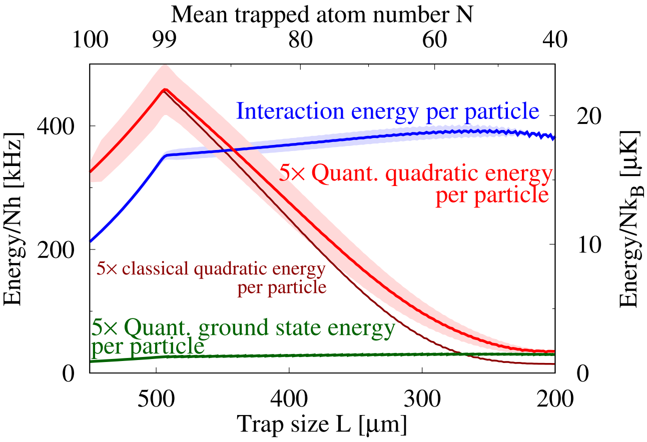

FIG. 4. Classical (dark red) and quantum (red) predictions for the mean quadratic energy, interaction (blue), and ground-state (green) energies per particle during the evaporation, starting from $N_I = 100$, $L_I = 550\ \mu$m, down to $N_F = 40$, $L_F = 200\ \mu$m. The shaded red and blue areas show the standard deviations on the quadratic and interaction energies. Energies are measured in kHz, with $h \times 100$ kHz $\sim k_B \times 5\ \mu$K.

VI. QUASIUNIVERSALITY FOR LONGER CHAINS

Finally, we focus on long chains with $N_I \approx 1000$, keeping $l_I = L_I/N_I = 5.5\ \mu$m. Then, the inhomogeneities near the trap edges are negligible, and both $S/N = s(l, T)$ and $U/N = u(l, T)$ only depend on $l = L/N$ and T. The evaporation is conveniently described in terms of l, s, u, and the atom number fraction $n = N/N_I$. The evaporation curve consists of two parts (see Fig. 5). First, the initial compression at constant N_I depends on $u_I = U_I/N_I$. The second part consists of all subsequent expulsions and compressions. The mean distance l increases at each expulsion and decreases during each compression; on average, l decreases. The quantities s and u always remain close to the universal curves $s_{\max}(l) = S_{\max}(N, L)/N$ and $u_{\max}(l) = U_{\max}(N, L)/N$, respectively (see Appendix A 5). Their fluctuations, visible in the insets of Fig. 5 for $N_I = 1000$ and $k_B T_I/h = 65$ kHz, decrease with increasing N_I for two reasons. First, the changes δu and δs in the energy and entropy per particle upon expelling an atom are decreasing functions of N. Second, larger N_I lead to smaller $\Delta U_I = U_I/\sqrt{N_I}$, and hence to smaller uncertainties on s and u. Quasiuniversality also applies to the fluctuations Δu and Δs on the energy and entropy (see Appendix A 5).

The fraction $n = N/N_I$ [Fig. 5(c)] is not universal (see Fig. 11 in the Appendix). For $N_I = 1000$, n reaches a stationary value n_F as u goes to $e_{\mathrm{ZP}}(l) = E_{\mathrm{ZP}}(l)/N$. The value $n_F(u_I)$ is a decreasing function of $u_I = U_I/N_I$. The curves in Fig. 5 are truncated at the minimum value $l = 4.4\ \mu$m, where $E_M^{\text{quant}} \gtrsim E_{\mathrm{ZP}} + \hbar\omega_N$. Then, for $k_B T_I/h = 65$ kHz, the chain comprises $N_F = 764$ atoms with the energy $U_F/(N_F h) = 8.5$ kHz, close to $E_{\mathrm{ZP}}/(N_F h) = 6.6$ kHz.

The final state of such a long chain is a crystal exhibiting true long-range order, with all spatial correlators $C_{nm} = \langle (u_n - u_m)^2 \rangle \ll l^2$ [see Fig. 6(c) in the Appendix]. This is only possible deep in the quantum regime, where thermal fluctuations are suppressed [14]. The crystalline order may be fully characterized experimentally through microwave spectroscopy, revealing the regularity and fluctuations of the lattice parameter, combined with spatially resolved ground-state imaging [33,64].

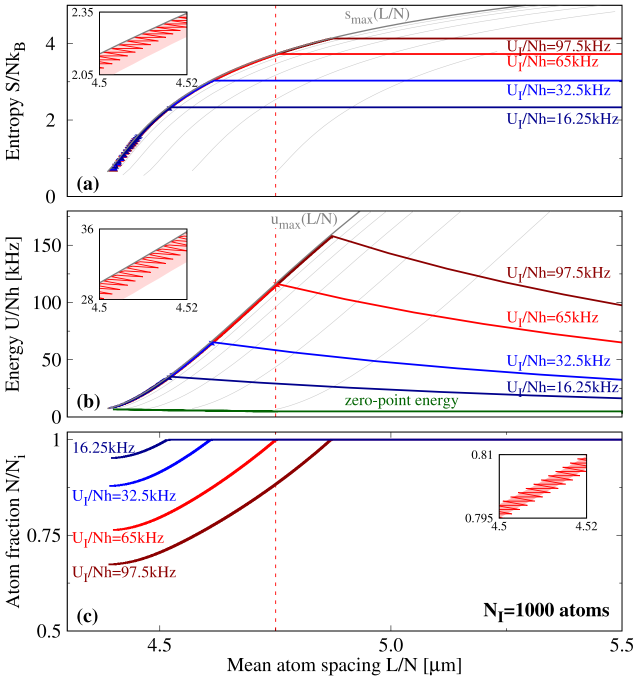

FIG. 5. Quasiuniversal evaporation of a chain with $N_I = 1000$ and $l_I = 5.5\ \mu$m, in terms of the mean (a) entropy and (b) energy per particle, for various initial energies. The thin gray lines show $S_{\max}(L/N)/N$ and $U_{\max}(L/N)/N$ for $N = 50$, 100, 200, 400, and 800 (from right to left), which converge toward $s_{\max}(l)$ and $u_{\max}(l)$ (thick gray lines). (c) Nonuniversal atom fraction N/N_I. The vertical red line shows the first expulsion for $U_I/(N_I h) = 65$ kHz. The insets zoom in on the same small fraction of the curves for $U_I/(N_I h) = 65$ kHz, and show the jagged curves obtained before averaging; the shaded areas show the standard deviations.

VII. CONCLUSION AND OUTLOOK

We have introduced a quantum thermodynamic model for the evaporative cooling of 1D Rydberg-atom chains [27]. Unlike the evaporative cooling of ground-state atoms, the final temperatures accessible with our scheme are not of the order of the barrier heights. Instead, they are determined by the maximum energy $u_{\max}(l)$ compatible with the trap. This reflects the many-body character of the evaporation scheme and leads to final temperatures that are radically lower than the barrier heights by three orders of magnitude. We have shown that, under realistic experimental conditions, this scheme yields large near-ground-state Rydberg crystal. The long-range spatial order of these 1D structures is a feature of the deep quantum regime. Our scheme will also apply to other interacting 1D systems such as polar molecules [65,66]. There, the nonzero-ranged interaction between the particles is provided by the dipole-dipole interaction, which scales with $1/r^3$ and may be made purely repulsive in low-dimensional geometries [67].

The following directions warrant further investigation. (i) For higher initial temperatures or mean atom spacings, the initial state is a liquid and Eq. (1) does not hold, but our scheme will still drive the system toward its crystalline ground state. (ii) For longer chains, a prolonged evaporation going beyond the regime of Fig. 5 leads to $E_M^{\text{quant}} \lesssim E_{\text{ZP}} + \hbar\omega_N$, in which case the calculation of the quantum thermodynamic functions is more involved. (iii) The timescale ensuring adiabaticity is set by the anharmonic processes neglected in Eq. (1). (iv) Our scheme is also applicable in two dimensions, where the expected ground state is a hexagonal crystal that we shall investigate both theoretically and experimentally.

ACKNOWLEDGMENTS

We acknowledge stimulating discussions with J. M. Raimond, P. Lecheminant, Y. Castin, T. Huillet, L. P. Pitaevskii, C. Sayrin, and G. V. Shlyapnikov.

APPENDIX

This Appendix provides complementary information on the following topics: (i) the applicability of the quadratic Hamiltonian; (ii) the anharmonic terms and their twofold role; (iii) the partition function and its numerical evaluation; (iv) the observability of the adiabatic plateaus with constant atom numbers; and (v) the quasiuniversal description for long chains and its limits.

1. The quadratic Hamiltonian

The Hamiltonian describing the harmonic vibrations of the atoms about their equilibrium positions $\{x_n^0\}$ [Eq. (1)] is applicable as soon as the chain exhibits local order. Indeed, in the chain bulk, the trapping potential is negligible and, within the nearest-neighbor approximation, the interaction energy of atom n is $E_n^I = C_6[1/(x_n - x_{n-1})^6 + 1/(x_n - x_{n+1})^6]$. Here, $x_n = x_n^0 + u_n$ is the position of atom n. Expanding E_n^I to second order in the displacements $\{u_n\}$, and exploiting the near-translational invariance, we find that the harmonic approximation is valid if $\eta_n = 21\,\langle (u_{n+1} - u_n)^2\rangle\,/l^2 < 1$, where $l = L/N$ is the mean interatomic distance and the average $\langle (u_{n+1} - u_n)^2\rangle$ is the spatial correlator between two neighboring atoms. For a thermal distribution, this condition reduces to $k_{\text{B}}T < 2C_6/l^6$. Accounting for the trap and the truncated thermodynamics, we find this criterion to be well satisfied all along the evaporation [see Fig. 6(a)] for the long chain of Fig. 5.

The present criterion is less stringent than asking for the chain to be in a crystalline phase. This is especially true in one dimension, where thermal fluctuations quickly rule out long-range order [14]. For example, the long chain of Fig. 5 exhibits no long-range spatial correlations in its initial state ($N_i = 1000$, $l_i = 5.5\ \mu$m, $k_{\text{B}}T_i/h = 65$ kHz). This can be seen in Fig. 6(b): the correlator $\langle (u_n - u_m)^2\rangle\,/l^2 > 1$ for distant atoms. However, our scheme brings the chain close to its quantum ground state, which does exhibit long-range correlations [$\langle (u_n - u_m)^2\rangle\,/l^2 \ll 1$ for all n and m; see Fig. 6(c)].

2. Anharmonic effects

The leading anharmonic contribution to the Hamiltonian follow from the third- and fourth-order terms in the displacements $\{u_n\}$. For gases, they yield two-body collisions that are essentially instantaneous. By contrast, for Rydberg chains, they generate many-body correlations over the characteristic time τ_{propag} for propagation along the chain, set by the sound velocity. They are mostly due to interactions and occur in the chain bulk, where their probability does not depend on position (see Fig. 7). They are much less probable near the edges, where the trapping potential leads to larger distances between the static equilibrium positions of the atoms.

The role of these anharmonic processes is twofold. First, they are responsible for thermalization and ergodicity on a timescale involving τ_{propag}. Second, they set the (longer) timescale ensuring the adiabaticity of the compression between two atomic expulsions. The classical-dynamics simulations reported in Ref. [27] have shown that, for the shorter chain of Fig. 3 ($N_i = 100$), compression rates of the order of 40 μm/ms are adequate. The optimal compression rate will be investigated elsewhere.

For gases, anharmonic processes directly drive the atomic expulsions, which immediately follow two-atom collisions during which one atom has acquired enough energy. Their relation to expulsions is more involved for Rydberg chains. If the trap size is such that an expulsion is expected ($T \rightarrow \infty$), ergodicity causes the system to explore various configurations until the leftmost atom is expelled with the energy V_L. If no expulsion is expected (T finite), the compression of the trap causes an increase in energy due to the atoms on the edges of

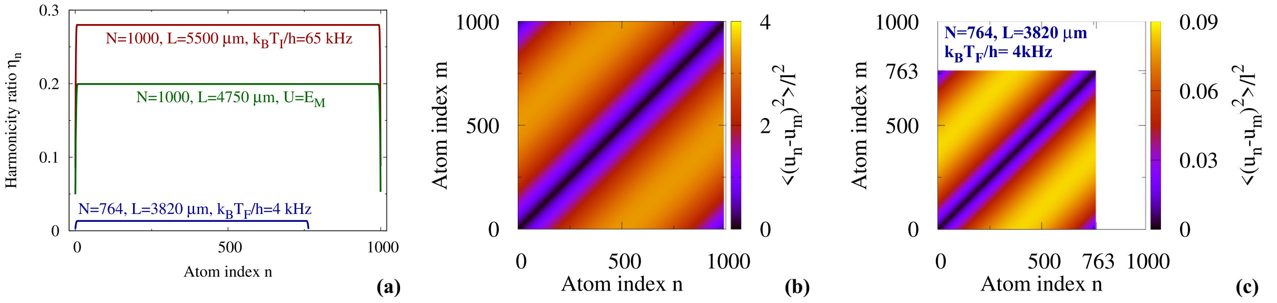

FIG. 6. (a) Harmonicity ratio η_n for the long chain of Fig. 5, at the beginning of the evaporation (red), just before the first expulsion (green), and at the end of the evaporation (blue). (b) and (c) Spatial correlator $\langle (u_n - u_m)^2\rangle\,/l^2$ at the beginning [(b), $N = 1000$, $L = 5500\ \mu$m] and the end [(c), $N = 764$, $L = 3820\ \mu$m] of the evaporation, in units of $l = L/N$.

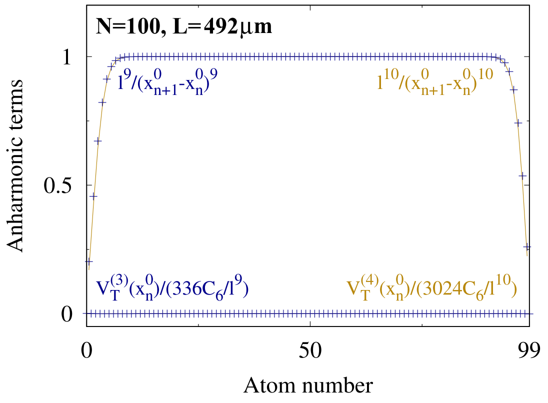

FIG. 7. Third- (blue crosses) and fourth-order (golden lines) anharmonic amplitudes from the interaction energy (nonzero amplitudes) and the trapping potential (negligible amplitudes), calculated for the shorter chain of Fig. 3, just before the first expulsion. They are expressed in units of their bulk values, namely $56C_6/l^9$ and $126C_6/l^{10}$.

the chain being set in motion toward the bulk. Expelling the leftmost atom before thermalization has taken place (i.e., with an energy $>V_L$) is likely to involve a two-atom collision at the open end of the trap. There, anharmonic terms are strongly suppressed (see Fig. 7), so that these higher-energy expulsions are rare. Instead, the energy increase is most often mediated, through harmonic vibrations, to the chain bulk where thermalization occurs. The rare cases in which the leftmost atom is expelled are not captured by our thermodynamic model. However, they are not a hindrance as long as their rate remains small: instead, they speed up the evaporation process with respect to our thermodynamic prediction. The presence of a single open end (the left end in Fig. 1) is favorable for two reasons: (i) it leads to longer propagation times, and hence more efficient thermalization; and (ii) it helps reduce the rate of nonthermalized expulsions.

3. The partition function

a. Normalized lower incomplete γ function

The thermodynamics of the (classical or quantum) truncated Boltzmann distribution involve the normalized lower incomplete γ function $P(a,z)$, defined as [59]

$$P(a,z)=\frac{\gamma(a,z)}{\Gamma(a)}=\frac{1}{\Gamma(a)}\int_0^a dt\, e^{-t}t^{z-1}. \tag{A1}$$

For given values of the trap size L and atom number N, the classical partition function Z^{cl} is proportional to $P(N,\beta E_M)/\beta^N$. Hence, a is of the order of N, whereas $z=\beta E_M$ is the ratio of the threshold energy to the temperature. For a given a, the function $P(a,z)$ resembles a step function [see Fig. 8(a)] which is equal to 0 for small z (representing the truncation for large T) and to 1 for large z (truncation plays no role for small T). The smooth transition occurs for $z\approx a$, so that truncation plays a role for $k_{\mathrm{B}}T/E_M \gtrsim 1/a$. The parameter $a=3$ for a gas in a truncated 3D harmonic trap [51], whereas for Rydberg chains $a\approx N$ ranges from 40 to 1000. Hence, Rydberg chains are affected by the truncation starting from much lower temperatures than gases are.

b. Quantum partition function

For a given L, and assuming $E_M^{\mathrm{quant}} \gg E_{\mathrm{ZP}}+\hbar\omega_N$, we evaluate the quantum partition function Z^{quant} for $k_{\mathrm{B}}T \gtrsim E_M^{\mathrm{quant}}/N$ using Eq. (2) in the main text, replacing E_M^{cl} by E_M^{quant}. We go beyond the quasiclassical integral expression and include the leading-order quantum correction, proportional to $\hbar^2$ (Ref. [61], Sec. 33). Hence, we write $Z^{\mathrm{quant}}=Z^{\mathrm{cl}}(1+\langle\hbar^2\chi_2\rangle)$, where the correction $\langle\hbar^2\chi_2\rangle$ is expressed in terms of the moments $\langle x_k^2\rangle_{\mathrm{cl}}$, $\langle p_k^2\rangle_{\mathrm{cl}}$, and $\langle x_k^2p_k^2\rangle_{\mathrm{cl}}$ of Z_{cl}. We find

$$\begin{aligned}&\langle\hbar^2\chi_2\rangle\, E_M^2\Big/\sum_{k=1}^{N}(\hbar\omega_k)^2\\&\quad=\frac{z^2}{24}\left(-1+[3z-5(N+1)]\frac{z^Ne^{-z}}{\Gamma(N+2)}\frac{1}{P(N,z)}\right),\end{aligned} \tag{A2}$$

with $z=\beta E_M$. For $k_{\mathrm{B}}T<E_M/N$, we use the quantum partition function $Z_0=\prod_{k=1}^{N}[\mathrm{csch}(\beta\hbar\omega_k/2)/2]$ of a nontruncated chain. The functions U^{quant} and S^{quant} overlap with those extracted from Z_0 for a range of values of $k_{\mathrm{B}}T$, thus yielding the full quantum thermodynamic functions. The classical and quantum predictions for U and S are compared in Fig. 8. At the beginning of the evaporation [panel (b)], they only differ over a narrow range of temperatures near $T=0$; the

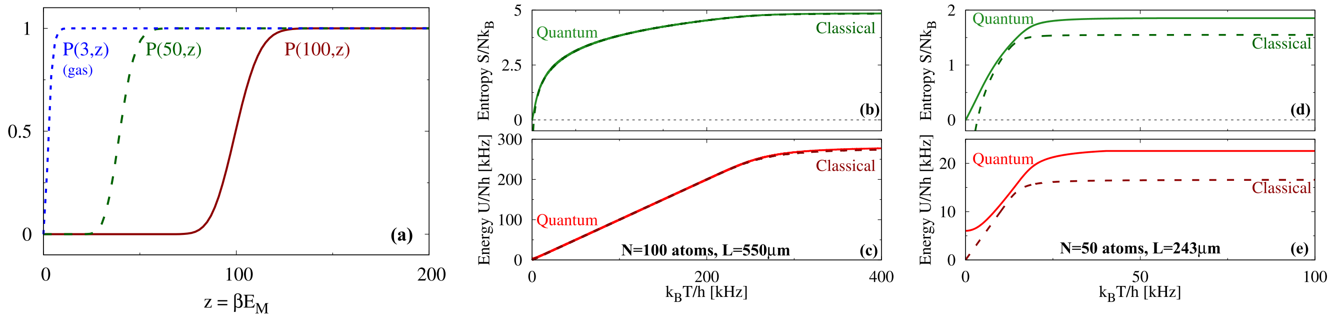

FIG. 8. (a) Normalized incomplete γ function $P(a,z)$ as a function of $z=\beta E_M$ for $a=3$, 50, and 100. (b) and (c) $s=S/N$ and $u=U/N$ as a function of T for 100 atoms in a trap of size $L=550\ \mu$m (beginning of the evaporation in Fig. 4 of the main text). (d) and (e) s and u for 50 atoms with $L=243\ \mu$m (close to the end of the evaporation in Fig. 4).

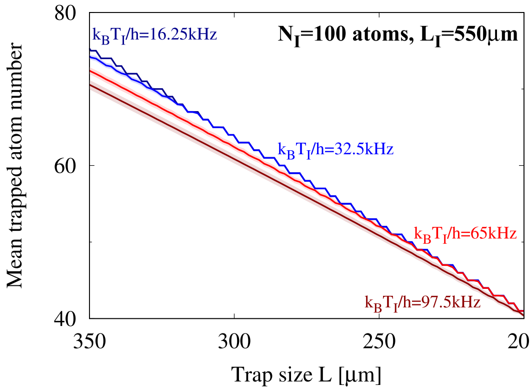

FIG. 9. Mean trapped atom number as a function of the trap size L for the short chain initially comprising $N_I = 100$ atoms with $L_I = 550\ \mu$m for various initial temperatures. The red curve, calculated for $k_B T_I = 65$ kHz, corresponds to Fig. 4 of the main text. The discrete steps on the atom number become visible at the end of the evaporation; for lower initial temperatures, they are well resolved earlier on. The shaded areas show the mean standard deviation due to the initial fluctuations $\Delta U_I = U_I/\sqrt{N_I}$ on the quadratic energy.

difference is more striking near the end of the evaporation [panel (c)].

c. Numerical evaluation

The evaluation of $U(L,T)$ and $S(L,T)$ involves calculating $P(a,z)$ for $40 \leqslant a \leqslant 1000$. To capture the steep variation of these functions for $z \sim a$, we resort to arbitrary-precision numerics using the BOOST.MULTIPRECISION C++ library [68].

4. Constant atom number plateaus

Between two atomic expulsions, the chain undergoes an adiabatic compression during which N remains constant (see Fig. 3). For $k_B T_I/h \sim 65$ kHz, these constant-N plateaus are smoothed out for most of the evaporation because of the uncertainty $\Delta U_I = U_I/\sqrt{N_I}$ on the initial energy. Indeed, it reflects on the entropy as $\Delta S_I = \Delta U_I/T_I$, and leads to sizable fluctuations $\Delta S^{(N)}$ during most of the evaporation. These yield the uncertainty $\Delta L_f^{(N)} = \Delta S^{(N)}/S_{\max}^{(N)\prime}(L_f)$ on the trap size $L_f^{(N)}$ at which the atom N is expelled.

For shorter chains, the constant-N plateaus become well resolved at the end of the evaporation, as the chain approaches its ground state. For Fig. 4 and $k_B T_I/h = 65$ kHz, these plateaus are visible when the remaining trapped atom number $N \lesssim 45$ (see Fig. 9), in agreement with the classical-dynamics results of Ref. [27]. The plateaus are resolved earlier on for lower initial temperatures and later on for higher ones.

5. Quasiuniversality

We now focus on longer chains with $N \sim 1000$ and $l \sim 5\ \mu$m. Then, the quadratic energy $U(N,L,T) = Nu(l,T)$, the entropy $S(N,L,T) = Ns(l,T)$, their maxima $U_{\max}(N,L) = Nu_{\max}(l)$ and $S_{\max}(N,L) = Ns_{\max}(l)$, and the zero-point energy $E_{\text{ZP}}(N,l) = Ne_{\text{ZP}}(l)$ are all extensive.

a. Energy and entropy

We consider two consecutive adiabatic plateaus corresponding to N and $N-1$ trapped atoms. Equation (5) provides the initial energy per particle $u_i^{(N-1)} = U_i^{(N-1)}/(N-1)$ for the second plateau in terms of its final value for the first one, $u_f^{(N)} = U_f^{(N)}/N$, and the mean distance $l_f^{(N)} = L_f^{(N)}/N$:

$$u_i^{(N-1)} = u_f^{(N)} + \big(u_f^{(N)} + 7C_6/l_f^{(N)6} - V_L\big)/N. \qquad (A3)$$

Hence, starting from the first atomic expulsion, u remains close to the universal curve $u = u_{\max}(l)$, within small deviations that decrease like $1/N$. Furthermore, the entropies $s^{(N)} = s_{\max}(l_f^{(N)})$, which are constant during each plateau, all lie near

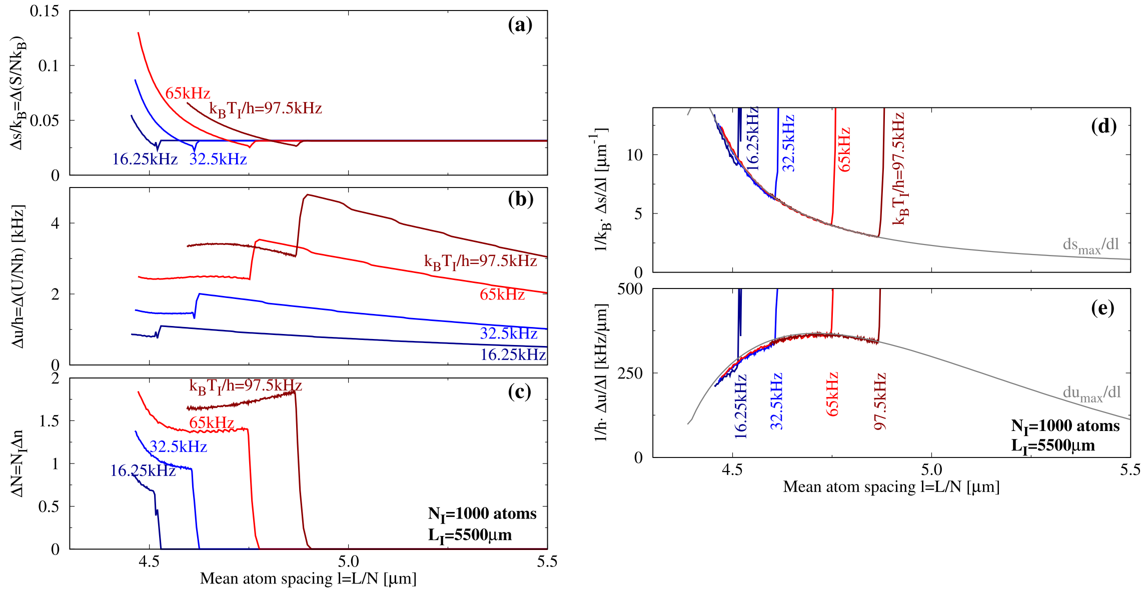

FIG. 10. Standard deviations (a) Δs, (b) Δu, and (c) Δn on the entropy per particle $s = S/N$, the energy per particle $u = U/N$, and the remaining atom fraction $n = N/N_I$, for the long chain of Fig. 5 in the main text. The ratios (d) $\Delta s/\Delta l$ and (e) $\Delta u/\Delta l$, with $\Delta l = (l/n)\Delta n$, closely follow the derivatives $ds_{\max}/dl$ and $du_{\max}/dl$ starting from the first expulsion.

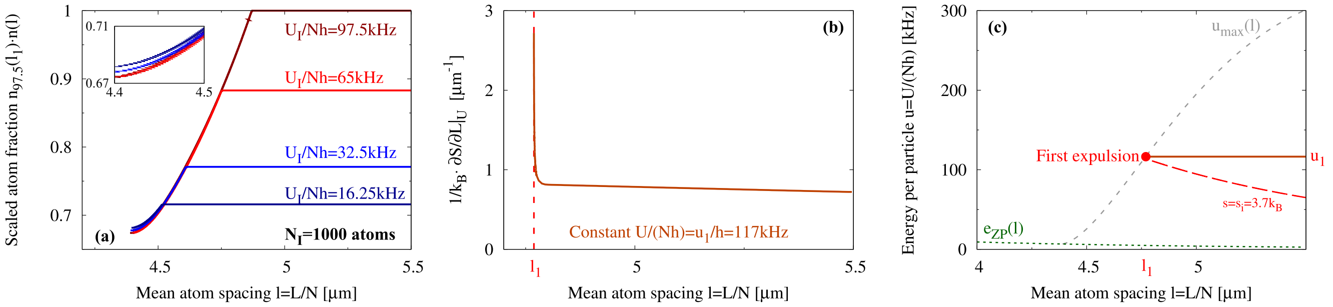

FIG. 11. (a) Scaled atom fraction $n = N/N_I$ for $N_I = 1000$ and various u_I, showing an approximate scaling whose breakdown is visible in the inset. (b) The derivative $\partial s/\partial l|_u$ calculated along the horizontal dark red path in panel (c). This path crosses the curve $u = u_{\max}(l)$ (dashed gray line) at the first expulsion point (l_1, u_1) for $u_I/h = 65$ kHz. The dotted-dashed red line shows the isentropic curve followed up to the first expulsion.

the universal curve $s = s_{\max}(l)$. Both of these properties are illustrated in Fig. 5 for various $u_I = U_I/N_I$, which set the mean atomic distance l_1 at which the first expulsion occurs.

b. Fluctuations

The quasiuniversality of the evaporation constrains the fluctuations Δu and Δs on the energy and entropy per particle to follow those on the atomic distance, Δl. Neglecting the small deviations from the universal curves $u = u_{\max}(l)$ and $s = s_{\max}(l)$, they satisfy $\Delta u/\Delta l = u'_{\max}(l)$ and $\Delta s/\Delta l = s'_{\max}(l)$ (see Fig. 10).

The constraint on $\Delta u/\Delta l$ has an important consequence. As l decreases, $u_{\max}(l)$ tends toward $e_{\mathrm{ZP}}(l)$ [see Fig. 5(b)]. Hence, the derivative $u'_{\max}(l)$ goes to zero. The fluctuations Δu do not vanish, therefore Δl increases and so does $\Delta n = (n/l)\Delta l$ [see Fig. 10(a)]. Thus, as long as the quasiuniversal regime holds, the constant-N plateaus will be poorly resolved. If the evaporation proceeds further, it will eventually drive the system out of the universal regime. Then, we expect to recover the short-chain behavior described in Appendix A 4. For the chain considered in Figs. 5 and 10, this occurs beyond the validity range of our assumption $E_M^{\mathrm{quant}} \gg E_{\mathrm{ZP}} + \hbar\omega_N$, and will be investigated elsewhere.

c. Nonuniversality of N/N_I

The entropy per particle $s(l, u)$ may be seen as a function of l and u. The derivative $\partial s/\partial u|_l = 1/T$ goes to zero on the curve $u = u_{\max}(l)$, which is reached for $T \to \infty$. However, our numerical results show that $\partial s/\partial l|_u$ diverges along the curve $u = u_{\max}(l)$ [see Fig. 11(b)]. Therefore, $s(l, u)$ may not be linearized near this curve, and the entropy difference $s^{(N-1)} - s^{(N)} = s(l_i^{(N-1)}, u_i^{(N-1)}) - s(l_f^{(N)}, u_f^{(N)})$ goes to zero slower than $1/N$. This rules out any exact universal behavior for the atom number fraction $n = N/N_I$. However, the deviation from universality is small. For a given N_I, we consider two initial energies $u_{I1} < u_{I2}$, and we compare the curves $n_{u_{I1}}(l)$ and $n_{u_{I2}}(l)$ for $l < l_1$, where l_1 is the mean atom spacing leading to the first expulsion for u_{I1}. Our numerical results show that these two curves nearly satisfy the scaling relation, which would have been exact had $\partial s/\partial l|_u$ not been divergent, namely $n_{u_{I2}}(l_1) n_{u_{I1}}(l) \approx n_{u_{I2}}(l)$ [see Fig. 11(a), whose inset highlights the breakdown of this scaling behavior].

The divergence of $\partial s/\partial l|_u = p/T$ along the curve $u = u_{\max}(l)$ signals that the pressure p goes to infinity faster than T does. This starkly contrasts with the behavior of the ideal gas, where $p/T = nk_{\mathrm{B}}$ is finite, its constant value being set by the particle density n.

[1] E. Wigner, Phys. Rev. **46**, 1002 (1934).
[2] C. C. Grimes and G. Adams, Phys. Rev. Lett. **42**, 795 (1979).
[3] J. G. Bohnet, B. C. Sawyer, J. W. Britton, M. L. Wall, A. M. Rey, M. Foss-Feig, and J. J. Bollinger, Science **352**, 1297 (2016).
[4] E. Jordan, K. A. Gilmore, A. Shankar, A. Safavi-Naini, J. G. Bohnet, M. J. Holland, and J. J. Bollinger, Phys. Rev. Lett. **122**, 053603 (2019).
[5] R. A. Guyer, Solid State Phys. **23**, 413 (1970).
[6] E. B. Sonin, Rev. Mod. Phys. **59**, 87 (1987).
[7] I. Coddington, P. Engels, V. Schweikhard, and E. A. Cornell, Phys. Rev. Lett. **91**, 100402 (2003).
[8] A. Haziot, X. Rojas, A. D. Fefferman, J. R. Beamish, and S. Balibar, Phys. Rev. Lett. **110**, 035301 (2013).
[9] J. Li, J. Lee, W. Huang, S. Burchevsky, B. Shteynas, F. C. Top, A. O. Jamison, and W. Ketterle, Nature (London) **543**, 91 (2017).
[10] J. Léonard, A. Morales, P. Zupancic, T. Esslinger, and T. Donner, Nature (London) **543**, 87 (2017).
[11] L. Tanzi, E. Lucioni, F. Famà, J. Catani, A. Fioretti, C. Gabbanini, R. N. Bisset, L. Santos, and G. Modugno, Phys. Rev. Lett. **122**, 130405 (2019).
[12] F. Böttcher, J. N. Schmidt, M. Wenzel, J. Hertkorn, M. Guo, T. Langen, and T. Pfau, Phys. Rev. X **9**, 011051 (2019).
[13] L. Chomaz, D. Petter, P. Ilzhöfer, G. Natale, A. Trautmann, C. Politi, G. Durastante, R. M. W. van Bijnen, A. Patscheider, M. Sohmen, M. J. Mark, and F. Ferlaino, Phys. Rev. X **9**, 021012 (2019).
[14] N. D. Mermin, Phys. Rev. **176**, 250 (1968).
[15] D. Vu and S. Das Sarma, Phys. Rev. B **101**, 125113 (2020).
[16] P. Jurcevic, B. P. Lanyon, P. Hauke, C. Hempel, P. Zoller, R. Blatt, and C. F. Roos, Nature (London) **511**, 202 (2014).

[17] P. Richerme, Z. Gong, A. Lee, C. Senko, J. Smith, M. Foss-Feig, S. Michalakis, A. V. Gorshkov, and C. Monroe, Nature (London) **511**, 198 (2014).

[18] C. Senko, J. Smith, P. Richerme, A. Lee, W. C. Campbell, and C. Monroe, Science **345**, 430 (2014).

[19] R. Lechner, C. Maier, C. Hempel, P. Jurcevic, B. P. Lanyon, T. Monz, M. Brownnutt, R. Blatt, and C. F. Roos, Phys. Rev. A **93**, 053401 (2016).

[20] V. V. Deshpande and M. Bockrath, Nature Phys. **4**, 314 (2008).

[21] I. Shapir, A. Hamo, S. Pecker, C. P. Moca, O. Legeza, G. Zarand, and S. Ilani, Science **364**, 870 (2019).

[22] S. Balibar, J. Beamish, A. Fefferman, A. Haziot, X. Rojas, and F. Souris, C. R. Phys. **17**, 264 (2016).

[23] H. L. Partner, R. Nigmatullin, T. Burgermeister, J. Keller, K. Pyka, M. B. Plenio, A. Retzker, W. H. Zurek, A. del Campo, and T. E. Mehlstäubler, Physica B **460**, 114 (2015).

[24] D. Kleppner, M. G. Littman, and M. L. Zimmerman, Sci. Am. **244**, 130 (1981).

[25] M. Saffman, T. G. Walker, and K. Mølmer, Rev. Mod. Phys. **82**, 2313 (2010).

[26] Y. Zeng, P. Xu, X. He, Y. Liu, M. Liu, J. Wang, D. J. Papoular, G. V. Shlyapnikov, and M. Zhan, Phys. Rev. Lett. **119**, 160502 (2017).

[27] T. L. Nguyen, J. M. Raimond, C. Sayrin, R. Cortiñas, T. Cantat-Moltrecht, F. Assemat, I. Dotsenko, S. Gleyzes, S. Haroche, G. Roux, T. Jolicoeur, and M. Brune, Phys. Rev. X **8**, 011032 (2018).

[28] H. Weimer, M. Müller, I. Lesanovsky, P. Zoller, and H. P. Büchler, Nat. Phys. **6**, 382 (2010).

[29] T. Pohl, E. Demler, and M. D. Lukin, Phys. Rev. Lett. **104**, 043002 (2010).

[30] P. Schauss, M. Cheneau, M. Endres, T. Fukuhura, S. Hild, A. Omran, T. Pohl, C. Gross, S. Kuhr, and I. Bloch, Nature (London) **491**, 87 (2012).

[31] P. Schauss, J. Zeiher, T. Fukuhara, S. Hild, M. Cheneau, T. Macri, T. Pohl, I. Bloch, and C. Gross, Science **347**, 1455 (2015).

[32] H. Bernien, S. Schwartz, A. Keesling, H. Levine, A. Omran, H. Pichler, S. Choi, A. S. Zibrov, M. Endres, M. Greiner, V. Vuletic, and M. D. Lukin, Nature (London) **551**, 579 (2017).

[33] D. Barredo, V. Lienhard, S. de Léséleuc, T. Lahaye, and A. Browaeys, Nature (London) **561**, 79 (2018).

[34] H. Labuhn, D. Barredo, S. Ravets, S. de Leseleuc, T. Macri, T. Lahaye, and A. Browaeys, Nature (London) **534**, 667 (2016).

[35] S. de Léséleuc, V. Lienhard, P. Scholl, D. Barredo, S. Weber, N. Lang, H. P. Büchler, T. Lahaye, and A. Browaeys, Science **365**, 775 (2019).

[36] G. Pupillo, A. Micheli, M. Boninsegni, I. Lesanovsky, and P. Zoller, Phys. Rev. Lett. **104**, 223002 (2010).

[37] Y. Jau, A. M. Hankin, T. Keating, I. H. Deutsch, and G. W. Biedermann, Nat. Phys. **12**, 71 (2016).

[38] J. Zeiher, R. van Bijnen, P. Schauss, S. Hild, J. Choi, T. Pohl, I. Bloch, and C. Gross, Nat. Phys. **12**, 1095 (2016).

[39] R. Löw, H. Weimer, J. Nipper, J. B. Balewski, B. Butscher, H. P. Büchler, and T. Pfau, J. Phys. B **45**, 113001 (2012).

[40] A. W. Glaetzle, M. Dalmonte, R. Nath, I. Rousochatzakis, R. Moessner, and P. Zoller, Phys. Rev. X **4**, 041037 (2014).

[41] H. Weimer, R. Löw, T. Pfau, and H. P. Büchler, Phys. Rev. Lett. **101**, 250601 (2008).

[42] R. Löw, H. Weimer, U. Krohn, R. Heidemann, V. Bendkowsky, B. Butscher, H. P. Büchler, and T. Pfau, Phys. Rev. A **80**, 033422 (2009).

[43] R. G. Hulet and D. Kleppner, Phys. Rev. Lett. **51**, 1430 (1983).

[44] D. A. Anderson, A. Schwarzkopf, R. E. Sapiro, and G. Raithel, Phys. Rev. A **88**, 031401(R) (2013).

[45] V. Zhelyazkova and S. D. Hogan, Phys. Rev. A **94**, 023415 (2016).

[46] A. Signoles, E. K. Dietsche, A. Facon, D. Grosso, S. Haroche, J. M. Raimond, M. Brune, and S. Gleyzes, Phys. Rev. Lett. **118**, 253603 (2017).

[47] D. Kleppner, Phys. Rev. Lett. **47**, 233 (1981).

[48] R. G. Hulet, E. S. Hilfer, and D. Kleppner, Phys. Rev. Lett. **55**, 2137 (1985).

[49] R. G. Cortiñas, M. Favier, B. Ravon, P. Méhaignerie, Y. Machu, J. M. Raimond, C. Sayrin, and M. Brune, Phys. Rev. Lett. **124**, 123201 (2020).

[50] M. Yamashita, M. Koashi, and N. Imoto, Phys. Rev. A **59**, 2243 (1999).

[51] O. J. Luiten, M. W. Reynolds, and J. T. M. Walraven, Phys. Rev. A **53**, 381 (1996).

[52] W. D. Johnston, Jr. and J. G. King, Phys. Rev. Lett. **16**, 1191 (1966).

[53] P. W. Anderson, Phys. Lett. A **29**, 563 (1969).

[54] F. Dalfovo, A. Fracchetti, A. Lastri, L. Pitaevskii, and S. Stringari, Phys. Rev. Lett. **75**, 2510 (1995).

[55] D. J. Papoular, L. P. Pitaevskii, and S. Stringari, Phys. Rev. A **94**, 023622 (2016).

[56] S. K. Dutta, J. R. Guest, D. Feldbaum, A. Walz-Flannigan, and G. Raithel, Phys. Rev. Lett. **85**, 5551 (2000).

[57] L. Allen, S. M. Barnett, and M. J. Padgett, *Optical Angular Momentum* (Institute of Physics, Bristol, UK, 2003).

[58] M. Brune and J. M. Raimond (private communication).

[59] DLMF, NIST Digital Library of Mathematical Functions, http://dlmf.nist.gov/ (2018).

[60] J. T. M. Walraven, *Quantum Dynamics of Simple Systems* (IOP, Bristol, UK, 1996).

[61] L. D. Landau and E. M. Lifshitz, *Statistical Physics, Part 1*, 3rd ed. (Elsevier, Amsterdam, 1980).

[62] G. Birkl, S. Kassner, and H. Walther, Nature (London) **357**, 310 (1992).

[63] H. Ikegami, H. Akimoto, D. G. Rees, and K. Kono, Phys. Rev. Lett. **109**, 236802 (2012).

[64] D. Barredo, S. de Léséleuc, V. Lienhard, T. Lahaye, and A. Browaeys, Science **354**, 1021 (2016).

[65] L. De Marco, G. Valtolina, K. Matsuda, W. G. Tobias, J. P. Covey, and J. Ye, Science **363**, 853 (2019).

[66] L. Anderegg, L. W. Cheuk, Y. Bao, S. Burchesky, W. Ketterle, K. Ni, and J. M. Doyle, Science **365**, 1156 (2019).

[67] M. A. Baranov, M. Dalmonte, G. Pupillo, and P. Zoller, Chem. Rev. **112**, 5012 (2012).

[68] BOOST.MULTIPRECISION library, https://www.boost.org/doc/libs/1_70_0/libs/multiprecision/doc/html/index.html (2019).

4 Mechanisms hindering ergodicity for three Rydberg atoms in a circular trap

This chapter summarises my most recent activity, devoted to semiclassical physics and chaos[1] in a three–body system. It is largely inspired by my published paper [4] and my recent preprint [5]. Both involve, as the sole other author, my PhD student Benoît Zumer.

This activity was initiated as my work on the evaporative cooling of a Rydberg atom chain, presented in chapter 3, was drawing to a close. There, my thermodynamic analysis hinged on the assumption that the system behaved ergodically during the evaporation. This assumption is not innocuous. The investigation of mechanisms impeding ergodicity, and their possible interplay with the evaporative cooling scheme, was a logical next step.

Various mechanisms impeding ergodicity have been investigated in the context of atomic systems. Among these, many–body localisation [68] usually relies on the presence of disorder. Integrability [69] is a property of specific models whose observation has required fine–tuning the trapping geometry [70]. Neither of these effects were expected to directly affect chains of Rydberg atoms.

By contrast, many–body scarring [29] had recently been experimentally identified in such a chain [22], and has been under intense theoretical scrutiny since then [71]. A key difficulty in its interpretation resides in it being observed in the quantum dynamics of a spin system, for which the construction of a classical analog is not straightforward [72].

This motivated the search for a simple system, involving spatial motion rather than spin dynamics, in which to look for ergodicity breaking. Inspired by recent experimental advances in Rydberg atom trapping [25, 26], we chose to focus on a trapped interacting few–body system. We consider a circular trapping geometry [73, Sec. II.C.2], with no dependence on the trapping potential in the longitudinal direction so as to avoid spurious single–particle effects. In this geometry, the total angular momentum along the axis of the trap is conserved, so that the two–particle problem is separable. We focus on the simplest non–separable case, namely, three repulsively interacting particles in a circular trap.

We formulate our proposal in terms of three identical bosonic Rydberg atoms, with parameters that are accessible in current experiments [28]. Then, the range of the interparticle interaction, which is of the order of $70\,\mu$m, exceeds the typical distance between the atoms, of the order of $12\,\mu$m. Hence, the system is not dilute, and the interaction may not be modelled by a contact potential. This sets our system apart from previous investigations of the three–body problem in the context of e.g. cold atoms [74, Sec. 2.1].

Similar phenomena are expected with magnetic atoms [17] or dipolar molecules [18].

---

[1] General references on these topics include the books [7, 63, 64] and the review articles [65–67].

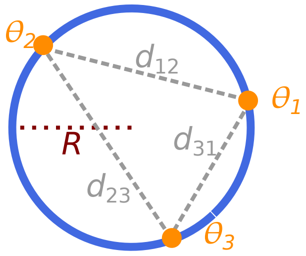

Figure 4.1: Three identical bosonic particles (orange disks) in a circular trap (blue) of radius R. Their positions are characterised by the three angular coordinates θ_1, θ_2, θ_3. Their distances d_{ij} satisfy $d_{ij} = 2R|\sin(\theta_i - \theta_j)/2|$.

4.1 The considered system

We consider three identical bosonic particles of mass m. Their internal state is assumed to be the same for all particles at all times, so that it drops out of the description. They are confined in a circular trap of radius R whose axis is perpendicular to the plane of Fig. 4.1. No single–particle trapping potential is added along the circle. The Hamiltonian reads:

$$H = \frac{l_1^2 + l_2^2 + l_3^2}{2mR^2} + V(\theta_1, \theta_2, \theta_3) \ , \tag{4.1}$$

where $l_i = mR^2\, d\theta_i/dt$ is the component of the angular momentum of particle i along the axis of the trap. The term V represents pair–wise interaction between the particles:

$$V(\theta_1, \theta_2, \theta_3) = v(d_{12}) + v(d_{23}) + v(d_{31}) \quad \text{with} \quad d_{ij} = 2R|\sin[(\theta_i - \theta_j)/2]|, \tag{4.2}$$

where we assume that the interaction $v(d_{ij})$ between particles i and j depends only on their distance d_{ij}. For circular Rydberg atoms whose electronic angular momenta are perpendicular to the plane, $v(d_{ij}) = C_6/d_{ij}^6$, where the interaction strength $C_6 > 0$, i.e. the two–atom interaction is repulsive.

4.1.1 Experimental prospects

We consider e.g. ^{87}Rb atoms in the circular Rydberg state $50C$, and consider energies (of the order of $h \times 200\,\text{kHz} = k_\text{B} \times 10\,\mu\text{K}$) and a spatial size for the trap (radius $7\,\mu$m) which are within the reach of ongoing experiments in the group led by M. Brune at LKB/Collège de France in Paris [28]. The considered geometry may be achieved owing to recent advances in Rydberg atom trapping [25, 26]. The ring–shaped trap may be realised optically using Laguerre–Gauss beams and light sheets [73, Sec. II.C]. The position of the atoms may be detected at a given time by turning on a 2D optical lattice trapping individual Rydberg atoms [24, 28] which freezes the dynamics, followed by atomic deexcitation and site–resolved ground–state imaging [75].

4.1.2 Rotational invariance: reduction to two degrees of freedom

In this section, we exploit a continuous symmetry to reduce the three–particle Hamiltonian of Eq. (4.1) to an effective Hamiltonian involving two degrees of freedom.

The interaction term of Eq. (4.2) satisfies $V(\theta_1, \theta_2, \theta_3) = V(\theta_1 + \theta_0, \theta_2 + \theta_0, \theta_3 + \theta_0)$ for any θ_0, i.e. the system exhibits rotational invariance. Hence, its total angular momentum is conserved. We separate it out using the Jacobi coordinates[2] (x, y, z) defined as:

$$\begin{cases} x = \left[(\theta_1 + \theta_2)/2 - \theta_3 + \pi\right]/\sqrt{3}\ , \\ y = (-\theta_1 + \theta_2)/2 - \pi/3\ , \\ z = (\theta_1 + \theta_2 + \theta_3)/3 - 2\pi/3\ , \end{cases} \qquad \text{that is,} \quad \begin{cases} \theta_1 = x/\sqrt{3} - y + z\ , \\ \theta_2 = x/\sqrt{3} + y + z + 2\pi/3\ , \\ \theta_3 = -2x/\sqrt{3} + z + 4\pi/3\ . \end{cases} \tag{4.3}$$

The constants $\pi/\sqrt{3}$, $-\pi/3$, $-2\pi/3$ appearing in Eq. (4.3) have been chosen such that the equilibrium position characterised by $\theta_1 = 0$, $\theta_2 = 2\pi/3$, $\theta_3 = 4\pi/3$ corresponds to $x = y = z = 0$. The momenta p_x, p_y, p_z conjugate to the coordinates x, y, z read $p_x = (l_1 + l_2 - 2l_3)/\sqrt{3}$, $p_y = -l_1 + l_2$, and $p_z = l_1 + l_2 + l_3$. In particular, p_z is the conserved total angular momentum. In terms of the coordinates x, y, z, and the momenta p_x, p_y, p_z, the Hamiltonian of Eq. (4.1) reads $H = p_z^2/(6mR^2) + H_{\mathrm{2D}}$, where:

$$H_{\mathrm{2D}} \quad = \quad (p_x^2 + p_y^2)/(4mR^2) \quad + \quad V(x, y)\ . \tag{4.4}$$

The effective Hamiltonian H_{2D} describes a fictitious particle of mass $2m$ and position $\boldsymbol{r} = (x, y)$, evolving in a 2D plane due to the potential $V(\boldsymbol{r}) = (C_6/R^6)\, \widetilde{V}(\boldsymbol{r})/64$, with

$$\widetilde{V}(\boldsymbol{r}) = \left[\frac{1}{\sin^6\left[\frac{\pi}{3} + y\right]} + \frac{1}{\sin^6\left[\frac{\pi}{3} - \frac{\sqrt{3}}{2}x - \frac{1}{2}y\right]} + \frac{1}{\sin^6\left[\pi/3 + \frac{\sqrt{3}}{2}x - \frac{1}{2}y\right]} - \frac{64}{9} \right]\ . \tag{4.5}$$

In Eq. (4.5), we take $V(\boldsymbol{r}) = V(\boldsymbol{\theta}) - 64/9 \times C_6/R^6$ so that $V(\boldsymbol{r} = \boldsymbol{0}) = 0$. The potential $V(\boldsymbol{r})$ does not depend on z, in accordance with the conservation of p_z.

The left panel of Figure 4.2 shows a few contour lines of $V(x, y)$ within the equilateral triangular region defined by the points $A(-\pi/\sqrt{3}, -\pi/3)$, $B(+\pi/\sqrt{3}, +\pi/3)$ and $C(0, 2\pi/3)$ in the (x, y) plane. This region corresponds to the condition $\theta_1 < \theta_2 < \theta_3 < \theta_1 + 2\pi$ on the angular coordinates. Each edge of the triangle corresponds to a collision between two particles, and $V(x, y) \to +\infty$ along all three edges, e.g. $V(x, y) \approx C_6/(y + \pi/3)^6$ near $[AB]$.

---

[2] The Jacobi coordinates play a role similar to the separation of the motion of two particles in terms of that of the centre of mass and that of the reduced particle. We use Faddeev's definition [76, Sec. 1.2.2] (rather than other existing definitions, see e.g. Ref. [77, Sec. 3.2]) because it leads to the momenta p_x, p_y appearing with the same mass $2m$ in the effective Hamiltonian H_{2D} of Eq. (4.4), hence easing the comparison with well–known models such as the Hénon–Heiles Hamiltonian of Eq. (4.11).

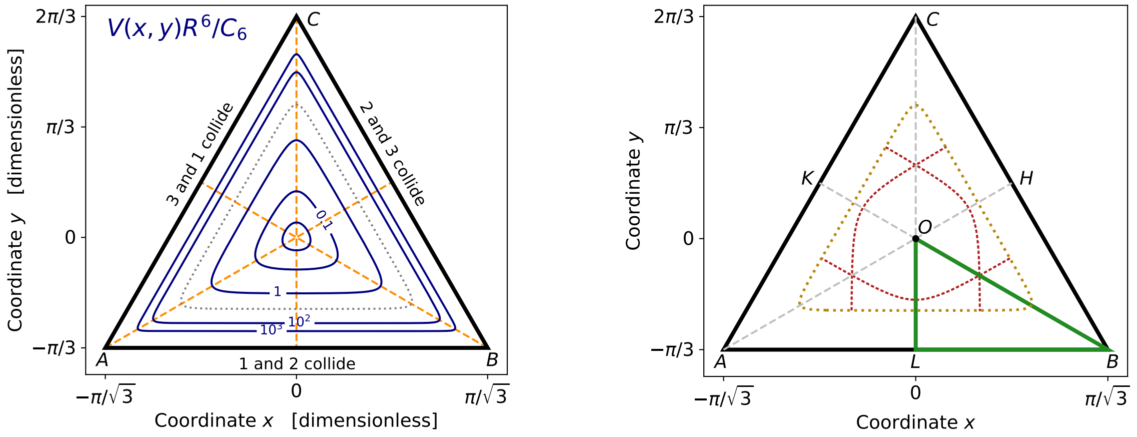

Figure 4.2: Left: Contour plot of the potential V of Eq. (4.5) within the equilateral triangular region ABC in the (x, y) plane, corresponding to $\theta_1 < \theta_2 < \theta_3 < \theta_1 + 2\pi$. **Right:** The (x, y) configuration space is the inside of the equilateral triangle defined by the points $A(-\pi/\sqrt{3}, -\pi/3)$, $B(+\pi/\sqrt{3}, -\pi/3)$, $C(0, 2\pi/3)$. The dashed golden line limits the classically accessible region for the energy $\epsilon = 7C_6/R^6$. The dotted red lines show the three classical periodic trajectories of type B for this energy. The small green triangle OLB is the asymmetric unit, i.e. the reduced configuration space within which wavefunctions are calculated.

4.1.3 Discrete symmetries of the interaction potential V

4.1.3.1 From angular coordinates to Jacobi coordinates

The interaction potential $V(\boldsymbol{\theta})$ of Eq. (4.2) exhibits three additional symmetry properties:

- (S_1) Angular periodicity:
$$V(\theta_1, \theta_2, \theta_3) = V(\theta_1 + 2\pi, \theta_2, \theta_3) = V(\theta_1, \theta_2 + 2\pi, \theta_3) = V(\theta_1, \theta_2, \theta_3 + 2\pi);$$
- (S_2) Symmetry under particle exchange: $V(\theta_1, \theta_2, \theta_3) = V(\theta_2, \theta_1, \theta_3) = V(\theta_1, \theta_3, \theta_2)$;
- (S_3) Three operations conserving both the particle ordering and their distances:
$$V(\theta_1, \theta_2, \theta_3) = V(-\theta_1 - 2\pi, -\theta_3, -\theta_2) = V(-\theta_3, -\theta_2, -\theta_1) = V(-\theta_2, -\theta_1, -\theta_3 + 2\pi)\ .$$

We now show that each of the properties (S_1), (S_2), and (S_3) yields a discrete symmetry leaving $V(\boldsymbol{r})$ invariant. These symmetries are defined in terms of the equilateral triangle ABC of Fig. 4.2 and the points O, H, K, L all defined on the right panel of the figure.

Angular periodicity. We start with the property (S_1). The operation expressed in terms of the angular coordinates as $\boldsymbol{\theta} \to \boldsymbol{\theta}'$, with $(\theta_1', \theta_2', \theta_3') = (\theta_1 + 2\pi, \theta_2, \theta_3)$, corresponds to a translation in terms of Jacobi coordinates: $\boldsymbol{r}, z \to \boldsymbol{r}', z'$ with $\boldsymbol{r}' = \boldsymbol{r} + \boldsymbol{CB}$ and $z' = z + 2\pi/3$. The potential $V(\boldsymbol{r})$ does not depend on z, hence, it is invariant under the translation $\boldsymbol{r} \to \boldsymbol{r} + \boldsymbol{CB}$. Similarly, it is invariant under the translations $\boldsymbol{r} \to \boldsymbol{r} + \boldsymbol{AC}$ and

$\boldsymbol{r} \to \boldsymbol{r} + \boldsymbol{BA}$. The associated shift $z \to z + 2\pi/3$, reflecting the change in the quantity $(\theta_1 + \theta_2 + \theta_3)/3$, is unimportant for classical mechanics, but it does play a role in quantum mechanics: see below and the third column of Table 4.1.

Symmetry under particle exchange. We turn to the property (S_2). The operation $\theta_1' = \theta_2$, $\theta_2' = \theta_1$, $\theta_3' = \theta_3$ exchanges particles 1 and 2. In terms of Jacobi coordinates, it corresponds to $\boldsymbol{r'} = \mathcal{S}_{(AB)}\boldsymbol{r}$ and $z' = z$, where $\mathcal{S}_\Delta$ is the reflection, in the (x, y) plane, about the axis Δ. Hence, $V(\boldsymbol{r})$ is invariant under the reflection $\mathcal{S}_{(AB)}$. Similarly, it is invariant under the reflections $\mathcal{S}_{(BC)}$ and $\mathcal{S}_{(CA)}$.

Three operations conserving both the particle ordering and their distances. Finally, we consider the property (S_3). Each of the three transformations considered there leaves the set of distances $\{d_{12}, d_{23}, d_{31}\}$ globally unchanged. Therefore, each leaves the potential V invariant. In terms of Jacobi coordinates, these operations read, respectively, $(\boldsymbol{r'} = \mathcal{S}_{(AH)}\boldsymbol{r}, z' = -z - 2\pi)$, $(\boldsymbol{r'} = \mathcal{S}_{(BK)}\boldsymbol{r}, z' = -z - 4\pi/3)$, and $(\boldsymbol{r'} = \mathcal{S}_{(CL)}\boldsymbol{r}, z' = -z - 2\pi/3)$. Here, $\mathcal{S}_{(AH)}$, $\mathcal{S}_{(BK)}$, and $\mathcal{S}_{(CL)}$ are the reflections, in the (x, y) plane, about the medians (AH), (BK), and (CL) of the triangle ABC. The potential $V(\boldsymbol{r})$ does not depend on z. Hence, $V(\boldsymbol{r})$ is invariant under these three reflections.

4.1.3.2 Plane group leaving the potential $V(\boldsymbol{r})$ invariant

The translations and reflections listed above generate the plane group leaving $V(\boldsymbol{r})$ invariant. This is an infinite group which contains, in particular,

(i) the translations through the vectors $\boldsymbol{AB}$ and $\boldsymbol{AC}$;

(ii) the rotation of order 6 about the point A: $\mathcal{R}_{A,\pi/3}$;

(iii) the reflections about the medians of the triangle ABC: $\mathcal{S}_{(AH)}$, $\mathcal{S}_{(BK)}$, and $\mathcal{S}_{(CL)}$;

(iv) the reflections about the edges of the triangle ABC: $\mathcal{S}_{(AB)}$, $\mathcal{S}_{(BC)}$, and $\mathcal{S}_{(CA)}$.

The plane group generated by these elements [78, part 6] is $p6mm$. This symbol should be interpreted as follows, using the elements *(i)–(iv)*. The initial lowercase 'p' means "primitive 2D lattice" (generated by *(i)* the vectors $\boldsymbol{AB}$ and $\boldsymbol{BC}$). The number '6' signals the presence of a rotation of order 6 (the rotation *(ii)* $\mathcal{R}_{A,\pi/3}$). The two letters 'm' signals the presence of two independent families of mirrors (the reflections about *(iii)* the medians of the triangle and *(iv)* its edges).

The reflections about the medians may not be expressed in terms of those about the edges (without using the rotation of order 6), because the product of two symmetries about lines that make up an angle $\pi/3$ (like (AB) and (AC)) is a rotation of angle $2\pi/3$, whereas rotations of angle $\pi/6$ or $\pi/2$ are required to relate the edges to the medians.

4.1.4 Classical mechanics

The Hamiltonian H of Eq. (4.1), or equivalently H_{2D} of Eq. (4.4), may represent either a classical system or a quantum one. We now examine these two points of view in turn.

In this section, we interpret H_{2D} as the Hamiltonian for a classical system. The classical trajectories of the system are identified by solving Newton's equation, $d\boldsymbol{p}/dt = -\nabla_{\boldsymbol{r}} H_{\mathrm{2D}}$.

In the change of variables specified by Eq. (4.3), the new coordinates (x, y, z) depend only on the old coordinates $\boldsymbol{\theta} = (\theta_1, \theta_2, \theta_3)$ (and not on the momenta l_i). Hence, this is a canonical transformation [79, §45], represented by the generating function $\Phi(\boldsymbol{\theta}; p_x, p_y, p_z) = x(\boldsymbol{\theta})\, p_x + y(\boldsymbol{\theta})\, p_y + z(\boldsymbol{\theta})\, p_z$.

4.1.4.1 Scaling property of the classical problem

The coordinates x, y are linear combinations of angles, hence, their conjugate momenta p_x, p_y carry the unit of action. Throughout this chapter, we express momenta, energies, and times in units of $P_{\mathrm{ref}} = (mC_6/R^4)^{1/2}$, $E_{\mathrm{ref}} = C_6/R^6$, and $T_{\mathrm{ref}} = (mR^8/C_6)^{1/2}$, respectively. Let $\widetilde{\boldsymbol{p}} = \boldsymbol{p}/P_{\mathrm{ref}}$ and $\widetilde{t} = t/T_{\mathrm{ref}}$. Then, Newton's equation governing the classical motion is $d\widetilde{\boldsymbol{p}}/d\widetilde{t} = -\nabla_{\boldsymbol{r}} \widetilde{V}$, which does not involve any of the experimental parameters m, C_6, and R. Hence, in these units, all *classical*[3] results are independent of these parameters.

4.1.4.2 Discrete symmetries within the equilateral triangle ABC

The fact that $V(\boldsymbol{r}) \to +\infty$ along the edges of the triangle ABC of Fig. 4.2 prevents the particles from crossing. Therefore, if the point $\boldsymbol{r}(t)$, representing classical motion in the (x, y) plane, is within the triangle at some initial time t_0, it remains within it at all times. Hence, we assume $\theta_1 < \theta_2 < \theta_3 < \theta_1 + 2\pi$ at all times, and the classical problem is reduced to a point moving in the 2D plane (x, y) within the equilateral triangle ABC, in the presence of the potential $V(x, y)$.

We focus on the interior of this triangle. Within it, the Hamiltonian H_{2D} of Eq. (4.4) is invariant under the point group C_{3v}, the centre O being a fixed point for all symmetry operations (see e.g. Ref. [80, §93]). The finite group[4] C_{3v} is a subgroup of the plane group $p6mm$ which consists of 6 discrete symmetry operations: the identity; the two rotations of order 3 about the origin O, namely, $\mathcal{R}_{O,+2\pi/3}$ and $\mathcal{R}_{O,-2\pi/3}$); and the three reflections about the medians (AH), (BK), (CL), namely, $\mathcal{S}_{(AH)}$, $\mathcal{S}_{(BK)}$, $\mathcal{S}_{(CL)}$. The points O, H, K, L involved in their definition all appear on the right panel of Fig. 4.2.

Each symmetry of the group C_{3v} transforms one classical trajectory with given energy ϵ into another one with the same energy, which may coincide with the initial one. For example, the right panel of Fig. 4.2 shows the three periodic trajectories of type B with the energy $\epsilon = 7C_6/R^6$ (see Sec. 4.3 for details) which correspond to each other through the rotations of C_{3v}, or equivalently its reflections. There are three, and not six, such trajectories because each of the corresponding curves in the (x, y) plane exhibits reflection symmetry about one median ($\mathcal{S}_{(AH)}$ or $\mathcal{S}_{(BK)}$ or $\mathcal{S}_{(CL)}$).

---

[3] This scaling no longer holds in quantum mechanics: see Sec. 4.1.5 below.

[4] We call the group C_{3v} (rather than D_3) because the potential $V(x, y)$ is translationally invariant under the direction z. Hence, the reflections $\mathcal{S}_{(AH)}$, $\mathcal{S}_{(BK)}$, $\mathcal{S}_{(CL)}$ are specular reflections within planes perpendicular to the (x, y) plane (rather than rotations about C_2 axes within the plane as in D_3).

4.1.5 Quantum mechanics

The Hamiltonian H of Eq. (4.1) is now an operator representing a quantum system. The angles $(\theta_i)_{1\leq i\leq 3}$ and angular momenta $l_i = -i\hbar\partial_{\theta_i}$ are also operators. Equation (4.3) maps them onto six operators $(x_i) = (x, y, z)$ and $(p_i) = (p_x, p_y, p_z)$. These satisfy the relation $p_i = -i\hbar\partial_{x_i}$ and, hence, the commutation rules $[x_i, p_i] = i\hbar\delta_{ij}$, $[x_i, x_j] = 0$, $[p_i, p_j] = 0$. We find the stationary states Ψ of the system by solving the stationary Schrödinger equation, $H\Psi = E\Psi$, with E being the energy corresponding to the eigenstate Ψ of H.

The reduced Planck constant $\hbar$ enters the description of the quantum system through the dimensionless ratio $\eta = \hbar/P_{\text{ref}} = \hbar R^2/(mC_6)^{1/2}$. The presence of this additional parameter with respect to classical mechanics signals the inapplicability of the classical scaling. Smaller values of η signal deeper quasiclassical behaviour. We choose $\eta = 0.01$, corresponding to realistic experimental parameters involving ^{87}Rb atoms in the circular Rydberg state $50C$ [28], for which $C_6/h = 3\,\text{GHz}\,\mu\text{m}^6$.

4.1.5.1 Accounting for rotational invariance

We now analyze the role of the continuous and discrete symmetries identified in Secs. 4.1.2 and 4.1.3 above for the quantum system. We start with (continuous) rotational invariance.

We consider wavefunctions corresponding to a well–defined value of the total angular momentum p_z. Hence, we seek the eigenfunctions of H in the form $\Psi_n(\boldsymbol{\theta}) = \psi_n(\boldsymbol{r})e^{inz}$. Here, Ψ_n is an eigenstate of H with the energy E_n. The wavefunction $\psi_n(\boldsymbol{r})$, which depends on the two coordinates $\boldsymbol{r} = (x, y)$, is an eigenstate of H_{2D} with the energy ϵ_n. The parameter n sets the value $p_z = n\hbar$. The energies E_n and ϵ_n are related through $E_n = \epsilon_n + \hbar^2 n^2/(6mR^2)$, where the term proportional to n^2 is the centrifugal energy.

4.1.5.2 Discrete symmetries of the wavefunction

There are two types of discrete symmetries of the *wavefunction* [69, chap. 2.5]. These are related to the properties (S_1) and (S_2) for the potential identified in Sec. 4.1.3, but come from physical considerations:

- (S_1) Univaluedness of the wavefunction:
  $\Psi(\theta_1 + 2\pi, \theta_2, \theta_3) = \Psi(\theta_1, \theta_2 + 2\pi, \theta_3) = \Psi(\theta_1, \theta_2, \theta_3 + 2\pi) = \Psi(\theta_1, \theta_2, \theta_3)$;
- (S_2) Bosonic symmetry: $\Psi(\theta_1, \theta_2, \theta_3) = \Psi(\theta_2, \theta_1, \theta_3) = \Psi(\theta_1, \theta_3, \theta_2)$.

Imposing conditions (S_1) and (S_2) on the wavefunction $\Psi_n(\boldsymbol{\theta})$ amounts to requiring that Ψ_n be a simultaneous eigenstate of H (eigenvalue ϵ, stationary Schrödinger equation); the single–particle rotation operators of angle 2π, $e^{-i2\pi l_1/\hbar}$, $e^{-i2\pi l_2/\hbar}$, $e^{-i2\pi l_3/\hbar}$ (eigenvalue 1, condition (S_1)); and the permutation operators $\mathcal{S}_{1,2}$, $\mathcal{S}_{2,3}$ exchanging the particles 1 and 2

Image of $\theta_1, \quad \theta_2, \quad \theta_3$	Image of $\boldsymbol{r}, \quad z$	Consequence for $\psi_n(\boldsymbol{r})$
Angular periodicity		
$\theta_1 + 2\pi, \quad \theta_2, \quad \theta_3$	$\boldsymbol{r} + \boldsymbol{CB}, \quad z + 2\pi/3$	$\psi_n(\boldsymbol{r} + \boldsymbol{CB}) = \psi_n(\boldsymbol{r}) e^{-i2n\pi/3}$
$\theta_1, \quad \theta_2 + 2\pi, \quad \theta_3$	$\boldsymbol{r} + \boldsymbol{AC}, \quad z + 2\pi/3$	$\psi_n(\boldsymbol{r} + \boldsymbol{AC}) = \psi_n(\boldsymbol{r}) e^{-i2n\pi/3}$
$\theta_1, \quad \theta_2, \quad \theta_3 + 2\pi$	$\boldsymbol{r} + \boldsymbol{BA}, \quad z + 2\pi/3$	$\psi_n(\boldsymbol{r} + \boldsymbol{BA}) = \psi_n(\boldsymbol{r}) e^{-i2n\pi/3}$
One pair of particles is exchanged		
$\theta_2, \quad \theta_1, \quad \theta_3$	$\mathcal{S}_{(AB)}\boldsymbol{r}, \quad z$	$\psi_n(\mathcal{S}_{(AB)}\boldsymbol{r}) = \psi_n(\boldsymbol{r})$
$\theta_1, \quad \theta_3, \quad \theta_2$	$\mathcal{S}_{(BC)}\boldsymbol{r}, \quad z$	$\psi_n(\mathcal{S}_{(BC)}\boldsymbol{r}) = \psi_n(\boldsymbol{r})$
$\theta_3 - 2\pi, \quad \theta_2, \quad \theta_1 + 2\pi$	$\mathcal{S}_{(CA)}\boldsymbol{r}, \quad z$	$\psi_n(\mathcal{S}_{(CA)}\boldsymbol{r}) = \psi_n(\boldsymbol{r})$
Two pairs of particles are exchanged		
$\theta_3 - 2\pi, \quad \theta_1, \quad \theta_2$	$\mathcal{R}_{(O,2\pi/3)}\boldsymbol{r}, \quad z - 2\pi/3$	$\psi_n(\mathcal{R}_{(O,2\pi/3)}\boldsymbol{r}) = \psi_n(\boldsymbol{r}) e^{i2n\pi/3}$

Table 4.1: Symmetry operations expressed in terms of the angular coordinates $(\theta_1, \theta_2, \theta_3)$ (left column) and in terms of the Jacobi coordinates $\boldsymbol{r} = (x, y)$, z (centre column). The right column shows their consequence for the wavefunction $\psi_n(\boldsymbol{r})$. The symbol $\mathcal{S}_\Delta$ represents a reflection about the straight line Δ in the (x, y) plane. The symbol $\mathcal{R}_{(\Omega,2\pi/3)}$ represents a rotation about the point Ω through the angle $2\pi/3$ in the (x, y) plane. (Both $\mathcal{S}_\Delta$ and $\mathcal{R}_{(\Omega,2\pi/3)}$ leave z unchanged.)

or 2 and 3 (eigenvalue 1, condition (S_2)). We now derive the consequences of these two properties, which are summarised in Table 4.1.

Univaluedness of the wavefunction. We consider the operation $\boldsymbol{\theta} \to \boldsymbol{\theta}'$, where $\theta'_1 = \theta_1 + 2\pi$, $\theta'_2 = \theta_2$, $\theta'_3 = \theta_3$. In terms of Jacobi coordinates, it corresponds to $(\boldsymbol{r}, z) \to (\boldsymbol{r}', z')$, with $\boldsymbol{r}' = \boldsymbol{r} + \boldsymbol{CB}$, $z' = z + 2\pi/3$. The wavefunction Ψ_n satisfies $\Psi_n(\boldsymbol{\theta}) = \Psi_n(\boldsymbol{\theta}')$, that is, $\psi_n(\boldsymbol{r})e^{inz} = \psi_n(\boldsymbol{r}')e^{inz'}$. Hence, $\psi_n(\boldsymbol{r} + \boldsymbol{CB}) = \psi_n(\boldsymbol{r})e^{-i2\pi n/3}$. Considering translations by 2π of the angles θ_2 and θ_3, we similarly obtain $\psi_n(\boldsymbol{r} + \boldsymbol{AC}) = \psi_n(\boldsymbol{r} + \boldsymbol{BA}) = \psi_n(\boldsymbol{r})e^{inz}$. Hence, the wavefunction $\psi_n(\boldsymbol{r})$ acquires a phase upon translation by a lattice vector[5] $\boldsymbol{CB}$, $\boldsymbol{AC}$, or $\boldsymbol{BA}$. These conditions are compatible if $\psi_n(\boldsymbol{r} + \boldsymbol{CB} + \boldsymbol{BA} + \boldsymbol{AC}) = \psi_n(\boldsymbol{r})$, which implies that n is an integer. Hence, the total angular momentum along the axis of the trap, $p_z = l_1 + l_2 + l_3$, is quantised, as expected [80, §27].

Bosonic symmetry. We now consider the operation represented by $\theta'_1 = \theta_2$, $\theta'_2 = \theta_1$, $\theta'_3 = \theta_3$, that is, we exchange particles 1 and 2. In terms of Jacobi coordinates, this reads $\boldsymbol{r}' = \mathcal{S}_{(\boldsymbol{AB})}(\boldsymbol{r})$ and $z' = z$. Here $\mathcal{S}_{(\boldsymbol{AB})}$ is the reflection, in the (x, y) plane, about the line (AB). Bosonic symmetry $\Psi(\boldsymbol{\theta}) = \Psi(\boldsymbol{\theta}')$ then leads to $\psi_n(\mathcal{S}_{(AB)}\boldsymbol{r}) = \psi_n(\boldsymbol{r})$. Exchanging particles 2 and 3, or 3 and 1, we find similar conditions involving reflections about the lines (BC) and (CA): $\psi_n(\boldsymbol{r}) = \psi_n(\mathcal{S}_{(BC)}\boldsymbol{r}) = \psi_n(\mathcal{S}_{(CA)}\boldsymbol{r})$. No phase is involved here, because the exchange of two particles leaves the quantity $(\theta_1 + \theta_2 + \theta_3)/3$ unchanged.

---

[5] The wavefunction $\psi_n(\boldsymbol{r})$ satisfies Bloch's theorem for discrete translations along the lattice spanned by $(\boldsymbol{a}_1 = \boldsymbol{AB},\ \boldsymbol{a}_2 = \boldsymbol{AC})$. For a given integer n, a single Bloch vector in the Brillouin zone is allowed. If $n = 0$ modulo 3, this vector is $\boldsymbol{k} = 0$. If $n = 1$ modulo 3, it is $\boldsymbol{k} = +2\pi(\boldsymbol{b}_1^* - \boldsymbol{b}_2^*)$. If $n = -1$ modulo 3, it is $\boldsymbol{k} = -2\pi(\boldsymbol{b}_1^* - \boldsymbol{b}_2^*)$. Here, $(\boldsymbol{b}_1^*, \boldsymbol{b}_2^*)$ is the reciprocal basis of the direct basis $(\boldsymbol{a}_1, \boldsymbol{a}_2)$ [81, chap. 1].

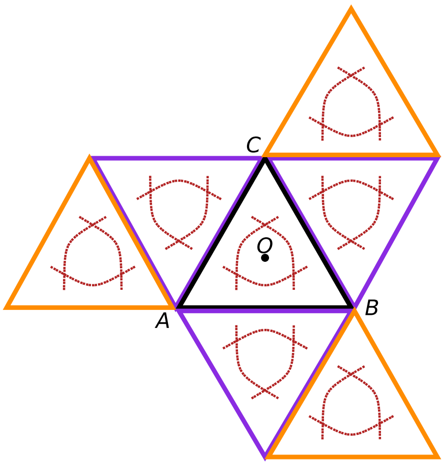

Figure 4.3: Tiling the (x, y) plane with the equilateral triangle ABC (in black) and its images (orange and purple triangles) through the symmetry operations of the right column of Table 4.1. Translations, leading to the orange triangles, are related to angular periodicity (e.g. $(\theta_1, \theta_2, \theta_3) \to (\theta_1 + 2\pi, \theta_2, \theta_3)$). Reflections, leading to the purple triangles, are related to bosonic exchange symmetry (e.g. $(\theta_1, \theta_2, \theta_3) \to (\theta_2, \theta_1, \theta_3)$). Within each triangle, the dotted red lines show the three periodic trajectories of type B with energy $\epsilon = 7C_6/R^6$, illustrating the symmetries with respect to the three medians of each triangle.

Combining the translations and rotations corresponding to the properties (S_1) and (S_2), we obtain:

Rotations about the point O. The transformation laws stated in the two previous paragraphs impose the behaviour of the wavefunction under the rotations of order 3, $\mathcal{R}_{O,2\pi/3}$ and $\mathcal{R}_{O,-2\pi/3}$, about the centre O of the equilateral triangle ABC. This follows from the following identities involving translations $\mathcal{T}$ and reflections $\mathcal{S}$:

$$\mathcal{R}_{(O,2\pi/3)} = \mathcal{S}_{(AB)}\,\mathcal{T}_{\boldsymbol{CA}}\,\mathcal{S}_{(BC)} = \mathcal{S}_{(BC)}\,\mathcal{T}_{\boldsymbol{AB}}\,\mathcal{S}_{(CA)} = \mathcal{S}_{(CA)}\,\mathcal{T}_{\boldsymbol{BC}}\,\mathcal{S}_{(AB)}\ . \tag{4.6}$$

All three relations of Eq. (4.6) lead to the same condition:

$$\psi_n(\mathcal{R}_{(O,2\pi/3)}\boldsymbol{r}) = e^{i2\pi/3}\psi_n(\boldsymbol{r})\ . \tag{4.7}$$

4.1.5.3 Reduction to the triangle ABC for the quantum problem

The derivation given above of the quantisation of the total angular momentum p_z hinges on translating the wavefunction $\psi_n(\boldsymbol{r})$ by lattice vectors. Hence, the wavefunction should be considered as defined over the whole (x, y) plane. We tile this plane with triangles as on Fig. 4.3. Combining lattice–vector translations and symmetries with respect to the three edges of the triangle ABC, the wavefunction ψ_n is invariant under the reflections about the edges of all triangles (only a few of which are shown on the figure). Therefore, it is fully determined by giving its values within the equilateral triangle ABC (see Sec. 4.1.4).

As stated in Sec. 4.1.2, the potential $V(x, y)$ strongly diverges along the edges of the triangle ABC, e.g. $V(x, y) \approx C_6/(y + \pi/3)^6$ near $[AB]$. Therefore, $\psi_n(x, y) = 0$ along all three edges. Hence, the wavefunction ψ_n may be calculated within the interior of the triangle ABC with this boundary condition. This domain coincides with the configuration space considered in classical physics (cf. Sec. 4.1.4).

4.1.5.4 Wavefunctions and representations of the C_{3v} group

The potential $V(x,y)$ exhibits one further symmetry property, (S_3). As stated in Sec. 4.1.4, once the problem has been restricted to the interior of the triangle ABC, this property leads to C_{3v} symmetry for the potential, the fixed point being the centre O of the triangle.

The classification of the eigenstates of $H_{2\mathrm{D}}$ in terms of the symmetry group C_{3v} hinges on its *irreducible representations* [80, §94–96]. Under a symmetry transformation, the wavefunctions of the stationary states of the system corresponding to a given energy level transform into linear combinations of one another. Hence, the eigenspace corresponding to a given energy is stable under the action of the symmetry group, i.e. it gives a representation of the group. Barring accidental degeneracies or additional symmetries not accounted in the symmetry group, the stable subspace may not be separated into two subspaces of strictly smaller dimension that would also be stable, i.e. the representation is irreducible.

The irreducible representations of the group C_{3v} are well known (see e.g. Table 7 in Ref. [80, §95]). There are three of them, named A_1, A_2, and E. Representations A_1 and A_2 are unidimensional, whereas representation E is two–dimensional[6]. The transformation laws for these representations may be formulated in terms of the rotation $\mathcal{R} = \mathcal{R}_{O,2\pi/3}$ about the point O through the angle $2\pi/3$, and the reflection $\mathcal{S} = \mathcal{S}_{(CK)}$ about the vertical median, which generate the group C_{3v}:

- Representation A_1:
  the *non–degenerate* level ψ_n satisfies $\psi_n(\mathcal{R}r) = +\psi_n(\boldsymbol{r}), \quad \psi_n(\mathcal{S}r) = +\psi_n(\boldsymbol{r})$.
- Representation A_2:
  the *non–degenerate* level ψ_n satisfies $\psi_n(\mathcal{R}r) = +\psi_n(\boldsymbol{r}), \quad \psi_n(\mathcal{S}r) = -\psi_n(\boldsymbol{r})$.
- Representation E:
  the *two–fold degenerate* level is spanned by 2 orthogonal wavefunctions. Because of Eq. (4.7), we choose basis functions[7] $\psi_n^{(+)}$, $\psi_n^{(-)}$ which diagonalise the action of $\mathcal{R}$:
  $\psi_n^{(+)}(\mathcal{R}^{-1}\boldsymbol{r}) = e^{+i2\pi/3}\psi_n^{(+)}(\boldsymbol{r}), \quad \psi_n^{(+)}(\mathcal{S}\boldsymbol{r}) = \psi_n^{(-)}(\boldsymbol{r})$;
  $\psi_n^{(-)}(\mathcal{R}^{-1}\boldsymbol{r}) = e^{-i2\pi/3}\psi_n^{(-)}(\boldsymbol{r}), \quad \psi_n^{(-)}(\mathcal{S}\boldsymbol{r}) = \psi_n^{(+)}(\boldsymbol{r})$.

The choice of a representation A_1, A_2, or E defines the action of the symmetry elements $\mathcal{S}$ and $\mathcal{R} = \mathcal{R}_{O,2\pi/3}$ within the triangle ABC. Comparing the transformation laws for the representations with Eq. (4.7), we conclude that the value of the angular momentum n modulo 3 pilots the accessible representations:

- If $n = 0$ modulo 3, ψ_n belongs to a 1D representation A_1 or A_2;
- If $n = \pm 1$ modulo 3, ψ_n belongs to a 2D representation E.

---

[6] The existence of the 2D representation follows from the non–commutativity of the group C_{3v}: for any rotation $\mathcal{R}$ and any reflection $\mathcal{S}$ in it, $\mathcal{S}\mathcal{R} = \mathcal{R}^{-1}\mathcal{S}$.

[7] The alternative basis vectors $\psi_n^{(+)} \pm \psi_n^{(-)}$ would lead to a representation of $\mathcal{R}$ and $\mathcal{S}$ in terms of real matrices. However, this choice is incompatible with Eq. (4.7).

Asymmetric unit. We focus on an eigenstate $\psi_n(\boldsymbol{r})$ of $H_{2\mathrm{D}}$ which transforms, under the symmetry elements of C_{3v}, according to a given representations A_1, A_2, or E. The transformation laws further reduce the domain containing the independent values of the function $\psi_n(\boldsymbol{r})$ to the small green triangle of the right panel of Fig. 4.2, whose area is one sixth of that of the complete triangle ABC.

4.1.5.5 Numerical solution of the stationary Schrödinger equation

We numerically solve the stationary Schrödinger equation for the Hamiltonian $H_{2\mathrm{D}}$ of Eq. (4.4) using the finite–element software FreeFEM [82]. We calculate stationary states belonging to the three irreducible representations A_1, A_2, E of the group C_{3v} separately. The calculation is performed within the asymmetric unit defined in the previous paragraph, and we formulate the transformation laws for each representation as a boundary condition applied on its edges. We use a triangular mesh which covers and slightly exceeds the classically accessible region (limited by the dashed golden line on the right panel of Fig. 4.2). The mesh comprises 1000 vertices along each edge. We thus numerically obtain the energies and wavefunctions for slightly more than 1200 consecutive energy levels for Representation A_1, 1200 levels for Representation A_2, and 1700 non–degenerate levels for Representation E, in energy intervals centred on $7C_6/R^6$.

We shall exploit these numerical results in the subsequent sections of this chapter. More specifically, we shall analyse the energy spectra in Sec. 4.2, and a few specific eigenstate wavefunctions (those localised near classical periodic trajectories) in Secs. 4.4 and 4.5.

Technical details for representations A_1 and A_2. Representations A_1 and A_2 are unidimensional. Hence, the wavefunctions $\psi_n(\boldsymbol{r})$ of the stationary states pertaining to them may be chosen to be real [80, §18]. The finite–element method hinges on formulating the weak form [83, chap. 3] of the considered eigenvalue problem $H_{2\mathrm{D}}\,\psi_n = \epsilon\psi_n$, which involves a bilinear form in the sought function ψ_n and a test function ϕ. For Representations A_1 and A_2, it reads:

$$\int d^2r \left[+\frac{\hbar^2}{4mR^2}(\nabla\phi)\cdot(\nabla\psi_n) + V(\boldsymbol{r})\,\phi\,\psi_n\right] = \epsilon \int d^2r\,\phi_n\,\psi\ . \tag{4.8}$$

Equation (4.8) is supplemented by the boundary conditions, which depend on the considered representation. For the representation A_1, $\psi_n = 0$ along $[LB]$, and the normal derivative $\partial\psi_n/\partial n = 0$ along $[BO]$ and $[OL]$. For the representation A_2, $\psi_n = 0$ along all three edges $[LB]$, $[BO]$, and $[OL]$.

Technical details for Representation E. Representation E is two–dimensional. It allows for some freedom in the choice of the basis vectors $\psi_n^{(+)}$ and $\psi_n^{(-)}$ (the transformation laws should then be adapted accordingly). Exploiting time–reversal symmetry, these may be chosen to be complex–conjugate: $\psi_n^{(+)}(\boldsymbol{r}) = \psi_n^{(-)*}(\boldsymbol{r})$. Then, with a suitable choice for the phases [4, Appendix, Sec. 2b], $\psi_n^{(+)}$ is characterised by:

$$\psi_n^{(+)}(\mathcal{R}^{-1}\boldsymbol{r}) = e^{i2\pi/3}\,\psi_n^{(+)}(\boldsymbol{r}) \quad \text{and} \quad \psi_n^{(+)}(\mathcal{S}r) = \psi_n^{(+)*}(\boldsymbol{r})\ . \tag{4.9}$$

The proof that a basis $(\psi_n^{(+)}, \psi_n^{(-)})$ for representation E exists which satisfies Eq. (4.9) along with $\psi_n^{(+)}(\boldsymbol{r}) = \psi_n^{(-)*}(\boldsymbol{r})$ is given in the next paragraph. In view of the numerical calculations, we write $\psi_n^{(+)}(\boldsymbol{r}) = (x - iy)[u_1(\boldsymbol{r}) + iu_2(\boldsymbol{r})]$, where u_1 and u_2 are two real functions satisfying coupled Schrödinger equations. The factor $(x - iy)$ accounts for the fact that $\psi_n^{(+)}(\boldsymbol{0}) = 0$, like for the states of the 2D isotropic harmonic oscillator carrying angular momentum [80, §112]. The boundary conditions read $u_1 = u_2 = 0$ along $[LB]$, and $u_1 = 0$, $\partial u_2/\partial n = 0$ along $[BO]$ and $[OL]$. A weak form may be written in terms of the functions u_1 and u_2: it is similar to, but lengthier than, Eq. (4.8). In accordance with the last line of Table 4.1, the physical wavefunction $\psi_n(\boldsymbol{r})$ satisfies $\psi_n = \psi_n^{(-)}$ if $n = +1$ modulo 3, and $\psi_n = \psi_n^{(+)}$ if $n = -1$ modulo 3.

Proof of the existence of the basis $(\psi_n^{(+)}, \psi_n^{(-)})$ satisfying Eq. (4.9). We start from a basis of functions $(\phi_n^{(+)}, \phi_n^{(-)})$, both normalised to 1, which satisfy the usual conditions for representation E [84, Sec. 5.3]:

$$\begin{cases} \phi_n^{(+)}(\mathcal{R}^{-1}\boldsymbol{r}) = e^{\ i2\pi/3}\,\phi_n^{(+)}(\boldsymbol{r})\ , \\ \phi_n^{(-)}(\mathcal{R}^{-1}\boldsymbol{r}) = e^{-i2\pi/3}\,\phi_n^{(-)}(\boldsymbol{r})\ , \end{cases} \qquad \begin{cases} \phi_n^{(+)}(\mathcal{S}\boldsymbol{r}) = \phi_n^{(-)}(\boldsymbol{r})\ , \\ \phi_n^{(-)}(\mathcal{S}\boldsymbol{r}) = \phi_n^{(+)}(\boldsymbol{r})\ . \end{cases} \tag{4.10}$$

Complex–conjugating the two relations in the left half of Eq. (4.10), we obtain $\phi_n^{(+)*}(\mathcal{R}^{-1}\boldsymbol{r}) = e^{-i2\pi/3}\phi_n^{(+)*}(\boldsymbol{r})$ and $\phi_n^{(-)*}(\mathcal{R}^{-1}\boldsymbol{r}) = e^{i2\pi/3}\phi_n^{(-)*}(\boldsymbol{r})$. Therefore, $\phi_n^{(+)*} = \alpha\phi_n^{(-)}$ and $\phi_n^{(-)*} = \beta\phi_n^{(+)}$, with α and β being complex numbers. The complex–conjugate functions $\phi_n^{(+)*}$ and $\phi_n^{(-)*}$ also have norm 1, so that $|\alpha| = |\beta| = 1$. The identity $[\phi_n^{(+)*}(\boldsymbol{r})]^* = \phi_n^{(+)}(\boldsymbol{r})$ leads to $\alpha^*\beta = 1$, so that $\alpha = \beta$. At this point, $\phi_n^{(+)}(\mathcal{S}\boldsymbol{r}) = \alpha^*\phi_n^{(+)*}(\boldsymbol{r})$. Now, choose any complex number γ such that $\gamma^2 = \alpha$, and let $\psi_n^{(+)} = \gamma\phi_n^{(+)}$, $\psi_n^{(-)} = \gamma\phi_n^{(-)}$. Then, all sought conditions hold: $\psi_n^{(+)}(\mathcal{R}^{-1}\boldsymbol{r}) = e^{i2\pi/3}\,\psi_n^{(+)}(\boldsymbol{r})$, $\psi_n^{(+)}(\mathcal{S}\boldsymbol{r}) = \psi_n^{(+)*}(\boldsymbol{r})$, and $\psi_n^{(+)*}(\boldsymbol{r}) = \psi_n^{(-)}(\boldsymbol{r})$.

4.1.6 Analogy with the Hénon–Heiles Hamiltonian

The Hénon–Heiles Hamiltonian (see e.g. Ref. [7, chap. 8.2]) has been extensively studied in the literature, both from the classical point of view and from the quantum one. It reads:

$$H_{\mathrm{HH}} \quad = \quad (p_x^2 + p_y^2)/(2m) \quad + \quad m\omega_0^2(x^2 + y^2)/2 \quad + \quad \alpha(x^2 y - y^3/3)\ . \tag{4.11}$$

In Eq. (4.11), the coordinates x and y carry the unit of length, the quantities p_x and p_y are their conjugate momenta, the parameters m and ω_0 denote a mass and a frequency, and the coefficient α sets the strength of the cubic term. The model supports bound classical trajectories with energies smaller than $(m\omega_0^2)^3/(6\alpha^2)$.

The Hénon–heiles model of Eq. (4.11) exhibits $C_{3\mathrm{v}}$ symmetry [85]. This allows for an analogy with the system we consider. In particular, the analysis of the symmetries of

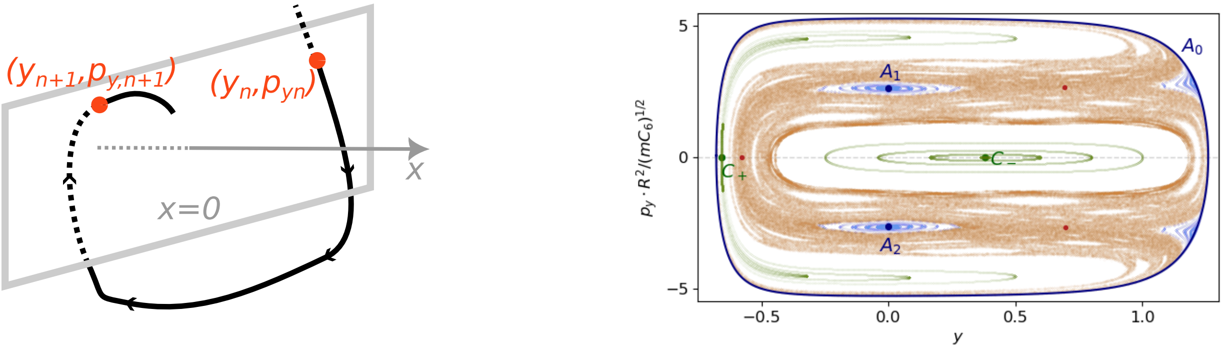

Figure 4.4: **Left:** Schematic representation of the definition of the surface of section. **Right:** Surface of section of the classical Hamiltonian $H_{2\mathrm{D}}$, for the energy $\epsilon = 7C_6/R^6$ and $x = 0$, $p_x > 0$.

classical periodic trajectories for the Hénon–Heiles potential [86] may be adapted to the potential of Eq. (4.5). The analogy with the Hénon–Heiles model is actually far–reaching: in addition to their shared symmetry group, both models also exhibit a mixed classical phase space (see Sec. 4.2.1 below). The realisation of our proposed system may thus be understood as the 'simulation' of the Hénon–Heiles Hamiltonian using a system from atomic physics.

The difference between the Hénon–Heiles model and the three–particle system we analyse resides in the considered geometry. The Hénon–Heiles Hamiltonian is defined over the whole (x, y) plane, whereas the circular trap leads us to restrict both the classical configuration space and the wavefunctions of the eigenstates of $H_{2\mathrm{D}}$ to the interior of the equilateral triangle ABC of Fig. 4.2. For the energies we consider ($\sim 7C_6/R^6$), the classically accessible region is noticeably smaller than the classical configuration space, and the wavefunctions of the quantum eigenstates do not substantially extend outside of it. Hence, the role[8] of this difference is minimal.

4.2 Mixed classical phase space, Berry–Robnik statistics

The nature of the classical phase space of a system is known to have an important impact on the statistics of the energy levels of the corresponding quantum system [7, chap. 16]. The effect should be sought in the fluctuations of the 'unfolded' (i.e. scaled, see below) energy level spacings. Two limiting cases allow for a straightforward formulation of the correspondence between classical phase space and quantum level statistics:

---

[8] The circular geometry yields a selection rule relating the eigenstates of $H_{2\mathrm{D}}$ belonging to different irreducible representations of the group C_{3v} to different values of the total angular momentum n modulo 3: see Sec. 4.1.5.4.

- Classical integrable systems [63, §49] (e.g. the 2D square billiard), which only support non–ergodic trajectories, lead to Poissonian level statistics;

- Classical chaotic systems (e.g. the 2D Bunimovich stadium billiard; general references include [65, §8], [64, chap. 3], and [7, chap. 10]), almost all of whose trajectories are ergodic, lead to Wigner level statistics.

This correspondence, put forward in Refs. [87, 88], has been extensively investigated numerically and experimentally (see [89, chap. 2] for a review of experiments involving billiards).

Most classical systems are neither integrable nor fully chaotic. Their classical phase space is mixed [67, Sec. 1], in the sense that they support both both non–ergodic trajectories and ergodic ones. The Hénon–Heiles model is such a system [7]. Their quantum energy level statistics are expected to obey neither the Poisson nor the Wigner distribution. More sophisticated distributions have been proposed to represent these level statistics [90, 91].

The goal of this section is two–fold. Firstly, we show that the classical phase space of the Hamiltonian H_{2D} of Eq. (4.4) is mixed. Secondly, turning to the corresponding quantum system, we justify that its energy level spacings obey Berry–Robnik statistics [91].

4.2.1 Mixed classical phase space

4.2.1.1 Regular and irregular trajectories

The Hamiltonian H_{2D} represents an effective system with two degrees of freedom, so that the classical phase space has dimension 4 (two coordinates x, y; two momenta p_x, p_y). The Hamiltonian H_{2D} does not depend on time, so that each classical trajectory has a well–defined energy ϵ. Hence, a given trajectory explores a subset of phase space whose dimension is at most 3. This trajectory densely covers a subset of phase space. We now consider two cases, depending on the dimension of this subset:

- If the dimension of the subset is 2 (or 1 for periodic trajectories), the trajectory is *regular*. In the case of bound motion considered here, it typically winds around a torus [63, §49 and appendix 8]. It is non–ergodic, because its dimension is strictly smaller than that of the energy surface (dimension 3);

- If the dimension of the subset is 3, the trajectory is *irregular*, and it ergodically explores part of phase space [7, Sec. 8.3].

The subset considered here is obtained by considering the whole classical trajectory, obtained from all times ranging from $-\infty$ to $+\infty$. The result is an object which no longer depends on time, and which may hence be compared to the eigenstates of the quantum Hamiltonian obtained by solving the stationary Schrödinger equation. For regular trajectories, the comparison may be formulated precisely [92, Table V], and it plays a key role in the semiclassical approach employed in Sec. 4.5 below.

4.2.1.2 Surface of section

The *surface of section* [93, Sec. 1.2] allows for a graphical representation of the classical phase space of a system, and the distinction between regular and irregular trajectories.

To each point (x, y, p_x, p_y) in phase space corresponds the energy of the single classical trajectory defined by the initial condition (x, y, p_x, p_y). The energy surface comprised of all points with the same energy ϵ has dimension 3; the intersection of this set with the hyperplane characterised by $x = 0$ has dimension 2. The conservation of the energy ϵ reads $p_x^2 = 4mR^2[\epsilon - V(x = 0, y)] - p_y^2$, so that to each point with energy ϵ, $x = 0$, and given values of y and p_y correspond two different trajectories which differ by the sign of p_x. Therefore, the surface of section is defined as the set of points in phase space having the energy ϵ with $x = 0$ and $p_x > 0$. Then, any point of the surface of section may be specified by the two values y and p_y, and leads to a single classical trajectory.

We show the surface of section for $H_{2\mathrm{D}}$, calculated for the experimentally accessible energy $\epsilon = 7C_6/R^6$, on the right panel of Fig. 4.4. It may be directly compared to the surfaces of section for the Hénon–Heiles model [7, Sec. 8.3]. In particular, the surfaces of section for both models exhibit reflection symmetry about the horizontal axis of the figure $[(y, p_y) \rightarrow (y, -p_y)]$, which results from the simultaneous presence of *(i)* spatial reflection symmetry about the $x = 0$ axis in the (x, y) plane, and *(ii)* time reversal symmetry.

Regular and irregular trajectories may be told apart visually by considering their intersections with the surface of section:

- Regular, non–ergodic trajectories, which wind around tori, lead to concentric closed *curves*. A few of these appear on Fig. 4.4 in blue and green.

- Non–regular, ergodic trajectories densely cover a fraction of the *area* of the surface of section. On Fig. 4.4, the $\approx 287\,000$ thin brown dots represent intersections which all belong to the same single ergodic trajectory.

Finally, the *fixed points* represent periodic trajectories, of which there are two types. *(i)* The fixed points A_0, A_1, C_+, C_- are surrounded by concentric closed curves signalling regular trajectories. Hence, the corresponding periodic trajectories are *stable*. *(ii)* The three fixed points represented in red are within the area covered by the ergodic trajectory. These fixed points signal the *unstable* trajectories B_1, B_2, and B_3. Periodic trajectories are analysed in detail in Sec. 4.3 below.

The key result of this paragraph is that the surface of section for $H_{2\mathrm{D}}$, calculated for the energy $\epsilon = 7C_6/R^6$, exhibits both regular and irregular trajectories. Hence, the classical system has a mixed phase space, as does the Hénon–Heiles model.

Numerical calculations. We obtain the classical trajectories, and their intersections with the surface of section of Fig. 4.4, by solving the equations of motion for the Hamiltonian $H_{2\mathrm{D}}$ numerically, using Python and its numerical libraries NumPy and SciPy [94, 95].

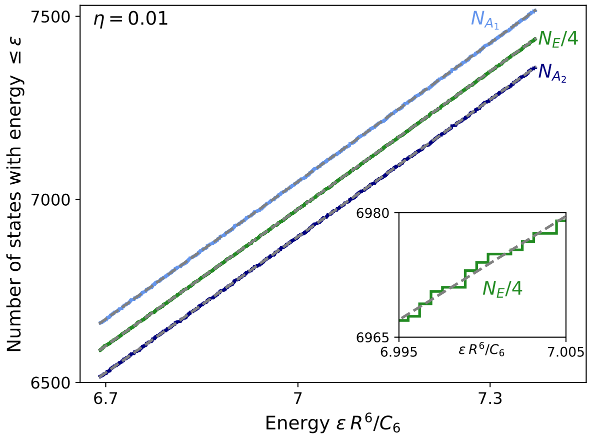

Figure 4.5: Integrated density of states $N_r(\epsilon)$ as a function of the energy for the three irreducible representations $r = A_1$ (light blue), A_2 (dark blue), and E (green), compared to their smooth Weyl expansion including orders $1/\hbar^2$ and $1/\hbar$ (dotted gray). The inset is a zoom on a narrow range of energies for the function $N_E(\epsilon)$ highlighting its staircase–like behaviour. The functions N_{A_1} and N_{A_2}, not shown in the inset, exhibit a similar behaviour.

We use an integration algorithm of the Runge–Kutta type [96, Sec. 17.2.4], 'DOP853', already used in our previous work involving the coupled–channels approach to quantum scattering [97, Sec. 12.4].

4.2.2 Berry–Robnik statistics for the quantum energy levels

In this section, we analyse the spectra of eigenvalues of the Hamiltonian $H_{2\mathrm{D}}$ obtained, for each of the three irreducible representations $r = A_1$, A_2, and E of the group C_{3v}, by solving the stationary Schrödinger equation.

The object we consider is $N_r(\epsilon)$, the integrated density of states [7, Sec. 16.2] for the Hamiltonian $H_{2\mathrm{D}}$ restricted to the representation r. This is a staircase–like function (see the inset in Fig. 4.5) counting the number of eigenstates of $H_{2\mathrm{D}}$ whose energies are $\leq E$. It has a smooth component, $\bar{N}(\epsilon)$, and exhibits fluctuations $N_{\mathrm{fl}}(\epsilon)$ about this smooth component [67, Sec. 5.4], so that $N(\epsilon) = \bar{N}(\epsilon) + N_{\mathrm{fl}}(\epsilon)$.

The link between the spectral fluctuations and the Poisson, Wigner, and Berry–Robnik distributions highlighted at the beginning of Sec. 4.2 does not apply to $N_{\mathrm{fl}}(\epsilon)$ directly. It holds for the 'unfolded' spectrum, i.e. the energy levels should be rescaled through $\hat{\epsilon}_i = \bar{N}_r(\epsilon_i)$ so that their mean spacing is equal to unity [67]. This allows for the comparison of the spectral fluctuations of systems whose smooth integrated densities are not the same.

The parameter $\eta = 0.01$. For each representation, our analysis involves more than 1000 consecutive eigenvalues within an energy interval centred on $7C_6/R^6$. We proceed in two steps. Firstly, we characterise the smooth component $\bar{N}_r(\epsilon)$ of the integrated density of states, for each representation r. Secondly, we show that the unfolded level spacings are well represented by Berry–Robnik statistics [91].

4.2.2.1 Smooth component of the integrated density of states

The integrated density of states $N_r(\epsilon)$ depends on the considered irreducible representation $r = A_1$, A_2, or E [98] (see also Ref. [99] which focuses on quantum billiards). Indeed, even

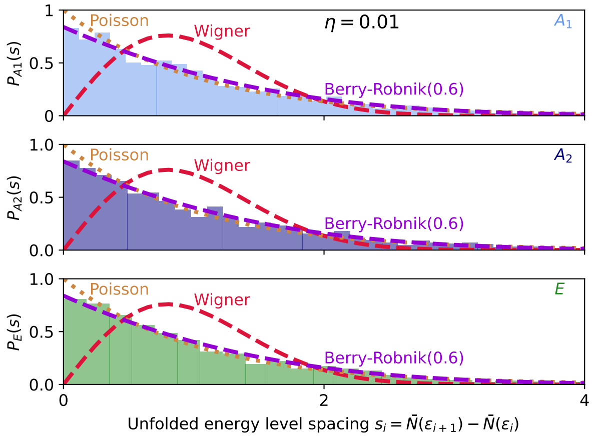

Figure 4.6: The histograms show the distribution of unfolded energy level spacings $s_{r,i} = \bar{N}_r(\epsilon_{i+1}) - \bar{N}_r(\epsilon_i)$, for states belonging to the three irreducible representations $r = A_1$ (top), A_2 (centre), and E (bottom), which are analysed separately. They differ from the Poisson (dotted golden line) and Wigner (dashed red line) distributions. They are well represented by the Berry–Robnik distribution, assuming a single chaotic region in phase space, with parameter $\rho_1 = 0.6$ for all three representations.

though the differential operator H_{2D} has the same form within the interior of the asymmetric unit, the boundary condition imposed on its edges differs from one representation to another, leading to different eigenstates and eigenvalues for H_{2D}. For the symmetry group C_{3v} considered in this work, the first few terms of the expansion of the smooth component $\bar{N}_r(\epsilon)$ in powers of $\hbar$ are known [98, Eqs. 33 and 50]. We retain the leading–order term, proportional to $1/\hbar^2$, and the first correction, proportional to $1/\hbar$, which leads to:

$$\begin{array}{rclll} \bar{N}_{A_1}(\epsilon) & = & \bar{N}_{-2}(\epsilon)/6 & +\,\bar{N}_{-1}(\epsilon)/2 & +O(\hbar^0), \\ \bar{N}_{A_2}(\epsilon) & = & \bar{N}_{-2}(\epsilon)/6 & -\,\bar{N}_{-1}(\epsilon)/2 & +O(\hbar^0), \\ \bar{N}_{E}(\epsilon) & = & 2\bar{N}_{-2}(\epsilon)/3 & & +O(\hbar^0), \end{array} \tag{4.12}$$

where the quantities $N_{-2}(\epsilon)$ and $N_{-1}(\epsilon)$, proportional to $1/\hbar^2$ and $1/\hbar$ respectively, read:

$$\bar{N}_{-2}(\epsilon) = \int \frac{d^2r\, d^2p}{(2\pi\hbar)^2}\, \theta(\epsilon - H_{\mathrm{2D}}) \quad \text{and} \quad \bar{N}_{-1}(\epsilon) = \frac{1}{2} \int \frac{dy\, dp_y}{2\pi\hbar}\, \theta(\epsilon - H_{\mathrm{2D}})|_{x=0,p_x=0} \,. \tag{4.13}$$

These integrals are taken over the part of classical phase space corresponding to energies smaller than ϵ. Their evaluation does not require the knowledge of the quantum eigenstates.

On Figure 4.5, we compare the full $N_r(\epsilon)$, calculated numerically from the spectrum of quantum energy eigenvalues, to its smooth component $\bar{N}_r(\epsilon)$, calculated from Eq. (4.12) without using our quantum–mechanical results, for all three representations $r = A_1$, A_2, and E. The agreement is excellent for all considered energies: the staircase–like features of $N_r(\epsilon)$, visible in the inset, closely follow the smooth function $\bar{N}_r(\epsilon)$.

4.2.2.2 Quantum energy level statistics

For each representation $r = A_1$, A_2, or E, we calculate the spacings $s_{i,r} = \bar{N}_r(\epsilon_{i+1}) - \bar{N}_r(\epsilon_i)$ between consecutive 'unfolded' energies [67, Sec. 5.4]. We plot their distribution on Fig. 4.6, where it is seen to differ from both the Poisson and the Wigner distributions [7, Secs. 16.3 & 16.4], as expected for a system with mixed classical phase space.

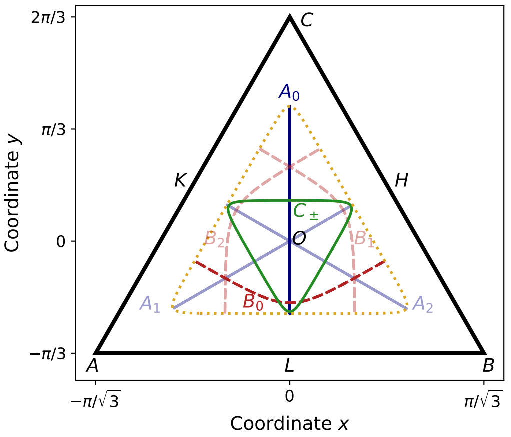

Figure 4.7: Periodic trajectories of types A (solid blue lines), B (dashed red lines), and C (solid green curve) in the (x, y) plane, for the energy $\epsilon = 7C_6/R^6$. For all three families, the trajectory drawn with a thick line is the one represented in Figs. 4.8 and 4.8. The dotted golden line shows the classically accessible region.

For a given representation r, we now compare the distribution of the unfolded energy spacings $s_{i,r}$ to the Berry–Robnik distribution [91], specially devised to represent systems with mixed classical phase space. In its simplest form, achieved when a single chaotic region in phase space contributes to the statistics, this distribution depends on a single parameter, the regular fraction ρ_1 (see Eq. 28 in Ref. [91]), and it smoothly interpolates between the Wigner distribution ($\rho_1 = 0$) and the Poisson distribution ($\rho_1 = 1$).

Figure 4.6 shows that the distribution of the unfolded energy spacings is well represented by this simplest Berry–Robnik distribution, with the same parameter $\rho_1 = 0.6$ for all three representations. Both the assumption of a single chaotic region and the value of the regular fraction $\rho_1 = 0.6$, are compatible with the surface of section of Fig. 4.4. Indeed, the single chaotic region represented on this figure occupies an area which is comparable to the total area covered by the concentric closed curves signalling regular trajectories.

The applicability of the Berry–Robnik distribution relies, in particular, on the statistical independence of the regular and chaotic sequences of levels. Counter–examples to this distribution have been identified, e.g. the hydrogen atom in a magnetic field [100] where Brody's phenomenological distribution [90] better represents the statistics of the level spacings for some choices of the parameters. The verification of Berry–Robnik statistics with billiards requires reaching the deep semiclassical limit [101]. By contrast, our result provides a realisation of the Berry–Robnik distribution in an experimentally accessible system involving smooth interatomic interactions rather than sharp billiard walls.

4.3 Classical periodic trajectories

Among the many trajectories supported by the classical Hamiltonian $H_{2\mathrm{D}}$ of Eq. (4.4), some are periodic in time. These play an essential role in the analysis of the corresponding quantum system in at least two respects, both illustrated in Secs. 4.4 and 4.5 below:

- Some eigenstates ψ_n of the quantum Hamiltonian $H_{2\mathrm{D}}$ are localised in the vicinity of these periodic trajectories, i.e. the density $|\psi_n(\boldsymbol{r})|^2$ is enhanced there, due to quantum

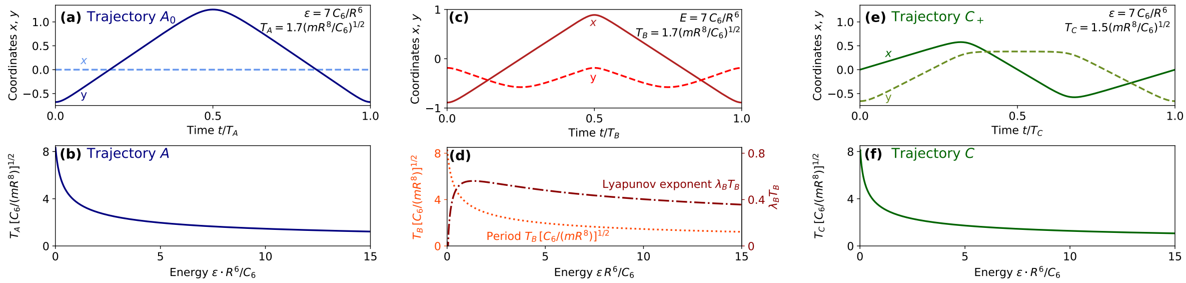

Figure 4.8: Periodic trajectories of type *(a, b)* A, *(c, d)* B, and *(e,f)* C. The top panels *(a,c,e)* represent the trajectories for the energy $\epsilon = 7C_6/R^6$ (corresponding to Fig. 4.9) as a function of time t over one period (T_A, T_B, or T_C) in terms of the Jacobi coordinates x and y. The bottom panels *(b,d,f)* show the periods of each trajectory for $0 \le \epsilon \le 7C_6/R^6$. The unstable trajectory B has a non–zero Lyapunov exponent λ_B, plotted as a function of ϵ on panel *(d)* (brown dash–dotted curve related to the vertical axis on the right edge of the figure).

scarring or classical localisation [102, chap. 22];

- The quantum density of states for the representation r, $n^{(r)}(\epsilon) = dN_r/d\epsilon$, is related to the classical periodic trajectories through the trace formula [7, chap. 17].

Stable and unstable trajectories. As previously mentioned in Sec. 4.2.1.2, classical periodic trajectories may be either *stable* or *unstable* against small perturbations. They yield fixed points on the surface of section (see Fig. 4.4), the stable trajectories being surrounded by tori whereas the unstable trajectories are embedded within the ergodic sea. Finding a periodic trajectory very close to an ergodic one may seem surprising at first sight. However, periodic trajectories are known to exist e.g. in chaotic billiards such as the Bunimovich stadium [102, chap. 3]. Their unstable character means that a slight perturbation in the initial conditions will grow exponentially with time and lead to a different, ergodic, trajectory.

Lyapunov exponent. The *Lyapunov exponent* λ [103] of a periodic trajectory is a positive quantity, carrying the unit of inverse time, which measures its instability. For stable trajectories, $\lambda = 0$. For unstable trajectories, $\lambda > 0$, and larger values of λ signal stronger instabilities. The value of λ is extracted from the *monodromy matrix* of the periodic trajectory [104], which encodes the evolution of a small mismatch in the positions and momenta at a given point on the trajectory in classical phase space, after it is propagated for a full period T under the linearised equation of motion. For stable periodic trajectories, its eigenvalues all have modulus 1. For unstable trajectories, its eigenvalue μ whose absolute value is the largest determines the Lyapunov exponent $\lambda > 0$ through $|\mu| = \exp(\lambda T)$.

Numerical calculations. We characterise the periodic trajectories of $H_{2\mathrm{D}}$ using our own implementation, in C++, of the numerical approach of Ref. [105, Sec. III]. This iterative

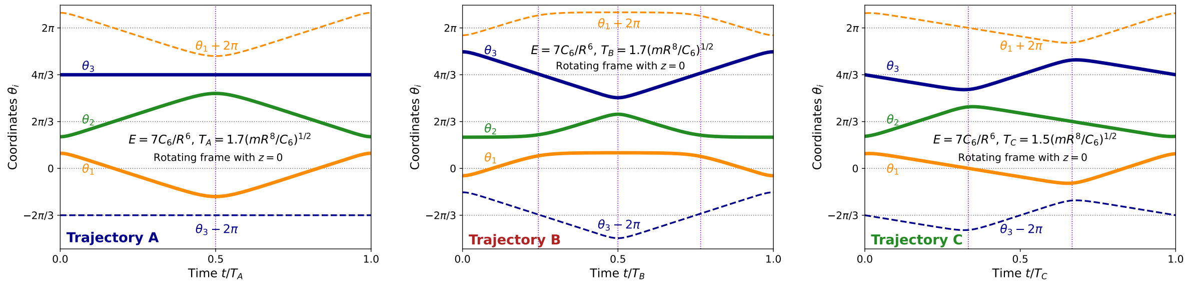

Figure 4.9: Periodic trajectories of types A (left), B (centre), and C (right) for the energy $\epsilon = 7C_6/R^6$ (corresponding to the panels *(a,c,e)* of Fig. 4.8), plotted as a function of time in terms of the three angular coordinates θ_1, θ_2, θ_3, in the rotating frame with $p_z = 0$ and $z = 0$. The vertical dotted lines highlight times at which collisions occur. We also show $\theta_1 + 2\pi$ and $\theta_3 - 2\pi$ so as to make collisions between atoms 1 and 3 apparent.

approach is a variant of the Newton–Raphson algorithm [96, Sec. 9.6] which simultaneously determines a periodic trajectory and its monodromy matrix. We have tested it by recovering the results of Ref. [86] concerning the Hénon–Heiles potential (Eq. (4.11) above).

Three families of periodic trajectories. The simplest periodic trajectories supported by the classical Hamiltonian H_{2D} belong to three families existing for all energies $\epsilon > 0$. They are represented in the (x, y) plane, for the energy $\epsilon = 7C_6/R^6$, on Fig. 4.7. For a given ϵ, there are three trajectories A_0, A_1, and A_2 which correspond to each other through rotations $\mathcal{R}_{O,\pm 2\pi/3}$ of order 3 about the centre O of the triangle ABC. Similarly, there are three trajectories B_0, B_1, and B_2. There are two closed trajectories of type C, labelled C_+ and C_- according to whether they rotate counterclockwise or clockwise as a function of time. They lead to a single closed curve on Fig. 4.7. The top panels *(a,c,e)* of Fig. 4.8 show the time dependence $(x(t), y(t))$ of the coordinates for one member of each family A, B, C over one period: this discriminates between C_+ (shown on panel *(e)*) and C_-. The three panels of Figure 4.9 show the same three periodic trajectories in terms of the atomic angular coordinates $(\theta_1(t), \theta_2(t), \theta_3(t))$, in the rotating frame such that $p_z = 0$ and $z = 0$.

For the considered range of energies, the periods T_A, T_B, T_C of the periodic trajectories of the three families A, B, C are comparable, i.e. a few $(mR^8/C_6)^{1/2}$ (see the lower panels *b,d,f* of Fig. 4.8). Using the experimentally accessible parameters of Sec. 4.1.1, all three periods are of the order of 1 ms. Thus, the ~ 30 ms lifetime of circular Rydberg atoms in current experiments [106] corresponds to a few tens of periods.

The trajectories of types A and C are stable for all considered energies (i.e. their Lyapunov exponent $\lambda = 0$). We shall analyse their impact on the quantum eigenstates of H_{2D} in Sec. 4.5. By contrast, the trajectories of type B are unstable for all energies, as shown by their Lyapunov exponent $\lambda_B > 0$ plotted as a function of ϵ on Fig. 4.8*(d)*. This figure shows that Trajectory B satisfies both conditions heralding a quantum scar: $\lambda_B T_B < 2\pi$ [102, chap. 22], and lower values of λ_B signal stronger scarring [64, Sec. 9.3]. We shall examine the corresponding quantum scarred states in Sec. 4.4.

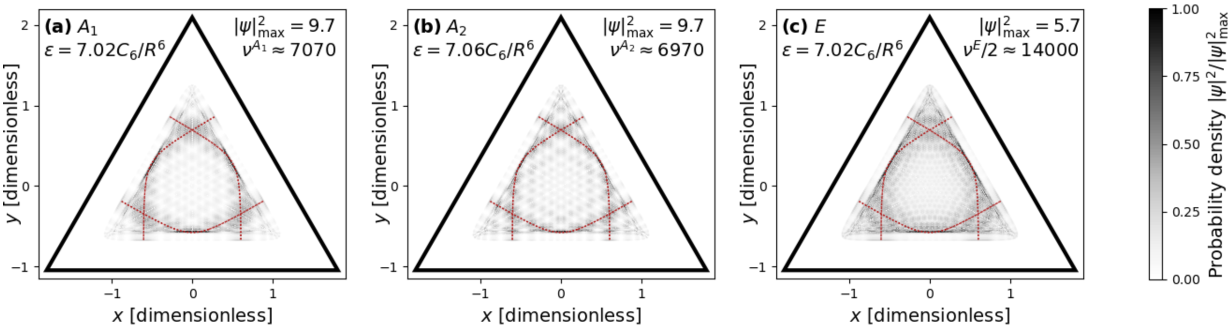

Figure 4.10: *Quantum states scarred by the unstable trajectories of family B.* We show the probability density $|\psi(x,y)|^2$ of the scarred quantum eigenstate whose energy is closest to $7C_6/R^6$ in each irreducible representation $r =$ *(a)* A_1, *(b)* A_2, and *(c)* E. The dashed red lines show the three classically unstable periodic trajectories of type B for the corresponding energy ϵ. The densities are maximal near the unstable trajectories, signalling the quantum scar. The integer $\nu^{(r)}$ is an approximation to the index of the shown quantum state in the representation r.

4.4 Quantum scars: Eigenstates localised near the unstable Trajectory B

4.4.1 Quantum scarred eigenstates for the Hamiltonian H_{2D}

For the majority of the numerically calculated quantum eigenstates of H_{2D}, the probability density $|\psi_n(x,y)|^2$ is unrelated to the periodic trajectories of type B. Nevertheless, for each irreducible representation $r = A_1$, A_2, E, we find multiple quantum states whose probability density is maximal near the three classically unstable trajectories B for the corresponding eigenenergy. Figure 4.10 shows one such state for each representation r. The energies of the multiple scarred states found in each representation are shown as the vertical dashed red lines in Fig. 4.11.

These states satisfy Heller's definition for a *quantum scar* as stated in Ref. [102, chap. 22]. Indeed, the mechanism stabilizing the classically unstable trajectory B requires quantum mechanics[9]. The effect is not present classically, because the unstable periodic trajectory is within the ergodic region of classical phase space, so that a small perturbation will drive the classical system away from the periodic trajectory and into a new, ergodic, trajectory.

Symmetry of the probability density $|\psi_n|^2$. The probability densities of the quantum scarred eigenstates shown on Fig. 4.10 are enhanced along all three trajectories of family B for the corresponding energy. More generally, the densities $|\psi_n(\boldsymbol{r})|^2$ of all numerically calculated eigenstates exhibit C_{3v} symmetry, i.e. $|\psi_n(\mathcal{R}\boldsymbol{r})|^2 = |\psi_n(\mathcal{S}\boldsymbol{r})|^2 = |\psi_n(\boldsymbol{r})|^2$ for any rotation $\mathcal{R}$ and any reflection $\mathcal{S}$ in the group C_{3v}. For the unidimensional representations A_1 and A_2, this follows from the fact that $\psi_n(\mathcal{R}\boldsymbol{r})$ and $\psi_n(\mathcal{S}\boldsymbol{r})$ are both proportional to $\psi_n(\boldsymbol{r})$,

---

[9] This contrasts with the classical localisation near stable periodic orbits described in Sec. 4.5 below.

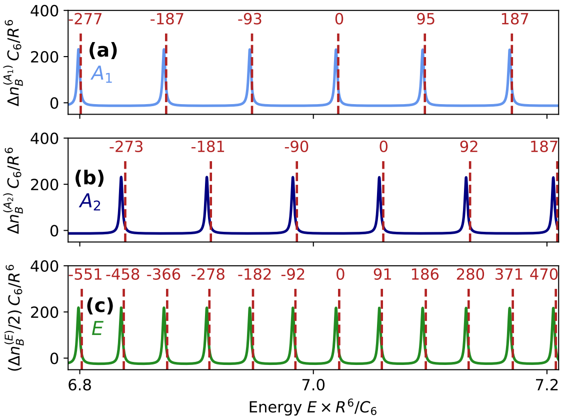

Figure 4.11: *Semiclassical analysis of the energies of the quantum scarred eigenstates.* For each representation $r =$ *(a)* A_1, *(b)* A_2, *(c)* E, the solid curve shows the semiclassical contribution $\Delta n_B^{(r)}$ [Eq. (4.14)] to the density of states $n^{(r)}$ due to the periodic trajectory B, as a function of the energy ϵ. The dashed vertical lines show the energies of the scarred quantum states, which closely match the maxima of $\Delta n_B^{(r)}$. The integers above them specify the relative state indices $\Delta\nu^{(A_1)}$, $\Delta\nu^{(A_2)}$, $\Delta\nu^{(E)}$ with respect to the index $\nu^{(r)}$ of the scarred states in Fig. 4.10.

	$T_B^{(r)}$	$S_B^{(r)}$	$\alpha_B^{(r)}$	$k^{(r)}$
A_1	$T_B/2$	$S_B/2$	$\lambda_B T_B/2$	k
A_2	$T_B/2$	$S_B/2$	$\lambda_B T_B/2$	$k-1/2$
E	$2T_B$	S_B	$\lambda_B T_B$	$k+1/2$

Table 4.2: Parameters $T_B^{(r)}$, $S_B^{(r)}$, $\alpha_B^{(r)}$, $k^{(r)}$ entering Eq. 4.14, depending on the irreducible representation $r = A_1$, A_2, or E.

with eigenvalues ±1. For the two–dimensional representation, it follows from our choice of basis vectors $\psi_n^{(+)}$, $\psi_n^{(-)}$ such that $\psi_n^{(+)}(\boldsymbol{\mathcal{S}r}) = \psi_n^{(+)*}(\boldsymbol{r})$ and $\psi_n^{(+)}(\mathcal{R}^{-1}\boldsymbol{r}) = e^{i2\pi/3}\psi_n^{(+)}(\boldsymbol{r})$.

4.4.2 Semiclassical analysis of quantum scars: trace formula

The semiclassical link between quantum mechanics and classical chaotic dynamics[10] is obtained through the trace formula [7, Sec. 17.4]. It relates the quantum density of states for the representation r, namely, $n^{(r)}(\epsilon) = dN_r/d\epsilon$ to a sum over all periodic orbits of the classical system. We isolate the contribution $\Delta n_B^{(r)}(\epsilon)$ to $n^{(r)}$ coming from the unstable periodic trajectory B [64, Sec. 9.3], which depends on the representation r [107, 108]:

$$(\Delta n_B^{(r)}\,2\pi\hbar/T_B^{(r)} + 1)/\alpha_B^{(r)} \quad = \quad \sum_{k=0}^{\infty} \left\{ [S_B^{(r)}/\hbar - 2\pi(k^{(r)} + 1/2)]^2 + (\alpha_B^{(r)}/2)^2 \right\}^{-1} . \quad (4.14)$$

The parameters $T_B^{(r)}$, $S_B^{(r)}$, $\alpha_B^{(r)}$ and k^r are defined in Table 4.2. They are directly related to classical quantities characterising the trajectory B at the energy ϵ: its period $T_B(\epsilon)$, the action $S_B(\epsilon) = \oint \boldsymbol{p}\cdot d\boldsymbol{x}$ along the trajectory, and the product $\lambda_B T_B$ with $\lambda_B(\epsilon)$ being its Lyapunov coefficient (see Sec. 4.3 above). The integer k is the summation index. Figure 4.11 shows the quantity $\Delta n_B^{(r)}$, over an energy window centred on $7C_6/R^6$, for $r = A_1$, A_2, and E. In all three cases, $\Delta n_B^{(r)}$ exhibits resonances, i.e. peaks with finite widths in energy.

Equation (4.14) is best understood in terms of the variable $S_B^{(r)}$, which is proportional to the classical action $S_B(\epsilon)$. In terms of this variable, the resonance maxima are evenly

---

[10] By contrast, in the case of regular classical dynamics, considered in Sec. 4.5 below, both the energy spectrum and the wavefunctions for the eigenstates may be constructed semiclassically.

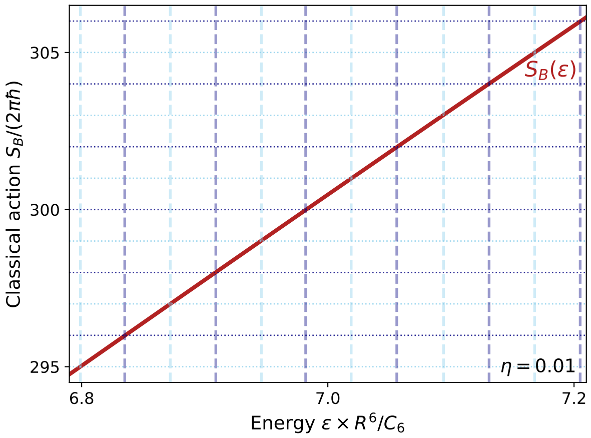

Figure 4.12: Solid red line: classical action $S_B = \oint \boldsymbol{p} \cdot d\boldsymbol{r}$ along trajectory B as a function of the energy ϵ. The dashed vertical lines show the energies leading to the maxima of $\Delta n_B^{(r)}(\epsilon)$ for the representations $r = A_1$ (light blue) and A_2 (dark blue). The quantity $\Delta n_B^{(E)}(\epsilon)$ exhibits maxima for both sets of energies (see Fig. 4.11).

spaced: $S_{B,\max}^{(r)}/(2\pi\hbar) = (k^{(r)} + 1/2)$. The resonance widths $\delta S_B^{(r)} = \alpha_B^{(r)}$, proportional to $\lambda_B T_B$, reflect the instability of trajectory B encoded in $\lambda_B(\epsilon)$. Within the considered energy range, $S_B(\epsilon)$ varies linearly with ϵ, as shown on Fig. 4.12. Thus, both of these properties translate directly to $\Delta n_B^{(r)}(\epsilon)$ considered as a function of ϵ. In particular, the series of scarred states found in each irreducible representation reflects the multiple resonances in $\Delta n_B^{(r)}(\epsilon)$, and the regularity of their energy spacing follows from the resonance maxima being evenly spaced in terms of the classical action $S_B^{(r)}$.

4.4.3 Comparison with other quantum scars and many–body scars

Quantum scars were discovered by Heller in 1984 [109] and first observed in microwave cavities in 1992 [110]. They have benefited from renewed interest following a recent experiment involving chains of Rydberg atoms [22]. We now briefly compare the three–body scar we have introduced in the present Sec. 4.4 to other experiments and proposals.

4.4.3.1 Single–particle physics versus interacting systems

Heller's theoretical proposal [109] was formulated in terms of a *single particle* in the 2D stadium billiard, which is classically chaotic. Its early experimental demonstration involved microwaves in a stadium–shaped cavity. The eigenvalue problem defining the solutions of Maxwell's equations compatible with this cavity is analogous to Schrödinger's equation for the stationary quantum states of a single particle in a billiard [89, 2.2]. In both cases, the required classical chaotic character is due to the shape of the considered enclosure.

By contrast, in the three–particle system we consider, classical chaos hinges on the presence of three interacting particles. Indeed, the single–particle problem and the interacting two–particle problem are both classically integrable, whereas the three–particle problem is not, as signalled by the presence of the ergodic sea on the surface of section of Fig. 4.4.

The essential role of the interparticle interaction allows for a comparison between the three–body quantum scar considered here and many–body scars [22, 29, 111] (though the considered systems are not equivalent, as argued in Sec. 4.4.3.2 below). The use of Jacobi coordinates (Eq. (4.3)) reduces the three–body problem to an *effective* single–particle problem governed by the Hamiltonian $H_{2\mathrm{D}}(\boldsymbol{r})$. However, the theoretical analysis of many–body scars also hinges on an effective description involving few degrees of freedom. Incidentally, the phase–space dimensionality of the three–particle problem we analyse (4, see Sec. 4.2.1.1 above) matches the maximum number of independent parameters introduced so far in the variational approaches applied to the many–body PXP model [112, Sec. III.A].

4.4.3.2 Spatial motion version internal–state dynamics

In the experiment of Ref. [22], the quantum dynamics affects the *internal states* of the individual atoms, each of which may be, at a given time, either in its ground state or in a Rydberg state. Hence, this system is described in terms of a spin model (the 'PXP' model, see e.g. Ref. [113]), the construction of whose classical analog is non–trivial and approximate [72]. By contrast, our three–body system affords an exact reduction to four parameters (see Sec. 4.1.2 above), and the identification of the classical analog is straightforward.

4.4.3.3 One important shared feature: 'towers' of scarred states

The system we consider exhibits 'towers' of quantum scarred states which are approximately evenly spaced in energy (see Fig. 4.11). These are also a recurring feature of many–body scars [71, 72]. In the present context, we fully explain them semiclassically (see Sec. 4.4.2 and Fig. 4.12) in the spirit of Heller's original argument [114, Fig. 22].

4.4.3.4 Quantum scar versus classical localisation

Despite the intense theoretical scrutiny [71], only two experiments [22, 115] and one explicit proposal [116] explore many–body scarring so far. In all three cases, the observed non–ergodic behaviour is linked to classical physics.

The proposal of Ref. [116] refers to spin helices. Their classical limit is stable, and from the quantum point of view they generalise helices predicted and observed in the integrable XXZ chain. Hence, the proximity of integrable models is expected to play a key role.

We now turn to the experiments of Refs. [22, 115]. These both probe the PXP model in regimes where the classical analog system explores the vicinity of classically stable periodic trajectories. Hence, the absence of thermalisation may be traced back to the classical Kolmogorov–Arnold–Moser theorem [112, Sec. VI]. In particular, on the surfaces of section shown as Figs. 2a and 5a of that reference, the considered periodic trajectories appear as fixed points surrounded by concentric closed curves, signalling their stability.

The suspected role of classical physics in these experiments suggests that further insight may be gained by considering another mechanism impeding ergodicity, namely, classical localisation in the vicinity of classically stable periodic trajectory. This second mechanism also occurs in the three–particle system we put forward in the present chapter, where one may address either the quantum scar or classical localisation simply by changing the initial condition defining the atomic motion. We analyse this second mechanism in section 4.5.

4.5 Classical localisation: Eigenstates localised near the stable Trajectories A and C

In this section, we focus on quantum eigenstates of H localised in the vicinity of the *stable* classical periodic trajectories A and C.

This localisation phenomenon superficially resembles the quantum scars stemming from the unstable periodic trajectory B, analysed in Sec. 4.4. However, the quantum states we consider in the present section do not satisfy Heller's definition for a quantum scar [102, chap. 22]. Indeed, in stark contrast to trajectory B, trajectories A and C are already stable from the classical point of view, so that quantum mechanics brings about no qualitative change in the behaviour of the system in their vicinity. This has at least two consequences which set the classically localised eigenstates of H_{2D} apart from the quantum scarred ones:

1. They obey selection rules reflecting the symmetries of the classical KAM tori;
2. Their energies and wavefunctions may be explicitly obtained semiclassically.

We analyse both features in detail, for trajectories A and C, in our recent preprint [5]. In this memoir, we focus on the second of these features, in the case of trajectory A.

Our analysis hinges on a well–established semiclassical approach. Among these, the Wentzel–Kramers–Brillouin (WKB) approach [80, §46, 47] is widely known, but its usual formulation is not generally applicable to problems involving two or more degrees of freedom. We employ its generalisation, the *Einstein–Brillouin–Keller* (EBK) approach [92, 117], which does not suffer from this limitation.

The EBK approach *is only applicable if the classical motion winds around a torus* [66, Sec. 3.2]. For systems involving a single degree of freedom, any bounded trajectory satisfies this property [79, §50], so that this restriction is not usually mentioned in the context of the WKB approach. However, for systems involving two or more degrees of freedom, irregular motion may occur. The presence of the brown 'sea' on the surface of section of Fig. 4.4, comprised of intersections due to a single irregular trajectory, confirms that it does occur for the Hamiltonian H_{2D} we are considering. The unstable periodic trajectories B, responsible for the quantum scars, are embedded within this sea. Therefore, the EBK approach is not applicable there. This is why our semiclassical analysis of the scars has relied on Gutzwiller's trace formula (see Sec. 4.4.2), which does account for the contribution of unstable periodic trajectories to the density of states, but provides neither specific energies[11] nor wavefunctions for the quantum states.

By contrast, in the cases where it is applicable, the semiclassical EBK approach provides both specific energies and wavefunctions. In this section, we obtain them for the quantum

---

[11] The finite widths of the resonances predicted by Eq. (4.14) cover multiple quantum states [64, Sec. 9.3].

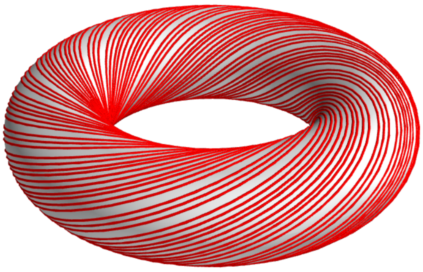

Figure 4.13: A classical trajectory winding around a torus, densely covering its surface. The angular frequencies ω_1 and ω_2, corresponding to motion around the tube and about the axis of the torus respectively, satisfy $\omega_1/\omega_2 = \sqrt{3}$. The trajectory is drawn for times t satisfying $0 \leq \omega_2 t \leq 300$.

states localised near trajectories A and C, and compare these semiclassical predictions to our numerical solution of the stationary Schrödinger equation (see Sec. 4.1.5.5). Our quantum and semiclassical results are in excellent agreement.

We now describe our own implementation of the EBK approach. This implementation is heavily influenced by Refs. [66, Secs. 3.1 & 3.2], [118], and [119]. The corresponding numerical calculations are performed in PYTHON, using the libraries NUMPY and SCIPY [94, 95].

4.5.1 Fourier analysis of conditionally periodic motion

We consider a non–ergodic classical trajectory supported by the Hamiltonian H_{2D}, stemming from initial conditions which are not too different from those yielding a stable periodic trajectory (e.g. trajectory A). We assume that this trajectory *(i)* is not periodic and *(ii)* that it winds around a torus[12] The considered system has two degrees of freedom (i.e. the effective coordinates $\boldsymbol{r} = (x, y)$), so that the torus is a two–dimensional surface in phase space which is equivalent to a usual torus in standard three–dimensional space (see Fig. 4.13). Hence, the motion $\boldsymbol{r}(t)$ is conditionally periodic, i.e. it may be written as a Fourier series involving two independent frequencies $\boldsymbol{\omega} = (\omega_1, \omega_2)$ [79, §52]:

$$\boldsymbol{r}(t) = \sum_{\boldsymbol{k}} \boldsymbol{r}_{\boldsymbol{k}} \exp(i\boldsymbol{k} \cdot \boldsymbol{\omega} t), \qquad \boldsymbol{p}(t) = 2mR^2 d\boldsymbol{r}/dt \ , \tag{4.15}$$

the sum being taken over all integer pairs $\boldsymbol{k} = (k_1, k_2)$. We extract the Fourier coefficients $\boldsymbol{r}_{\boldsymbol{k}}$ entering Eq. (4.15) from the real–time trajectory $\boldsymbol{r}(t)$ by taking its fast Fourier transform

---

[12] A non–ergodic trajectory may densely cover an invariant surface which is not a torus: an explicit example is given in Ref. [120]. We have not encountered this scenario in our numerical calculations with H_{2D}.

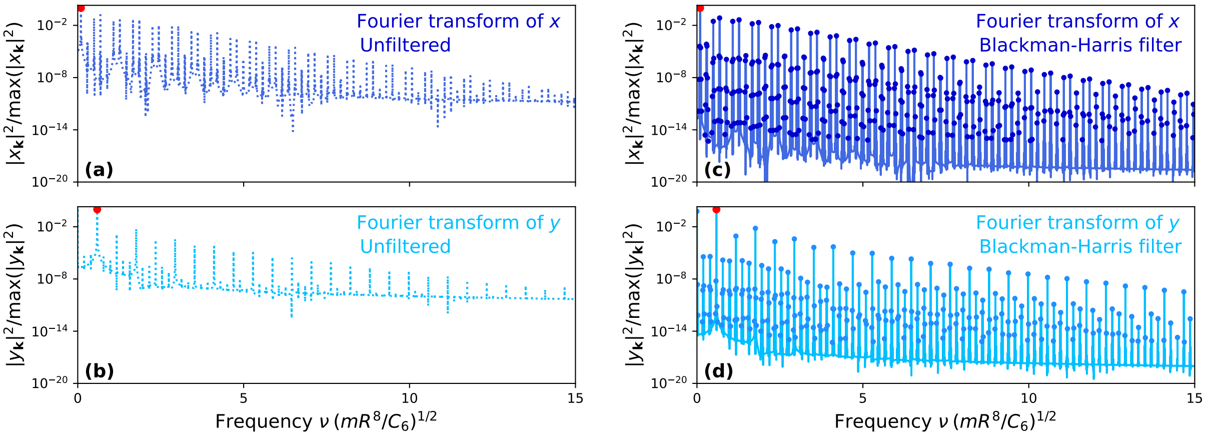

Figure 4.14: Squared moduli $|x_{\boldsymbol{k}}|^2$, $|y_{\boldsymbol{k}}|^2$ of the Fourier series of a regular trajectory in the vicinity of the stable trajectory A (note the logarithmic scale along the vertical axes). The Fourier components $\boldsymbol{r_k} = (x_{\boldsymbol{k}}, y_{\boldsymbol{k}})$ entering Eq. (4.15) are obtained through the fast Fourier transform of the classical unfiltered trajectory (panels (*a*) and (*b*)) or after applying the Blackman–Harris filter suggested in Ref. [118] (panels (*c*) and (*d*)). The red disks appearing on all four panels show our choices for the fundamental frequencies $\boldsymbol{\omega} = (\omega_1, \omega_2)$. The blue disks on panels (*c*) and (*d*) are their integer combinations $\boldsymbol{k} \cdot \omega$, which are in excellent agreement with the peaks in the spectrum.

[121, chap. 9], using the Blackman–Harris filtering procedure suggested in Ref. [118]. The fundamental frequencies (ω_1, ω_2) are not uniquely defined: we choose them as in Ref. [118, Fig. 8(b)]. This Fourier analysis procedure is illustrated in Fig. 4.14.

Action–angle coordinates. We have assumed that the considered trajectory is dense on the surface of the invariant torus. This allows for the introduction of angle coordinates $\boldsymbol{\theta} = (\theta_1, \theta_2)$ on the torus [118, Sec. II.A]. These are defined by setting $\boldsymbol{\omega} t = \boldsymbol{\theta}$ in Eq. (4.15), so that $\boldsymbol{r}(\boldsymbol{\theta}) = \sum_{\boldsymbol{k}} \boldsymbol{r_k} \exp(i\boldsymbol{k} \cdot \boldsymbol{\theta})$, with a similar expression for $\boldsymbol{p}(\boldsymbol{\theta})$. Two independent closed circuits $\mathcal{C}_1$ and $\mathcal{C}_2$ may be drawn on the torus *(i)* either by varying θ_1 from 0 to 2π while keeping θ_2 fixed, *(ii)* or by varying θ_2 from 0 to 2π while keeping θ_1 fixed. These depend on the choice of (ω_1, ω_2). Those reflecting our choice are shown in Fig. 4.15(a).

We now consider the stability region surrounding trajectory A as a whole. Following Ref. [67, Sec. 4.1], we ignore narrow instability subregions and approximate the whole stability region by a set of concentric tori. We introduce angle coordinates on each of torus in the region. A given such torus is uniquely determined by its actions I_x, I_y, defined by $I_i = \oint \boldsymbol{p} \cdot d\boldsymbol{r}/(2\pi)$ for $i = x, y$. This leads to a set of action–angle coordinates $(\boldsymbol{I}, \boldsymbol{\theta})$ valid over the whole stability region (but not over all phase space).

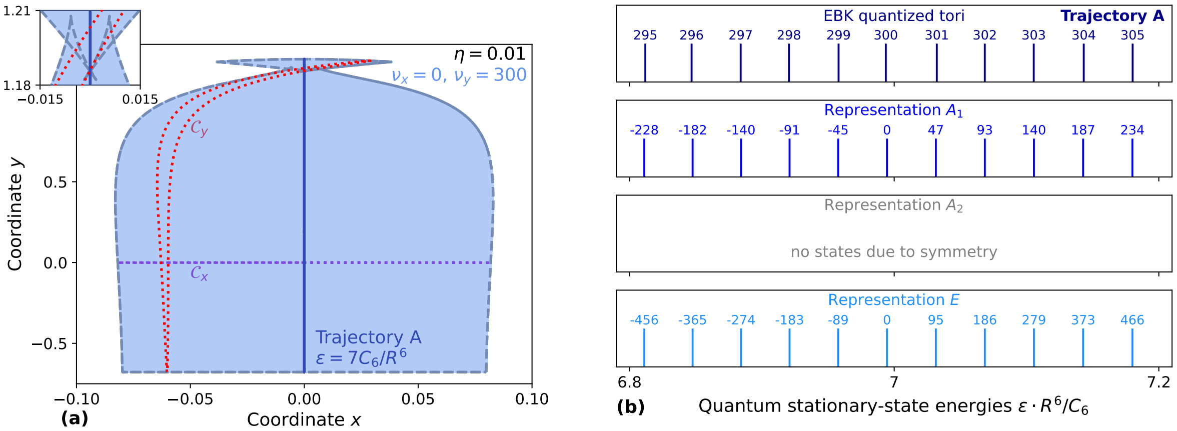

Figure 4.15: *(a)* Classical trajectory A (solid dark blue) for the energy $\epsilon = 7C_6/R^6$, the nearest–energy trajectory satisfying the quantisation condition for $\eta = 0.01$ (densely covering the light blue area), and two independent circuits $\mathcal{C}_x$ (dotted purple) and $\mathcal{C}_y$ (dotted red) circling the torus. The dashed gray lines show the caustics of this trajectory. The top left inset zooms in on the narrow region near $(x = 0, y = 1.2)$ to reveal the self–intersection of the caustics. *(b)* Top panel: energies of the EBK wavefunctions for $\nu_x = 0$ and $295 \leq \nu_y \leq 305$. Centre and bottom panels: energies of the corresponding quasidegenerate quantum states in representations A_1 and E, obtained through our finite–element numerical calculations, labelled by their relative indices with respect to the quantum state related to Trajectory A whose energy is closest to $7C_6/R^6$.

4.5.2 Semiclassical energies

4.5.2.1 Quantisation conditions

Up to now, our analysis has been completely classical. We now turn to semiclassical mechanics. Among the tori in the stability region surrounding trajectory A, the EBK approach associates a quantum eigenstate to those satisfying a quantisation condition of the form $I_i = \hbar(\nu_i + \alpha_i/4)$ for $i = x,\ y$ [92, Sec. V]. Here, the ν_i are positive integers, and the Maslov index α_i is a number characterising the condition to be applied along the circuit $\mathcal{C}_i$. In the usual one–dimensional context, $\alpha = 2$ [80, §48], but this is not always true for systems involving two or more degrees of freedom. The Maslov index α_i for the circuit $\mathcal{C}_i$ is calculated using the algorithm presented in Ref. [92, Sec. II.C], in terms of the following quantities, all available in our numerical calculation (see Fig. 4.16):

- The signature of the Jacobian matrix $\partial \boldsymbol{p}/\partial \boldsymbol{r}$, i.e. the number of its positive eigenvalues minus the number of its negative eigenvalues;
- The intersections of $\mathcal{C}_i$ with the $\boldsymbol{r}$–caustics and $\boldsymbol{p}$–caustics of the trajectory, along which the Jacobian determinants $\det[\partial \boldsymbol{r}/\partial \boldsymbol{\theta}] = 0$ or $\det[\partial \boldsymbol{p}/\partial \boldsymbol{\theta}] = 0$, respectively.

We thus obtain the quantisation condition for the tori near trajectory A:

$$I_x = \hbar(\nu_x + 1/2) \text{ and } I_y = \hbar(\nu_y + 1)\ , \tag{4.16}$$

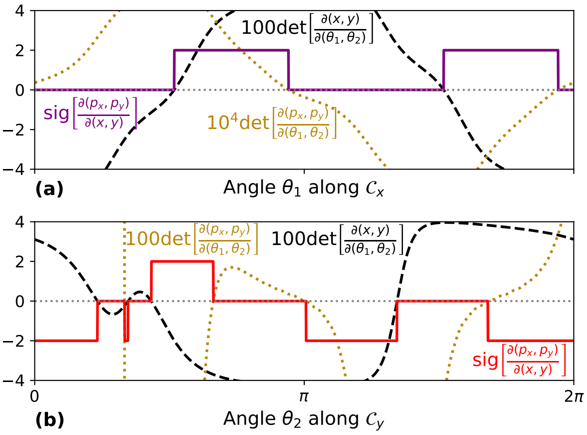

Figure 4.16: Quantities entering the determination of the Maslov index α_i along the circuits *(a)* $\mathcal{C}_x$ and *(b)* $\mathcal{C}_y$. The solid purple and red lines show the signature of the Jacobian matrix $\partial\boldsymbol{p}/\partial\boldsymbol{r}$. The zeros of the Jacobian determinants $\det[\partial\boldsymbol{r}/\partial\boldsymbol{\theta}] = 0$ (dashed black line) and $\det[\partial\boldsymbol{p}/\partial\boldsymbol{\theta}] = 0$ (dotted golden line) signal that the circuit $\mathcal{C}_i$ encounters an $\boldsymbol{r}$–caustic or a $\boldsymbol{p}$–caustic, respectively.

where the positive integers ν_x and ν_y are the EBK quantum numbers. The action $I_x \geq \hbar/2$, so that the periodic trajectory A_0 itself does not satisfy Eq. (4.16).

4.5.2.2 Numerical procedure

For any torus, quantised or not, in the stability region near trajectory A, we integrate the classical equation of motion over a time interval of duration up to $t_{\max} = 3700(mR^8/C_6)^{1/2}$. We represent the resulting conditionally–periodic motion in terms of the Fourier series of Eq. (4.15), keeping up to 3200 terms in the series. We calculate the actions J_x and J_y specifying the considered torus in terms of the Fourier components [122]:

$$J_i = \sum_{i'=1,2} \sum_{\boldsymbol{k}} k_i \, |\boldsymbol{r_k}|^2 k_{i'} \, \omega_{i'} \ . \tag{4.17}$$

We find the tori satisfying Eq. (4.16) numerically in the following way. We choose target values $I_x^0 = \hbar(\nu_x^0 + 1/2)$ and $I_y^0 = \hbar(\nu_y^0 + 1)$. We start from an initial condition chosen near the periodic trajectory A and adjust it to achieve $(J_x - I_x^0, J_y - I_y^0) = (0, 0)$ through SciPy's multidimensional root finding algorithm.

4.5.2.3 Comparison of the EBK energies to our finite–element results.

The tori satisfying Eq. (4.16) which are closest to trajectory A_0 are those with $\nu_x = 0$: the corresponding energies within a window centered on $\epsilon = 7C_6/R^6$ are shown on the top line of Fig. 4.15(b). We compare them to the energies of the stationary quantum states of $H_{2\mathrm{D}}$ belonging to representations A_1 and E localized near the trajectories A_0, A_1, and A_2, obtained through our finite–element calculations. These are shown on Fig. 4.15(b), middle and bottom lines, and are in excellent agreement with the EBK results.

Figure 4.15(b) shows that the energy of each EBK state with the quantum number $\nu_x = 0$ corresponds to three eigenstates of $H_{2\mathrm{D}}$ found using the finite–element method: one state in the representation A_1 and two degenerate states in the representation E. This is because the EBK wavefunction reflects the symmetries of the classical torus, but

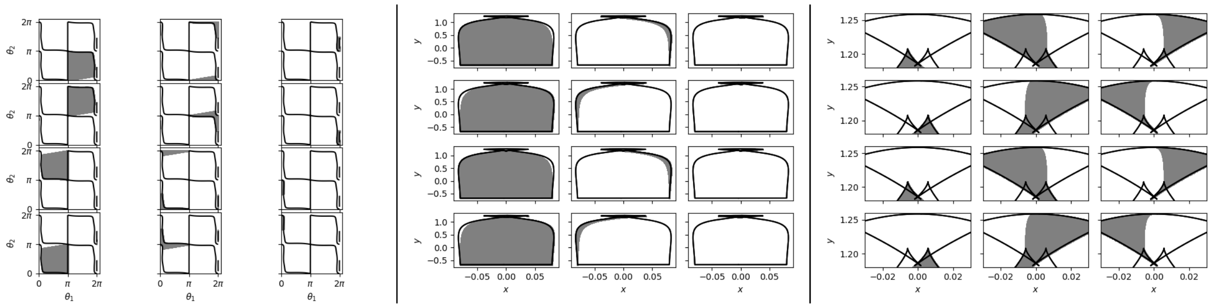

Figure 4.17: Representation of the invariant torus corresponding to the trajectory of Fig. 4.15(a) in terms of 12 sheets. Their boundaries are shown in the (θ_1, θ_2) plane (left panel) and in the (x, y) plane (centre panel). The right panel shows a zoom, in the (x, y) plane, of the region where the caustics self–intersect.

does not automatically satisfy the symmetry requirements of any representation. Hence, it should then be projected onto the irreducible representations A_1, A_2, and E [80, §94]. The projection is non–zero for representations A_1 and E. By contrast, the projection vanishes for representation A_2: we justify this in Ref. [5, Secs. IV.A & IV.B.1]. This explains the absence of quantum states localised near Trajectory A belonging to the representation A_2.

The quasidegeneracy of the quantum states belonging to different representations A_1 and E, but related to the same EBK state with quantum numbers $(\nu_x = 0, \nu_y)$, is lifted by small couplings neglected in the EBK approach. Their small energy difference, of the order of $10^{-6} C_6/R^6$, is resolved in our finite–element results.

4.5.3 Semiclassical wavefunctions

We now turn to the construction of EBK wavefunctions. We illustrate it on the specific case of the EBK state in the vicinity of trajectory A, with the quantum numbers $\nu_x = 0$, $\nu_y = 300$, whose energy is closest to $7C_6/R^6$. The corresponding classical trajectory and its caustics are shown in Fig. 4.15.

4.5.3.1 Sheeting the torus

The classical trajectory defines the coordinate vector $\boldsymbol{r}(\theta)$ and the momentum $\boldsymbol{p}(\boldsymbol{\theta})$ everywhere on the surface of the invariant torus, parametrised by the angle variables $\boldsymbol{\theta} = (\theta_1, \theta_2)$ of Sec. 4.5.1. We represent this torus in terms of multiple sheets, on each of which the relation $\boldsymbol{p}(\boldsymbol{r})$ is univalued. The $\boldsymbol{r}$–caustics, represented by the thick black lines of the various panels of Fig. 4.17, provide some of the boundaries between these sheets. However, when drawn in the (x, y) plane, these caustics self–intersect (see the inset of Fig. 4.15(a)), and the sheeting must be constructed accordingly. We find that the univaluedness of $\boldsymbol{p}(\boldsymbol{r})$ may be achieved using the twelve sheets represented in Fig. 4.17.

4.5.3.2 Construction of the EBK wavefunction

The EBK wavefunction results from the interference of the contributions coming from individual sheets [64, Sec. 7.2]:

$$\psi_{\mathrm{EBK}}(\boldsymbol{r}) \quad = \quad c \sum_j |\det\left[\partial\boldsymbol{\theta}/\partial\boldsymbol{r}\right]|^{1/2} \, \exp[i(S_j(\boldsymbol{r})/\hbar + \alpha_j)] \; . \tag{4.18}$$

In Eq. (4.18), the sum is taken over the sheets $j = 1$ to 12. The amplitude of each contribution is set by the Jacobian determinant $\det[\partial\boldsymbol{\theta}/\partial\boldsymbol{r}]$ representing the change of coordinates from $\boldsymbol{r}$ to $\boldsymbol{\theta}$. The classical action $S_j(\boldsymbol{r})$ is calculated along the classical trajectory. The Maslov phases α_j are chosen such that the total phase $[S_j(\boldsymbol{r})/\hbar + \alpha_j]$ decreases by $\pi/2$ each time the classical trajectory traverses a caustic. Finally, c is a normalisation coefficient.

Numerical evaluation. We calculate the quantities $\partial\boldsymbol{\theta}/\partial\boldsymbol{r}$ and S_j entering Eq. (4.18) as a function of the angles $\boldsymbol{\theta}$, starting from Eq. (4.15). Then, we isolate the contribution of the various sheets using masks whose boundaries are shown on Fig. 4.17.

4.5.3.3 Comparison between our semiclassical and finite–element results

Figure 4.18 compares the semiclassical wavefunctions obtained from Eq. (4.18), after projection onto the irreducible representations A_1 and E, to our corresponding finite–element results. The agreement between the two approaches is excellent, including in the regions where the caustics self–intersect, shown in the upper left insets.

Primitive EBK wavefunctions do not account for the quantum penetration of the wavefunctions through the caustics. Instead, they diverge along the caustics as in the WKB approach [80, §46] and vanish outside the classical torus. This is illustrated in Fig. 4.19, which compares the semiclassical wavefunctions to the full numerical ones along the horizontal and vertical axes. This limitation of the semiclassical wavefunctions leads to numerical inaccuracies near the caustics which hinder their normalization. Hence, each of our EBK wavefunctions matches the finite–element wavefunction up to an overall normalization factor of order 2. We eliminate it by scaling the EBK wavefunction so that it matches the finite–element result at one single point chosen far from the caustics.

The quantum penetration through the caustics may be accounted for, and hence this limitation be overcome, using a uniform approximation to the wavefunction [64, Sec. 7.2]. This goes beyond the scope of the present work.

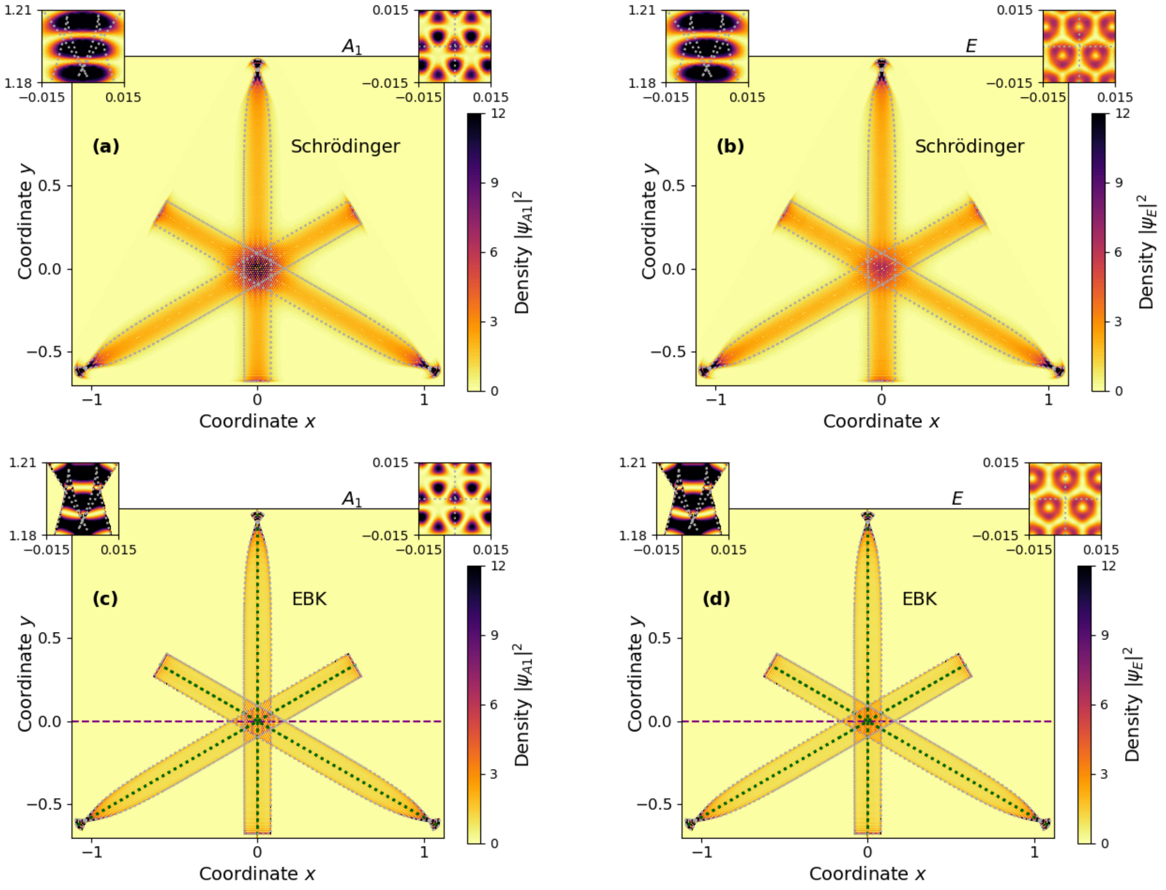

Figure 4.18: *Quantum states localized near the trajectories of family A. (a,b)* Wavefunction densities $|\psi^{A_1}(\boldsymbol{r})|^2$ and $|\psi^{E}(\boldsymbol{r})|^2$ for the two quasidegenerate eigenstates of H_{2D} localized near the periodic trajectories of family A whose energies are closest to C_6/R^6, obtained through our finite–element numerical calculations. *(c,d)* The corresponding squared EBK wavefunctions $|\psi^{A_1}_{\mathrm{EBK}}(\boldsymbol{r})|^2$ and $|\psi^{E}_{\mathrm{EBK}}(\boldsymbol{r})|^2$, built from the KAM torus satisfying Eq. (4.16) with $\nu_x = 0$, $\nu_y = 300$ (see Fig. 4.15(a)). On all four panels, the left inset details the region where the caustics self–intersect, and the right one shows the region near $(x = 0, y = 0)$.

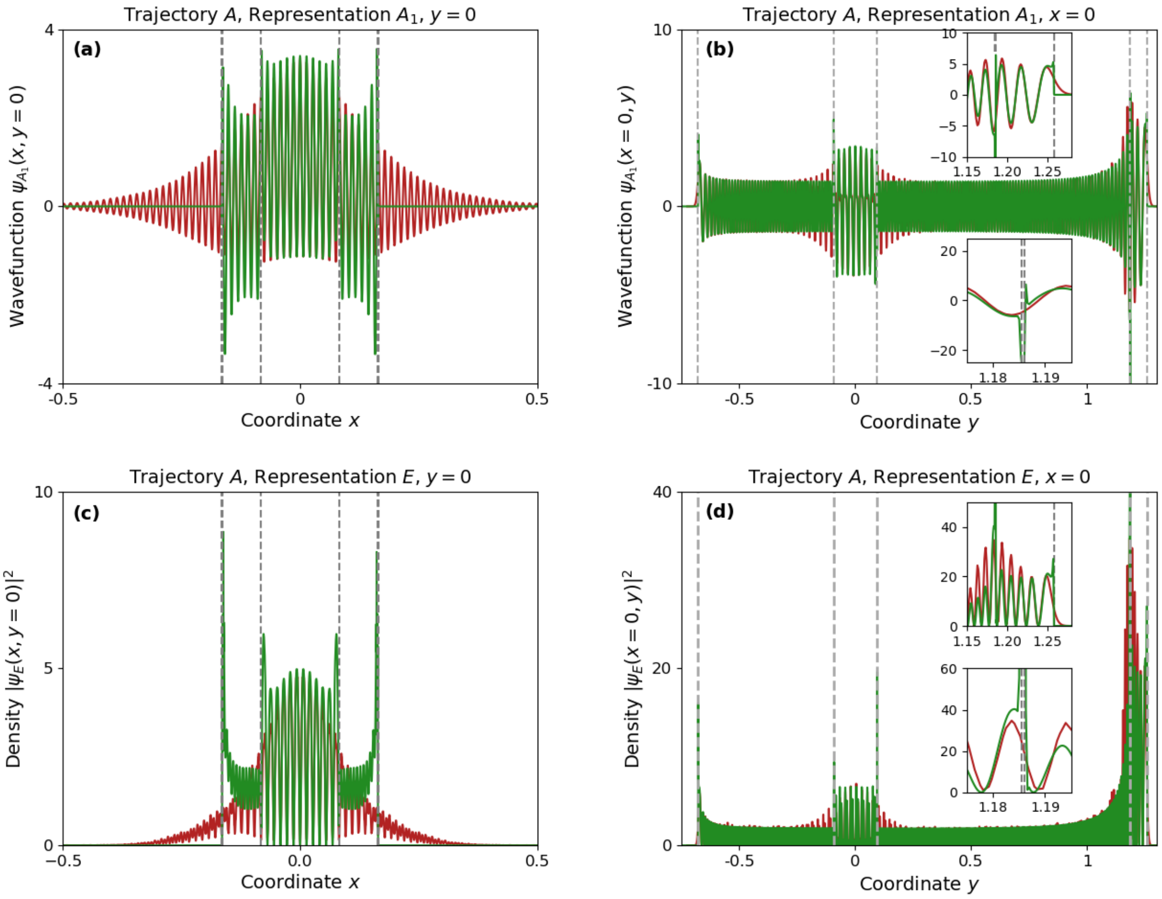

Figure 4.19: *Quantum states localized near the classical trajectory A: sections along the axes.* Comparison of the EBK *(a,b)* real wavefunction $\psi^{A_1}_{\mathrm{EBK}}$ and *(c,d)* density $|\psi^{E}_{\mathrm{EBK}}|^2$ associated with the complex wavefunction ψ^{E}_{EBK} (green) with the corresponding quantities obtained through finite–element numerics (red) shown on Fig. 4.18. The semiclassical and quantum quantities are compared along the horizontal *(a,c)* and vertical *(b,d)* axes. The insets illustrate their behaviour near the caustics (vertical dashed gray lines). Each EBK wavefunction has been scaled to match the finite–element wavefunction at the point $(x = 0, y = 0.5)$.

4.6 Conclusion

The system comprised of three interacting atoms in a circular trap may be described theoretically using an exact mapping to a single effective particle in a plane, described by a Hamiltonian which is reminiscent of the Hénon–Heiles model. In particular, the effective problem exhibits C_{3v} symmetry and its classical phase space is mixed.

We have analysed this system using well–established tools presented e.g. in Ref. [67] in the context of model potentials. By contrast, the system we put forward has been made experimentally accessible by recent advances in Rydberg atom trapping.

First, focussing on experimentally viable values for the parameters and energies, we have studied the spectral statistics for each of the irreducible representations, and found that they are well described by Berry–Robnik statistics.

Second, we have identified two mechanisms hindering ergodicity in this system. The first mechanism is a quantum scar, analysed in Sec. 4.4. It leads to the existence of quantum eigenstates which are localised in the vicinity of a classically unstable periodic trajectory. The second mechanism is deeply rooted in classical mechanics. The stable classical periodic trajectories supported by the system are surrounded by aperiodic non–ergodic trajectories winding around tori. These lead to quantum eigenstates localised in the vicinity of the stable periodic trajectories. We have obtained both their energies and their wavefunctions using the EBK semiclassical approach. Our semiclassical results are in excellent agreement with our full–fledged finite–element solution of the Schrödinger equation.

These mechanisms occur for the same values of the atomic mass, interaction strength, and trap radius. They also occur within the same range of energies. One may address one effect or the other simply by changing the initial condition defining the motion of the atoms. This is promising in view of an experimental comparison of the two mechanisms.

The chosen circular geometry, with no longitudinal dependence of the potential along the circle, minimises the role of single–particle traps. Accordingly, the mechanisms we have described rely on the interaction between the particles. Hence, they may be compared to many–body scars, with which they share at least one observable feature, namely, localised states that are approximately evenly spaced in energy.

PHYSICAL REVIEW A **107**, 022217 (2023)

Quantum scar affecting the motion of three interacting particles in a circular trap

D. J. Papoular [*] and B. Zumer
LPTM, UMR8089 CNRS & CY Cergy Paris Université, 95032 Cergy-Pontoise, France

(Received 26 September 2022; revised 21 January 2023; accepted 31 January 2023; published 17 February 2023)

We propose theoretically a quantum scar affecting the motion of three interacting particles in a circular trap. We numerically calculate the quantum eigenstates of the system and show that some of them are scarred by a classically unstable periodic trajectory, in the vicinity of which the classical analog exhibits chaos. The few-body scar we consider is stabilized by quantum mechanics, and we analyze it along the lines of the original quantum scarring mechanism [Phys. Rev. Lett. **53**, 1515 (1984)]. In particular, we identify towers of scarred quantum states which we fully explain in terms of the unstable classical trajectory underlying the scar. Our proposal is within experimental reach owing to very recent advances in Rydberg atom trapping.

DOI: 10.1103/PhysRevA.107.022217

I. INTRODUCTION

The thermalization of closed interacting quantum systems [1] may be impeded by various mechanisms [2,3] whose investigation is strongly motivated by contemporary applications [4,5]. Indeed, slowly thermalizing systems retain memory of their initial state over longer times [6], making them useful for quantum simulation [4] and quantum information processing [5]. Atomic systems are an excellent test-bed for chaos [7–9], and techniques for the individual manipulation [10] of Rydberg atoms [11] have extended its exploration to interacting systems. A recent experiment on Rydberg atom arrays [12] has initiated the investigation of weak ergodicity breaking in many-body systems [13,14]. Systems exhibiting this phenomenon thermalize rapidly for most initial conditions, but specific initial states yield nonergodic dynamics. This behavior is analogous to the quantum scars initially predicted [15] and observed [16] in the absence of interactions, which also lead to weak ergodicity breaking [17] by impacting some [[18], chap. 22] quantum eigenstates. Hence, it is also called "many–body scarring" [19]. A similar phenomenon has been predicted in the context of the Dicke model [20], where the quantum scars are due to the collective light–matter interaction and impact many quantum eigenstates [21].

Despite the intense theoretical scrutiny [22], only two experiments [12,23] and one explicit proposal [19] explore many-body scarring so far [12,19,23]. In all three cases, the observed nonergodic behavior is linked to classical physics. The experiments of Refs. [12,23] both probe the PXP model [24] in regimes where the classical analog system [25] explores the vicinity of classically stable periodic trajectories, so that the absence of thermalization may be traced back to the classical Kolmogorov–Arnold–Moser theorem [[26], Sec. VI]. The proposal of Ref. [19] refers to spin helices in various geometries. Their classical limit is stable [27], and from the quantum point of view they generalize helices predicted [28] and observed [19] in the integrable XXZ chain. Hence, the proximity of integrable models is expected to play a key role.

In this article, we propose a three-body system hosting a quantum scar which relies on the interaction between particles. It may be realized experimentally owing to very recent advances in Rydberg atom trapping [29,30]. It is simple enough to be fully analyzed by combining the numerical calculation of stationary states and well-established tools for the analysis of chaotic systems [31], in the spirit of Heller's original proposal [15].

The system we consider exhibits "towers" of scarred states which are approximately evenly spaced in energy. These are a key feature of both quantum scars [32] and many-body scars [13,14,22,23,33]. In the present context, we explain them in terms of the classically unstable periodic trajectory causing the scar, in the spirit of Heller's original argument [[32], Fig. 22]. The phase-space dimensionality of the few-body system we consider [(4), see below] matches the maximum number of independent parameters introduced so far in the variational approaches applied to the many-body PXP model and its generalizations [[26], §III.A]. In stark contrast with the many-body PXP model where approximate classical limits have to be cleverly constructed [25], our few-body system affords an exact reduction to four parameters and the identification of the classical analog is straightforward.

We formulate our proposal in terms of trapped Rydberg atoms [29,30]. However, we expect other interacting systems with the same symmetries to exhibit similar quantum scars. We substantiate this claim in the Appendix (Sec. A 1) by identifying the quantum scar for the Hénon–Heiles (HH) potential [34]. In particular, the scar may be probed using three dipolar particles [35].

II. THE CONSIDERED SYSTEM

We consider three identical bosonic particles of mass m in a circular trap of radius R. The Hamiltonian reads

$$H = \left(l_1^2 + l_2^2 + l_3^2\right)\big/(2mR^2) + v(d_{12}) + v(d_{23}) + v(d_{31}), \qquad (1)$$

---

[*] david.papoular@cyu.fr

2469-9926/2023/107(2)/022217(8)

©2023 American Physical Society

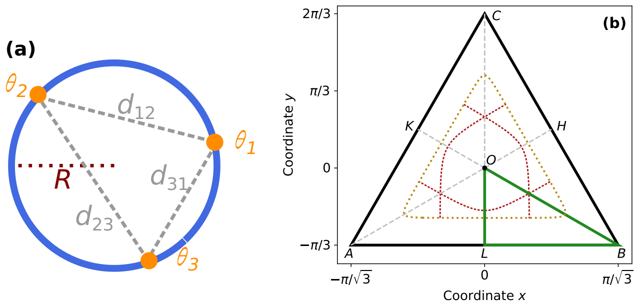

FIG. 1. (a) Three particles (orange disks) interacting via a repulsive van der Waals interaction of strength $C_6 > 0$, constrained to move on a circle of radius R, their angular coordinates θ_i and distances d_{ij}. (b) The (x, y) configuration space is the inside of the triangle defined by the points $A(-\pi/\sqrt{3}, -\pi/3)$, $B(+\pi/\sqrt{3}, -\pi/3)$, $C(0, 2\pi/3)$. The dashed golden line limits the classically accessible region for the energy $E = 7C_6/R^6$. The three dotted red lines show the three classical periodic trajectories of type B for this energy. The small green triangle OLB is the reduced configuration space within which quantum wave functions are calculated.

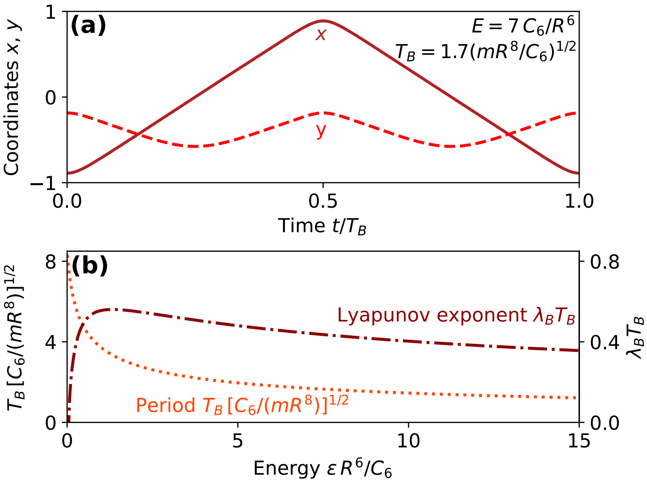

FIG. 2. (a) Periodic trajectory B for the energy $\epsilon = 7\,C_6/R^6$, described by its coordinates $x(t)$ and $y(t)$ as a function of time t. (b) The period $T_B(\epsilon)$, and the product $\lambda_B T_B$ of the Lyapunov exponent and the period, for the periodic trajectory B as a function of the energy ϵ.

where l_i is the component of the angular momentum of particle i along the rotation axis, which is perpendicular to Fig. 1(a). We assume that the interaction $v(d_{ij})$ between the particles i and j only depends on their distance $d_{ij} = 2R|\sin[(\theta_i - \theta_j)/2]|$. For circular Rydberg atoms whose electronic angular momenta are perpendicular to the plane, $v(d_{ij}) = C_6/d_{ij}^6$ with $C_6 > 0$ [[36], Appendix A].

We introduce the Jacobi coordinates [[38], §1.2.2] $x = [(\theta_1 + \theta_2)/2 - \theta_3 + \pi]/\sqrt{3}, y = (\theta_2 - \theta_1)/2 - \pi/3, z = (\theta_1 + \theta_2 + \theta_3)/3 - 2\pi/3$, and their conjugate momenta p_x, p_y, p_z (which carry the unit of action). In terms of these, $H = p_z^2/(3mR^2) + H_{2\text{D}}$, where

$$H_{2\text{D}} = \left(p_x^2 + p_y^2\right)/(4mR^2) + V(x, y). \qquad (2)$$

Here, $V(x, y) = v(x, y)C_6/R^6$, with

$$v(x, y) = [\sin^{-6}(\pi/3 + y) + \sin^{-6}(\pi/3 + x\sqrt{3}/2 - y/2) + \sin^{-6}(\pi/3 - x\sqrt{3}/2 - y/2)]/64 - 1/9, \qquad (3)$$

energies being measured from the minimum $V(\mathbf{0})$. The free motion of the coordinate z reflects the conservation of the total angular momentum $p_z = l_1 + l_2 + l_3$. The Hamiltonian H is invariant[1] under the point group C_{3v} [[40], §93], generated by the threefold rotation about the axis $(x = y = 0)$ and the reflection in the plane $(x = 0)$.

III. CLASSICAL PHYSICS

We first analyze the classical dynamics described by the Hamiltonian H. Expressing momenta, energies, and times in units of $P_{\text{ref}} = (mC_6/R^4)^{1/2}$, C_6/R^6, and $(mR^8/C_6)^{1/2}$, respectively, the classical results are independent of m, C_6, and R, leading to the scaled predictions in Figs. 1–4. We choose the rotating reference frame such that $p_z = 0$ and $z = 0$. The divergence of $v(d_{ij})$ prevents the particles from crossing, so that we assume $\theta_1 < \theta_2 < \theta_3 < \theta_1 + 2\pi$ at all times. Hence, the classical problem is reduced to a point moving in the two-dimensional (2D) plane (x, y) within the equilateral triangle of Fig. 1(b), in the presence of the potential $V(x, y)$.

We have characterized the periodic trajectories of V using our own C++ implementation of the numerical approach of Ref. [41]. We find three families of periodic trajectories, existing for all energies $\epsilon > 0$: we label them A, B, C in analogy with the results for the HH potential [42]. We shall analyze them and their bifurcations in a forthcoming presentation [43]. Here, we focus on family B, which yields the quantum scar. For a given ϵ, there are three trajectories of type B, due to the threefold rotational symmetry of the potential V. They are represented in the (x, y) plane in Fig. 1(b), and the one which

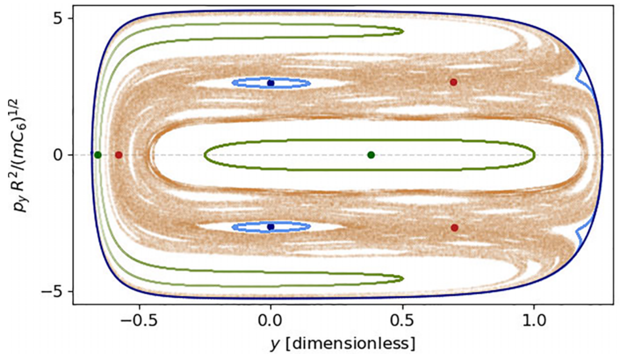

FIG. 3. Classical surface of section [[37], §1.2] for the Hamiltonian of Eq. (2) with $p_z = 0$, $\epsilon = 7C_6/R^6$, $x = 0$, and $p_x \geqslant 0$. The dark blue dots and outer curve indicate the periodic trajectories of type A; the red and green dots show those of types B, and C. The closed blue and green curves show nonergodic trajectories near A and C. The ≈287 000 thin brown dots all belong to the same ergodic trajectory. The periodic trajectories of type B, which yield the quantum scar, are all within the classically ergodic region.

---

[1] The full plane group characterizing the symmetries of $v(x, y)$ is $p6mm$ [[39], Part 6].

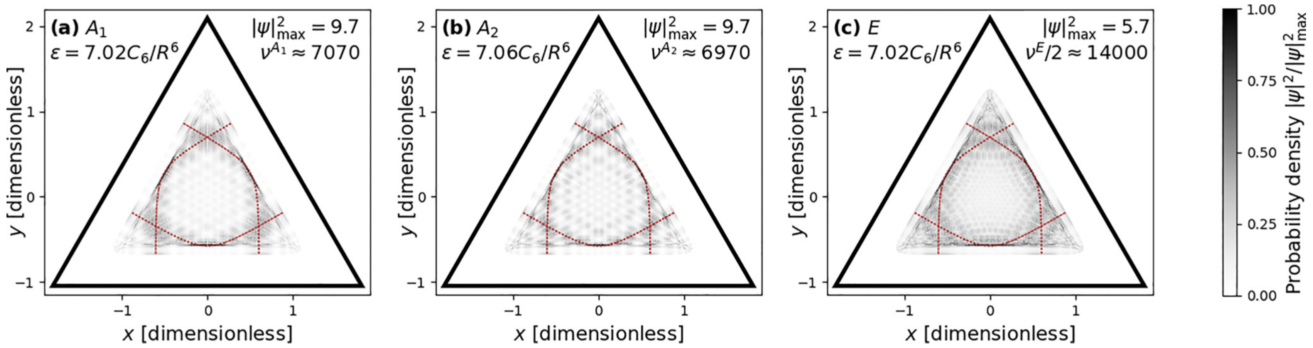

FIG. 4. Probability density $|\psi(x, y)|^2$ of the scarred quantum eigenstate whose energy is closest to $7C_6/R^6$ in each irreducible representation $\rho =$ (a) A_1, (b) A_2, and (c) E. The dashed red lines show the three classically unstable periodic trajectories of type B for the corresponding energy ϵ. The densities are maximal near the unstable trajectories, signaling the quantum scar. The integer $\nu^{(\rho)}$ in an approximation to the index of the shown quantum state in the representation ρ.

is symmetric about the vertical axis is shown as a function of time in Fig. 2(a). They are unstable for all energies, as shown by the Lyapunov exponent $\lambda_B > 0$ in Fig. 2(b). Figure 2(b) shows that trajectory B satisfies both conditions heralding a quantum scar: $\lambda_B T_B < 2\pi$ [[18], ch. 22], and lower values of $\lambda_B T_B$ signal stronger scarring [[44], §9.3]. The unstable trajectory B does not bifurcate [[44], §2.5], so that the scar strengths associated with it for all $E > 0$ do not benefit from the classical enhancement due to the proximity of bifurcations [45]. This sets it apart from a previous proposal involving a scar hinging on this enhancement [46] so that, in stark contrast to ours, it is captured by Einstein–Brillouin–Keller quantization [47].

To visualize effects beyond the linear regime, Fig. 3 shows the surface of section [[37], §1.2] of H for $\epsilon = 7C_6/R^6$ and the conditions $x = 0$, $p_x > 0$ (allowing for a comparison with the HH potential [48]). It exhibits both nonergodic regions comprising tori [[49], Appendix 8] and an ergodic region, as is typical for a nonintegrable system [[50], §1]. The three fixed points corresponding to trajectories B are all located in the ergodic region. This precludes their stabilization by any classical mechanism.

IV. QUANTUM PHYSICS

We seek the eigenfunctions of H in the form $\Psi_n(\theta_1, \theta_2, \theta_3) = \psi_n(\mathbf{r})e^{inz}$, where $\mathbf{r} = (x, y)$ and $n = p_z/\hbar$. The wave function ψ_n is an eigenstate of H_{2D} with the energy ϵ. It is defined on the whole (x, y) plane. Its symmetries are related to (i) angular periodicity, (ii) bosonic symmetry, and (iii) the point group C_{3v}.

We first discuss (i) and (ii). (i) The 2π periodicity of Ψ_n in terms of $(\theta_i)_{1\leqslant i\leqslant 3}$ yields $\psi_n(\mathbf{r} - \mathbf{BC}) = \psi_n(\mathbf{r} - \mathbf{CA}) = \psi_n(\mathbf{r} - \mathbf{AB}) = \psi_n(\mathbf{r})e^{-i2\pi n/3}$, so that n is an integer. (ii) The bosonic symmetry of Ψ_n leads to $\psi_n(\mathcal{S}\mathbf{r}) = +\psi_n(\mathbf{r})$, where $\mathcal{S}$ is the symmetry about any of the lines (AB), (BC), or (CA) in the (x, y) plane. Hence, we may restrict the configuration space to the inside of the triangle ABC of Fig. 1(b). Along its edges, $v(x, y)$ strongly diverges [e.g., $v \approx (y + \pi/3)^{-6}$ near $[AB]$], so that $\psi_n = 0$ there. Combining (i) and (ii), and calling $\mathcal{R}$ the rotation of angle $2\pi/3$ about O, $\psi_n(\mathcal{R}\mathbf{r}) = \psi_n(\mathbf{r})e^{2in\pi/3}$.

We now analyze the role of the point group C_{3v}. We classify the energy levels in terms of its three irreducible representations $\rho = A_1$, A_2, and E [[40], §95]. Hence, the Hilbert space is split into three unconnected blocks. These may be told apart through the behavior of ψ_n under two operations in the (x, y) plane [51]: $\mathcal{R}$ and the reflection $\mathcal{S}_\Delta$ about the line $\Delta = (CL)$ [see Fig. 1(b)]. Wave functions pertaining to the one-dimensional (1D) representations A_1 or A_2 satisfy $\psi_n(\mathcal{R}\mathbf{r}) = \psi_n(\mathbf{r})$, so that $n = 0$ modulo 3. Under reflection, $\psi_n(\mathcal{S}_\Delta\mathbf{r}) = \pm\psi_n$, where the $+$ and $-$ signs hold for A_1 and A_2, respectively. Wave functions pertaining to the 2D representation E satisfy $\psi_n(\mathcal{R}\mathbf{r}) = \exp(\pm 2i\pi/3)\psi_n(\mathbf{r})$, so that $n = \pm 1$ modulo 3 [52]. Then, exploiting time-reversal invariance we may choose the two degenerate basis states to be ψ_n and its complex conjugate ψ_n^* with $\psi_n(\mathcal{S}_\Delta\mathbf{r}) = \psi_n^*(\mathbf{r})$.

These symmetry considerations further reduce the configuration space to the green triangle OLB of Fig. 1(b). We deal with representations A_1, A_2, and E separately by applying different boundary conditions on its edges (see Sec. A 2b in the Appendix). We solve the resulting stationary Schrödinger equations using the finite-element software FREEFEM [53]. The classical scaling no longer holds. Instead, the energy spectra and wave functions depend on the dimensionless ratio $\eta = \hbar/P_{\mathrm{ref}} = \hbar R^2/(mC_6)^{1/2}$. Smaller values of η signal deeper quasiclassical behavior: we choose $\eta = 0.01$. We focus on energies $\epsilon \sim 7C_6/R^6$, which are large enough for the classical ergodic trajectory (brown dots on Fig. 3) to occupy a substantial part of phase space.

Figure 4 shows the probability density for the quantum scarred state whose energy is closest to $7C_6/R^6$ for each ρ. It is maximal near the three classical trajectories B. This signals a stabilization of trajectory B, whose origin is purely quantum since the unstable trajectories belong to the ergodic region of classical phase space (see Fig. 3).

V. SEMICLASSICAL ANALYSIS

For the majority of the calculated quantum states, the probability density $|\psi(x, y)|^2$ is unrelated to the periodic trajectories of type B. Nevertheless, for each representation, we find multiple scarred quantum states, represented by the vertical dashed lines in Fig. 5, whose energy spacing is approximately regular. This is analogous to the tower of scarred

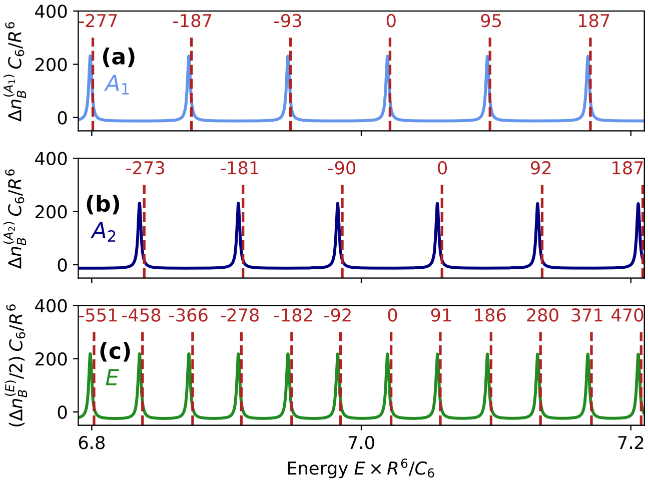

FIG. 5. For each irreducible representation $\rho =$ (a) A_1, (b) A_2, and (c) E, the solid curve shows the semiclassical contribution Δn_B [Eq. (4)] to the density of states n due to the periodic trajectory B, as a function of the energy ϵ. The dashed vertical lines show the energies of the scarred quantum states, which closely match the maxima of Δn_B. The integers above them specify the relative state indices $\Delta\nu^{A_1}$, $\Delta\nu^{A_2}$, $\Delta\nu^{E}/2$ with respect to the index $\nu^{(\rho)}$ of the scarred states in Fig. 4.

many-body states with an approximately constant energy separation found in a PXP chain [13], which is a recurrent feature in theoretical analyses of weak ergodicity breaking [14,22,33]. In the present context, we explain the series of scarred quantum states semiclassically. We use Gutzwiller's trace formula [[31], chap. 17] describing the impact of the classical periodic trajectories on the quantum density of states $n(\epsilon)$. We isolate the contribution $\Delta n_B^{(\rho)}$ to n coming from the unstable trajectory B, which depends on the representation ρ [54,55]:

$$\begin{aligned}&\left(\Delta n_B^{(\rho)} 2\pi\hbar/T_B^{(\rho)} + 1\right)/\,\alpha_B^{(\rho)}\\&= \sum_{k=0}^{\infty}\left\{\left[S_B(\rho)/\hbar - 2\pi(k^{(\rho)}+1/2)\right]^2 + \left(\alpha_B^{(\rho)}/2\right)^2\right\}^{-1}.\end{aligned} \tag{4}$$

The parameters $T_B^{(\rho)}(\epsilon)$, $S_B^{(\rho)}(\epsilon)$, $\alpha_B^{(\rho)}(\epsilon)$, and $k^{(\rho)}$ in Eq. (4) are defined in Table I for each representation. They are directly related to the classical period $T_B(\epsilon)$ and action $S_B(\epsilon) = \oint \mathbf{p}\cdot d\mathbf{x}$ along one trajectory B, the product $\lambda_B(\epsilon)T_B(\epsilon)$, and the summation index k, respectively. Figure 5 shows $\Delta n_B^{(\rho)}(\epsilon)$ for each representation. Its maxima agree with the energies of the scarred states. Hence, the series of scarred states found in each representation reflects the multiple resonances in $n(\epsilon)$ due to the unstable trajectory B. The regularity in their energy spacing follows from the resonance maxima being evenly spaced in terms of the classical action, $S_{B\max}^{(\rho)}/\hbar = 2\pi(k^{(\rho)} + 1/2)$.

TABLE I. Parameters $T_B^{(\rho)}$, $S_B^{(\rho)}$, $\alpha_B^{(\rho)}$, $k^{(\rho)}$ for Eq. (4), depending on the irreducible representation $\rho = A_1, A_2$, or E.

	$T_B^{(\rho)}$	$S_B^{(\rho)}$	$\alpha_B^{(\rho)}$	$k^{(\rho)}$
A_1	$T_B/2$	$S_B/2$	$\lambda_B T_B/2$	k
A_2	$T_B/2$	$S_B/2$	$\lambda_B T_B/2$	$k-1/2$
E	$2T_B$	S_B	$\lambda_B T_B$	$k+1/2$

VI. EXPERIMENTAL PROSPECTS AND OUTLOOK

We consider e.g., ^{87}Rb atoms in the $50C$ circular Rydberg state [36,56], for which $C_6/h = 3$ GHz μm^6. The value $\eta = 0.01$ corresponds to $R = 7$ μm. The ring-shaped trap may be realized optically using Laguerre–Gauss laser beams and light sheets [[57], §II.C.2]. The energy $\epsilon = 7C_6/R^6 = h \times 200$ kHz is within experimental reach [36]. For small angular momenta, the centrifugal energy, which is proportional to $(\eta n)^2/3$, is negligible compared with ϵ. The position of the atoms may be detected at a given time by turning on a 2D optical lattice trapping individual Rydberg atoms [36,58], which freezes the dynamics, followed by atomic deexcitation and site-resolved ground-state imaging [59].

Further investigation will be devoted to the stability of the quantum scar. Recent experiments [23,60] have shown that it may be enhanced by periodically modulating the parameters. Depending on the stabilization mechanism (see, e.g., Ref. [61] or Ref. [[62], §27]), this may lead to a discrete time crystal [63] which is either quantum or classical.

ACKNOWLEDGMENTS

We acknowledge stimulating discussions with M. Brune and J. M. Raimond (LKB, Collège de France) and R. J. Papoular (IRAMIS, CEA Saclay).

APPENDIX

The goal of this Appendix is twofold. In Sec. A 1, we identify quantum scars supported by the Hénon–Heiles Hamiltonian, and characterize them using the same semiclassical argument as in the main text. In Sec. A 2, for each of the three irreducible representations of the group C_{3v}, we derive boundary conditions defining quantum stationary states within the reduced configuration space.

1. Quantum scars in the Hénon–Heiles model

In this Section, we briefly describe our results, analogous to those of the main text, for the Henon–Heiles Hamiltonian [34] $H_{\rm HH} = (p_x^2 + p_y^2)/(2m) + V_{\rm HH}$, where

$$V_{\rm HH} = m\omega_0^2(x^2+y^2)/2 + \alpha(x^2y - y^3/3). \tag{A1}$$

Equation (A1) is written in the dimensional form of Refs. [[64], §5.6.4] which assumes that the coordinates x and y carry the unit of length. The quantities p_x, p_y are their conjugate momenta, the parameters m and ω_0 denote a mass and a frequency, and the coefficient α sets the strength of the cubic term. If lengths, momenta, energies, and times are expressed in units of $L_{\rm HH} = m\omega_0^2/\alpha$, $P_{\rm HH} = m^2\omega_0^3/\alpha$, $E_{\rm HH} = m^3\omega_0^6/\alpha^2$, $T_{\rm HH} = 1/\omega_0$, the dimensionless form matches that of Ref. [34]. As in the main text, in terms of these units, the classical dynamics is independent of m, $\omega_0\alpha$. As for quantum physics, the classical scaling no longer holds, and the energy spectra and wave functions depend on the dimensionless

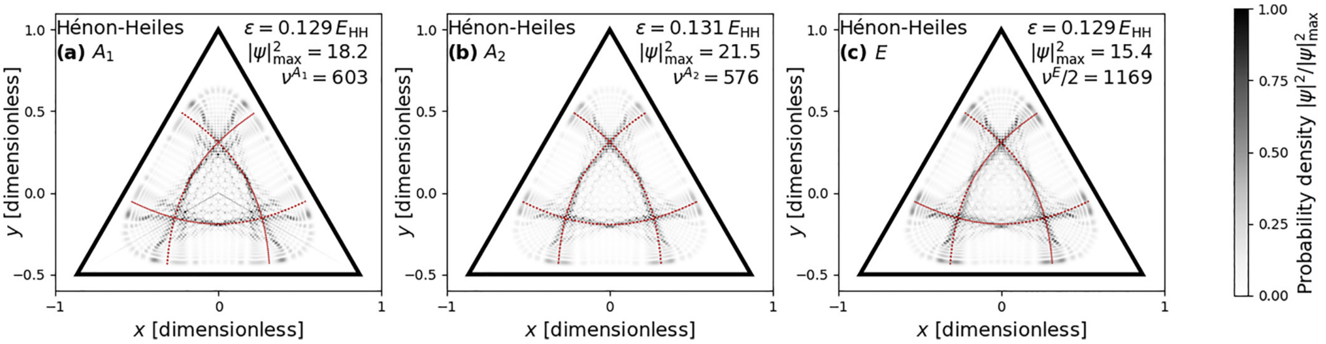

FIG. 6. Probability density $|\psi_{(x,y)}|^2$ of the scarred quantum eigenstate of the Hénon–Heiles Hamiltonian $H_{\rm HH}$ whose energy is closest to $0.13E_{\rm HH}$ in each irreducible representation (a) A_1, (b) A_2, and (c) E. The dashed red lines show the three classically unstable periodic trajectories of type B for the corresponding energy ϵ. The densities are maximal near the unstable trajectories, signaling the quantum scar. The integer $\nu^{(\rho)}$ is the index of the shown quantum state in the representation ρ. (This figure is the analog, for the Hénon–Heiles potential, of Fig. 4 in the main text.)

parameter $\eta_{\rm HH} = \hbar/(L_{\rm HH}P_{\rm HH}) = \hbar\alpha^2/(m^3\omega_0^5)$. Smaller values of $\eta_{\rm HH}$ signal deeper quasiclassical behavior.

The Hénon–Heiles potential is related to our main discussion for two reasons. First, its symmetry group is C_{3v} [55], which is the point group of the system analyzed in the main text. Second, expanding Eq. (3) there to third order in x and y near the equilibrium position O shows that it reduces to Eq. (A1) in the low-energy limit.

The Hénon–Heiles Hamiltonian has been extensively studied (see, e.g., Ref. [[37], §1.4]). Our goal in revisiting it was twofold. First, we have calibrated our codes against published results for this potential. Second, we have identified quantum scars for the Hénon–Heiles Hamiltonian. At the end of the section, we point out the relevance of the Hénon-Heiles potential in relation to a broad family of systems, which includes the case of dipolar particles.

a. Calibration

We have used our codes to reproduce the known classical periodic trajectories of $H_{\rm HH}$, their periods and Lyapunov exponents [42], and its surfaces of section for various energies [48]. We have also recovered the quantum energy levels and wave functions, belonging to all three representations, in Refs. [51,65] for $\eta_{\rm HH} = 1/80$ and in Ref. [52] for $\eta_{\rm HH} = 0.06^2$.

b. Quantum scars for the Hénon–Heiles potential

We now turn to the lower value $\eta = 0.04^2$, so as to consider the deep quasiclassical regime. We focus on energies $\epsilon \sim 0.13\,E_{\rm HH}$: these are large enough for the ergodic region to occupy a substantial part of phase space [48], while remaining below the threshold energy $E_{\rm HH}/6$ above which $H_{\rm HH}$ supports trajectories that are not bound [42]. Figure 6 shows the probability density density for the scarred state with the energy ϵ closest to $0.13\,E_{\rm HH}$ for each representation. It is maximal near the three trajectories B for the energy ϵ, signaling the scar.

In each irreducible representation $\rho = A_1$, A_2, and E, we find multiple scarred quantum states for the Hénon–Heiles potential (vertical dashed lines in Fig. 7) whose energy spacing is approximately regular, in direct analogy with the results of the main text. They may be explained by using the same semiclassical argument relying on Gutzwiller's trace formula. We isolate the contribution $\Delta n_B^{(\rho)}$ to the density of states n for each representation ρ due to the unstable trajectory B. Both Eq. (4) and Table I in the main text are applicable to the Hénon–Heiles potential with no change. We have calculated the required period T_B, action S_B and Lyapunov exponent λ_B characterizing the periodic trajectory B in the Hénon–Heiles potential as a function of the energy ϵ using our codes. Figure 7 shows $\Delta n_B^{(\rho)}$ for each representation ρ. Just like in the main text, its maxima coincide with the energies of the scarred states. Hence, the same conclusion holds, and we may ascribe the regularity in their energy spacing to the resonance maxima being equally spaced in terms of the classical action S_B.

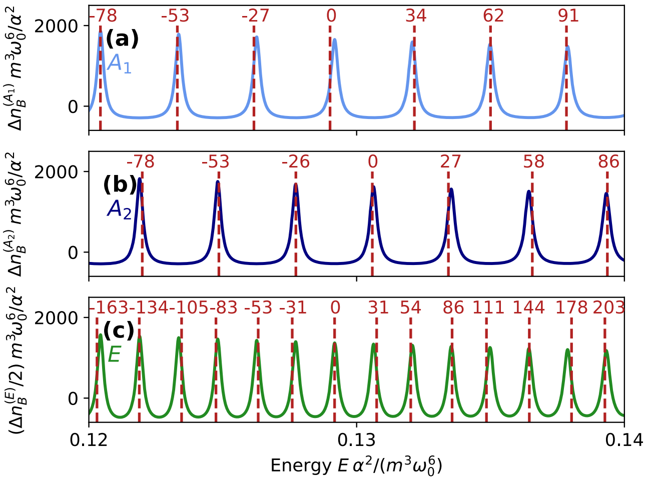

FIG. 7. For each irreducible representation $\rho =$ (a) A_1, (b) A_2, and (c) E, the solid curve shows the semiclassical contribution Δn_B to the density of states n of the Hénon–Heiles potential due to the periodic trajectory B as a function of the energy ϵ. The dashed vertical lines show the energies of the scarred quantum states, which closely match the maxima of Δn_B. The integers above them specify the relative state indices $\Delta\nu^{A_1}$, $\Delta\nu^{A_2}$, $\Delta\nu^{E}/2$ with respect to the index $\nu^{(\rho)}$ of the scarred states in Fig. 6. (This figure is the analog, for the Hénon–Heiles potential, of Fig. 5 in the main text.)

c. Generality of the Hénon–Heiles potential

The potential V_{HH} combines a 2D isotropic harmonic trap with a two-variable cubic polynomial function. Hence, it may be seen as the simplest possible 2D potential exhibiting C_{3v} symmetry. The three-body Hamiltonian given by Eq. (1) in the main text reduces to it near one of its (equivalent) minima for the repulsive pair-wise interaction $v(d_{ij}) = a\, d_{ij}^{-\alpha}$ regardless of the power-law exponent $\alpha > 0$. The presence of quantum scars in the Hénon–Heiles model leads us to expect similar scars in all of these systems. In particular, the dipole–dipole interaction [35] in the case where all three dipole moments are polarized perpendicular to the plane, corresponding to $\alpha = 3$, is expected to yield the same phenomena.

2. Boundary conditions defining a basis of quantum stationary states

In this section, we exploit the spatial symmetries of the point group C_{3v} and time-reversal symmetry to state boundary conditions uniquely defining a basis of quantum stationary states. We state our reasoning in terms of the system considered in the main text, but it applies without change to the Hénon–Heiles Hamiltonian discussed in Sec. A 1 above.

We expect the quantum states scarred by the classically unstable periodic trajectory B to exhibit an enhanced probability density along all three trajectories B at a given energy [red dotted lines in Figs. 1(a) and 4(a)–4(c) in the main text for the system discussed there, and in Figs. 6(a)–6(c) in the present Appendix for the Hénon–Heiles model]. Hence, the probability density for the scarred states is expected to exhibit C_{3v} symmetry. Therefore, we construct a basis of quantum stationary states whose corresponding density profiles all exhibit this symmetry. This property is not automatically satisfied and requires choosing appropriate basis functions. For example, Figs. 7(a) and 7(b) in Ref. [51] show probability densities corresponding to eigenstates of the Hénon–Heiles model which do not exhibit C_{3v} symmetry despite the fact that the Hamiltonian does, see Sec. A 1 above.

The group C_{3v} admits three irreducible representations, $\rho = A_1, A_2$, and E [[40], §95]. Representations A_1 and A_2 are 1D, whereas representation E is 2D. For each representation, we shall formulate a boundary condition defining basis functions belonging to it. All wave functions $\psi(\mathbf{r})$ are normalized according to $\iint_{ABC} d^2r|\psi(\mathbf{r})|^2 = 1$, the integral being taken over the triangle ABC.

a. One-dimensional representations A_1 and A_2

We first consider a 1D representation $\rho = A_1$ or A_2. Let ψ be an eigenstate of H_{2D} for the energy ϵ transforming according to ρ. We call $\mathcal{S}_1, \mathcal{S}_2, \mathcal{S}_3 = \mathcal{S}_\Delta$ the reflections about (AH), (BK), (CL) in the (x, y) plane (see Fig. 8). The wave function $\psi(\mathcal{S}_i\mathbf{r})$ is also an eigenstate of H_{2D} for the same energy ϵ. Because ρ is 1D, $\psi(\mathcal{S}_i\mathbf{r}) = \chi_i\psi(\mathbf{r})$ for some complex number χ_i. The reflections $\mathcal{S}_i$ satisfy $\mathcal{S}_i^2 = 1$, so that $\chi_i = \pm 1$. They also satisfy $\mathcal{S}_2\mathcal{S}_1 = \mathcal{S}_3\mathcal{S}_2 = \mathcal{R}$, with $\mathcal{R}$ being the rotation of angle $2\pi/3$ about the point O. The transformation $\mathcal{R}^3 = 1$, so that $(\chi_1\chi_2)^3 = (\chi_2\chi_3)^3 = 1$. Hence, $\chi_1 = \chi_2 = \chi_3 = \pm 1$.

The case $\chi_1 = \chi_2 = \chi_3 = 1$ leads to $\rho(\mathcal{R}) = \rho(\mathcal{S}_i) = 1$, so that $\rho = A_1$ [[40], §95, Table 7]. Then, $\psi(\mathcal{S}_i\mathbf{r}) = +\psi(\mathbf{r})$, leading to the boundary condition $\partial_n\psi = 0$ along the sides $[LO]$ and $[OB]$ of the green triangle OBL in Fig. 8. Combined with the condition $\psi = 0$ along the side $[LB]$ derived in the main text, it defines a basis of wave functions ψ for Representation A_1.

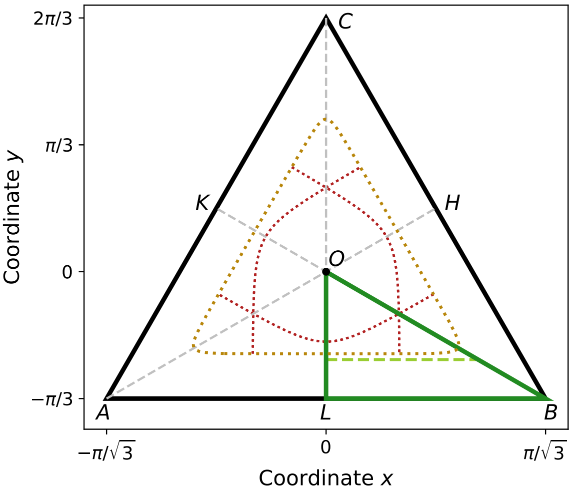

FIG. 8. The black triangle ABC is the classical configuration space for the Hamiltonian H_{2D} of the main text. The smaller green triangle OLB is the reduced configuration space within which we solve for the quantum stationary states. The classically accessible region, limited by the dotted golden line, is shown for the energy $\epsilon = 7C_6/R^6$. We enforce the boundary condition $\psi = 0$ on the quantum wave functions along the horizontal dashed green line. The three classical periodic trajectories B (dotted red lines) are also shown.

The case $\chi_1 = \chi_2 = \chi_3 = -1$ leads to $\rho(\mathcal{R}) = 1$ and $\rho(\mathcal{S}_i) = -1$, so that $\rho = A_2$. Then, $\psi(\mathcal{S}_i\mathbf{r}) = -\psi(\mathbf{r})$, leading to the condition $\psi = 0$ along the sides $[LO]$ and $[OB]$. Hence, imposing the Dirichlet boundary condition on the three edges of the triangle OBL defines a basis of wave functions ψ for Representation A_2.

The energy levels transforming according to the 1D representations A_1 and A_2 are nondegenerate, hence, the time-reversal invariance of H_{2D} allows us to choose all basis wave functions $\psi(\mathbf{r})$ to be real [[40], §18]. Furthermore, $\psi(\mathbf{r}) = \psi(\mathcal{R}^{-1}\mathbf{r}) = \chi_i\psi(\mathcal{S}_i\mathbf{r})$ differ by a sign at most. Hence, the corresponding probability densities coincide, and $|\psi(\mathbf{r})|^2$ does exhibit C_{3v} symmetry.

b. Two-dimensional representation E

We now turn to the 2D representation $\rho = E$. Let ϵ be a twice–degenerate energy level of H_{2D}. The corresponding eigenspace is spanned by two complex wave functions, ϕ_+ and ϕ_- which transform according to ρ:

$$\phi_\pm(\mathcal{R}^{-1}\mathbf{r}) = e^{\pm i2\pi/3}\phi_\pm(\mathbf{r}), \tag{A2a}$$

$$\phi_\pm(\mathcal{S}_\Delta\mathbf{r}) = \phi_\mp(\mathbf{r}), \tag{A2b}$$

where the transformations $\mathcal{R}$ and $\mathcal{S}_\Delta$ are defined as in Sec. A 2 a above and the main text.

The time-reversal invariance [[40], §18] of H_{2D} entails that the complex-conjugate wave functions $\phi_+^*(\mathbf{r})$ and $\phi_-^*(\mathbf{r})$ are also eigenstates of H_{2D} with the same energy ϵ. Complex-conjugating Eqs. (A2a), accounting for normalization, and writing $(\phi_+^*)^* = \phi_+$ lead to $\phi_\pm^* = e^{i\alpha}\phi_\mp$, where $e^{i\alpha}$ is a complex number of modulus 1. Introducing the new basis wave functions $\psi_+(\mathbf{r}) = e^{i\alpha/2}\phi_+(\mathbf{r})$ and $\psi_-(\mathbf{r}) = \psi_+^*(\mathbf{r})$, Eqs. (A2) reduce to two conditions on ψ_+:

$$\psi_+(\mathcal{R}^{-1}\mathbf{r}) = e^{i2\pi/3}\psi_+(\mathbf{r}), \tag{A3a}$$

$$\psi_+(\mathcal{S}_\Delta\mathbf{r}) = \psi_+^*(\mathbf{r}). \tag{A3b}$$

The probability densities $|\psi_+(\mathbf{r})|^2 = |\psi_+(\mathcal{R}^{-1}\mathbf{r})|^2 = |\psi_+(\mathcal{S}_\Delta\mathbf{r})|^2$ coincide. Hence, $|\psi_+(\mathbf{r})|^2$ exhibits C_{3v} symmetry: this is the probability density plotted in Figs. 4(a)–4(c) of the main text (three Rydberg atoms) and Figs. 6(a)–6(c) (Hénon–Heiles model).

We seek $\psi_+(\mathbf{r})$ in the following form, which is more amenable to numerical computation:

$$\psi_+(\mathbf{r}) = (x - iy)[u_1(\mathbf{r}) + iu_2(\mathbf{r})], \tag{A4}$$

where u_1 and u_2 are two real functions satisfying coupled Schrödinger equations. In Eq. (A4), the factor $(x - iy)$ accounts for the fact that $\psi_+(\mathbf{0}) = 0$, like for the stationary states of the 2D isotropic harmonic oscillator carrying angular momentum [[40], §112]. Equations (A3) yield the boundary conditions $u_1 = 0$, $\partial_n u_2 = 0$ along both $[LO]$ and $[OB]$ (see Fig. 8). Combined with the condition $\psi = 0$ along $[LB]$ derived in the main text, they define a basis of stationary states related to Representation E. For each of the twice-degenerate energy levels, $\psi_+(\mathbf{r})$ is given by Eq. (A4) and the second basis function is $\psi_+^*(\mathbf{r})$.

c. Spatial extent of the wave functions

For a given energy level ϵ, the spatial extent of the stationary states defined in Secs. A 2 a and A 2 b barely exceeds the classically accessible region (limited by the dotted golden line in Fig. 8 for the Hamiltonian $H_{2\mathrm{D}}$ of the main text and $\epsilon = 7C_6/R^6$). Therefore, we restrict the region within which we solve for the wave functions to a part of the triangle OLB which slightly exceeds this region. In other words, we enforce the condition $\psi = 0$ not on $[LB]$, but on the horizontal dashed line in Fig. 8.

d. Indices of the quantum states

We order the quantum states pertaining to a given irreducible representation ρ by increasing energies. This gives rise to the state index $\nu^{(\rho)}$ appearing in Figs. 4 and 5 in the main text, and Figs. 6 and 7 in the present Appendix. The irreducible representations A_1 and A_2 have dimension 1, so that, barring accidental degeneracies, the corresponding energy levels are nondegenerate. By contrast, the irreducible representation E has dimension 2, meaning that each energy level is twice degenerate. For this representation, we consistently indicate one half of the state index, $\nu^{(E)}/2$, and one half of the density of states contribution $\Delta n_B^{(E)}/2$.

The relative level indices $\Delta\nu^{(\rho)}$ given in Fig. 5 of the main text and in Fig. 7 of this Appendix are exact. The level indices of Fig. 6, concerning the Hénon–Heiles model, are also exact. We obtain approximations to the level indices of Fig. 4 in the main text, concerning three Rydberg atoms moving along a circle, using the semiclassical approximation to the density of states, accounting for the role of discrete spatial symmetries [66].

---

[1] A. Polkovnikov, K. Sengupta, A. Silva, and M. Vengalattore, Rev. Mod. Phys. **83**, 863 (2011).

[2] B. Sutherland, *Beautiful Models* (World Scientific, Singapore, 2004).

[3] D. A. Abanin, E. Altman, I. Bloch, and M. Serbyn, Rev. Mod. Phys. **91**, 021001 (2019).

[4] C. Gross and I. Bloch, Science **357**, 995 (2017).

[5] Q. Zhu, Z. H. Sun, M. Gong, F. Chen, Y. R. Zhang, Y. Wu, Y. Ye, C. Zha, S. Li, S. Guo, H. Qian, H. L. Huang, J. Yu, H. Deng, H. Rong, J. Lin, Y. Xu, L. Sun, C. Guo, N. Li, F. Liang, C. Z. Peng, H. Fan, X. Zhu, and J. W. Pan, Phys. Rev. Lett. **128**, 160502 (2022).

[6] F. Alet and N. Laflorencie, C. R. Phys. **19**, 498 (2018).

[7] R. Blümel and W. P. Reinhardt, *Chaos in Atomic Physics* (Cambridge University Press, Cambridge, UK, 1997).

[8] H. Friedrich and D. Wintgen, Phys. Rep. **183**, 37 (1989).

[9] M. Courtney, N. Spellmeyer, H. Jiao, and D. Kleppner, Phys. Rev. A **51**, 3604 (1995).

[10] A. Browaeys and T. Lahaye, Nat. Phys. **16**, 132 (2020).

[11] M. Saffman, T. G. Walker, and K. Mølmer, Rev. Mod. Phys. **82**, 2313 (2010).

[12] H. Bernien, S. Schwartz, A. Keesling, H. Levine, A. Omran, H. Pichler, S. Choi, A. S. Zibrov, M. Endres, M. Greiner, V. Vuletić, and M. D. Lukin, Nature (London) **551**, 579 (2017).

[13] C. J. Turner, A. A. Michailidis, D. A. Abanin, M. Serbyn, and Z. Papić, Nat. Phys. **14**, 745 (2018).

[14] M. Serbyn, D. A. Abanin, and Z. Papić, Nat. Phys. **17**, 675 (2021).

[15] E. J. Heller, Phys. Rev. Lett. **53**, 1515 (1984).

[16] J. Stein and H. J. Stöckmann, Phys. Rev. Lett. **68**, 2867 (1992).

[17] M. Berry, Proc. R. Soc. London, Ser. A **423**, 219 (1989).

[18] E. J. Heller, *The Semiclassical Way to Physics and Spectroscopy* (Princeton University Press, Princeton, New Jersey, USA, 2018).

[19] P. N. Jepsen, Y. K. Lee, H. Liu, I. Dimitrova, Y. Margalit, W. W. Ho, and W. Ketterle, Nat. Phys. **18**, 899 (2022).

[20] K. Furuya, M. A. M. D. Aguiar, C. H. Lewenkopf, and M. C. Nemes, Ann. Phys. (NY) **216**, 313 (1992).

[21] S. Pilatowsky-Cameo, D. Villaseñor, M. A. Bastarrachea-Magnani, S. Lerma-Hernández, L. F. Santos, and J. G. Hirsch, Nat. Commun. **12**, 852 (2021).

[22] S. Moudgalya, B. A. Bernevig, and N. Regnault, Rep. Prog. Phys. **85**, 086501 (2022).

[23] G. Su, H. Sun, A. Hudomal, J. Desaules, Z. Zhou, B. Yang, J. C. Halimeh, Z. Yuan, Z. Papić, and J. Pan, arXiv:2201.00821.

[24] W. W. Ho, S. Choi, H. Pichler, and M. D. Lukin, Phys. Rev. Lett. **122**, 040603 (2019).

[25] C. J. Turner, J. Y. Desaules, K. Bull, and Z. Papić, Phys. Rev. X **11**, 021021 (2021).

[26] A. A. Michailidis, C. J. Turner, Z. Papić, D. A. Abanin, and M. Serbyn, Phys. Rev. X **10**, 011055 (2020).

[27] P. N. Jepsen, W. W. Ho, J. Amato-Grill, I. Dimitrova, E. Demler, and W. Ketterle, Phys. Rev. X **11**, 041054 (2021).

[28] V. Popkov, X. Zhang, and A. Klümper, Phys. Rev. B **104**, L081410 (2021).

[29] D. Barredo, V. Lienhard, P. Scholl, S. de Léséleuc, T. Boulier, A. Browaeys, and T. Lahaye, Phys. Rev. Lett. **124**, 023201 (2020).

[30] R. G. Cortiñas, M. Favier, B. Ravon, P. Méhaignerie, Y. Machu, J. M. Raimond, C. Sayrin, and M. Brune, Phys. Rev. Lett. **124**, 123201 (2020).

[31] M. C. Gutzwiller, *Chaos in Classical and Quantum Mechanics* (Springer, New York, USA, 1990).

[32] E. J. Heller, *Les Houches Session LII (1989): Chaos and Quantum Physics*, edited by M. J. Giannoni, A. Voros, and J. Zinn-Justin (Elsevier, Amsterdam, The Netherlands, 1991).

[33] S. Choi, C. J. Turner, H. Pichler, W. W. Ho, A. A. Michailidis, Z. Papić, M. Serbyn, M. D. Lukin, and D. A. Abanin, Phys. Rev. Lett. **122**, 220603 (2019).

[34] M. Hénon and C. Heiles, Astron. J. **69**, 73 (1964).

[35] M. A. Baranov, M. Dalmonte, G. Pupillo, and P. Zoller, Chem. Rev. (Washington, DC, US) **112**, 5012 (2012).

[36] T. L. Nguyen, J. M. Raimond, C. Sayrin, R. Cortiñas, T. Cantat-Moltrecht, F. Assemat, I. Dotsenko, S. Gleyzes, S. Haroche, G. Roux, T. Jolicoeur, and M. Brune, Phys. Rev. X **8**, 011032 (2018).

[37] A. J. Lichtenberg and M. A. Lieberman, *Regular and Stochastic Dynamics*, 2nd ed. (Springer, New York, USA, 1992).

[38] L. D. Faddeev and S. P. Merkuriev, *Quantum Scattering Theory for Several Particle Systems* (Springer, Dordrecht, The Netherlands, 1993).

[39] *International Tables for Crystallography Volume A: Space-Group Symmetry*, edited by T. Hahn (Springer, Dordrecht, The Netherlands, 2005).

[40] L. D. Landau and E. M. Lifshitz, *Quantum Mechanics, Non-Relativistic Theory* (Butterworth-Heinemann, Oxford, UK, 1977).

[41] M. Baranger, K. T. R. Davies, and J. H. Mahoney, Ann. Phys. (NY) **186**, 95 (1988).

[42] K. T. R. Davies, T. E. Huston, and M. Baranger, Chaos **2**, 215 (1992).

[43] D. J. Papoular and B. Zumer, in preparation (2023).

[44] A. Ozorio de Almeida, *Hamiltonian Systems: Chaos and Quantization* (Cambridge University Press, Cambridge, UK, 1988).

[45] J. P. Keating and S. D. Prado, Proc. R. Soc. London, Ser. A **457**, 1855 (2001).

[46] S. D. Prado, E. Vergini, R. M. Benito, and F. Borondo, Europhys. Lett. **88**, 40003 (2009).

[47] A. A. Zembekov, F. Borondo, and R. M. Benito, J. Chem. Phys. **107**, 7934 (1997).

[48] F. G. Gustavson, Astron. J. **71**, 670 (1966).

[49] V. I. Arnold, *Mathematical Methods of Classical Mechanics*, 2nd ed. (Springer, New York, USA, 1989).

[50] O. Bohigas, S. Tomsovic, and D. Ullmo, Phys. Rep. **223**, 43 (1993).

[51] M. D. Feit, J. A. Fleck, J. A. Fleck, Jr., and A. Steiger, J. Comput. Phys. **47**, 412 (1982).

[52] M. Brack, R. K. Bhaduri, J. Law, C. Maier, and M. V. N. Murthy, Chaos **5**, 317 (1998).

[53] F. Hecht, J. Numer. Math. **20**, 251 (2012).

[54] J. M. Robbins, Phys. Rev. A **40**, 2128 (1989).

[55] B. Lauritzen, Phys. Rev. A **43**, 603 (1991).

[56] M. Brune and D. J. Papoular, Phys. Rev. Res. **2**, 023014 (2020).

[57] L. Amico, D. Anderson, M. Boshier, J.-P. Brantut, L.-C. Kwek, A. Minguzzi, and W. von Klitzing, Rev. Mod. Phys. **94**, 041001 (2022).

[58] S. E. Anderson, K. C. Younge, and G. Raithel, Phys. Rev. Lett. **107**, 263001 (2011).

[59] P. Scholl, H. J. Williams, G. Bornet, F. Wallner, D. Barredo, L. Henriet, A. Signoles, C. Hainaut, T. Franz, S. Geier, A. Tebben, A. Salzinger, G. Zürn, T. Lahaye, M. Weidemüller, and A. Browaeys, PRX Quantum **3**, 020303 (2022).

[60] D. Bluvstein, A. Omran, H. Levine, A. Keesling, G. Semeghini, S. Ebadi, T. T. Wang, A. A. Michailidis, N. Maskara, W. W. Ho, S. Choi, M. Serbyn, M. Greiner, V. Vuletić, and M. D. Lukin, Science **371**, 1355 (2021).

[61] A. Hudomal, J. Y. Desaules, B. Mukherjee, G. X. Su, J. C. Halimeh, and Z. Papić, Phys. Rev. B **106**, 104302 (2022).

[62] L. D. Landau and E. M. Lifshitz, *Mechanics*, 3rd ed. (Butterworth-Heinemann, Oxford, UK, 1976).

[63] D. V. Else, C. Monroe, C. Nayak, and N. Y. Yao, Annu. Rev. Condens. Matter Phys. **11**, 467 (2020).

[64] M. Brack and R. K. Bhaduri, *Semiclassical Physics* (Addison-Wesley, Reading, Massachusetts, USA, 1997).

[65] M. J. David and E. J. Heller, J. Chem. Phys. **71**, 3383 (1979).

[66] B. Lauritzen and N. D. Whelan, Ann. Phys. (NY) **244**, 112 (1995).

arXiv:2404.18265v1 [quant-ph] 28 Apr 2024

Quantum signatures of the mixed classical phase space for three interacting particles in a circular trap

D.J. Papoular* and B. Zumer
LPTM, UMR 8089 CNRS & CY Cergy Paris Université, Cergy–Pontoise, France

(Dated: April 30, 2024)

We study theoretically two consequences of the mixed classical phase space for three repulsively–interacting bosonic particles in a circular trap. First, we show that the energy levels of the corresponding quantum system are well described by a Berry–Robnik distribution. Second, we identify stationary quantum states whose density is enhanced along the stable classical periodic trajectories, and calculate their energies and wavefunctions using the semiclassical Einstein–Brillouin–Keller (EBK) theory. Our EBK results are in excellent agreement with our full–fledged finite–element numerics. We discuss the impact of discrete symmetries, including bosonic exchange symmetry, on these classically localized states. They are within experimental reach, and occur in the same range of energies as the quantum scar reported in our previous work [Phys. Rev. A **107**, 022217 (2023)].

I. INTRODUCTION

The suppression of ergodicity in quantum systems has long been under intense scrutiny [1, chap. 8], and atomic systems are very well suited to its investigation Refs. [2, chap. 4]. The mechanisms leading to it in many–body systems, relying on e.g. integrability [3], the presence of disorder [4], many–body scarring [5, 6], or periodic driving [7], hold promises for quantum information processing over long times, but may hinder cooling mechanisms [8].

In the case of Hamiltonian systems, comparing the quantum system to its classical analog has been very fruitful in identifying such mechanisms [9]. Most classical systems have a mixed phase space hosting both ergodic and non–ergodic trajectories. Ergodic trajectories densely cover a substantial fraction of the energy surface; non–ergodic ones wind around tori found within the Kolmogorov–Arnold–Moser (KAM) regions of phase space, well described using KAM theory [10, appendix 8]. Ergodicity in the quantum system may be suppressed in a phase space region corresponding to classical ergodic motion, e.g. by a quantum scar [11]. The quantum system is also known to exhibit regular levels reflecting the classical non–ergodic trajectories [9, Sec. 4]. These levels may be studied using the semiclassical Einstein–Brillouin–Keller (EBK) theory [12, 13]. In contrast to the semiclassical approaches applicable to the classically chaotic region, which mainly provide information concerning the density of states [14, chap. 17], EBK theory applied to the classical KAM regions yields both quantum energy eigenvalues and eigenfunctions constructed from classically non–ergodic trajectories. The full energy spectrum, including both the regular levels to which EBK theory applies and the remaining levels related to chaotic dynamics [9, Sec. 5], exhibits energy level statistics which significantly deviate [15, 16] from both the Poisson and Wigner distributions respectively associated with classical integrability and chaos [14, chap. 16].

Mixed classical phase spaces are relevant for the description of many–body systems. The many–body scar affecting the spin dynamics of a Rydberg atom chain observed in Ref. [5] provides a recent example. The classical analog system, whose construction is involved [17], exhibits mixed phase space, and KAM regions play a key role in the many–body quantum revivals [18]. Motivated by these recent developments, we introduced in our previous article [19] the system of three interacting particles in a circular trap. We analyzed this experimentally accessible system through well–established theories applied to a phase space whose dimension matches the number of independent parameters introduced in Ref. [18], and identified a quantum scar affecting the motion of the atoms.

In this paper, we analyze the role of its mixed classical phase space. First, we show that the parameters we investigated in Ref. [19] fall within a range where the quantum energy level statistics are well described by the Berry–Robnik distribution [16]. Then, we identify quantum states whose probability density is enhanced near stable classical periodic trajectories. Using EBK theory, we characterize their energy eigenvalues and explicitly construct their wavefunctions. Our results are in excellent agreement with our full–fledged numerical solution of the Schrödinger equation using the finite–element method. We highlight the role of discrete symmetries, including bosonic echange symmetry, and their observable consequence, on the energies and wavefunctions of the considered localized states.

We formulate our analysis in terms of trapped Rydberg atoms, made accessible by recent experimental advances [20, 21]. However, similar phenomena are expected to occur with systems of magnetic atoms [22] or polar molecules [23] exhibiting the same symmetries. The classically–localized states [24, chap. 22] identified in the present paper occur for the same parameters and energy range as the previously identified quantum scar [19]. One may address one effect or the other simply by changing the initial condition defining the atomic motion. Hence, the simple, well–controlled atomic system we are proposing offers an opportunity for a detailed experimental comparison of the two effects.

---

* Electronic address: david.papoular@cyu.fr

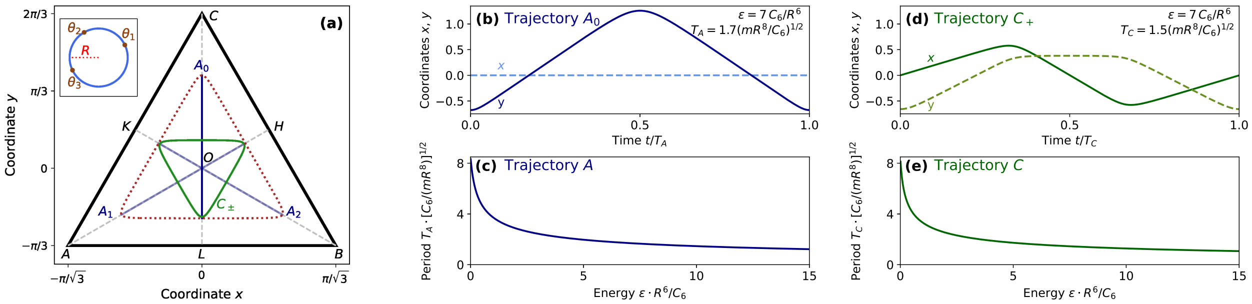

FIG. 1. *(a)* The periodic trajectories A_0, A_1, A_2 (straight blue lines) and C_+, C_- (the closed green trajectory is followed anticlockwise for C_+ and clockwise for C_-), shown in the (x, y) plane for the energy $\epsilon = 7C_6/R^6$. The dotted brown line shows the classically accessible region. The inset shows the considered physical system: three interacting particles in a circular trap. *(b)* Periodic trajectory A_0 as a function of time for $\epsilon = 7C_6/R^6$ in terms of its coordinates $x(t)$ (solid line) and $y(t)$ (dashed line). *(c)* Period $T_A(\epsilon)$ of trajectory A as a function of the energy ϵ. Panels *(d)* and *(e)* show the corresponding quantities for trajectory C_+. Trajectories A and C are stable for the considered range of energies.

The paper is organized as follows. In Sec. II, we introduce the considered system, and briefly summarize its properties described in detail in our previous article [19]. In Sec. III, we show that its quantum energy levels are well represented by the Berry–Robnik distribution. In Sec. IV, we apply EBK theory to identify the energy levels for the quantum states localized near stable periodic trajectories and construct the corresponding EBK wavefunctions, and we compare them to our finite–element numerical results. In Sec. V, we discuss experimental prospects. The article ends with the conclusive Sec. VI.

II. THE CONSIDERED SYSTEM

The system we analyze has been introduced in our previous article [19]. We briefly summarize its key features.

We consider three identical bosonic particles of mass m in a circular trap of radius R (Fig. 1(a),inset). We assume that the interaction $v(d_{ij})$ between the particles i and j only depends on their distance $d_{ij} = 2R|\sin[(\theta_i - \theta_j)/2]|$. For circular Rydberg atoms whose electronic angular momenta are perpendicular to the plane, $v(d_{ij}) = C_6/d_{ij}^6$ with $C_6 > 0$. We introduce the Jacobi coordinates $x = [(\theta_1 + \theta_2)/2 - \theta_3 + \pi]/\sqrt{3}$, $y = (\theta_2 - \theta_1)/2 - \pi/3$, $z = (\theta_1 + \theta_2 + \theta_3)/3 - 2\pi/3$, and their conjugate momenta p_x, p_y, p_z (which carry the unit of action). Then, the Hamiltonian reads $H = p_z^2/(3mR^2) + H_{\rm 2D}$, where

$$H_{\rm 2D} = \frac{p_x^2 + p_y^2}{4mR^2} + V(x, y) \ . \tag{1}$$

Here, $V(x, y) = v(x, y)\, C_6/R^6$, with

$$\begin{aligned} v(x, y) = {} & [\sin^{-6}(\pi/3 + y) + \sin^{-6}(\pi/3 + x\sqrt{3}/2 - y/2) \\ & + \sin^{-6}(\pi/3 - x\sqrt{3}/2 - y/2)]/64 - 1/9, \end{aligned} \tag{2}$$

energies being measured from the minimum $V(\mathbf{0})$. The Hamiltonian H may be understood as describing either a classical system or its quantum counterpart. It is invariant under the point group C_{3v}, generated by the rotation of order 3 about the axis $(x = y = 0)$ and the reflection in the plane $(x = 0)$. The free motion of the coordinate z reflects the conservation of the total angular momentum p_z. Once the latter is fixed, the system is reduced to an effective point in the two–dimensional (2D) plane (x, y) within the equilateral triangle ABC of Fig. 1(a), in the presence of the potential $V(x, y)$.

From the quantum point of view, we seek the 3–atom eigenstates of H in the form $\Psi_n(\theta_1, \theta_2, \theta_3) = \psi_n(\boldsymbol{r})\, e^{inz}$, where $\boldsymbol{r} = (x, y)$, and n is an integer setting the value of the quantized angular momentum p_z. The wavefunction $\psi_n(\boldsymbol{r})$ is fully determined by its values within the triangle ABC and vanishes along AB, BC, and CA. The constraint $\Psi_n(\theta_1, \theta_2, \theta_3) = \Psi_n(\theta_3 - 2\pi, \theta_1, \theta_2)$, combining bosonic symmetry and angular periodicity, yields:

$$\psi_n(\mathcal{R}\boldsymbol{r}) = \psi_n(\boldsymbol{r})\, e^{2in\pi/3} \ , \tag{3}$$

where $\mathcal{R}$ is the rotation of angle $2\pi/3$ about O in the (x, y) plane. We sort the energy levels in terms of the three irreducible representations A_1, A_2, E of C_{3v}. Owing to Eq. (3), wavefunctions pertaining to the one–dimensional (1D) representations A_1 or A_2 have $n = 0$ modulo 3, whereas those pertaining to the 2D representation E have $n \neq 0$ modulo 3.

As in Ref. [19], we set the ratio $\eta = \hbar R^2/(mC_6)^{1/2}$ to 0.01, and we consider energies $\epsilon \sim 7C_6/R^6$.

III. MIXED CLASSICAL PHASE SPACE AND QUANTUM ENERGY LEVEL STATISTICS

A. Classical periodic trajectories

We have characterized the periodic trajectories of the model of Eq. (1) using our own C++ implementation of the numerical approach of Ref. [25]. We find three families of periodic trajectories existing for all energies

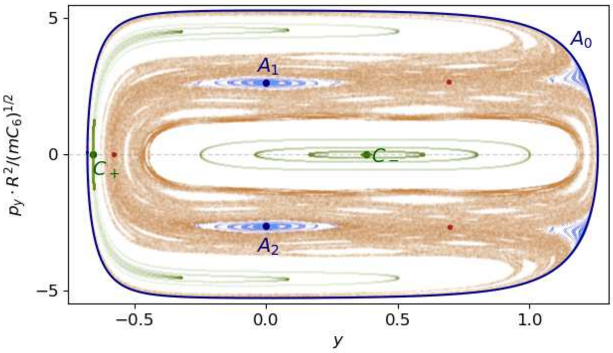

FIG. 2. Surface of section for Eq. (2), with $p_z = 0$, $\epsilon = 7C_6/R^6$, $x = 0$, and $p_x > 0$. The periodic trajectory A_0 appears as the dark blue closed boundary of the figure. All other periodic trajectories appear as fixed points, shown in dark blue for A_1 and A_2; dark red for B_1, B_2, and B_3; and dark green for C_+ and C_-. The stable trajectories A_i and C_j are surrounded by (light blue and light green) tori; no tori are present near the unstable trajectories B_k. The ≈ 287000 thin brown dots all belong to the same ergodic trajectory.

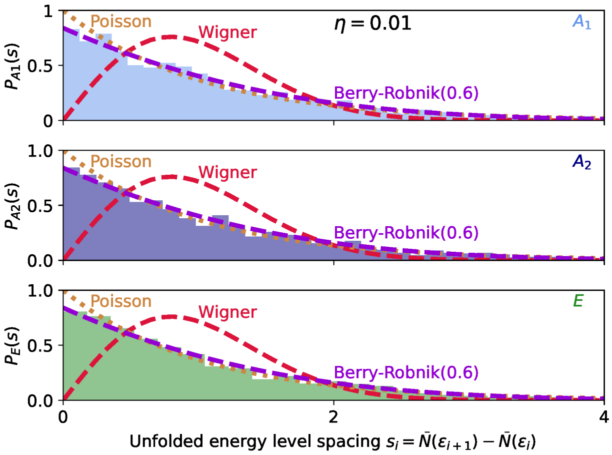

FIG. 3. The histograms show the distribution of unfolded energy level spacings $s_{r,i} = \bar{N}_r(\epsilon_i + 1) - \bar{N}_r(\epsilon_i)$ for states belonging to the three irreducible representations $r = A_1$ (top), A_2 (center), E (bottom), which are analyzed separately. They differ from the Poisson (dotted golden line) and Wigner (dashed red line). They are well represented by the Berry–Robnik distribution, assuming a single chaotic region in phase space, with parameter $\rho_1 = 0.6$ for all three representations.

$\epsilon > 0$: we label them A, B, C in analogy with those of the Hénon–Heiles potential [26]. We have analyzed the unstable trajectories of family B (i.e their Lyapunov exponent > 0), along with the quantum scar it yields, in our previous article [19]. By contrast, the trajectories of families A and C are stable for all considered energies (i.e. their Lyapunov exponents $= 0$).

For a given energy ϵ, family A contains three straight–line trajectories A_0, A_1, A_2, which follow the medians of the triangular configuration space, and transform into one another under rotations of order 3. Family C contains two trajectories C_+ and C_-, which are closed loops around the center O: C_+ is followed anticlockwise and C_- clockwise, and they transform into each other under reflections about any of the three medians. All five trajectories are represented in the (x, y) plane on Fig. 1(a). The vertical trajectory A_0 and the trajectory C_+ are shown as functions of time on Figs. 1(b, d). Trajectories of a given family have the same period as a function of energy $T_A(\epsilon)$ and $T_C(\epsilon)$: these are plotted on Figs. 1(c, e) and are both of the order of $(mR^8/C_6)^{1/2}$ for $\epsilon \sim 7C_6/R^6$.

The simultaneous existence of stable and unstable periodic trajectories signals that the classical system represented by H_{2D} is neither integrable nor fully chaotic: its phase space is mixed. This is apparent on the surface of section of Fig. 2 [19]. There, the non–ergodic trajectories are represented by the closed blue and green curves, which are sections in the two–dimensional plane of the KAM tori [10, appendix 8] surrounding the stable trajectories A and C. We numerically find that the fraction of the surface of section not occupied by tori is densely covered by the intersections from a single ergodic trajectory, comprising the single ergodic zone visible on Fig. 2, within which lie the 3 unstable trajectories of family B.

B. Quantum energy level statistics

The quantum spectra of systems with mixed classical phase space satisfy neither the Poisson nor the Wigner distribution [14, Sec. 16.8]. We now verify this for the model of Eq. (2), and show that its energy level statistics are well represented by a Berry–Robnik distribution [16].

We numerically solve the Schrödinger equation for the Hamiltonian of Eq. (1) using the finite–element software FreeFem [27]. We calculate stationary states belonging to the three irreducible representations A_1, A_2, E of the point group C_{3v} separately. We exploit discrete symmetries to reduce the configuration space to a triangle which slightly exceeds 1/6 of the classically accessible region for a given energy: details are given in our previous paper [19, Appendix 2]. We use a triangular mesh comprising 1000 vertices along each edge. We thus numerically obtain the energies and wavefunctions for slightly more than 1200 consecutive energy levels for Representation A_1, 1200 levels for Representation A_2, and 1700 non–degenerate levels for Representation E, in energy windows centered on $7C_6/R^6$.

For each irreducible representation $r = A_1$, A_2, and E of C_{3v}, we introduce the integrated density of states $N_r(\epsilon)$, which is the staircase–like function giving the number of stationary quantum states whose energies are smaller than ϵ [14, Sec. 16.2]. We describe its smooth component $\bar{N}_r(\epsilon)$ through its Weyl expansion, accounting for discrete symmetries [28]. We retain the leading–order term, proportional to $1/\hbar^2$, and the first correction, proportional to $1/\hbar$. We calculate the spacings $s_{r,i} = \bar{N}_r(\epsilon_i + 1) - \bar{N}_r(\epsilon_i)$ between consecutive 'unfolded' energies $\bar{N}_r(\epsilon_i)$ [9, Sec. 5.4]. We plot their distribution on Fig. 3, where it is seen to differ from both the Poisson and the Wigner distributions [14, Secs. 16.3 & 16.4], as expected for a system with mixed classical phase space.

Figure 3 shows that the distribution of unfolded energy level spacings is well represented by the Berry–Robnik distribution [16], assuming that a single chaotic region in phase space contributes to the statistics, with the same parameter $\rho_1 = 0.6$ for all three representations. Both the assumption of a single chaotic region and the value $\rho_1 = 0.6$, representing the fraction of the energy surface over which motion is regular, are compatible with the surface of section of Fig. 2. The applicability of the Berry–Robnik distribution hinges on the statistical independence of the regular and chaotic sequences of levels. Counter–examples have been identified, e.g. the hydrogen atom in a magnetic field [29], and its numerical verification with billiards requires reaching the deep semiclassical limit [30]. By contrast, our result provides a realization of the Berry–Robnik distribution in an experimentally accessible system involving smooth interatomic interactions rather than sharp billiard walls.

IV. QUANTUM STATIONARY STATES LOCALIZED NEAR THE CLASSICALLY STABLE PERIODIC TRAJECTORIES *A* AND *C*

For the majority of the stationary quantum states of the Hamiltonian $H_{2\mathrm{D}}$ that we have obtained numerically, the probability density $|\psi(x, y)|^2$ is not directly related to the periodic trajectories of types A and C. Nevertheless, we find multiple eigenstates whose probability density is enhanced along one or the other of these trajectories. Figures 6(a,b) and 7(a,b) illustrate this phenomenon for trajectories A and C, respectively: in each case, we show the probability density for the quantum states closest to the energy $\epsilon = 7C_6/R^6$. This phenomenon superficially resembles the quantum scars stemming from trajectory B which we have identified in our previous article [19]. However, the quantum states we consider in the present article do not satisfy Heller's definition for a quantum scar [24, chap. 22]. Indeed, in stark contrast to the classically unstable trajectory B, trajectories A and C are both classically stable. Hence, quantum mechanics yields no qualitative change in the behavior of the system in their vicinity. In this section, we illustrate this statement with two results. First, calculating the energies of the quantum states related to trajectories A and C semiclassically, we justify that they obey selection rules which we entirely explain in terms of the symmetries of the classical KAM tori. Second, we construct semiclassical wavefunctions for these quantum states. Our semiclassical results for both the energies and the wavefunctions are in excellent agreement with our full quantum calculation.

A. Symmetries of the regular classical trajectories

We first consider the regular classical trajectories in the KAM regions of phase space surrounding the stable periodic trajectories of families A and C. Our numerical results show that the tori lying close to the periodic trajectories inherit the discrete symmetry properties of the corresponding periodic trajectories, namely: *(i)* A torus T_A near the periodic trajectory of type A invariant under the reflection $\mathcal{S}$ exhibits reflection symmetry, i.e. if the point $(\boldsymbol{r}, \boldsymbol{p})$ belongs to T_A, then so does $(\mathcal{S}\boldsymbol{r}, \mathcal{S}\boldsymbol{p})$; *(ii)* A torus T_C near a periodic trajectory of type C is invariant under rotations $\mathcal{R}$ of order 3, i.e. if the point $(\boldsymbol{r}, \boldsymbol{p})$ belongs to T_C, then so does $(\mathcal{R}\boldsymbol{r}, \mathcal{R}\boldsymbol{p})$.

We justify properties *(i)* and *(ii)* through the following argument. We rely on an approximation introduced in Ref. [9, Sec. 4.1]: we ignore narrow instability subregions and approximate the whole KAM region by a set of concentric tori. Our numerical results for the surface of section, shown on Fig. 2, confirm that it is very well satisfied for the inner tori, close to the periodic trajectories, which are of interest in this work (it breaks down for the outer tori in the vicinity of the ergodic zone, which we do not consider). This allows for the introduction of local action–angle coordinates, valid within this region. These are defined through the consistent choice of fundamental frequencies $\boldsymbol{\omega} = (\omega_1, \omega_2)$ [31, Sec. III.E] on each torus within the region. Then, any conditionally–periodic trajectory $(\boldsymbol{r}(t), \boldsymbol{p}(t))$ winding around one such torus may be written as a Fourier series [32, §52]:

$$\boldsymbol{r}(t) = \sum_{\boldsymbol{k}} \boldsymbol{r}_{\boldsymbol{k}} \exp(i\boldsymbol{k} \cdot \boldsymbol{\omega} t), \quad \boldsymbol{p}(t) = 2mR^2 d\boldsymbol{r}/dt \ , \tag{4}$$

the sum being taken over all integer pairs $\boldsymbol{k} = (k_1, k_2)$. The considered torus is uniquely determined by its actions $\boldsymbol{J} = (J_1, J_2)$, which are given by [33]:

$$J_\alpha = \sum_{\alpha'=1,2} \sum_{\boldsymbol{k}} k_\alpha |\boldsymbol{r}_{\boldsymbol{k}}|^2 k_{\alpha'} \omega_{\alpha'} \ . \tag{5}$$

Let us justify statement *(ii)*, concerning tori in the vicinity of a periodic trajectory of type C. We consider a point $(\boldsymbol{r}, \boldsymbol{p})$ belonging to the KAM region surrounding trajectory C_+, and the rotated point $(\boldsymbol{r}', \boldsymbol{p}')$ with $\boldsymbol{r}' = \mathcal{R}_{2\pi/3}\boldsymbol{r}$ and $\boldsymbol{p}' = \mathcal{R}_{2\pi/3}\boldsymbol{p}$. Trajectory C_+ is invariant under rotations of order 3, so that $(\boldsymbol{r}', \boldsymbol{p}')$ also belongs to the same KAM region. We compare the two trajectories $(\boldsymbol{q}(t), \boldsymbol{p}(t))$ and $(\boldsymbol{q}'(t), \boldsymbol{p}'(t))$ obtained from the initial conditions $(\boldsymbol{r}, \boldsymbol{p})$ and $(\boldsymbol{r}', \boldsymbol{p}')$. Their Fourier components $\boldsymbol{r}_{\boldsymbol{k}}$ and $\boldsymbol{r}'_{\boldsymbol{k}}$, defined by Eq. (4), satisfy $\boldsymbol{r}'_{\boldsymbol{k}} = \mathcal{R}_{2\pi/3}\boldsymbol{r}_{\boldsymbol{k}}$, so that $|\boldsymbol{r}'_{\boldsymbol{k}}| = |\boldsymbol{r}_{\boldsymbol{k}}|$. According to Eq. (5), the actions J_α only depend on the modulus $|\boldsymbol{r}_{\boldsymbol{k}}|$, hence, they are the same for both trajectories. Therefore, the points $(\boldsymbol{r}, \boldsymbol{p})$ and $(\boldsymbol{r}', \boldsymbol{p}')$ belong to the same torus T_{C_+}. Statement *(i)* may be justified similarly.

B. EBK quantization: energy levels

In this section, we obtain semiclassical predictions for the energies of the quantum levels related to trajectories A and C, which are in excellent agreement with the values obtained through our numerical solution of the Schrödinger equation (see Figs. 4(b) and 5(c)). We also explain quasidegeneracies and derive selection rules, both of which are direct consequences of the discrete symmetries of the KAM tori presented in Sec. IV A above.

Our semiclassical description relies on Einstein–Brillouin–Keller (EBK) theory [12], accounting for the Maslov phase corrections [34, §7]. This theory generalizes the Wentzel–Kramers–Brillouin approach [35, §48] to the quantization of regular classical motion with more than one degree of freedom [13]. We use our own implementation as a Python script of the EBK approach, based on Refs. [31, 36], which hinges on the representation of conditionally–periodic motion in terms of the Fourier series of Eq. (4). We integrate classical trajectories over time intervals of lengths up to $t_{\max} = 3700(mR^8/C_6)^{1/2}$ and keep up to 3200 terms in Eq. (4).

We now characterize the quantum stationary states localized near the classically stable trajectories A and C. In Sections IV B 1 and IV B 2 below, we derive the EBK energies for these states, considered as eigenstates of $H_{2\mathrm{D}}$, whose wavefunctions depend on $\boldsymbol{r} = (x, y)$. In Section IV B 3, we analyze the role of angular momentum so as to discuss the stationary states of the three–particle Hamiltonian H, whose wavefunctions depend on (x, y, z).

1. *Quantum states localized near trajectory A*

For a given energy ϵ, the three periodic trajectories A_0, A_1, and A_2 (see Fig. 1(a)) and the tori surrounding them are mapped one onto the other through the rotations $\mathcal{R}$ and $\mathcal{R}^{-1}$. Hence, we focus on the vertical trajectory A_0. In Eq. (4), we choose the fundamental frequencies $\boldsymbol{\omega} = (\omega_1, \omega_2)$ as in Ref. [31, Fig. 8(b)]. This leads to the independent circuits $\mathcal{C}_x$ and $\mathcal{C}_y$ on Fig. 4(a). Calculating their Maslov indices [13, Sec. II.C], we obtain the EBK quantization condition for the tori near trajectory A:

$$I_x = \hbar(\nu_x + 1/2) \text{ and } I_y = \hbar(\nu_y + 1) \ , \qquad (6)$$

where $I_{x,y}$ are the action integrals for the circuits $\mathcal{C}_{x,y}$, $\hbar$ is the reduced Planck's constant, and the integers $\nu_{x,y} \geq 0$ are the EBK quantum numbers. The action $I_x \geq \hbar/2$, so that the periodic trajectory A_0 itself does not satisfy Eq. (6). The tori satisfying Eq. (6) which are closest to trajectory A_0 are those with $\nu_x = 0$: the corresponding energies within a window centered on $\epsilon = 7C_6/R^6$ are shown on the top line of Fig. 4(b). We compare them to the energies of the stationary quantum states of $H_{2\mathrm{D}}$ belonging to representations A_1 and E localized near the trajectories A_0, A_1, and A_2, obtained through our finite–element calculations (see Fig. 6(a,b)). These are shown on Fig. 4(b), middle and bottom lines, and are in excellent agreement with the EBK results.

Figure 4(b) reveals that each EBK energy corresponds to quasidegenerate quantum states pertaining to representations A_1 and E. Furthermore, no quantum stationary states pertaining to representation A_2 exhibit density profiles similar to Fig. 6(a,b). Both of these properties follow from the symmetries of the regular trajectories identified in Sec. IV A above, through a mechanism identified in Refs. [37] and [9, Sec. 4.2] in the case where the discrete symmetry at play had order 2. The system we consider provides examples of the same phenomenon involving C_{3v} symmetry, as we now show.

We consider the EBK wavefunction $\psi_{\mathrm{EBK}}(\boldsymbol{r})$, corresponding to a torus in the vicinity of trajectory A_0, with the energy ϵ_{EBK}, satisfying Eq. (6) with $\nu_x = 0$. This torus is invariant under the reflection $\mathcal{S}$ about the vertical axis $x = 0$. Therefore, as shown in [9, Sec. 4.2]:

$$\psi_{\mathrm{EBK}}(\mathcal{S}\boldsymbol{r}) = (-1)^{\nu_x}\psi_{\mathrm{EBK}}(\boldsymbol{r}) = \psi_{\mathrm{EBK}}(\boldsymbol{r}) \ . \qquad (7)$$

The EBK wavefunction ψ_{EBK} reflects the symmetry of the corresponding classical torus, but does not automatically satisfy the symmetry requirements of any representation. We now project it onto the irreducible representations [35, §94] A_1, A_2, and E. This yields three linearly independent wavefunctions, $\psi^{A_1}_{\mathrm{EBK}}$ and $\psi^{E,\pm}_{\mathrm{EBK}}$, pertaining to the representations A_1 and E, corresponding to the same semiclassical energy. In terms of kets $|\psi\rangle$, with $\langle \boldsymbol{r}|\mathcal{R}|\psi\rangle = \psi(\mathcal{R}^{-1}\boldsymbol{r})$ and $\langle \boldsymbol{r}|\mathcal{S}|\psi\rangle = \psi(\mathcal{S}\boldsymbol{r})$, they read:

$$\begin{cases} |\psi^{A_1}_{\mathrm{EBK}}\rangle & = \alpha_{A_1}(1 + \mathcal{R} + \mathcal{R}^{-1})\,|\psi_{\mathrm{EBK}}\rangle \\ |\psi^{E,+}_{\mathrm{EBK}}\rangle & = \alpha_E(1 + j^*\,\mathcal{R} + j\,\mathcal{R}^{-1})\,|\psi_{\mathrm{EBK}}\rangle \ , \\ |\psi^{E,-}_{\mathrm{EBK}}\rangle & = \alpha_E(1 + j\,\mathcal{R} + j^*\,\mathcal{R}^{-1})\,|\psi_{\mathrm{EBK}}\rangle \ , \end{cases} \qquad (8)$$

In Eq. (8), $\alpha_{A_1,E}$ are normalization coefficients, and $j = e^{2i\pi/3}$. We have used the relations $\mathcal{SRS} = \mathcal{R}^{-1}$ and Eq. (7). The states $|\psi^{A_1}_{\mathrm{EBK}}\rangle$ and $|\psi^{E,\pm}_{\mathrm{EBK}}\rangle$ satisfy $\mathcal{R}\,|\psi^{A_1}_{\mathrm{EBK}}\rangle = |\psi^{A_1}_{\mathrm{EBK}}\rangle$, $\mathcal{R}\,|\psi^{E,\pm}_{\mathrm{EBK}}\rangle = \pm j\,|\psi^{E,\pm}_{\mathrm{EBK}}\rangle$ and $|\psi^{E,-}_{\mathrm{EBK}}\rangle = \mathcal{S}\,|\psi^{E,+}_{\mathrm{EBK}}\rangle$. The component of ψ_{EBK} pertaining to representation A_2, proportional to $(1 + \mathcal{R} + \mathcal{R}^{-1})(1 - \mathcal{S})\,|\psi_{\mathrm{EBK}}\rangle$, is 0 because of Eq. (7).

2. *Quantum states localized near trajectory C*

We proceed as in Sec. IV B 1. For a given energy ϵ, the two periodic trajectories C_+ and C_- (see Fig. 1(a)) and the tori surrounding them are mapped onto each other through the reflection $\mathcal{S}$. Hence, we focus on the trajectory C_+. In Eq. (4), we choose the fundamental frequencies $\boldsymbol{\omega} = (\omega_1, \omega_2)$ as in Ref. [31, Fig. 8(a)], leading to the independent circuits $\mathcal{C}_r$ and $\mathcal{C}_l$ on Fig. 5(a). Calculating their Maslov indices, we obtain the EBK quantization condition for the tori near trajectory C:

$$I_r = \hbar(\nu_r + 1/2) \text{ and } I_l = \hbar(\nu_l + 1/2) \ , \qquad (9)$$

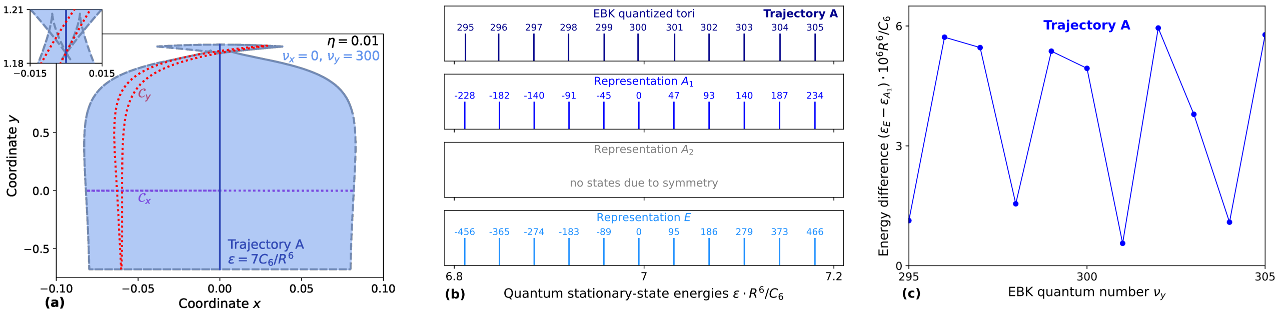

FIG. 4. *(a)* Classical trajectory A (solid dark blue) for the energy $\epsilon = 7C_6/R^6$, the nearest–energy trajectory satisfying Eq. (6) for $\eta = 0.01$ (densely covering the light blue area), and two independent circuits $\mathcal{C}_x$ (dotted purple) and $\mathcal{C}_y$ (dotted red) circling the torus, in terms of which the quantum numbers are $\nu_x = 0$ and $\nu_y = 300$. The dashed gray lines show the caustics of this trajectory. The top left inset zooms in on the narrow region near $(x = 0, y = 1.2)$ to reveal the self–intersection of the caustics. *(b)* Top panel: energies of the EBK wavefunctions for $\nu_x = 0$ and $295 \leq \nu_y \leq 305$. Center and bottom panels: energies of the corresponding quasidegenerate quantum stationary states belonging to representations A_1 (center) and E (bottom), obtained through our finite–element numerical calculations. Because of the torus symmetries, there are no states in representation A_2 corresponding to the EBK quantum numbers $(\nu_x = 0, \nu_y)$. The integers in the center and bottom panels specify the relative state indices within each representation, $\Delta\nu^{A_1}$ and $\Delta\nu^{E}/2$, with respect to the quantum state related to Trajectory A whose energy is closest to $7C_6/R^6$. *(c)* Small energy differences between the quasidegenerate states of representations A_1 and E.

where $I_{r,l}$ are the action integrals for the circuits $\mathcal{C}_{r,l}$, and the integers $\nu_{r,l} \geq 0$ are the EBK quantum numbers. The trajectory C_+ does not satisfy Eq. (9). The tori satisfying it which are closest to C_+ are those with $\nu_r = 0$: their energies are shown on the top line of Fig. 5(b). We compare them to the energies of the stationary quantum states of $H_{2\mathrm{D}}$ belonging to representations A_1, A_2, and E localized near the trajectories C_+ and C_-, obtained through our finite–element calculations (see Fig. 7(a,b)). These are shown on the three lower lines of Fig. 5(b), and are in excellent agreement with the EBK results.

Figure 5(b) shows that each EBK energy with $\nu_r = 0$ and $\nu_l = 0$ modulo 3 corresponds to two quasidegenerate quantum states pertaining to representations A_1 and A_2. By contrast, each EBK energy with $\nu_r = 0$ and $\nu_l \neq 0$ modulo 3 corresponds to two exactly degenerate quantum states spanning a representation E. As for the states localized near trajectory A (see Sec. IV B 1 above), these properties follow from the symmetries of the regular trajectories (Sec. IV A). These are different from the symmetries of the tori surrounding trajectory A, leading to different selection rules, which we now derive.

We consider the EBK wavefunction $\chi_{\mathrm{EBK}}(\boldsymbol{r})$, corresponding to a torus in the vicinity of trajectory C_+, with the energy ϵ_{EBK}, satisfying Eq. (9) with $\nu_r = 0$. This torus is invariant under the rotation $\mathcal{R}$. A straightforward generalization of the argument in Ref. [9, Sec. 4.2] to symmetry operations of order 3 leads to $\chi_{\mathrm{EBK}}(\mathcal{R}\boldsymbol{r}) = j^{\nu_l}\,\chi_{\mathrm{EBK}}(\boldsymbol{r})$. We now project χ_{EBK} onto the irreducible representations A_1, A_2, and E. For each ν_l, this yields two linearly independent, degenerate EBK wavefunctions. If $\nu_l = 0$ modulo 3, the non–vanishing wavefunctions pertain to representations A_1 and A_2:

$$|\chi_{\mathrm{EBK}}^{A_1,A_2}\rangle = \beta_{A_1,A_2}(1 \pm \mathcal{S})\,|\chi_{\mathrm{EBK}}\rangle \ , \qquad (10)$$

with β_{A_1,A_2} being two normalization factors, whereas the component along E vanishes. By contrast, if $\nu_l \neq 0$ modulo 3, the components along A_1 and A_2 vanish, whereas the two non–vanishing wavefunctions $|\chi_{\mathrm{EBK}}^{E,\pm}\rangle$ span a representation E. For $\nu_l = -1$ modulo 3, $|\chi_{\mathrm{EBK}}^{E,+}\rangle = |\chi_{\mathrm{EBK}}\rangle$ and $|\chi_{\mathrm{EBK}}^{E,-}\rangle = \mathcal{S}\,|\chi_{\mathrm{EBK}}\rangle$, and the opposite assignment holds for $\nu_l = +1$ modulo 3.

3. *The role of angular momentum*

To discuss the three–particle eigenstates of H in terms of the eigenstates of $H_{2\mathrm{D}}$ identified in Secs. IV B 1 and IV B 2, we now analyze the role of angular momentum.

We first consider quantum states localized near the periodic trajectories of family A. The two states $\psi_{\nu_y}^{E,\pm}(\boldsymbol{r})$ obtained for a given ν_y, are exactly degenerate eigenstates of $H_{2\mathrm{D}}$ which span a 2D representation E. However, in terms of three–atom eigenstates of H, the states $\psi_{\nu_y}^{E,\pm}(\boldsymbol{r})e^{inz}$ occur if the total angular momentum $n = \mp 1$ modulo 3 because of Eq. (3).

The states $\psi_{\nu_y}^{A_1}(\boldsymbol{r})$ and $\psi_{\nu_y}^{E,\pm}(\boldsymbol{r})$ obtained for a given ν_y belong to different representations A_1 and E. Their quasidegeneracy is lifted by small couplings neglected in the EBK approach [9, Sec. 4.5], and the small energy difference is resolved in our finite–element numerical results, as shown on Fig. 4(c). Because of Eq. (3), the three–atom states $\psi_{\nu_y}^{A_1}(\boldsymbol{r})e^{inz}$ occur if $n = 0$ modulo 3, so that none of the three states $\psi_{\nu_y}^{A_1,E\pm}(\boldsymbol{r})e^{inz}$ may occur for the same value of n. They do not reduce to an EBK wavefunction corresponding to a single classical trajectory. Instead, Eq. (8) shows that they represent coherent superpositions of the three atoms undergoing motion near the trajectories A_0, A_1, and A_2.

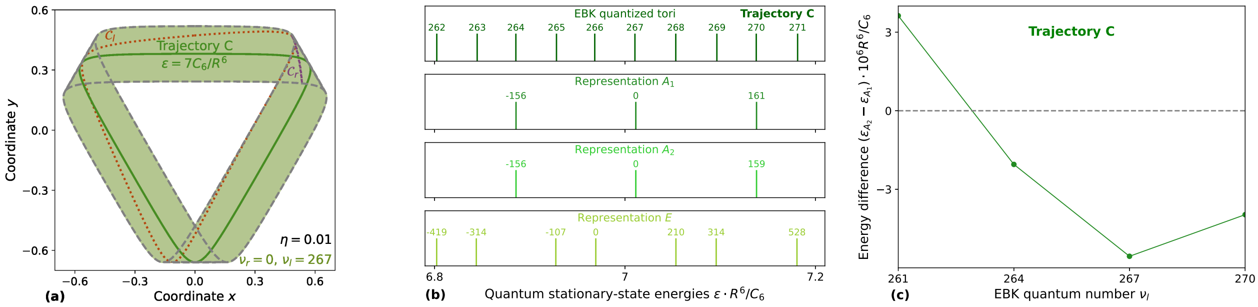

FIG. 5. *(a)* Classical trajectory C (solid dark green) for the energy $\epsilon = 7C_6/R^6$, the nearest–energy trajectory satisfying Eq. (9) for $\eta = 0.01$ (densely covering the light green area), and two independent circuits $\mathcal{C}_r$ (purple) and $\mathcal{C}_l$ (red) circling the torus, in terms of which the quantum numbers are $\nu_r = 0$, $\nu_l = 267$. The dashed gray lines show the caustics of this trajectory, which self–intersect in the top left, top right, and bottom regions. *(b)* Top panel: energies of the EBK wavefunctions for $\nu_r = 0$ and $262 \leq \nu_l \leq 271$. Three lower panels: energies of the corresponding quantum eigenstates belonging to representations A_1, A_2, and E, obtained through our finite–element numerical calculations. States in representations A_1 and A_2 exhibit quasidegeneracies and correspond to the EBK quantum numbers $\nu_r = 0$, $\nu_l = 0$ modulo 3; each EBK torus with quantum numbers $\nu_r = 0$, $\nu_l \neq 0$ modulo 3 yields two degenerate states in representation E. The integers specify the relative state indices within each representation, $\Delta\nu^{A_1}$, $\Delta\nu^{A_2}$ and $\Delta\nu^{E}/2$, with respect to the quantum state related to trajectory C whose energy is closest to $7C_6/R^6$. *(c)* Small energy differences between the quasidegenerate states of representations A_1 and A_2.

We now turn to quantum states localized near the periodic trajectories of family C. The two states $\chi^{E,\pm}_{\nu_l}(\boldsymbol{r})$, obtained for a given $\nu_l \neq 0$ modulo 3, are exactly degenerate. The three–atom states $\chi^{E,\pm}_{\nu_l}(\boldsymbol{r})e^{inz}$ occur for $n = \mp 1$ modulo 3, and opposite values of n lead to atoms rotating along C in opposite directions. The two states $\chi^{A_1,A_2}_{\nu_l}(\boldsymbol{r})$ obtained for a given $\nu_l = 0$ modulo 3 belong to different representations and, hence, are quasidegenerate: their small energy difference is shown on Fig. 5(c). The three–atom states $\chi^{A_1,A_2}_{\nu_l}(\boldsymbol{r})e^{inz}$ may occur for the same value of $n = 0$ modulo 3.

C. EBK quantization: wavefunctions

To further illustrate the applicability of the EBK approach to the quantum states localized near the stable periodic trajectories of families A and C, we construct primitive EBK wavefunctions for these states [38]. We focus on a given KAM torus satisfying the quantization conditions of either Eq. (6) or Eq. (9), depending on whether it lies near a trajectory of family A or C. To obtain the corresponding EBK wavefunctions ψ_{EBK} and χ_{EBK} of sections IV B 1 and IV B 2 above, the key extra required step with respect to the approach of Refs. [31, 36] is to describe the torus in terms of multiple sheets on each of which the classical momentum is univalued [13, Sec. III.A]. These sheets join along the caustics of the classical trajectory in the (x, y) plane, shown as the dashed gray lines on Figs. 4(a) and 5(a). The caustics self–intersect, signalling the occurrence of catastrophes [39], and the torus sheetings must be constructed accordingly. We find that 12 sheets are required to describe tori near a trajectory of family A with $\nu_x = 0$, and that 6 sheets are required to describe tori near a trajectory of family C with $\nu_r = 0$. We then obtain the wavefunctions ψ_{EBK} and χ_{EBK} from the Fourier series of Eq. (4), in terms of linear superpositions of the contribution of each sheet [13, III.C]. Finally, we project ψ_{EBK} and χ_{EBK} onto the irreducible representations A_1, A_2, and E.

Figure 6(c,d) shows the resulting EBK wavefunctions for the quasidegenerate quantum states $\psi^{A_1,E}(\boldsymbol{r})$ localized near the trajectories of family A whose energies are closest to $7C_6/R^6$. We compare them to the corresponding wavefunctions obtained through our finite–element numerical calculations (Fig. 6(a,b)). We show the analogous results for the states $\chi^{A_1,A_2}(\boldsymbol{r})$, localized near the trajectories of family C, on figure 6. The agreement between the finite–element and EBK results is excellent, including in the catastrophe regions where the classical caustics self–intersect, shown in the upper left insets.

Primitive EBK wavefunctions do not account for the quantum penetration of the wavefunctions through the caustics. Instead, they diverge along the caustics as in the WKB approach [35, §46] and vanish outside the classical torus, as illustrated on Figs. 8 and 9 in the appendix. This causes the two limitations of the EBK wavefunctions considered here. First, interference phenomena involving decaying waves outside the torus are not captured: the top left insets of Fig. 7 provide an example. Second, the divergence of the wavefunctions leads to numerical inaccuracies near the caustics which hinder their normalization. Hence, each of our EBK wavefunctions matches the finite–element wavefunction up to an overall normalization factor of order 2. We eliminate it by scaling the EBK wavefunction so that it matches the finite–element result at one single point chosen far from the caustics. The quantum penetration through the caustics may be accounted for, and hence both limitations be overcome, using a uniform approximation to the wavefunction [40,

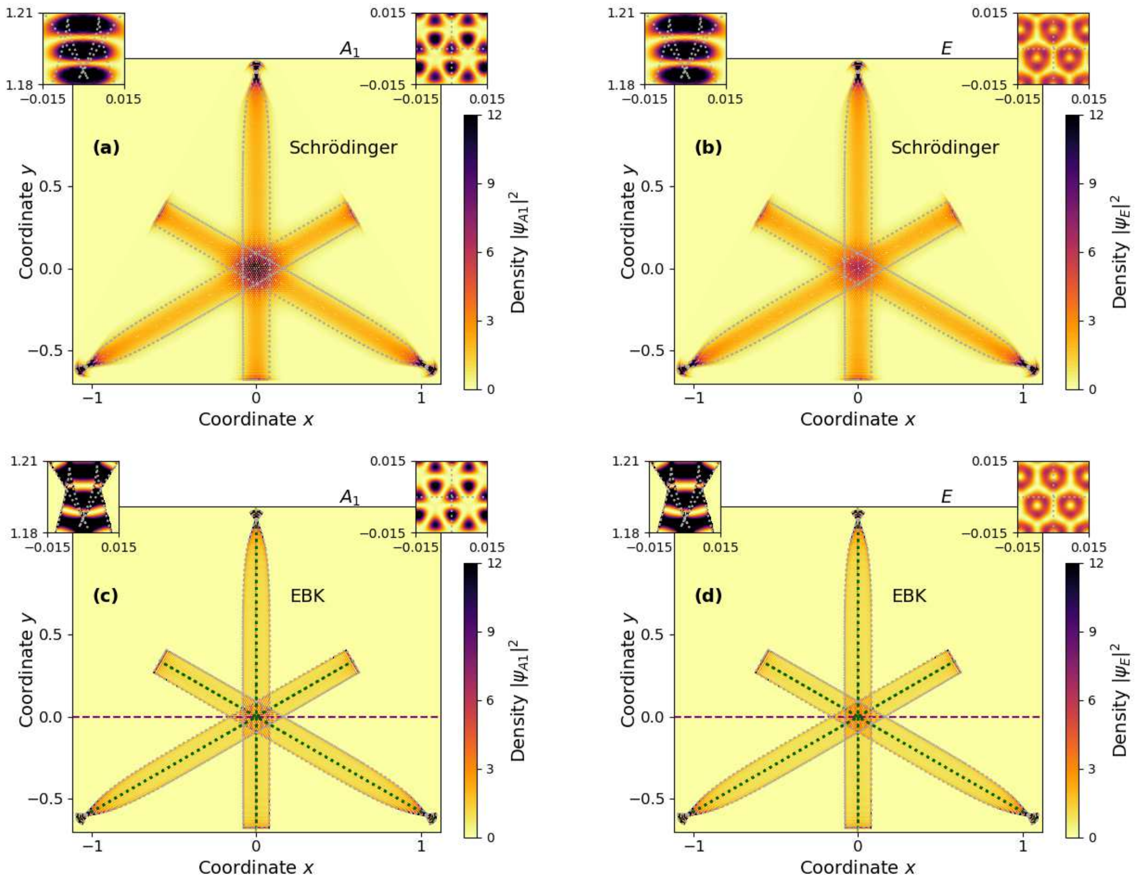

FIG. 6. *Quantum states localized near the trajectories of family A. (a,b)* Wavefunction densities $|\psi^{A_1}(\boldsymbol{r})|^2$ and $|\psi^{E}(\boldsymbol{r})|^2$ for the two quasidegenerate eigenstates of $H_{2\mathrm{D}}$ localized near the periodic trajectories of family A whose energies are closest to C_6/R^6, obtained through our finite–element numerical calculations. *(c,d)* The corresponding squared EBK wavefunctions $|\psi^{A_1}_{\mathrm{EBK}}(\boldsymbol{r})|^2$ and $|\psi^{E}_{\mathrm{EBK}}(\boldsymbol{r})|^2$, built from the KAM torus satisfying Eq. (6) with $\nu_x = 0$, $\nu_y = 300$ (see Fig. 4(a)). On all four panels, the left inset details the region where the caustics self–intersect, and the right one shows the region near $(x = 0, y = 0)$.

Sec. 7.2]. This goes beyond the scope of the present work.

V. EXPERIMENTAL PROSPECTS AND OUTLOOK

The effects considered here may be realized e.g. on the system already considered in Ref. [19]: ^{87}Rb atoms in the circular Rydberg state $50C$, for which $C_6/h = 3\,\mathrm{GHz}\,\mu\mathrm{m}^6$. Then, the value $\eta = 0.01$ is achieved in a circular trap of radius $R = 7\,\mu$m. The energy $\epsilon = 7C_6/R^6 = h \times 200\,\mathrm{kHz}$ is within experimental reach. For these parameters, the periodic trajectories of families A, B, and C all have periods of the order of 1 ms. The position of the atoms may be detected at a given time by turning on a 2D optical lattice to freeze the dynamics, followed by atomic deexcitation and site–resolved ground state imaging. We focus on realizations where the total three–atom angular momentum n is well defined.

A key difference between the quantum scar of Ref. [19] and the localization near stable orbits considered here concerns the timescale over which quantum particles follow the classical periodic trajectories. For the quantum scar, the timescale over which quantum particles follow the classically unstable periodic trajectory is expected to depend on its inverse Lyapunov exponent [24, ch. 22]. No such constraint exists for the dynamics near a classically stable orbit, so that recurrences of the initial state may be sought for over the lifetime of the trapped atoms.

Next, we point out a consequence of quantum coherence. According to Sec. IV B 3, the quantum states localized near the trajectories of family A are equal–weight superpositions of states localized near the three periodic trajectories of family A (rather than just one trajectory). This is the impact of bosonic symmetry. By contrast, motion along a single trajectory C_+ or C_- may be observed.

The following point warrants further investigation. Three atoms launched with angular momentum $n = 0$ modulo 3 near the periodic trajectory C_+ may undergo dynamical tunneling [41] to the trajectory C_-. The ex-

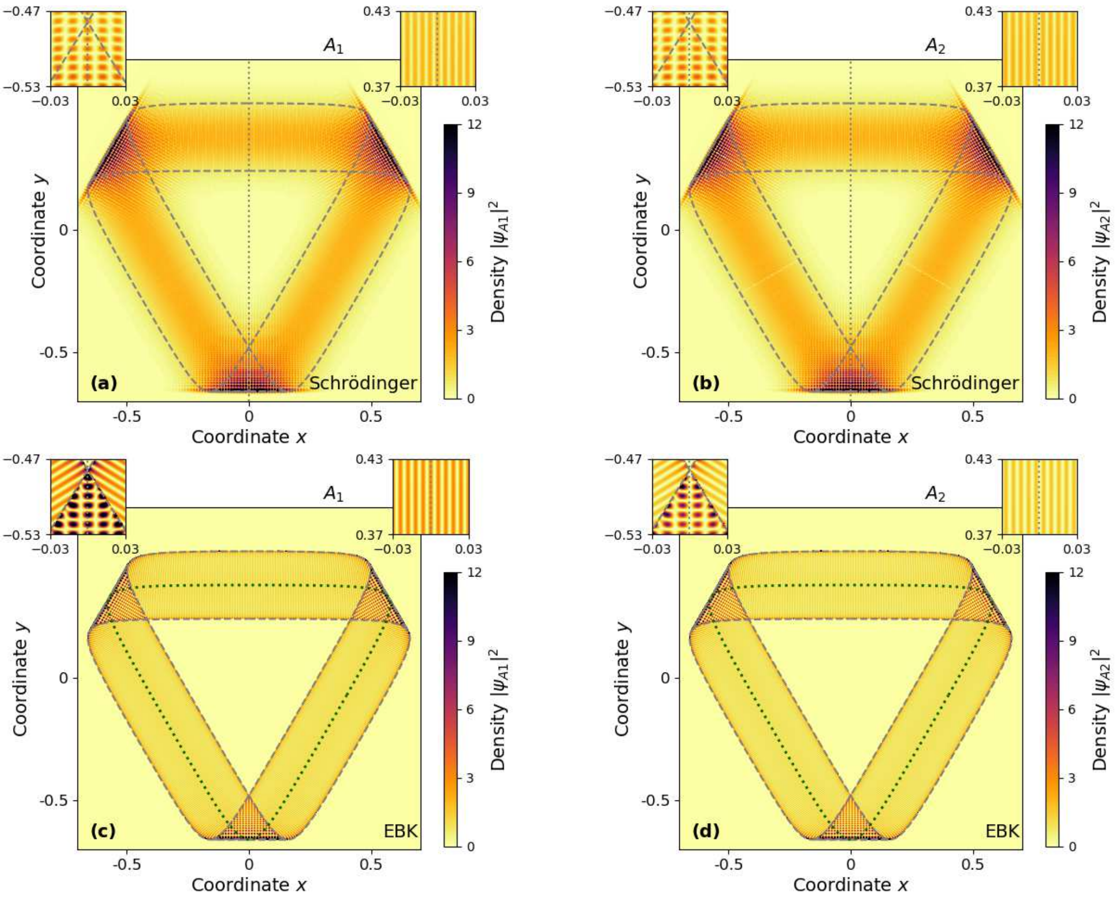

FIG. 7. *Quantum states localized near the trajectories of family C. (a,b)* Wavefunction densities $|\chi^{A_1}(\boldsymbol{r})|^2$ and $|\chi^{A_2}(\boldsymbol{r})|^2$ for the two quasidegenerate eigenstates of $H_{2\mathrm{D}}$ localized near the periodic trajectories of family C whose energies are closest to C_6/R^6, obtained through our finite–element numerical calculations. *(c,d)* The corresponding squared EBK wavefunctions $|\chi^{A_1}_{\mathrm{EBK}}(\boldsymbol{r})|^2$ and $|\chi^{A_2}_{\mathrm{EBK}}(\boldsymbol{r})|^2$, built from the KAM torus satisfying Eq. (9) with $\nu_r = 0$ and $\nu_l = 267$ (see Fig. 5(a)). On all four panels, the left inset details the region where the caustics self–intersect, and the right one shows the region near $(x = 0, y = 0.4)$.

pected oscillation period, set by $h/(\epsilon_{\nu_l,A_2} - \epsilon_{\nu_l,A_1})$, is $\sim 25\,\mathrm{s}$ for the parameters of Fig. 5(c). This very long timescale is out of reach of current setups, but should become accessible in new experiments currently under construction promising atomic lifetimes ~ 1 minute [42, 43]. Furthermore, the period may be minimized by varying the energy ϵ and the parameter η. Dynamical tunneling has already been observed for non–interacting, periodically–driven atoms [44, 45]. The system we consider would provide an example involving interacting atoms described by a time–independent Hamiltonian.

VI. CONCLUSION

We have revisited the system of three interacting bosonic particles in a circular trap that we had first considered in Ref. [19]. We have illustrated the mixed nature of its classical phase space, and shown that the statistics of the quantum levels are well described by a Berry–Robnik distribution. We have analyzed the symmetries of the quantum states localized along the classically stable periodic trajectories A and C, calculated their energies semiclassically using EBK theory, and constructed the corresponding EBK wavefunctions. Our semiclassical EBK results, regarding both the energies and the wavefunctions, are in excellent agreement with the quantum eigenstates and energies which we have obtained through finite–element numerical calculations. Thus, the considered system hosts both a quantum scar, analyzed in Ref. [19], and classical localization near stable periodic orbits, analyzed in the present work. These phenomena, all within experimental reach, occur in the same energy range: to observe one or the other, one simply adapts the initial conditions so as to launch the three atoms along a classical periodic orbit which is either unstable or stable. Hence, the system we propose appears promising in view of a detailed experimental comparison between quantum scars and classically localized states.

Appendix A: Comparison between Schrödinger and EBK wavefunctions

The supplementary figures 8 and 9 on the next page compare the behavior of the EBK wavefunctions to those obtained by solving the Schrödinger equation for the Hamiltonian H_{2D} through finite–element numerics along the horizontal and vertical axes. They show excellent agreement between the two approaches, and highlight the key limitation of the EBK wavefunctions: the quantum penetration through the caustics is not accounted for, and is replaced by a divergence along the caustics.

ACKNOWLEDGMENTS

We acknowledge stimulating discussions with M. Brune and J.M. Raimond (LKB, Collège de France), F. Dunlop (LPTM, Cergy–Pontoise), and R.J. Papoular (IRAMIS, CEA Saclay).

[1] F. Haake, S. Gnutzmann, and M. Kuś, *Quantum signatures of chaos*, 4th ed. (Springer, 2018).

[2] H.-J. Stöckmann, *Quantum chaos: an introduction* (Cambridge University Press, 1999).

[3] X. Guan and P. He, Rep. Prog. Phys. **85**, 114001 (2022).

[4] D. A. Abanin, E. Altman, I. Bloch, and M. Serbyn, Rev. Mod. Phys. **91**, 021001 (2019).

[5] H. Bernien, S. Schwartz, A. Keesling, H. Levine, A. Omran, H. Pichler, S. Choi, A. S. Zibrov, M. Endres, M. Greiner, V. Vuletić, and M. D. Lukin, Nature **551**, 579 (2017).

[6] C. J. Turner, A. A. Michailidis, D. A. Abanin, M. Serbyn, and Z. Papić, Nat. Phys. **14**, 745 (2018).

[7] D. Bluvstein, A. Omran, H. Levine, A. Keesling, G. Semeghini, S. Ebadi, T. T. Wang, A. A. Michailidis, N. Maskara, W. H. Ho, S. Choi, M. Serbyn, M. Greiner, V. Vuletić, and M. D. Lukin, Science **371**, 1355 (2021).

[8] M. Brune and D. J. Papoular, Phys. Rev. Research **2**, 023014 (2020).

[9] O. Bohigas, S. Tomsovic, and D. Ullmo, Phys. Rep. **223**, 43 (1993).

[10] V. I. Arnold, *Mathematical methods of classical mechanics*, 2nd ed. (Springer, 1989).

[11] E. J. Heller, Phys. Rev. Lett. **53**, 1515 (1984).

[12] J. B. Keller, Ann. Phys. **4**, 180 (1958).

[13] I. C. Percival, Advances in Chemical Physics **36**, 1 (1977).

[14] M. C. Gutzwiller, *Chaos in classical and quantum mechanics* (Springer, 1990).

[15] T. A. Brody, Lett. Nuovo Cimento **7**, 482 (1973).

[16] M. V. Berry and M. Robnik, J. Phys. A **17**, 2413 (1984).

[17] C. J. Turner, J.-Y. Desaules, K. Bull, and Z. Papić, Phys. Rev. X **11**, 021021 (2021).

[18] A. A. Michailidis, C. J. Turner, Z. Papić, D. A. Abanin, and M. Serbyn, Phys. Rev. X **10**, 011055 (2020).

[19] D. J. Papoular and B. Zumer, Phys. Rev. A **107**, 022217 (2023).

[20] R. G. Cortiñas, M. Favier, B. Ravon, P. Méhaignerie, Y. Machu, J. M. Raimond, C. Sayrin, and M. Brune, Phys. Rev. Lett. **124**, 123201 (2020).

[21] D. Barredo, V. Lienhard, P. Scholl, S. de Léséleuc, T. Boulier, A. Browaeys, and T. Lahaye, Phys. Rev. Lett. **124**, 023201 (2020).

[22] L. Chomaz, I. Ferrier-Barbut, F. Ferlaino, B. Laburthe-Tolra, B. L. Lev, and T. Pfau, Rep. Prog. Phys. **86**, 026401 (2023).

[23] J. L. Bohn, A. M. Rey, and J. Ye, Science **357**, 1002 (2017).

[24] E. J. Heller, *The semiclassical way to dynamics and spectroscopy* (Princeton University Press, 2018).

[25] M. Baranger, K. T. R. Davies, and J. H. Mahoney, Ann. Phys. **186**, 95 (1988).

[26] K. T. R. Davies, T. E. Huston, and M. Baranger, Chaos **2**, 215 (1992).

[27] F. Hecht, J. Numer. Math. **20**, 251 (2012).

[28] B. Lauritzen and N. D. Whelan, Ann. Phys. **244**, 112 (1995).

[29] D. Wintgen and H. Friedrich, Phys. Rev. A **35**, 1464(R) (1987).

[30] T. Prosen, J. Phys. A **31**, 7023 (1998).

[31] C. C. Martens and G. S. Ezra, J. Chem. Phys. **86**, 279 (1987).

[32] L. D. Landau and E. M. Lifshitz, *Mechanics*, 3rd ed. (Butterworth Heinemann, 1976).

[33] I. C. Percival, J. Phys. A **7**, 794 (1974).

[34] V. P. Maslov and M. V. Fedoriuk, *Semi-classical approximations in quantum mechanics* (Reidel, 1981).

[35] L. D. Landau and E. M. Lifshitz, *Quantum mechanics, non-relativistic theory*, 3rd ed. (Butterworth Heinemann, 1977).

[36] C. C. Martens and G. S. Ezra, J. Chem. Phys. **83**, 2990 (1985).

[37] J. G. Leopold, I. C. Percival, and D. Richards, J. Phys. A **15**, 805 (1982).

[38] S. K. Knudson, J. B. Delos, and D. W. Noid, J. Chem. Phys. **84**, 6886 (1986).

[39] J. B. Delos, J. Chem. Phys. **86**, 425 (1987).

[40] A. M. Ozorio de Almeida, *Hamiltonian systems: chaos and quantization* (Cambridge University Press, 1988).

[41] S. Tomsovic, Phys. Scr. **T90**, 162 (2001).

[42] T. L. Nguyen, J. M. Raimond, C. Sayrin, R. Cortiñas, T. Cantat-Moltrecht, F. Assemat, I. Dotsenko, S. Gleyzes, S. Haroche, G. Roux, T. Jolicoeur, and M. Brune, Phys. Rev. X **8**, 011032 (2018).

[43] P. Méhaignerie, C. Sayrin, J. M. Raimond, M. Brune, and G. Roux, Phys. Rev. A **107**, 063106 (2023).

[44] W. K. Hensinger, H. Häffner, A. Browaeys, N. R. Heckenberg, K. Helmerson, C. McKenzie, G. J. Milburn, W. D. Phillips, S. L. Rolston, H. Rubinsztein-Dunlop, and B. Upcroft, Nature **412**, 52 (2001).

[45] D. A. Steck, W. H. Oskay, and M. G. Raizen, Science **293**, 274 (2001).

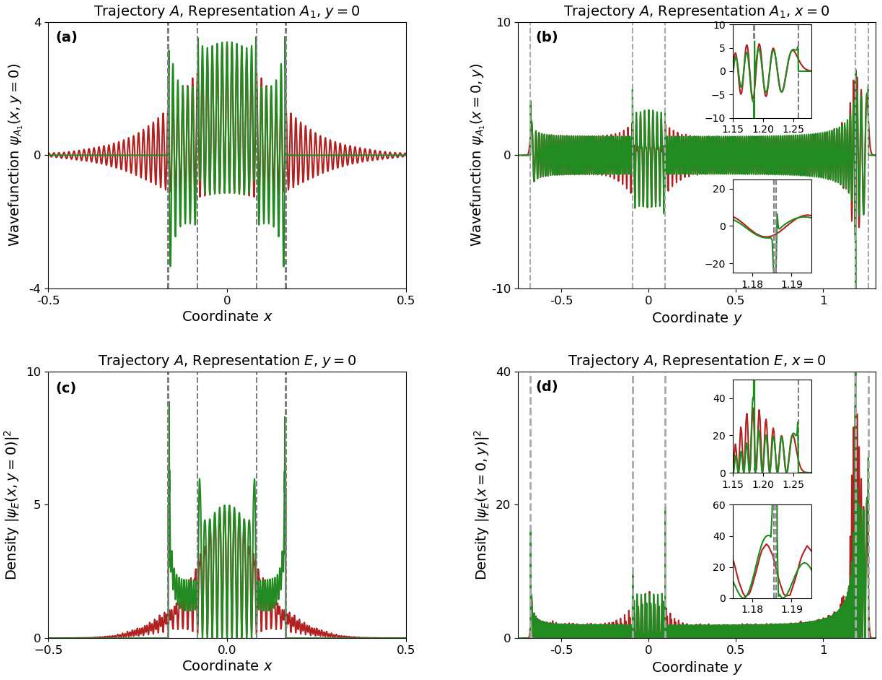

FIG. 8. *Quantum states localized near the trajectories of family A.* Comparison of the EBK *(a,b)* wavefunction $\psi^{A_1}_{\text{EBK}}$ and *(c,d)* density $|\psi^{E}_{\text{EBK}}|^2$ (green) with the corresponding quantities obtained through finite–element numerics (red) shown on Fig. 4, along the horizontal *(a,c)* and vertical *(b,d)* axes. The insets illustrate their behaviour near the caustics (vertical dashed gray lines). Each EBK wavefunction has been scaled to match the finite–element wavefunction at the point $(x = 0, y = 0.5)$.

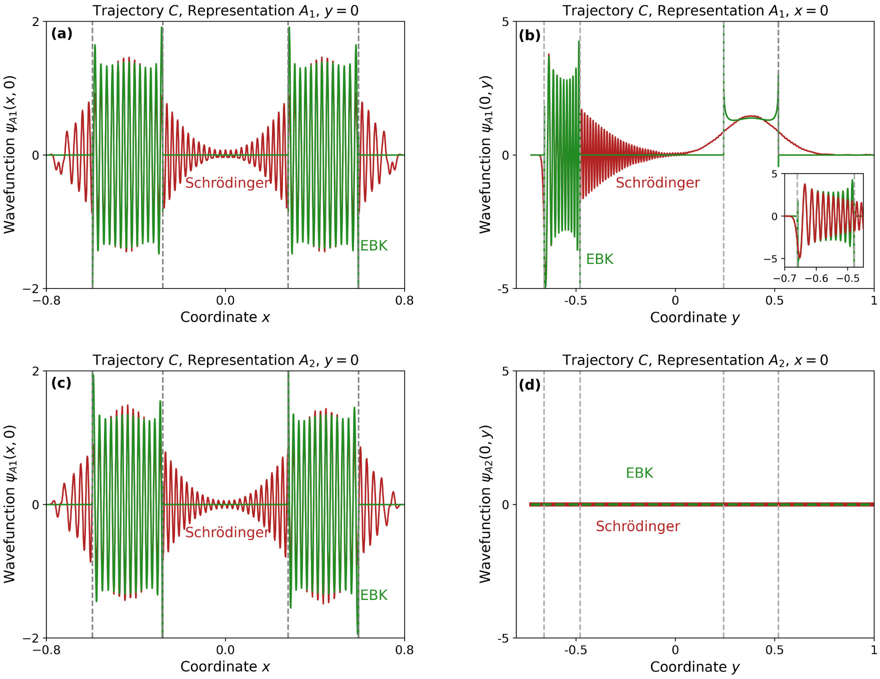

FIG. 9. *Quantum states localized near the trajectories of family C.* Comparison of the EBK wavefunctions (green) *(a,b)* $\chi^{A_1}_{\text{EBK}}$ and *(c,d)* $\chi^{A_2}_{\text{EBK}}$ and the corresponding wavefunctions obtained through finite–element numerics (red) shown on Fig. 5, along the horizontal (a, c) and vertical (b, d) axes. The insets illustrate their behaviour near the caustics (vertical dashed gray lines). Each EBK wavefunction has been scaled to match the finite–element wavefunction at the point $(x = 0.5, y = 0)$.

5 Prospects for future work

Atomic systems [123, 124], and in particular single Rydberg atoms [125, 126], have been an excellent testbed for chaos. Recent experimental advances concerning Rydberg atom manipulation and trapping [25, 26] are now enabling the realisation of systems comprised of multiple, interacting atoms where chaos may also be characterised. In this context, many–particle systems currently attract lots of attention [29, 71].

The theoretical investigation of simple, well–controlled few–atom systems, such as the three–atom Rydberg system of chapter 4, is likely to provide information on quantum scars and classical localisation phenomena which is complementary to that acquired through the experiments on many–body scars [22, 115] and the intense theoretical effort they have spawned [29, 71]. These few–body systems may be analysed through well–established tools. Among these, the Kolmogorov–Arnold–Moser theory for perturbed integrable systems [63, Appendix 8] has recently started to attract attention in the context of trapped atomic systems [112]. Applied in this novel context, and combined with the semiclassical approaches developed in the context of chaos [64, chaps. 7–9], it may improve our understanding of localisation phenomena by highlighting the classical roots of some of them.

In this chapter, we briefly mention a few questions which we plan on addressing in the coming years. They are all related to my recent work presented in chapter 4. Section 5.6 also pertains to my work on the interactions in atomic systems, illustrated in Sec. 2.2.

5.1 Classical periodic trajectories beyond families A, B, C

We have focused on the simplest periodic trajectories supported by the classical Hamiltonian H_{2D}, i.e. those of families A, B, and C, and on the eigenstates of the quantum Hamiltonian which are localised near these trajectories. However, the classical H_{2D} supports many other periodic trajectories, and the quantum H_{2D} has many other eigenstates. Figure 5.1 shows three of these which are not directly related to trajectories A, B, or C.

Additional periodic trajectories originate from those of families A, B, and C through bifurcations [104]. These additional periodic trajectories lead to the holes visible within the ergodic sea on the surface of section of Fig. 4.4. As demonstrated for the Hénon–Heiles Hamiltonian by the authors of the algorithm [86], these bifurcations may be identified using the numerical approach of Ref. [105] which we have already implemented and used in Sec. 4.3. Some of these bifurcations are stable and others are unstable. They may lead to the classical localisation or quantum scarring of other quantum eigenstates of H_{2D}. The identification of the bifurcations will help in narrowing down candidates for eigenstates which are not localised, and which might be interpreted in terms of random waves [127].

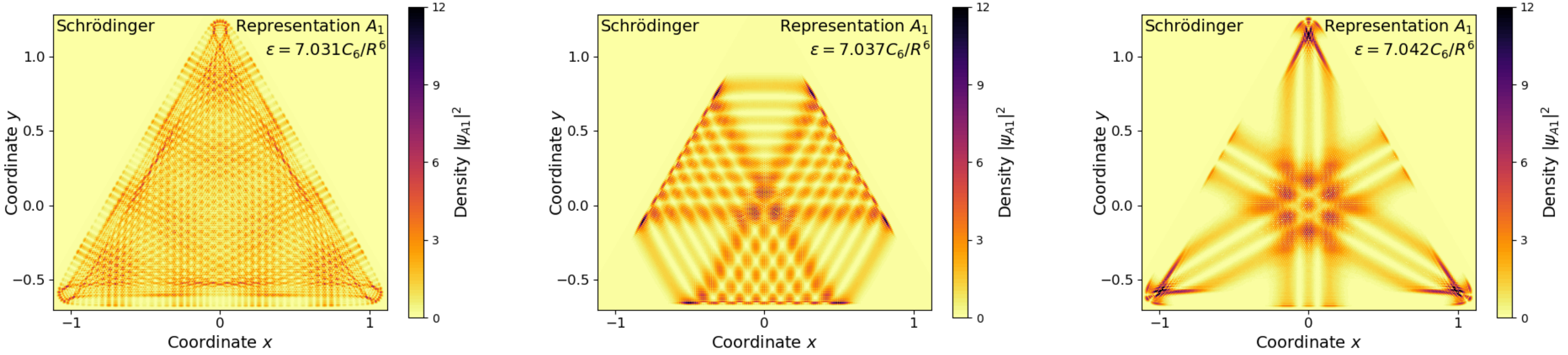

Figure 5.1: Densities $|\psi_n(x, y)|^2$ for three eigenstates pertaining to Representation A_1, whose energies are close to $7C_6/R^6$, and which are not related to the periodic trajectories A, B, or C. The centre and right panels show eigenstates which are candidates for localisation in the vicinity of bifurcations of trajectories C and A, respectively. The localisation properties of the eigenstate shown on the left panel, if any, seem less straightforward to guess.

5.2 Dynamics of the quantum scar

Up to now, our analysis of the quantum scar due to trajectory B has relied on the solution of the stationary Schrödinger equation. We now intend to investigate its dynamics, by characterizing the evolution in time of a quantum wavepacket initially launched along the classically *unstable* periodic trajectory B. This evolution is dictated by the time–dependent Schrödinger equation for the potential $V_{2D}(x, y)$ (which is constant in time). Its numerical solution is accessible with the finite–element software we are using, i.e. FreeFEM [82].

The wavepacket is expected to follow the unstable trajectory for short times. A key question concerns the number of visible periods of this trajectory before the wavepacket becomes too distorted to be compared to the initial one. This timescale is expected to involve the Lyapunov exponent λ_B of the trajectory [102, Fig. 22.3].

For comparison, in the experiments on many–body scars, the number of observed revivals of the initial state ranges from 4 [22] to 8 [115]. To our knowledge, the comparison to the Lyapunov exponent of the underlying classical trajectory is not available in the literature.

We shall perform a similar calculation for a quantum wavepacket launched along a classically *stable* trajectory. In this second context, related to classical localisation, we expect the quantum dynamics to follow the classical prediction over longer times. Comparing the quantum dynamics in the cases where the classical trajectory is unstable or stable, we hope to identify experimentally–accessible observables which tell the two regimes apart.

5.3 From the quantum regime to the semiclassical one

From the classical point of view, the system considered in chapter 4 exhibits a scaling property, described in Sec. 4.1.4.1, which accounts for the roles of the atomic mass m, the interaction strength C_6, and the trap radius R. From the quantum point of view, the classical scaling breaks down, and the experimental parameters enter the dimensionless ratio $\eta = \hbar\, R^2/(mC_6)^{1/2}$. Smaller values of η signal deeper quasiclassical behaviour.

A similar dimensionless ratio may be introduced e.g. for the Hénon–Heiles potential [4, appendix 1]. However, our system is particularly appealing in this respect because the value of η may be varied experimentally, by choosing appropriate values for m, R, or[1] C_6.

This motivates the theoretical exploration of the impact of η on our results:

- Ref. [101, Fig. 2], concerning billiards, highlights the deviation of the spectral statistics from the Berry–Robnik distribution in less semiclassical regimes. In the system we consider, the Berry–Robnik distribution is applicable for the relatively low value $\eta = 0.01$. We shall investigate possible deviations from it as η is increased.

- For $\eta = 0.01$, we have found a single quantum scarred state near each resonance due to trajectory B in the trace formula (see Fig. 4.11). However, the widths of these resonances cover multiple states, and such a one–to–one correspondence between their peaks and the energies of the scarred states was not expected [64]. We shall investigate whether it still holds for smaller and for larger values of η.

---

[1] The interaction strength C_6 depends on the principal quantum number n of the considered Rydberg state [27, Sec. II.B]. A range of different values of n is accessible in current experiments. For those performed at Collège de France [28], n ranges from 48 to 52.

5.4 Four particles in a circular trap

The time–independent Hamiltonian describing a system of four particles (instead of three) may be a relevant generalisation of the system we have studied. An important issue in this context is whether the fraction of classical phase space leading to ergodic dynamics becomes larger or smaller as the particle number is increased. Answering this question would be a first step in conciliating *(i)* the importance of non–ergodic phenomena in the three–particle system we have studied with *(ii)* the classically chaotic behaviour for the chain of 100 atoms reported in Ref. [28, appendix E].

5.5 Stabilising Trajectory B through periodic modulation

Recent experiments involving many–body scars [30, 115] have shown that the periodic modulation of one of the system parameters[2] has two effects:

- Many more revivals of the initial state are observable than for a time–independent Hamiltonian (e.g. the lifetime of the effect is multiplied by 5 in Ref. [30, Fig. 3B]);
- These revivals occur at the frequency $\omega_m/2$, where ω_m is the modulation frequency.

We shall look for a similar stabilization phenomenon in the system comprised of three Rydberg atoms in a circular trap considered in Chap. 4. More specifically, we shall investigate the possibility of stabilising the unstable trajectory B by modulating the pairwise interparticle interactions. The interaction between two particles reads C_6/r^6, where r is the interparticle distance and C_6 is the interaction strength. This coefficient depends on the amplitude of the external electric field used to stabilise the circular Rydberg state [28, Sec. II and Fig. 11] (see Sec. 5.6 below for a related question). Hence, modulating this amplitude with a frequency comparable to the inverse period of trajectory B (a few kHz, i.e. in the radiofrequency range) will achieve the desired modulation of the coefficient C_6.

An important issue is whether or not this stabilisation requires quantum mechanics. This question may be settled by solving the *classical* equation of motion for the three–particle system governed by the time–dependent Hamiltonian with an initial condition along trajectory B. The subharmonic response with frequency $\omega_m/2$ observed in experiments is a hint that classical mechanics may indeed play a role, because this is the frequency at which parametric resonance is expected [79, §27].

---

[2] The modulated parameter is the detuning with respect to the two–photon transition transferring the atoms from the ground to the Rydberg states in Ref. [30], and the geometry of the optical lattice trapping the cold atoms in Ref. [115].

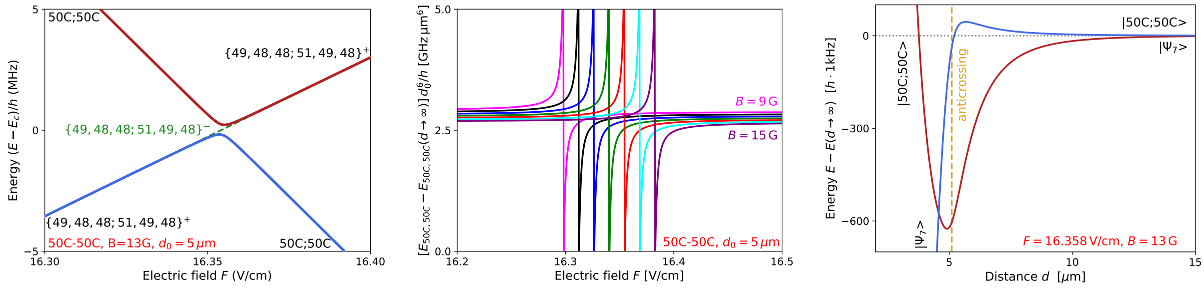

Figure 5.2: Left: Anticrossing due to the dipole–dipole interaction, involving the two–atom states $|50C;50C\rangle$ and $|\Psi_7\rangle = |49,48,48;51,49,48\rangle$, occurring for experimentally accessible values of the electric field F, magnetic field B, and interatomic distance d. **Centre:** Impact of the resonance on the two–atom interaction in the case where the anticrossing is traversed by varying F at fixed d. **Right:** Impact of the resonance in the case where the anticrossing is traversed by varying d at constant F: the two–atom interaction does not depend monotonically on d.

5.6 Resonance in the interaction between Rydberg atoms

In this section, we consider two trapped atoms, prepared in the same circular Rydberg state. We wish to characterise their interaction. Throughout chapter 4, we have represented this interaction using the potential C_6/r^6. This follows from the properties of the dipole–dipole interaction [80, §89], which couples two atoms in the same circular Rydberg state to second order, and it holds for the experimental conditions considered up to now [28, Sec. II].

However, for specific values of the external electric and magnetic fields, and of the interatomic distance, the dipole–dipole interaction causes anticrossings between two two–atom states. The left panel of Fig. 5.2 shows such an anticrossing, which occurs for electric fields of the order of 16.3 V/cm if the interatomic distance is $d = 5\,\mu$m: these are experimentally accessible parameters comparable to those used in Ref. [28]. These anticrossings cause resonances in the interaction between the two atoms.

A given anticrossing may be traversed either by maintaining the interatomic distance d fixed and varying the external electric field F, as on the left and centre panels of Fig. 5.2, or by varying d at constant F, as on the right panel of the figure. In the first scenario, the resonance shows up as a discontinuous feature in the interaction energy, visible on the centre panel. In the second scenario, it causes the interaction energy to vary non–monotonically as a function of the interatomic distance, which precludes its modelling using the usual van der Waals interaction term C_6/r^6.

To our knowledge, these resonances have not yet been discussed. They may be identified by numerically diagonalising the two–atom interaction Hamiltonian restricted to a relevant subspace, whose dimension is typically about one thousand. Our preliminary calculations (see Fig. 5.2) indicate that some of them are within experimental reach. We intend to map their positions and characterise their impact on the two–atom interaction properties.

Bibliography

[1] D. J. Papoular, L. P. Pitaevskii, and S. Stringari, Quantized conductance through the quantum evaporation of bosonic atoms, Phys. Rev. A **94**, 023622 (2016).

[2] Y. Zeng, P. Xu, X. He, Y. Liu, M. Liu, J. Wang, D. J. Papoular, G. V. Shlyapnikov, and M. Zhan, Entangling two individual atoms of different isotopes via Rydberg blockade, Phys. Rev. Lett. **119**, 160502 (2017).

[3] M. Brune and D. J. Papoular, Evaporative cooling to a Rydberg crystal close to its ground state, Phys. Rev. Research **2**, 023014 (2020).

[4] D. J. Papoular and B. Zumer, Quantum scar affecting the motion of three interacting particles in a circular trap, Phys. Rev. A **107**, 022217 (2023).

[5] D. J. Papoular and B. Zumer, Quantum signatures of the mixed classical phase space for three interacting particles in a circular trap, arXiv preprint 10.48550/arXiv.2404.18265 (2024).

[6] O. J. Luiten, M. W. Reynolds, and J. T. M. Walraven, Kinetic theory of the evaporative cooling of a trapped gas, Phys. Rev. A **53**, 381 (1996).

[7] M. C. Gutzwiller, *Chaos in classical and quantum mechanics* (Springer, 1990).

[8] B. M. Smirnov and M. I. Chibisov, Electron exchange and changes in the hyperfine state of colliding alkaline metal atoms, Sov. Phys. JETP **21**, 624 (1965).

[9] C. Cohen-Tannoudji and D. Guéry-Odelin, *Advances in atomic physics: an overview* (World Scientific, 2011).

[10] L. P. Pitaevskii and S. Stringari, *Bose-Einstein condensation and superfluidity*, 2nd ed. (Oxford, 2016).

[11] K. M. Jones, E. Tiesinga, P. D. Lett., and P. S. Julienne, Ultracold photoassociation spectroscopy: long-range molecules and atomic scattering, Rev. Mod. Phys. **78**, 483 (2006).

[12] M. A. Nielsen and I. L. Chuang, *Quantum computation and quantum information* (Cambridge, 2000).

[13] J. R. Abo-Shaeer, C. Raman, J. M. Vogels, and W. Ketterle, Observation of vortex lattices in Bose-Einstein condensates, Science **292**, 476 (2001).

[14] M. W. Zwierlein, J. R. Abo-Shaeer, A. Schirotzek, C. H. Schunck, and W. Ketterle, Vortices and superfluidity in a strongly interacting Fermi gas, Nature **435**, 1047 (2005).

[15] V. Milner, J. L. Hanssen, W. C. Campbell, and M. G. Raizen, Optical billiards for atoms, Phys. Rev. Lett. **86**, 1514 (2001).

[16] W. K. Hensinger, H. Häffner, A. Browaeys, N. R. Heckenberg, K. Helmerson, C. McKenzie, G. J. Milburn, W. D. Phillips, S. L. Rolston, H. Rubinsztein-Dunlop, and B. Upcroft, Dynamical tunnelling of cold atoms, Nature **412**, 52 (2001).

[17] L. Chomaz, I. Ferrier-Barbut, F. Ferlaino, B. Laburthe-Tolra, B. L. Lev, and T. Pfau, Dipolar physics: a review of the experiments with magnetic quantum gases, Rep. Prog. Phys. **86**, 026401 (2023).

[18] J. L. Bohn, A. M. Rey, and J. Ye, Cold molecules: progress in quantum engineering of chemistry and quantum matter, Science **357**, 1002 (2017).

[19] D. Kleppner, M. G. Littman, and M. L. Zimmerman, Highly excited atoms, Sci. Am. **244(5)**, 130 (1981).

[20] S. Haroche and J.-M. Raimond, *Exploring the quantum: atoms, cavities and photons* (Oxford, 2006).

[21] R. G. Hulet and D. Kleppner, Rydberg atoms in "circular" states, Phys. Rev. Lett. **51**, 1430 (1983).

[22] H. Bernien, S. Schwartz, A. Keesling, H. Levine, A. Omran, H. Pichler, S. Choi, A. S. Zibrov, M. Endres, M. Greiner, V. Vuletić, and M. D. Lukin, Probing many-body dynamics on a 51-atom quantum simulator, Nature **551**, 579 (2017).

[23] A. Browaeys and T. Lahaye, Many-body physics with individually controlled Rydberg atoms, Nat. Phys. **16**, 132 (2020).

[24] S. E. Anderson, K. C. Younge, and G. Raithel, Trapping Rydberg atoms in an optical lattice, Phys. Rev. Lett. **107**, 263001 (2011).

[25] D. Barredo, V. Lienhard, P. Scholl, S. de Léséleuc, T. Boulier, A. Browaeys, and T. Lahaye, Three-dimensional trapping of individual Rydberg atoms in ponderomotive bottle beam traps, Phys. Rev. Lett. **124**, 023201 (2020).

[26] R. G. Cortiñas, M. Favier, B. Ravon, P. Méhaignerie, Y. Machu, J. M. Raimond, C. Sayrin, and M. Brune, Laser trapping of circular Rydberg atoms, Phys. Rev. Lett. **124**, 123201 (2020).

[27] M. Saffman, T. G. Walker, and K. Mølmer, Quantum information with Rydberg atoms, Rev. Mod. Phys. **82**, 2313 (2010).

[28] T. L. Nguyen, J. M. Raimond, C. Sayrin, R. Cortiñas, T. Cantat-Moltrecht, F. Assemat, I. Dotsenko, S. Gleyzes, S. Haroche, G. Roux, T. Jolicoeur, and M. Brune, Towards quantum simulation with circular Rydberg atoms, Phys. Rev. X **8**, 011032 (2018).

[29] M. Serbyn, D. A. Abanin, and Z. Papić, Quantum many-body scars and weak breaking of ergodicity, Nat. Phys. **17**, 675 (2021).

[30] D. Bluvstein, A. Omran, H. Levine, A. Keesling, G. Semeghini, S. Ebadi, T. T. Wang, A. A. Michailidis, N. Maskara, W. H. Ho, S. Choi, M. Serbyn, M. Greiner, V. Vuletić, and M. D. Lukin, Controlling quantum many–body dynamics in driven Rydberg atom arrays, Science **371**, 1355 (2021).

[31] D. J. Papoular, G. Ferrari, L. P. Pitaevskii, and S. Stringari, Increasing quantum degeneracy by heating a superfluid, Phys. Rev. Lett. **109**, 084501 (2012).

[32] D. J. Papoular, L. P. Pitaevskii, and S. Stringari, Fast thermalization and Helmholtz oscillations of an ultracold Bose gas, Phys. Rev. Lett. **113**, 170601 (2014).

[33] Y. V. Nazarov and Y. M. Blanter, *Quantum transport: introduction to nanoscience* (Cambridge, 2009).

[34] B. J. van Wees, H. van Houten, C. W. J. Beenakker, J. G. Williamson, L. P. Kouwenhoven, D. van der Marel, and C. T. Foxon, Quantized conductance of point contacts in a two-dimensional electron gas, Phys. Rev. Lett. **60**, 848 (1988).

[35] W. D. Johnston Jr. and J. G. King, Measurement of velocity distributions of atoms evaporating from liquid helium II, Phys. Rev. Lett. **16**, 1191 (1966).

[36] F. R. Hope, M. J. Baird, and A. F. G. Wyatt, Quantum evaporation from liquid helium 4 by rotons, Phys. Rev. Lett. **52**, 1528 (1984).

[37] P. W. Anderson, Interpretation of the Johnston-King experiment on evaporation of liquid Helium, Phys. Letters **29A**, 563 (1969).

[38] F. Dalfovo, A. Fracchetti, A. Lastri, L. Pitaevskii, and S. Stringari, Rotons and quantum evaporation from superfluid helium 4, Phys. Rev. Lett. **75**, 2510 (1995).

[39] S. Krinner, D. Stadler, D. Husmann, J. Brantut, and T. Esslinger, Observation of quantized conductance in neutral matter, Nature **517**, 64 (2015).

[40] S. Eckel, J. G. Lee, F. Jendrezjewski, C. J. Lobb, G. K. Campbell, and W. T. Hill, Contact resistance and phase slips in mesoscopic superfluid atom transport, Phys. Rev. A **93**, 063619 (2016).

[41] P. Xu, J. Yang, M. Liu, X. He, Y. Zeng, K. Wang, J. Wang, D. J. Papoular, G. V. Shlyapnikov, and M. Zhan, Interaction-induced decay of a heteronuclear two-atom system, Nat. Commun. **6**, 7803 (2015).

[42] L. Isenhower, E. Urban, X. L. Zhang, A. T. Gill, T. Henage, T. A. Johnson, T. G. Walker, and M. Saffman, Demonstration of a neutral atom Controlled-NOT quantum gate, Phys. Rev. Lett. **104**, 010503 (2010).

[43] T. Wilk, A. Gaëtan, C. Evellin, J. Wolters, Y. Miroshnychenko, P. Grangier, and A. Browaeys, Entanglement of two individual neutral atoms using Rydberg blockade, Phys. Rev. Lett. **104**, 010502 (2010).

[44] W. Ketterle and N. J. van Druten, Evaporative cooling of trapped atoms, Advances in Atomic, Molecular, and Optical physics **37**, 181 (1996).

[45] E. Wigner, On the interaction of electrons in metals, Phys. Rev. **46**, 1002 (1934).

[46] C. C. Grimes and G. Adams, Evidence for a liquid-to-crystal phase transition in a classical, two-dimensional sheet of electrons, Phys. Rev. Lett. **42**, 795 (1979).

[47] J. G. Bohnet, B. C. Sawyer, J. W. Britton, M. L. Wall, A. M. Rey, M. Foss-Feig, and J. J. Bollinger, Quantum spin dynamics and entanglement generation with hundreds of trapped ions, Science **352**, 1297 (2016).

[48] N. D. Mermin, Crystalline order in two dimensions, Phys. Rev. **176**, 250 (1968).

[49] C. Senko, J. Smith, P. Richerme, A. Lee, W. C. Campbell, and C. Monroe, Coherent imaging spectroscopy of a quantum many-body spin system, Science **345**, 430 (2014).

[50] I. Shapir, A. Hamo, S. Pecker, C. P. Moca, O. Legeza, G. Zarand, and S. Ilani, Imaging the electronic Wigner crystal in one dimension, Science **364**, 870 (2019).

[51] M. Yamashita, M. Koashi, and N. Imoto, Quantum kinetic theory for evaporative cooling of trapped atoms: growth of Bose-Einstein condensates, Phys. Rev. A **59**, 2243 (1999).

[52] L. D. Landau and E. M. Lifshitz, *Statistical physics, part 1*, 3rd ed. (Butterworth Heinemann, 1980).

[53] H. F. Hess, G. P. Kochanski, J. M. Doyle, N. Masuhara, D. Kleppner, and T. J. Greytak, Magnetic trapping of spin-polarized atomic hydrogen, Phys. Rev. Lett. **59**, 672 (1987).

[54] S. Stellmer, B. Pasquiou, R. Grimm, and F. Schreck, Laser cooling to quantum degeneracy, Phys. Rev. Lett. **110**, 263003 (2013).

[55] J. Hu, A. Urvoy, Z. Vendeiro, V. Crépel, W. Chen, and V. Vuletić, Creation of a Bose-condensed gas of 87Rb by laser cooling, Science **358**, 1078 (2017).

[56] A. Urvoy, Z. Vendeiro, J. Ramette, A. Adiyatullin, and V. Vuletić, Direct laser cooling to Bose-Einstein condensation in a dipole trap, Phys. Rev. Lett. **122**, 203202 (2019).

[57] L. Allen, S. M. Barnett, and M. J. Padgett, *Optical angular momentum* (CRC Press, 2003).

[58] K. Huang, *Statistical Mechanics*, 2nd ed. (Wiley, 1987).

[59] NIST Digital Library of Mathematical Functions, chapter 8, http://dlmf.nist.gov/8 (2010).

[60] Boost.Multiprecision library, `https://www.boost.org/doc/libs/1_70_0/libs/multiprecision/doc/html/index.html` (2019).

[61] D. Barredo, V. Lienhard, S. de Léséleuc, T. Lahaye, and A. Browaeys, Synthetic three-dimensional atomic structures assembled atom by atom, Nature **561**, 79 (2018).

[62] D. Barredo, S. de Léséleuc, V. Lienhard, T. Lahaye, and A. Browaeys, An atom-by-atom assembler of defect-free arbitrary two-dimensional atomic arrays, Science **354**, 1021 (2016).

[63] V. I. Arnold, *Mathematical methods of classical mechanics*, 2nd ed. (Springer, 1989).

[64] A. M. O. de Almeida, *Hamiltonian systems: chaos and quantization* (Cambridge University Press, 1988).

[65] M. V. Berry, Regular and irregular motion, in *Topics in nonlinear mechanics*, Vol. 46, edited by S. Jorna (1978) p. 16.

[66] M. V. Berry, Semiclassical mechanics of regular and irregular motion, in *Les Houches lecture series session XXXVI*, edited by G. Iooss, R. H. G. Helleman, and R. Stora (North Holland, Amsterdam, 1983) p. 171.

[67] O. Bohigas, S. Tomsovic, and D. Ullmo, Manifestations of classical phase space structures in quantum mechanics, Phys. Rep. **223**, 43 (1993).

[68] D. A. Abanin, E. Altman, I. Bloch, and M. Serbyn, Many–body localization, thermalization, and entanglement, Rev. Mod. Phys. **91**, 021001 (2019).

[69] B. Sutherland, *Beautiful models: 70 years of exactly solved quantum many-body problems* (World Scientific, 2004).

[70] T. Kinoshita, T. Wenger, and D. S. Weiss, A quantum Newton's cradle, Nature **440**, 900 (2006).

[71] S. Moudgalya, B. A. Bernevig, and N. Regnault, Quantum many-body scars and Hilbert space fragmentation: a review of exact results, Rep. Prog. Phys. **85**, 086501 (2022).

[72] C. J. Turner, J. Desaules, K. Bull, and Z. Papić, Correspondence principle for many-body scars in ultracold Rydberg atoms, Phys. Rev. X **11**, 021021 (2021).

[73] L. Amico, D. Anderson, M. Boshier, J. P. Brantut, L. Kwek, A. Minguzzi, and W. von Klitzking, Atomtronic circuits: from many-body circuits to quantum technologies, Rev. Mod. Phys. **94**, 041001 (2022).

[74] P. Naidon and S. Endo, Efimov physics: a review, Rep. Prog. Phys. **80**, 056001 (2017).

[75] P. Scholl, H. J. Williams, G. Bornet, F. Wallner, D. Barredo, L. Henriet, A. Signoles, C. Hainaut, T. Franz, S. Geier, A. Tebben, A. Salzinger, G. Zürn, T. Lahaye, M. Weidemüller, and A. Browaeys, Microwave engineering of programmable XXZ Hamiltonians in arrays of Rydberg atoms, PRX Quantum **3**, 020303 (2022).

[76] L. D. Faddeev and S. P. Merkuriev, *Quantum scattering theory for several particle systems* (Springer, 1993).

[77] V. I. Arnold, V. V. Kozlov, and A. I. Neishtadt, *Mathematical aspects of classical and celestial mechanics* (Springer, 2006).

[78] T. Hahn, *International tables for crystallography volume A: space-group symmetry* (Springer, 2005).

[79] L. D. Landau and E. M. Lifshitz, *Mechanics*, 3rd ed. (Butterworth Heinemann, 1976).

[80] L. D. Landau and E. M. Lifshitz, *Quantum mechanics, non-relativistic theory*, 3rd ed. (Butterworth Heinemann, 1977).

[81] J. M. Ziman, *Principles of the theory of solids*, 2nd ed. (Cambridge University Press, 1972).

[82] F. Hecht, New development in FreeFem++, J. Numer. Math. **20**, 251–265 (2012).

[83] O. C. Zienkiewicz, R. L. Taylor, and J. Z. Zhu, *The finite element method: its basis and fundamentals*, 7th ed. (Butterworth Heinemann, 2017).

[84] J. P. Serre, *Linear representations of finite groups* (Springer, 1977).

[85] M. Baranger, M. R. Haggerty, B. Lauritzen, D. C. Meredith, and D. Provost, Periodic orbits of nonscaling Hamiltonian systems from quantum mechanics, Chaos **5**, 261 (1995).

[86] K. T. R. Davies, T. E. Huston, and M. Baranger, Calculation of periodic trajectories for the Hénon–Heiles Hamiltonian using the monodromy method, Chaos **2**, 215 (1992).

[87] M. V. Berry and M. Tabor, Level clustering in the regular spectrum, Proc. R. Soc. A **356**, 375 (1977).

[88] O. Bohigas, M. J. Giannoni, and C. Schmidt, Characterization of chaotic quantum spectra and universality of level fluctuation laws, Phys. Rev. Lett. **52**, 1 (1984).

[89] H. Stöckmann, *Quantum chaos: an introduction* (Cambridge University Press, 1999).

[90] T. A. Brody, A statistical measure for the repulsion of energy levels, Lettere al Nuovo Cimento **7**, 482 (1973).

[91] M. V. Berry and M. Robnik, Semiclassical level spacings when regular and chaotic orbits exist, J. Phys. A **17**, 2413 (1984).

[92] I. C. Percival, Semiclassical theory of bound states, Advances in Chemical Physics **36**, 1 (1977).

[93] A. J. Lichtenberg and M. A. Lieberman, *Regular and stochastic dynamics*, 2nd ed. (Springer, 1992).

[94] C. R. Harris *et al.*, Array programming with NumPy, Nature **585**, 357 (2020).

[95] P. Virtanen *et al.*, SciPy 1.0: Fundamental Algorithms for Scientific Computing in Python, Nature Methods **17**, 261 (2020).

[96] W. H. Press, S. A. Teukolsky, W. T. Vetterling, and B. P. Flannery, *Numerical Recipes*, 3rd ed. (Cambridge University Press, 2007).

[97] D. J. Papoular, *Manipulation of interactions in quantum gases: a theoretical approach*, Ph.D. thesis, Université Paris-Sud, Orsay, France (2011).

[98] B. Lauritzen and N. D. Whelan, Weyl expansion for symmetric potentials, Ann. Phys. **244**, 112 (1995).

[99] N. Pavloff, Discrete symmetries in the Weyl expansion for quantum billiards, J. Phys. A **27**, 4317 (1994).

[100] D. Wintgen and H. Friedrich, Classical and quantum-mechanical transition between regularity and irregularity in a Hamiltonian system, Phys. Rev. A **35**, 1464(R) (1987).

[101] T. Prosen, Berry-Robnik level statistics in a smooth billiard system, J. Phys. A **31**, 7023 (1998).

[102] E. J. Heller, *The semiclassical way to dynamics and spectroscopy* (Princeton University Press, 2018).

[103] H. Meyer, Theory of the Liapunov exponents of Hamiltonian systems and a numerical study on the transition from regular to irregular classical motion, J. Chem. Phys. **84**, 3147 (1986).

[104] M. A. M. de Aguiar, C. P. Malta, M. Baranger, and K. T. R. Davies, Bifurcations of periodic trajectories in non-integrable Hamiltonian systems with two degrees of freedom: numerical and analytical results, Ann. Phys. **180**, 167 (1987).

[105] M. Baranger, K. T. R. Davies, and J. H. Mahoney, The calculation of periodic trajectories, Ann. Phys. **186**, 95 (1988).

[106] B. Ravon, P. Méhaignerie, Y. Machu, A. Durán Hernández, M. Favier, J. M. Raimond, M. Brune, and C. Sayrin, Array of individual circular Rydberg atoms trapped in optical tweezers, Phys. Rev. Lett. **131**, 093401 (2023).

[107] J. M. Robbins, Discrete symmetries in periodic-orbit theory, Phys. Rev. A **40**, 2128 (1989).

[108] B. Lauritzen, Discrete symmetries and the periodic-orbit expansions, Phys. Rev. A **43**, 603 (1991).

[109] E. J. Heller, Bound-state eigenfunctions of classically chaotic Hamiltonian systems: scars of periodic orbits, Phys. Rev. Lett. **53**, 1515 (1984).

[110] J. Stein and H. Stöckmann, Experimental determination of billiard wavefunctions, Phys. Rev. Lett. **68**, 2867 (1992).

[111] C. J. Turner, A. A. Michailidis, D. A. Abanin, M. Serbyn, and Z. Papić, Weak ergodicity breaking from quantum many-body scars, Nat. Phys. **14**, 745 (2018).

[112] A. A. Michailidis, C. J. Turner, Z. Papić, D. A. Abanin, and M. Serbyn, Slow quantum thermalization and many-body revivals from mixed phase space, Phys. Rev. X **10**, 011055 (2020).

[113] W. W. Ho, S. Choi, H. Pichler, and M. D. Lukin, Periodic orbits, entanglement, and quantum many-body scars in constrained models: matrix product state approach, Phys. Rev. Lett. **122**, 040603 (2019).

[114] E. J. Heller, Wavepacket dynamics and quantum chaology, in *Les Houches Session LII (1989): chaos and quantum physics*, edited by M. J. Giannoni, A. Voros, and J. Zinn-Justin (Elsevier, 1991).

[115] G. Su, H. Sun, A. Hudomal, J. Desaules, Z. Zhou, B. Yang, J. C. Halimeh, Z. Yuan, Z. Papić, and J. Pan, Observation of many-body scarring in a quantum simulator, Phys. Rev. Rsearch **5**, 023010 (2023).

[116] P. N. Jepsen, Y. K. Lee, H. Liu, I. Dimitrova, Y. Margalit, W. W. Ho, and W. Ketterle, Long-lived spin-helix states in Heisenberg magnets, Nat. Phys. **18**, 899 (2022).

[117] J. B. Keller, Corrected Bohr-Sommerfeld quantum conditions for nonseparable systems, Ann. Phys. **4**, 180 (1958).

[118] C. C. Martens and G. S. Ezra, Classical and semiclassical mechanics of strongly resonant systems: a Fourier transform approach, J. Chem. Phys. **86**, 279 (1987).

[119] S. K. Knudson, J. B. Delos, and D. W. Noid, Bound state semiclassical wave functions, J. Chem. Phys. **84**, 6886 (1986).

[120] P. J. Richens and M. V. Berry, Pseudointegrable systems in classical and quantum mechanics, Physica 2D **2**, 495 (1981).

[121] E. O. Brigham, *The Fast Fourier Transform and its applications* (Prentice Hall, 1988).

[122] I. C. Percival, Variational principles for the invariant toroids of classical dynamics, J. Phys. A **7**, 794 (1974).

[123] H. Friedrich and D. Wintgen, The hydrogen atom in a uniform magnetic field - an example of chaos, Phys. Rep. **183**, 37 (1989).

[124] R. Blümel and W. P. Reinhardt, *Chaos in atomic physics* (Cambridge University Press, 1997).

[125] C. Iu, G. R. Welch, M. M. Kash, and D. Kleppner, Diamagnetic Rydberg atom: confrontation of calculated and observed spectra, Phys. Rev. Lett. **66**, 145 (1991).

[126] M. Courtney, H. Jiao, N. Spellmeyer, D. Kleppner, J. Gao, and J. B. Delos, Closed-orbit bifurcations in continuum Stark spectra, Phys. Rev. Lett. **74**, 1538 (1995).

[127] M. V. Berry, Regular and irregular wavefunctions, J. Phys. A **1977**, 2083 (1977).

David Papoular
LPTM, CNRS & Univ. Cergy–Pontoise
2 avenue A. Chauvin, Pontoise
F–95302 Cergy–Pontoise cedex, France
Phone: +331 34 25 75 07
Email : `david.papoular@u-cergy.fr`
Web page: `http://www.normalesup.org/~papoular`

Born June 10th, 1984 in Paris
Citizenship: French
Single

Member of the American Physical Society
Frequent referee for PRL, PRA, JSTAT

Curriculum

2015 –	**Faculty researcher at CNRS (currently Chargé de Recherche CRCN7)** Laboratoire de Physique Théorique et Modélisation, CNRS & Univ. Cergy–Pontoise, UMR 8089 (France)
2011 – 2015	**Four–year post–doctoral fellow at the BEC Center, University of Trento, Italy** Advisors: Profs. L.P. Pitaevskii & S. Stringari.
2007 – 2011	**PhD student at Laboratoire de Physique Théorique et Modèles Statistiques** (CNRS — Univ. Paris–Sud, France). Advisor: Prof. G.V. Shlyapnikov. Title: *Manipulation of Interactions in Quantum gases: a theoretical approach.* PhD thesis defended on July 11th, 2011 (passed with honours).
2006–2007	**Graduate studies program at ENS–Ulm, Paris** (*M2 Physique Quantique CFP*, passed with honours)
2004–2006	Undergraduate studies in Physics and Mathematics at ENS–Ulm, Paris (passed with honours)
July 2004	**Admitted at École Normale Supérieure, Ulm, Paris**
2001–2004	***Classes préparatoires*, Mathematics and Physics** (MPSI & MP*, Lycée Louis–le–Grand, Paris 5e)

Laboratory experience

Feb. – Aug. 2006	**Internship in Prof. W.D. Phillips's *Laser Cooling and Trapping* group** (NIST, Maryland, USA)
July 2005	**Internship in Prof. S. Haroche's *Cavity Quantum Electrodynamics* group** (LKB, ENS Paris)

Organization of scientific events

June 2016	**Main organizer of the workshop entitled "Dynamics & Transport in Quantum Gases"** 4–day workshop at Cergy–Pontoise University, co–organized with Profs. A. Honecker and Ph. Lecheminant

Student supervision

2021 –	**Supervision of Benoît Zumer's PhD thesis** Defence planned for December 2024 Title: Quantum and classical mechanisms blocking the thermalisation of interacting Rydberg atoms One joint publication in Phys. Rev. A (published in 2023), one submitted (April 2024)
Apr.–Jul. 2020	**Four–month co–supervision of Emily Qiu's M2 (graduate) internship**
2012 – 2013	**One–year co–supervision of a PhD student** (N. Bartolo, Trento ; 1 joint publication in Phys. Rev. A (2013))

Teaching experience

2018 –	**Graduate teaching, ENS Ulm (Paris)** , ICFP graduate quantum physics programme Exercise sessions for 5th–year (M2) Physics students.
2015 –	**Graduate teaching at Université de Cergy–Pontoise** M2 lectures (2017–) and exercise sessions (2015–2017) for 2nd (L2) and 5th–year (M2) Physics students.
2005 – 2011	**Undergraduate teaching assistant,** U. Paris–Sud & Lycée Louis–le–Grand, Paris 5e (classes préparatoires) Lectures and exercise sessions for 2nd (L2 & MP*) and 4th–year (M1) Physics students.

Computer skills

C++, Python ; Matlab, Mathematica . . . ; LaTeX, Microsoft Word.

Language skills

French: native speaker ; **English**: fluent ; **Italian**: read, written, and spoken.